Non-stoichiometry and radiation damage effects in zirconium carbide and layered carbide ceramics for nuclear fuel cladding applications

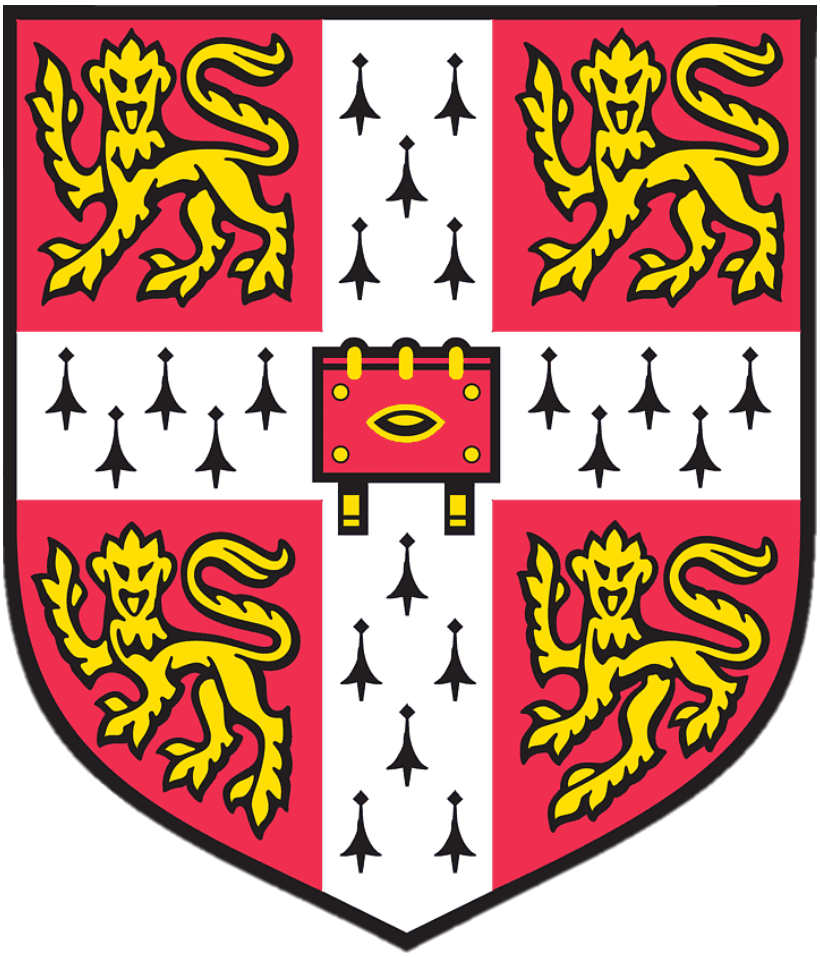

Dhan-sham Bharat Kumar Rana

Department of Earth Sciences

Darwin College, University of Cambridge

This dissertation is submitted for the degree of

Doctor of Philosophy

November 2020

Declaration

This thesis is the result of my own work and includes nothing which is the outcome of work done in collaboration except as declared in the preface and specified in the text. It is not substantially the same as any work that has already been submitted before for any degree or other qualification except as declared in the preface and specified in the text. It does not exceed the prescribed word limit for the relevant Degree Committee.

Non-stoichiometry and radiation damage effects in zirconium carbide and layered carbide ceramics for nuclear fuel cladding applications

Dhan-sham Bharat Kumar Rana

Summary

Sub-stoichiometric Zirconium Carbide (ZrC) is a viable candidate for use in nuclear environments as it has shown desirable thermo-physical properties and an ability to tolerate radiation damage. The thermo-physical properties have been reported to be sensitive to the stoichiometry of the rock salt form of ZrC which ranges from C/Zr = 1.00 to 0.55 in the phase diagram. However, there is a scatter in the reported physical properties as a function of carbon content that varies based on synthesis methods, fabrication conditions and methods of carbon content measurement. Thus, accurately determining the carbon content of ZrC is essential to understanding this physical property variation.

ZrC pellets of nominal stoichiometries ranging from 0.6 to 1.00 were prepared by reactively hot-pressing zirconium hydride and graphite powders in varying ratios, which were then sintered at 1500, 1700 and 2000°C to produce pellets. The total carbon content was evaluated using combustion carbon analysis and the values were lower than the nominal (as mixed) carbon content.

ZrC samples were further analysed by ^{13}C nuclear magnetic resonance (NMR) spectroscopy, which revealed the presence of carbon in three different environments: carbon bound within ZrC, graphitic and amorphous carbon. Total carbon content values were corrected to reflect the proportion of ZrC bonded carbon which were, in some cases, significantly lower than analysed values. The centre of gravity of the ZrC bonded carbon resonance was observed to shift to a higher frequency (more positive ppm), for lower carbon content samples, consistent with a more metallic response. The ZrC cell parameter for all samples increased ~linearly with carbon content, matching one of the two trends observed in the literature. Scanning electron microscopy (SEM) images showed that increasing grain size with decreasing carbon content in ZrC was accompanied by increasing of inter-and intragranular carbon as the carbon content of the sample decreased.

ZrC samples sintered at 2000°C were irradiated with 5 MeV protons to doses of 0.015 and 0.031 dpa to examine the effects of radiation damage. A systematic increase and emergence in the intensity of a shoulder to the main peak, in the NMR spectrum, was observed at higher frequencies with increasing irradiation dose in the C/Zr = 1.00 (nominal). This behaviour was consistent with the pristine NMR

spectra of more metallic samples indicating that a number of vacancies occurred due to irradiation. An increase in Raman signal intensities (inter/intra-granular dark regions) with increasing irradiation dose suggests that carbon displaced from the ZrC lattice via irradiations migrates toward these areas – in addition to vacant sites. Sink efficiency was proposed to be supplemented by grain size and boundary width. ZrC was observed to maintain its rock salt structure after irradiation. Additionally, the Nb_4AlC_3 layered carbide phase was investigated as it has also shown the ability to tolerate vacancies on carbon sites. NMR of Nb_4AlC_3 showed that multiple carbon environments were present in the sample. The intensity of vacant sites was observed to fit the vacancy avoidance model best.

Publications

1. Rana, D.B.K., Solvas, E.Z., Lee, W.E. et al. An investigation of the long-range and local structure of sub-stoichiometric zirconium carbide sintered at different temperatures. Sci Rep 10, 3096 (2020)

2. Gasparini, C., Rana, D.B.K, Le Brun, N., Horlait D, Markides CN, Farnan I, Lee WE. On the stoichiometry of zirconium carbide. Sci Rep 10, 6347 (2020).

Review article:

3. Yutai Katoh, Gokul Vasudevamurthy, Takashi Nozawa, Dhan-Sham Rana, Ian Farnan and Lance L. Snead. Properties of Zirconium Carbide for Nuclear Fuel Applications. Reference Module in Materials Science and Materials Engineering, Comprehensive Nuclear Materials (Second Edition), Volume 7 (2020)

“I don’t believe in no win scenarios” – James T. Kirk

In memoriam

I would like to dedicate this thesis to my mother, who passed away at the start of my PhD. Thank you for always encouraging me to strive for more, believing in me, teaching me kindness, and making me a better person. Life has been tough without you but the memories we made I hold close to my heart. You are loved and missed dearly – I wish you could see what is to yet come. I hope I have made you proud and that I am on my way to becoming the man you would have wanted me to become.

I would like to thank my father – who has been a beacon of light, hope and strength throughout these years. Your spirit, drive, optimism, and passion for life are inspiring. You came to the U.K. from Tanzania when you were 13 years old and worked every day of your life, to help your family and eventually your children and wife setting aside your ambitions and aspirations. This is also for you dad.

I would like to thank my fantastic sister Jem, who has done more for me than I can mention here, and my wonderful brother-in-law Baz for their unconditional support and love as well as providing a place to stay whilst I worked at Imperial and studied for my MRes. I owe you both more than I can express here, and I am lucky to have you both in my life.

Acknowledgements

I would like to thank Westinghouse Electric Company LLC, Westinghouse Electric Sweden AB, The U.S. Department of Energy (Award Number DOE -NE-00082222) and the Engineering and Physical Sciences Research Council (EPSRC) for sponsoring this project.

I would like to thank Professor Ian Farnan for guiding me, being kind, pushing me and believing in me – no matter how busy you were you always tried to make time for stimulating discussion. Thank you for sharing your foundational knowledge and methods of reasoning with me about being a good scientist. Many of the valuable, golden nuggets of advice that you imparted onto me will stay with me for the rest of my life. I would also like to thank Claire Armstrong who has regularly gone above and beyond to help me, whether that be with emergency conference travel or with arranging meetings, or just being there to listen. You are wonderful, my time at Cambridge would have not been the same without you.

I would like to thank the following people who have helped with the setting up or have aided with parts of this project: Dr Eugenio Zapata-Solvas for his immense help in sample fabrication at Imperial College and guiding me through multiple lab processes as well as being a good mentor. Professor Bill Lee for imparting his knowledge of ZrC to me. Professor Michael Carpenter who let me occupy a portion of his lab for two years and allowed me to use the planetary ball miller. Dr Emilie Ringe, Professor Simon Redfern and Dr Marion Louvel for their help with Raman spectroscopy. Dr Iris Buisman for her help on the SEM. Dr Simon Middleburgh and Lars Hallstadiu of Westinghouse Electric Company. Dr Claudia Gasparrini for her stimulating conversations on ZrC and for co-authoring a paper with me. The Dalton Cumbrian Facility and the Flerov Laboratory of Nuclear Reactions (Joint Institute for Nuclear Research) and all their staff for providing assistance during irradiation campaigns. I would also like to thank my brother Bups Daya for numerous conversations and for uplifting me through tough times.

I am eternally grateful for Dr Giulio Isacco Lampronti who spent hours and hours in conversation with me discussing experimental results and techniques – these conversations were foundational in my development as a scientist – thank you. Furthermore, thank you for trusting me to work unsupervised for days on end and under tight deadlines – it helped develop my confidence and competence as a scientist.

I would also like to acknowledge everyone in the workshops who helped me across the University of Cambridge, especially Christopher Parish (The Department of Earth Sciences) who helped me source components when experiments broke. Richard Nightingale (The Department of Chemistry who helped create a custom stage for the irradiation experiments). Alistair Ross (The Department of Engineering) who helped me with EDM machining of ZrC samples.

From Darwin College I would like to sincerely thank Dr Duncan Needham and Dr Aylwyn Scally who were able to arrange funding from a range of sources and find emergency accommodation when unexpected events struck. I would also like to thank the former master of Darwin College, Professor Mary Fowler, for inviting me to many lunches and always being warm and friendly and finally all the staff and students at Darwin College who made my time enjoyable.

Within the wider circles of Cambridge University, I would like to thank:
Maria Juliet Livadiotis of ΛΔΠ at The University of Cambridge. Your influence has been formative, your guidance has been enlightening, and your unconditional support has been transformative.
Muhammad Tahir, Joe Koebele, Andrey Andreev, Billy Suwanto, for their support and encouragement and belief in me, especially in my first year, and for being all round a fantastic group of people.

From Imperial College London and within the CDT I would like to thank the following people: Arun Khuttan and Yadu Krishnan - your boundless enthusiasm, friendship, belief in me and encouragement kept me sane through some difficult phases and life in general- I am lucky to have you as close friends. Dr Sokratia Georgaka and Dr. Alex Kenich for their friendship, camaraderie, and many good times.

I would like to thank a lot of the people I met throughout my PhD journey - you got me through writing up this thesis and the last experiments with COVID.
Joe Lillington, for keeping me caffeinated and reminding me to take breaks over these many years and have just generally for a great friend. Roshni Modhvadia it is very clear you maintained my sanity throughout these times our friendship is very dear to me. Luca, thank you for making sure I looked after both my physical and mental health during the lockdown and for being a great friend. Amber I would like to thank you for being one of the best flat mates and always making me laugh often. Tom Goût for your company and camaraderie throughout my PhD. Dr Aleksej Popel for being a source of company and good spirits in my final year. I would also like to thank all the people that read my thesis – most of

whom are listed above. I would also like to thank my academic peers: Joe Lillington, Giles Rought Whitta, Tom Goût, Dr Aleksej Popel, Amy Chen and Emma Perry.

My friends from wider collegiate Cambridge made my experience more enjoyable. Hamsini Marada and Vinitika Vij you made my third year at Cambridge and kept me motivated through long nights of experiments, thank you for being two of my biggest fans. Thanks to Jordan Braganza, Adrian Gallie, Chris Davis, Indigo Orton, Lucas Caiado, Richard Mervin, Jaspreet Singh, Nick Wilson, Rebecca Caeser, Sarah Fallon, Isabelle Esain, Swati Keshri.

Last but by no means least, I would like to show my sincere appreciation to my friends from home Sagar Shah, Priyen Patel, Arjun Kotecha Amit Mistry, Sunny Tank and most recently Dr Shu Sachdev. I am very lucky to have had your support and fierce friendship throughout these years. Sagar, thanks for being there for me in my first and second years you made all the difference. Dr Andrew Ward for his enduring friendship and encouragement. Sanjeev Kumar Mistry for his support and stimulating conversations. Dr Joshua Argyle for instilling many positive values in me and being a great example during my undergraduate degree and beyond. In no order; Henry Lau, Parth Upadhyay, Daniel Robson, Ben Pepper, David Thomas, Matt Duggan, Heidi Thiemann, Louise McCaul, George Weaver, Reena Magudia, Dr Rosie Johnson, Áine O'Brien, Dr Sheila Person, Dr Stephanie Kellet, Dr Tim Hewlett, Lucy Williams, Jack Hampson, and Dr Tracy Dickens of SSUK, for the many laughs and good times. I would like to thank those members of my wider family who supported us through times of crisis and Arun and Bhanu Patel, for checking up on me throughout my PhD and making sure my father was ok whilst I was away.

Abstract

Sub-stoichiometric Zirconium Carbide (ZrC) is a viable candidate for use in nuclear environments as it has shown desirable thermo-physical properties and an ability to tolerate radiation damage. These thermophysical properties, in some cases, are sensitive to stoichiometry making ZrC a customisable and versatile material whose properties can be optimised by varying the carbon content. Whilst the majority of studies have focused on producing and measuring different properties of ZrC, very few studies have focused on accurately measuring the carbon content for a specified fabrication route resulting in a scatter in the data of some physical properties (for example the lattice parameter). Accurately determining the carbon content is key to correctly referencing the thermo-physical properties.

To study variations in the carbon content and the influence of sintering temperature during fabrication, sub-stoichiometric zirconium carbide pellets of nominal stoichiometries ranging from C/Zr = 0.5 to 1.00 were prepared by reactive hot-pressing precursor powders of zirconium hydride and graphite in varying ratios at sintering temperatures of 1500, 1700 and 2000˚C. A novel method using ^{13}C nuclear magnetic resonance (^{13}C NMR) was used to identify carbon present within and dissociated from the ZrC structure, allowing the true stoichiometry of the ZrC phase to be determined.

Combustion carbon analysis was used to determine the total carbon content of the samples. These samples showed lower carbon contents than the nominal values reported in the literature. Solid-state, static ^{13}C NMR spectroscopy of the samples revealed the presence of carbon bonded in the ZrC structure, amorphous carbon, and graphitic carbon. Results presented here show that the standard methods of obtaining the carbon content such as carbon analysis and nominal methods in overestimate the ZrC bonded carbon in the samples. The NMR corrected carbon content for the lowest nominal carbon content sample was found to have C/Zr = 0.50 which is lower than the stable compositional limit for ZrC according to the phase diagram (C/Zr = 0.55). This result was in good agreement with theoretically stable carbon contents predicted by recent density functional theory calculations in the literature. For the samples sintered at

2000˚C, the main ZrC carbon resonance was observed to systematically shift to higher frequency (ppm) for lower carbon content samples.

SEM on samples sintered at 2000˚C revealed the presence of microscale inter- and intra-granular dark structures throughout the sample. These were observed to become increasingly connected as the carbon content of the sample was reduced. An increase in the grain size was also observed for samples of lower carbon content.

The layered Nb_4AlC_3 MAX phase was also investigated due to its previously reported ability to accommodate a large number of carbon vacancies and its high yield. This sample was revealed to be deficient in carbon by 36.6% with respect to the nominal carbon content but did not exhibit exsolved sp^2 phases. Two shoulders observed in the main resonance indicated that multiple carbon environments exist within the material. The intensities and the location of these resonances were observed to best fit a vacancy avoidance model.

Irradiations, with 5 MeV protons to 0.015 and 0.031 dpa, on samples sintered at 2000 ˚C produced a rearrangement of the ZrC bonded carbon within the sample. This was predominantly observed through systematic changes in the ^{13}C NMR line shape with increasing irradiation dose. Comparison of the pristine and irradiated nominal C/Zr = 1.00 and 0.60 NMR spectra clearly showed the emergence and growth of a shoulder to the main peak at higher frequencies (more positive ppm). The intensity of this shoulder increased with increasing carbon content. Although no significant change in the centre of gravity was observed in the sample due to irradiation, the systematic evolution of this shouldering peak at higher ppm indicated that vacancies might have been created in the ZrC structure due to irradiation. This was evidenced by the NMR spectra of pristine samples of successively decreasing carbon contents which exhibited similar systematic line shape evolution. The possible creation of vacancies and the exsolution of carbon from within the ZrC structure was further evidenced by an increase in the signal strength of the Raman spectra in the dark regions of the sample with increasing irradiation dose, which implied that the quantity of carbon within this region increased. Irradiations were also observed to increase the lattice parameters of the samples for a given stoichiometry which increased with successive irradiation doses. This result indicated

that the swelling of the lattice parameter increased with increasing irradiation dose. Irradiations to 2.4 dpa using 158 MeV Xe confirmed the trends observed in the Raman and SEM investigations on the lower dose proton irradiated samples. Increasing the irradiation dose to 2.4 dpa with (158 MeV Xe) resulted in an increase in the lattice parameter as well as a decrease in the average grain size with the exception of the nominal C/Zr = 0.60 sample. These results indicated that the irradiation damage continued to accumulate for samples irradiated to higher doses.

The rock salt structure of ZrC was retained for all samples after irradiation demonstrating that ZrC remains stable under the irradiation conditions used in this study. However, it was revealed that a redistribution of carbon environments occur within the sample during irradiation with exsolution to unincorporated sp^2 carbon environments consistent with graphene sheets in various states of disorder. The exsolution of carbon and the production of lower carbon content ZrC appears to be the radiation response of the material under heavy (Xe) and light (^1H) ion irradiation.

Contents

Abbreviations and nomenclature

μ_{ind}	Induced dipole moment
B_0	External magnetic field (NMR)
M_z	z component of the net magnetisation (A/m)
d	Interplanar distance (nm) (XRD)
λ_l	Laser wavelength (nm) (Raman)
μ_0	Permeability of free space (1.257 × 10-6m kg s^{-2} A^{-2})
ν_f	Electromagnetic frequency (NMR)
ω_0	Larmor (Hz) (NMR)
μ	Classical magnetic moment (NMR)
C/Zr	The atomic ratio of carbon/zirconium
CG	Centre of gravity
CPMG	Carr–Purcell–Meiboom–Gill
FWHM	Full width at half maximum
h	6.626×10^{-34} J·s (NMR)
$\hbar$	Reduced Plank's constant (h/2π)
h, k, l	Miller indices
ICSD	Inorganic Crystal Structure Database
IR	Infra-red
m	Meters
MAS	Magic angle spinning (54.74°)
MHz	Megahertz (1 x 10^6 Hz (hertz))
MPa	Mega pascal (1 x 10^6 pa (pascal))
nm	Nanometres (1 x 10^{-9} meters)
^{13}C NMR	Carbon-13 nuclear magnetic resonance
Nominal carbon content	The proportion of carbon in the final sample as determined from the precursor powder carbon content

ppm	Parts per million (NMR)
RF	Radio frequency
rpm	Revolutions per minute
s	Seconds
SEM	Scanning electron microscopy
T1	Longitudinal relaxation time
T2	Transverse relaxation time
TMS	Tetramethylsilane (NMR)
W	Watt (Joule/second)
XRD	X-ray powder diffraction
ZrC	Sub-stoichiometric zirconium carbide
θ	Angle of incidence in XRD
μm	Micrometres (1 x 10^{-6} meters)
a	Lattice parameter
c	Vacuum speed of light (299 792 458 m/s)
f	Frequency (Hz)
v	Wavenumber (cm^{-1})
E	Electric field (N/C)
I	Quantum mechanical angular momentum of spin (NMR)
α	Molecular polarisability (C m^2 V^{-1})
γ	Gyromagnetic ratio (rad·s^{-1} ·T^{-1}) (NMR)
δ	NMR shift (ppm) (NMR)
ε	Microstrain
ε_0	Permittivity of free space (8.854× 10^{-12} m^{-3} kg^{-1} s^4 A^2)
λ	Wavelength of X-rays (XRD)
ρ	Resistivity (μΩ cm)
σ	chemical shielding (NMR)
L_a	The sp^2 crystallite size (nm) (Raman)

dpa	Displacements per atom
MeV	Mega electron volts (1 x 10^6 eV)
eV	1.602 x 10^{-19} Joules
SRIM	Stopping and range of ions in matter
Dose 1 (protons)	0.015 dpa
Dose 2 (protons)	0.031 dpa
kHz	Kilo hertz (1 x10^3 Hz)
DFT	Density functional theory
UO_2	Uranium dioxide
Å	Angstrom (1 x 10^{-10} m)
TEM	Transmission electron microscopy
CAFFE	Carbides for Future Fission Environments
ZrC	Sub-stochiometric ZrC used interchangeably with ZrC_{1-x} – unless explicitly stated as being stoichiometric ZrC

Table of Figures

Table of tables

Chapter 1 Context and methods

1.1 Introduction and context

Nuclear energy is currently one of the only modes of electricity generation that is capable of meeting the requirements for reliable, safe, low carbon and baseload energy supply. To meet these ever-increasing demands, the Gen IV (generation IV) [1], [2] international forum (GIF) was established (circa 2000). The Gen IV forum proposed a range of reactor designs that are designed to be inherently safer, more economical, and more efficient than previous and current nuclear reactors. Aside from conventional electricity generation, the Gen IV forum specifies reactor concepts that are intended to be used in a diverse range of applications such as the production of high-quality process heat and district heating [1], [3].

To achieve higher economic, safety and power outputs as compared to conventional reactors, Gen IV reactors are designed to operate in non-typical nuclear conditions. In these scenarios, components within the primary coolant loop may be exposed to a range of operational environments including high radiation flux and high temperatures. As such, non-traditional nuclear materials must be considered for Gen IV reactor components [4]. In particular, the fuel cladding must be radiation resistant but also must provide integrity to the fuel element structure and prevent contamination of the primary coolant loop from fission products [5], [6].

1.1.1 Rationale for choice of materials used in this study.

The initial focus of this PhD was to characterise layered Zr carbide MAX phases and their associated radiation tolerance. Preliminary investigations were to be carried out on ZrC which forms a component of the ZrAlC MAX phase structures in addition to appearing as a secondary phase. For other MAX phases, the M and X elements often appear in their binary carbide form, after irradiation.

Due to a combination of the low yield of ZrAlC MAX phases and interesting and complex behaviour exhibited by the ZrC samples in preliminary experiments (Chapter 2) as well as in the literature [7], [8] – it was decided that this thesis would focus primarily on stoichiometry and defect distribution in ZrC_{1-x} (chapters 2 and 3). Furthermore, a high yield Nb_4AlC_3 MAX phase became available for study that has also been reported to exhibit non-stoichiometry and ordering of vacancies similar to ZrC_{1-x} [9], [10], [11, p. 4].

ZrC has long been considered for use as a coating for nuclear fuel structures, due to its favourable, thermophysical properties such as thermal conductivity and thermal expansion under irradiation[1]. ZrC has also been shown to have good fission retention and very good irradiation tolerance. It has a high melting point which makes it ideal for applications in high-temperature nuclear reactors and aerospace applications such as rocket nozzle exhausts [12], [13]. These material characteristics would be essential for high-temperature reactor environments such as the high-temperature gas-cooled reactor (HTGR) concept proposed in the Generation IV International Forum (GIF).

The HTGR operates at significantly higher temperatures as compared to conventional nuclear reactors. Typically, previous HGTR designs such as the Dragon reactor in the UK, the Arbeitsgemeinschaft Versuchsreaktor reactor in Germany, and even envisaged future HTGR reactor designs have used or intend to use either prismatic or pebble bed fuel geometries comprised of Tri-structural Isotropic particle fuel (TRISO).

The core of a typical TRISO fuel consists of a fuel kernel (uranium or thorium) containing the fissile isotope material. The fissile material is surrounded by a number of concentric layers that contribute to the structural integrity, fission product retention capability and performance of the fuel. These layers, in order from the fuel kernel, consist of a porous carbon buffer layer, an

[1] Thermophysical properties are discussed in detail in [12], a publication that was updated due to new findings from this project.

inner pyrolytic carbon layer, an interlayer (typically made/ designated to be made from Silicon Carbide (SiC)) and finally an outer pyrolytic carbon layer.

Elaborating on the composition of each layer; the buffer layer, made from porous carbon, provides a sink for gaseous fission products produced within the fuel kernel during reactor operation. The inner pyrolytic carbon layer further acts as a support for the subsequent SiC layer reducing stress and protects the fuel kernel in the SiC deposition manufacturing process. The SiC layer provides the mechanical strength to the fuel particle through the fabrication process, whilst acting as a fission product retention barrier. And finally, the outer layer protects the fuel particle and specifically the SiC layer [14]–[16].

In the context of TRISO fuel, a ZrC layer has been proposed as a substitute SiC layer as ZrC can readily adopt a wide range of non-stoichiometry on carbon sites, unlike SiC. It is the presence of these vacant sites that have been hypothesised to act as a sink for fission products and defects produced during irradiation. As fission product retention is a key feature of the TRISO fuel interlayer exploring how stoichiometry affects the ability to sink defects is essential.

In addition, ZrC is an extraordinary material as it can tolerate a large number of vacancies on carbon sites (~55%). It has been shown in the literature, that a vast proportion of the thermal and physical properties of ZrC vary as a function of stoichiometry [12], [13], [17]. The sensitivity of the thermophysical properties of ZrC with respect to the carbon content makes ZrC a highly customisable and versatile material that can be tailored to a plethora of applications [7]–[9]. However, scatter exists in the values of physical properties with respect to the carbon content that makes the determination of physical property trends, in some instances, difficult.

This scatter, for example in the lattice parameter with respect to the carbon content, produces two trends (see section 1.2 for further details). Various explanations have been proposed as to

the nature and the mechanism behind these two trends, however, little work has been undertaken in understanding if the carbon content used to reference these property values is accurate. This is essential given the sensitivity of the physical properties to ZrC, the range of fabrication methods used to fabricate ZrC, and ultimately understanding the radiation tolerance of ZrC with respect to stoichiometry. Finally, the ability to correctly determine the carbon content becomes essential especially in a nuclear environment where strict materials qualification procedures must be adhered to.

Almost all previous studies (see section 1.2) have treated conventional carbon analysis techniques almost as a black box – with little or no understanding of how individual fabrication procedures influence the carbon content.

1.2 Literature review

The literature review of pristine ZrC irradiated ZrC and the Nb_4AlC_3 MAX phase are presented within this section. These are divided into three parts to reflect the three main results sections of the thesis.

1.2.1 Pristine ZrC literature review

Zirconium carbide can be viewed as an FCC version arrangement of Zr and C, where Zr takes on an FCC structure, and carbons are located on the octahedral sites to form the rock salt structure.

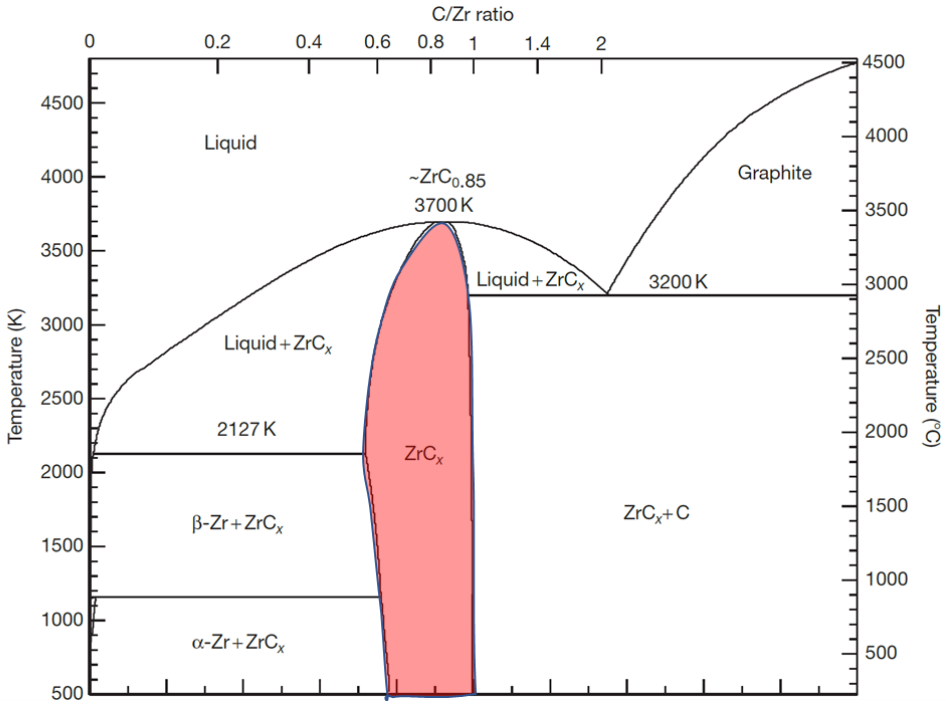

Figure 1 Phase diagram of ZrC. The section highlighted in red indicates the homogeneity region, where ZrC exists [13].

The phase diagram of the Zr-C system consists of several different regions and boundaries which have been determined theoretically and experimentally validated [18], [19]. The main region of interest in the phase diagram is highlighted in red in Figure 1. This denotes the region where ZrC can exist and spans a range from C/Zr 0.60 to 1.00. Previously, the maximum value of the phase melting temperature was reported to be 3420°C [20] to 3426°C [18] with the carbon content C/Zr ~ 0.78 [18] to 0.85 [13]. At hyper-stoichiometric carbon contents (C/Zr > 1.00) stoichiometric ZrC is observed to exist in addition to excess carbon. Below C/Zr = 0.85 a ZrC eutectic is formed accompanied by an increase in the melting point from ~ 1853 to ~3426°C. From C/Zr = 0.85 onward the melting is seen to decrease from 3426 to 2826°C. Below 1926°C and above C/Zr = 1.00, ZrC and graphite exist together.

The renewed interest in sub-stoichiometric ZrC arises from the fact that it readily adopts non-stoichiometry on the carbon sites within the unit cell, producing a sub-stoichiometric material. Within the homogeneity region of the phase diagram (Figure 1), ZrC is seen to exist over a wide sub-stoichiometric range tolerating up to ~45% vacancy concentration. Although ZrC has

been observed to maintain its structure over this sub-stoichiometric range – the reduction in the carbon content is seen in the literature to have a significant impact on the variation of the material properties. Seminal literature reviews of ZrC [12], [13], [17], [18] have drawn together a previously fragmented field uncovering apparent trends in material property measurements of ZrC that vary with stoichiometry.

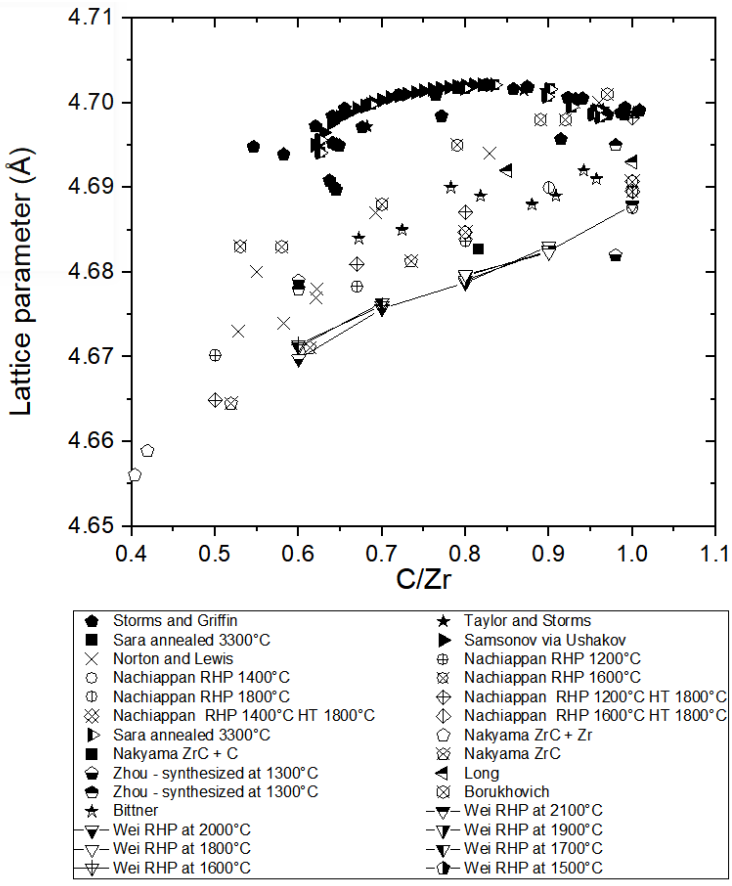

Figure 2 Lattice parameter plotted with respect to the carbon content for studies from the literature

The lattice parameter of ZrC is an example of a physical property that is seen to vary non-monotonically with carbon content (Figure 2). A degree of scatter present within the lattice parameter data makes determining the lattice parameter associated with a particular stoichiometry challenging and introduces uncertainty in the validity of the trends. Two trends exist in the lattice parameter data plotted with respect to the carbon content (Figure 2); the first is an almost linear trend, and the second is a parabolic non-monotonic trend. It has been

proposed that the parabolic trend occurs due to competing effects of vacant environments (at lower C/Zr) and increased bonding strength at higher C/Zr [13]. It has also been proposed that vacancies in the lattice cause a change in the uniform strain of the material and hence cause a change in the lattice parameter [4]. More recently, Xie *et al.* have suggested that an increase in the lattice parameter may be due to the increasing anisotropy and order of the carbon vacancies [21]. Due to the sensitivity of ZrC to vacancies, the majority of previous studies have likely produced vastly different materials of varying stoichiometries as a result of using different precursor powders, different fabrication methods and different carbon determination methods. Naturally, as ZrC can adopt a wide range of stoichiometries, these factors are important and likely lead to scatter in the data as is seen in Figure 2, in addition to the misreferencing of values. The presence of two lattice parameter trends in the literature indicates that factors such as accurate composition and C/Zr determination under a controlled environment are the first steps in understanding the origins of why these two trends exist. As the fabrication route directly affects the final sample [22], [23], characterising how different parameters, if varied, affect the final sample composition [24] is important.

Several different ZrC fabrication routes have been utilised in the literature. These routes include solution-based fabrication [25], [26], vapour phase fabrication [27], [28] [21], and solid-state fabrication [29]–[32] based techniques. Typically, in each study different fabrication techniques have been chosen to demonstrate different goals for instance vapour fabrication – pulse layer deposition for studying coatings and solid-state fabrication techniques provide a method of producing a relatively large quantity of high quality, machinable material for semiconductor research. In addition, the availability of equipment was the reason for choosing the solid-state fabrication route for this PhD project and more specifically uniaxial reactive hot-pressing (the details of this fabrication route is elaborated in the methods section). The following section of this literature review will focus on previous studies that have used hot-pressing to fabricate ZrC samples.

A number of studies have used commercially produced, reactively hot-pressed pellets to study ZrC [33]–[35], an acceptable approach when studying a well-characterised system. However, prefabricated pellets should not be used for studies involving ZrC due to the complexity of the system. Understanding how variables such as the sintering temperature and nominal precursor powder mixing ratios influence the final product is crucial. Once reliable fabrication routes have been established,

Common precursor powders that have been used in reactive hot-pressing include ZrO_2 reacted with graphite to produce ZrC and CO gas [29]–[32] and ZrH_2, and graphite powders to form ZrC and H_2 [12], [13], [22], [24]. In this study, the latter fabrication precursor powders will be used as the first method involves the use of a precursor power that contains oxygen. This may increase the probability of forming oxy-carbide phases and thus a less pure ZrC final product.

The most relevant systematic study, with respect to reactive hot pressing and material characterisation, was conducted by Wei *et al.* [22] who investigated the quality of ZrC_{1-x} (from here one referred to as ZrC) fabricated under different conditions. Cold-pressed ZrC pellets (nominal C/Zr = 0.60, 0.70, 0.80, 0.90 and 1.00) consisting of mixed ZrH_2 (Jinzhou Haixin Metal Materials Company, Jinzhou, China) and ZrC (Changsha Weihui Materials Company, Changsha, China), were produced using reactive hot-pressing. The two-stage hot-pressing process consisted of a first stage pressureless sintering (1300°C for 30 minutes) which facilitated the H_2 to burn off from the ZrH_2 precursor powder. The second stage was used to produce the combustion reaction and dense pellets with the addition of applied pressure (1500, 1600, 1700, 1800, 1900, 2000°C under 30 Mpa for 1 hour).

In stage 1, at a temperature of 1300°C ZrC planes were fully indexable with very weak precursor powder peaks. At 1500°C all precursor peaks had disappeared and fully indexable ZrC peaks remained. Zr diffraction peaks were also observed in the nominal C/Zr = 0.60 samples; however, these disappeared at temperatures of 1500°C. In stage two, the samples were heated to a range of sintering temperatures from 1500 to 2100°C, depending on the sample, at

30 MPa (applied 200°C below sintering temperature) with a dwell time of 60 minutes. The nominal C/Zr = 0.60 samples heated to 1500°C showed evidence of weak XRD attributed to ordered Zr_2C. These samples were further studied in a later paper by Wei *et al.* [22] but were not observed at sintering temperatures above 1500°C. Wei *et al.* observed a linear increase in the lattice parameter with decreasing carbon content which is in agreement with the approximately linear trend reported by the majority of studies (Figure 2).

An increase in the average grain size with decreasing C/Zr of hot-pressed ZrC has also been observed in several studies [22], [23]. It has been proposed that the presence of vacancies in sub-stoichiometric ZrC increases the mass transport in samples leading to larger grain growth [22]. Wei *et al.* also observed a distribution of inter and intra-granular pores and a bias for pores to migrate toward grain boundaries.

Lower temperature synthesis by hot-pressing was also investigated by Chakrabarti *et al.* [36] – in this study, Zr and ZrC were reacted to produce the desired final stoichiometry. Samples were heated to a temperature of 300°C (5ºC/min), 600°C and to their final sintering temperatures (900 to 1600°C at 6°C/min). Two oxygen (carbon monoxide) outgassing steps were used, which consisted of a hold for 15 and 10 minutes at 300 and 900°C. In the reactive hot-pressing step, temperatures were held for 30 minutes under pressure. Samples were then cooled in the oven at a rate of 10°C with pressure being released after 10 minutes into cooling. Unreacted Zr diffraction peaks were observed in samples sintered at the highest temperature indicating that either the synthesis temperature was not high enough and/or the duration of the second step was not long enough.

Zhou *et al.*[37] produced reactively hot pressed nominal C/Zr = 0.60 and 0.98 by mixing varying proportions of ZrH_2 (Chemadyne, LLC., Canoga Park, CA, USA purity 95.5%) and carbon black (BP-1100, Cabot Corporation, Alpharetta, GA, USA). The nominal mixtures were then mixed in acetone using zirconia balls for 12 hours at a speed of 50 rpm and subsequently dried. Powders were then placed into a graphite die for hot-pressing and sintering.

A two-step reactive hot-press and sintering protocol was used under an argon atmosphere. In step one, samples were heated for 2 hrs at 800°C at a ramp rate of 10°C/min which promoted the decomposition via the reaction:

$$ZrH_2 \rightarrow Zr + H_2. \quad (1.1)$$

Powders were then heated at 1300 and 2000°C for the two sample sets for a period of two hours to sinter the precursor powders and ideally produce ZrC as per the reaction below:

$$Zr + C \rightarrow ZrC. \quad (1.2)$$

Both stoichiometries of carbon produced only ZrC diffraction peaks however, ZrC diffraction peaks moved to lower 2θ for samples sintered at temperatures of 2000°C as compared with 1300°C. TEM micrographs of the nominal C/Zr = 0.98 sample showed the presence of excess carbon at 1300°C however, this disappeared after sintering at 2000°C. In contrast, no amorphous carbon was observed in the nominal C/Zr = 0.60 sample. Interestingly, the lattice parameter of the nominal C/Zr = 0.98 sample was observed to increase with increasing sintering temperature which could suggest the annealing of defects in the material, such as oxygen, at higher temperatures.

Inaccurate determination of the carbon content of samples is another area that likely contributes to scatter in the data. To correctly reference the material properties to carbon content, we must first assess if the methods used to determine the carbon content are accurate. In previous studies, nominal carbon content [37]–[42] and combustion carbon analysis [37], [42]–[49] are typically quoted. The nominal carbon content of a ZrC sample is the stoichiometric ratio of C/Zr elements that are present in the precursor powders. It is an underlying assumption in studies that quote only this value that the precursor powders fully react but, in many cases, XRD analyses show the presence of extra phases. The combustion carbon analyser technique gives the total amount of carbon in a sample which is detected upon combustion at high temperatures by IR sensors (see methods section 1.3.2). Again, in this technique, the main assumption is that the total carbon content represents carbon located in the ZrC lattice. However, TEM studies on these materials, as detailed above, have demonstrated that carbon

can exist entirely dissociated from the ZrC unit cell and that this was not detectable in XRD studies. The presence of pristine and partially destroyed graphite [50], [51] has also been previously observed in Raman investigations on ZrC [52], [53]. It is apparent that more accurate quantitative corrections are needed to determine the correct carbon content. This would address the gap in the literature where the ZrC_{1-x} phase coexists with ex-solved carbon phases. Additional literature reviews on the local structure of ZrC are introduced where experimental results are presented and discussed later.

1.2.1 Heavy ion studies on ZrC

Several studies have been undertaken in the literature that involve irradiation of different stoichiometries of ZrC using different elemental heavy-ions, with different energies, fluences and irradiation temperatures. Studies that have investigated the irradiation of ZrC with heavy-ions in any capacity are listed in Table 1.1 below, along with their relevant parameters. The purpose of this literature review is to present and summarise salient points from these studies and to highlight gaps in the literature.

The majority of studies have focused on the heavy-ion irradiation of stoichiometric ZrC whose carbon content has been determined from either the nominal ratios or through carbon analysis [4] –[10], [12], [13]. Although many studies claim that the vacancy concentration plays a key role in sinking the defects caused by irradiation, only a select number of studies [22], [46] have investigated this by conducting experiments on sub-stoichiometric ZrC.

A limited number of Raman investigations have been conducted on samples of nominally stoichiometric ZrC [52], [54], [58]. The D and G bands in the Raman spectrum provide a semi-quantitative understanding of the relative quantity of disordered graphite and pristine graphite, respectively. Irradiation of ZrC with 1.2 MeV gold ions to 0.5, 2.5, 5, 10 and 15 dpa (2.4×10^{14} to 3×10^{16} and 2×10^{13} to 4×10^{15} ions/ cm^{-1}) for single crystals (MaTecK-Germany) and polycrystals (CEA), respectively, revealed an evolution in the response with irradiation dose.

Table 1.1 - Key studies that have irradiated ZrC with heavy-ions.

Study/ Year	C/Zr	Irradiation particle	Energy	Fluence (ions/cm$^{2)}$	Dpa	Irradiation Temperature ºC
Florez, 2020 [54]	0.99	Au	10 MeV	5.00 x 10^{13}, 2.50 x 10^{14}, 5.00 x 10^{14}, 1.00 x 10^{15}, 2.5 x 10^{15} 3 x 10^{15}	0.5 2.5 5 10 25 30	800
Wei, 2018 [22]	0.60	Au	4 MeV	Up to 2.00 x 10^{16}	130	room temperature
Craciun, 2016 [59]	1.00	Ar	0.8 KeV	1.00 x 10 ^{14}, 1.00 x 10^{15}, 2.00 x10^{15}	0.2 2 4	500
Gan, 2006 [47]	1.01	Kr	1 MeV	2.52E+15 7.56 x 10^{15} 2.52 x 10^{15} 1.72 x 10^{16}	10 30 10 70	27 800
Gosset,2008 [55]	1.00	Au	4 MeV	1.00 x 10^{11} to 5.00 x 10 ^{15}	0.7 1.5	room temperature
Pellegrino	1.00	Au	1.2 MeV	2 x 10 ^{13} 2 x 10^{14} 4 x 10^{15} 3 x 10^{16}	0.12 1.22 24 182	room temperature
Pellegrino, 2013 [52]	1.00	Au	1.2 MeV Au	 3.3 x 10^{15} 2.8 x 10^{14}	1.55 1.31	room temperature
Pellegrino, 2016 [56]	1.00	Au	1.2 MeV	3.30 x 10^{15} 2.40 x 10^{14} 1.50 x 10 ^{14} 5.00 x 10^{13}	1.55 1.13 0.70 0.23	room temperature
Ulmer, 2015 [46]	0.60 0.80	Kr	1 MeV	1.52 x 10^{19} 2.50 x 10^{19} 4.99 x 10^{19}	3.9 6.4 12.8	-253, -223, 27, 200, 400, 600,700, 800
Vasile	1.00	Ar	800 keV	2.00 x 10^{15}	2.37	room temperature

Initially, pristine ZrC samples [52] showed no distinguishable D and G resonance intensities which in turn indicated no presence of disordered or pristine graphite. With increasing damage, however, activation of the D and G modes was observed. Irradiation to a fluence of 15 dpa (2.4 x 10^{14} ions/cm) resulted in the appearance of the D and G bands centred in the ranges of 1300-1400 cm^{-1} and 1550-1600 cm^{-1} indicating the presence of disordered and pristine graphite respectively after irradiation. Initially, at a fluence of 15 dpa (2.4 x 10^{14} ions/cm^2) the D and G resonance peaks remained resolvable. However, increasing the fluence increased the overlap between the two peaks, indicative of increasing disorder in the exsolved graphite. No further information was provided regarding the sampling region, which could be an issue in a sample that is spatially inhomogeneous and contains a mixture of phases.

The results from this heavy-ion study are consistent with the results from earlier proton irradiation studies [55] where TEM investigations showed that below 1 x 10^{15} ions/cm^2 the coalescence of the defects occurs and, above this fluence, the presence of extended defects such as dislocation loops and vacancy clusters occur. Thus, extended defects of carbons that have been displaced from their original lattice sites would produce a Raman signal, and if these are sunk at grain boundaries, then these are detected with Raman spectroscopy [24]. Raman can be used to gain an understanding of the evolution in the exsolution of carbon from the ZrC lattice with irradiation dose with respect to the stoichiometry. As ZrC can adopt a wide range of non-stoichiometry, analysing only the nominally stoichiometric variant gives a limited understanding of the irradiation resistance and damage accumulation in different sub-stoichiometries.

GIXRD (grazing incidence XRD) has previously been used to investigate the changes in the crystal structure of ZrC with irradiation, for all studies, grazing incidence angles have been used due to the shallow penetration depth of heavy ions. These studies on irradiated ZrC confirm that the NaCl structure is maintained after irradiation [54], [57], [60]–[62]- which is not surprising as the ZrC is widely known for its irradiation tolerance [12]. In the GIXRD

diffraction patterns, scattering from the (111) plane has been observed to decrease relative to the (200) plane [57] with increasing radiation dose. This change is attributed to some disruption of the long-range ZrC structure due to irradiation which results in a loss of scattering coherence and a decrease in the XRD intensity [54], [57].

Comparing the lattice parameter changes from XRD studies allows us to compare unit cell scale changes that occur due to radiation damage. When comparing lattice parameters of ZrC from different studies, difficulty arises due to the compositional variability of the samples which can alter lattice parameters significantly with the presence of impurities, but also with the fabrication route [12], [17], [24], [63], [64]. In addition, the lack of accuracy in C/Zr analysis techniques, which are used to reference the lattice parameter values, can lead to variability in results when comparing values from different studies. This uncertainty is further compounded by the effect of complex nonmonotonic trends reported in the lattice parameter with increasing carbon content [12], [13], [24], [64].

10 MeV Au irradiations by Florez *et al.* [54] on ZrC (C/Zr = 0.99) at 800°C to 2.5 dpa acted to rapidly increase the lattice parameter from its original value of 4.67 Å to up to 4.714 Å in ZrC (C/Zr =0.99) (as values are not explicitly reported data extracted read from a figure). A rapid increase in the lattice parameter to 4.715 was observed at a dose of 5 dpa (5 x 10^{14} ions/cm^2), after which the lattice parameter was seen to decrease by approximately 0.01 Å up to doses of 30 dpa. It was proposed that as the dose increases the scale of the defects increases, consistent with TEM work by Gosset *et al.* [55]. These defects plastically deform the surrounding lattice and induce uniform strain in the material, causing the lattice parameter to decrease [55]. It was not apparent as to why the lattice parameter continues to decrease with increasing dose; however, it was proposed that residual oxygen/impurities in the irradiation chamber could occupy lattice sites - a hypothesis that was supported by the presence of ZrO_2 phases in GIXRD. Nano-scale nodules of Zirconia were also observed on the irradiated samples. It was postulated that the different diffusion paths could be facilitated by material defects including vacant sites and dislocation lines.

Irradiations with lower energy 4 MeV Au ions by Gosset *et al.* [55] for stoichiometric ZrC for fluences of (0.0005 ,0.005, 0.05 ,0.5, 25 dpa) 1 x 10^{12}, 10^{13}, 10^{14} and 5 x 10^{15} ions/cm^2 at room temperature were observed to be approximately 4.698, 4.702, 4.703 and 4.702 Å, respectively. These values are not numerically reported but, instead, this data was determined from the graph. Each lattice value appears to also have a standard error of 0.0015 associated with it. It is evident that the lattice parameter values obtained after irradiation to fluences between 0.005 and 25 dpa (1 x 10^{13} and 5 x 10^{15} ions/cm^2) are within error of one another, which may indicate that a saturation condition occurs at these doses. This plateauing of the lattice parameter values were also observed in the previous study, suggesting that this may be a common feature at higher dpa. The values for the pristine lattice parameter are not reported in this study, but instead, an increase of 0.2% in the lattice parameter was arbitrarily reported. These lattice parameters, observed in the study by Gosset *et al.*[55], are much lower than that of the previous study - highlighting the variability of the initial material.

At lower stoichiometries of nominal C/Zr = 0.60, Wei *et al.* irradiated the ZrC with 4 MeV Au ions at room temperature [61] to a fluence of 130 dpa (2 x 10^{16} ions/cm^2), this caused an increase in the lattice parameter, from its pristine value of 4.6704 Å to its irradiated value of 4.6711 Å. Even at such a high dose, the lattice parameter remains lower than that reported by Florez *et al.*, for 25 dpa at 800^{o}C, despite the irradiation being at room temperature, in which, very little annealing of defects occurs. This bolsters the proposition that vacant sites act to sink radiation damage and thus, lower the density of extended radiation damage and lower swelling at low carbon contents.

Irradiation of ZrC (C/Zr = 1.01) with 1 MeV Kr to 10 and 30 dpa at 27 C (2.52 x 10^{15} and to 7.56 x 10^{15} ions/cm^2) by Gan *et al.* [47] resulted in an increase in the lattice parameter by 0.7 and 0.9%, respectively. Increasing the temperature to 800^{o}C and irradiating to doses 10 and 70 dpa (2.52 x 10^{15} and 1.76 x 10^{16}) resulted in a 0.6 % and 0.7% increase in the lattice parameter with respect to its pristine value. This is somewhat contradictory to another study in which ZrC

(C/Zr = 0.80 and 0.90 ZrC) was irradiated with 1 MeV Kr to 4.99 x 10^{19} ions/cm^2 and no increase in the lattice parameters was observed [46]. Accompanying this, TEM studies showed a high density of black dot type defects at irradiations at 27°C and a greater quantity of extended defects at 800°C.

It is clear from the above literature review that although great importance is placed on the vacancies as being sinks for radiation damage, the effect of high dpa radiation damage on vacancy concentrations and their distributions has not been systematically investigated. This is important as the radiation tolerance of ZrC is often attributed to the presence of vacancies. However, this has not yet been systematically investigated – which is an objective of this thesis.

1.2.2 Previous proton studies on ZrC

Previously four studies (Table 1.2) have investigated the irradiation response of ZrC with proton irradiation.

Table 1.2 - Overview of the key studies that irradiated ZrC with protons.

Study/ Year	C/Zr	Energy	Fluence (protons/cm$^{2)}$	Dose (dpa)	Irradiation Temperature ^{o}C
Yang *et al.*, 2014 [60]	0.81, 0.84, 0.92, 0.95, 0.98	2 MeV	2.0×10^{19}	2	1125
Huang *et al.*, 2014 [42]	0.9, 1.00, 1.1, 1.2	2 MeV	--------	3	800
Yang *et al.*, 2008 [65]	1.01	2.6 MeV	2.6×10^{19}	0.7, 1.5	800
Gan *et al.*, 2009 [47]	1.01	2.6 MeV	2.75×10^{19}	1.8	800

The small number of ZrC irradiation studies have all focussed on the extensive use of TEM to characterise damage. In such studies, TEM has been used to study the evolution of defects. Whilst TEM was not used to probe the material presented in this chapter, it provides a powerful tracer for understanding changes in defects down to the nanoscale at different irradiation doses. Constructing a comprehensive understanding of the irradiation response of ZrC is difficult, as obtaining time for proton irradiation at international facilities is competitive and slots are limited. The main studies in the literature have typically used energy ranges between 2.0 and 2.6 MeV, as only a small penetration depth was required for the post-irradiation analysis ~50 μm.

The similarity between studies (proton energy, the fluence and material composition) is unsurprising as three out of the four studies - Yang *et al.* (2014), (2006) and Gan *et al.* (2009)- have common contributing authors and thus investigated the irradiation of ZrC with similar

energy protons and to similar fluences varying the changes in irradiation temperature. All TEM investigations showed evidence of material defects.

Yang *et al.* [65] investigated proton irradiations to 0.7 dpa at 800°C of commercial ZrC (CERCOM). Irradiations showed the presence of extended defect Frank loops (average size = 4.3 ± 0.5 nm, average loop density = 0.22 x 10^{23} ± 0.04 cm^{-3}) [65]. An increase in the average loop size (5.8 ± 0.6 nm) was observed at the higher dose of 1.5 dpa accompanied by a significant increase in the loop density (3.37 x 10^{23} ± 0.12 cm^{-3}) – which is to be expected for higher irradiation doses. This result contradicts the significantly lower loop densities (4.2 x 10^{16} cm^{3}) seen in ZrC purchased from the same company and irradiated in similar conditions (1.8 dpa, fluence = 2.75 × 10^{19} protons/$cm^{2,}$ energy = 2.6 MeV) by Gan *et al.* The average loop diameter increased in accordance with dose, as expected. It is not clear why orders of magnitude discrepancy in the defect density was observed between the two studies given the many experimental similarities that exist between them. One possible explanation for this could be the ion milling protocols used for TEM sample preparation, where Gan *et al.* used longer periods and higher energies compared with Yang *et al.* (5 kV as opposed to 4 kV). Higher energy would impart more damage into the sample, but also increase the local heating of the samples, enhancing the defect mobility and allowing the defects to sink at grain boundaries. 'Black dot' damage (clusters of defects less than 2 nm [66]) were observed in both studies as a result of ion milling [33], [65].

Another possible source of discrepancy in irradiation behaviour could be different stoichiometries produced by different fabrication conditions as supplied by the same vendor in both studies above (CERCOM). It has been postulated for some time now that vacant carbon sites present in sub-stoichiometric ZrC, repress the coalescence and nucleation of defects by acting as sinks for displaced carbon atoms from the irradiation process [12], [22], [66]. Evidence for this was observed in proton irradiation studies (2 MeV protons at 1125°C) on sub-stoichiometric C/Zr = 0.84, 0.89, 0.95, as similar loop dislocation sizes were observed for all samples (~10 nm) that were well within error of one another. This is contrary to the

significantly larger average loop sizes observed in hyper-stoichiometric samples C/Zr = 1.05, 1.17 (14.4 and 53.0 nm respectively).

All the studies discussed above examined the irradiation response of ZrC within the typical expected operational range (850 – 1350°C) of TRISO fuel particles in which ZrC would replace SiC as the buffer layer [67]. Irradiation at high temperatures causes the annealing of defects, thus the above material response is a combination of the damage caused by irradiation and damage recovery. Exploring proton damage at lower temperatures provides a separate understanding of how damage affects ZrC. At cryogenic temperatures of -253°C, 'Black dot' type damage was observed to occur at 0.4 dpa (2 MeV protons) in commercial ZrC (C/Zr = 0.90) samples [34]. The concentration of black dot damage was seen to increase rapidly as damage increased up to 3 dpa and then subsequently increased at a slower rate at higher doses. It should also be considered that the analytical techniques that used primarily TEM, are only capable of showing damage on the nm scale. Few other techniques have been used to characterise the multi-scale changes in ZrC after irradiations.

Lattice parameter changes under irradiation show highly variable results from study to study and use different sample compositions and stoichiometries, which complicates the matter further. The lattice parameter of hyper-stoichiometric ZrC (C/Zr = 1.01) 2.6 MeV irradiated at 800°C to 1.8 dpa showed no change from its pristine value within the 0.2% uncertainty bound [33]. This is contrary to the lattice parameter of ZrC irradiated with 2 MeV protons at 800°C to 0.70 and 1.5 dpa that showed a 0.09% and 0.11% increase from pristine values, respectively [65]. As no error was reported in the latter study it is difficult to compare the two results. No systematic study of the change in the lattice parameter with respect to stoichiometry has been conducted previously, but there remains a major need to investigate this effect. In line with previous studies, only one instance [65] of pre and post-irradiation SEM reported a thin oxide layer on the surface of irradiated ZrC samples.

It is clear from the above literature review that previous work has investigated nanoscale changes and the accumulation of defects with irradiation using predominantly TEM. As a result, very little work using other techniques has been undertaken. Techniques such as NMR, Raman and XRD can add significant value to understanding how the material response changes with irradiation. Analysis of radiation-induced defects on multiple length scales and how they vary with irradiation dose and stoichiometry will be addressed in this thesis. This is important as the radiation tolerance of ZrC is often attributed to the presence of vacancies. However, this has not yet been systematically investigated – which is an objective of this thesis.

1.2.3 Nb_4AlC_3

To date, 211, 312 and 413 layered materials have been fabricated with varying degrees of purity and with the aid of various dopants (e.g., silicon or additional M elements) to increase phase pure yield. However, the ZrAlC 211, 312, or 413 phases have not been fabricated with more than approximately 70% yield [11]. The M_4AC_{3-x} system can be synthesised in single-phase and represents a similar system to Zr_4AlC_3. Furthermore, it has drawn attention due to the discovery of vacancy ordering on carbon sites which would provide an extra dimension of customisability and microstructural control [68].

Of the 413 MAX phases, Nb_4AlC_3 has shown particular promise of radiation resistance through a combination of theoretical work, investigating ordering, and complementary experimental [9], [68] work. To date, little work has been conducted exploring the properties of Nb_4AlC_3 due to how recently the phase was discovered – the key results are discussed below.

Nb has a smaller absorption cross-section for thermal neutrons (1.16 b), than other M elements such as Ti^{46} (73 % abundant, 8.3 b) but is smaller than that of Zr^{90} (0.10 b) [69] making it suitable for reactors that have thermal neutronic profiles. As discussed earlier, the vacancy tolerance of a material has been linked to an augmentation in a material's ability to sink radiation damage thus it is possible that Nb_4AlC_3 could have a similar radiation response as seen in the ZrC if it can accommodate a large number of vacancies.

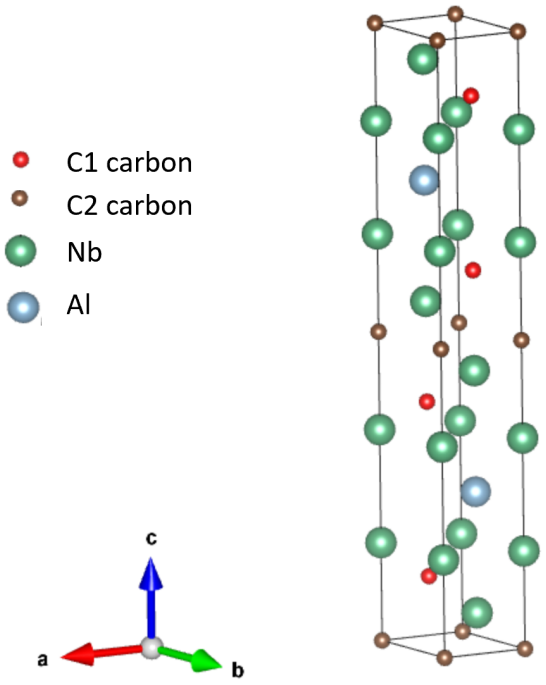

Figure 3 The unit cell of the Nb_4AlC_3 max phase. The number of formula units in the unit cell is 2. C1 and C2 carbons are red and brown, Nb atoms are green and Al atoms are blue.

Nb_4AlC_3 was recently (2007) synthesised for the first time by annealing Nb_2AlC in a crucible at 1700 ˚C for 1 hour [10]. The production of the new Nb_4AlC_3 phase was confirmed by matching the indexed planes to that of other 413 MAX phase samples that have the same crystal structure. The hexagonal Nb_4AlC_3 (Figure 3), referred to as α-Nb_4AlC_3 [10], [70] had lattice constants that were reported to be a = 3.1296 Å c = 24.1208 Å. As with the ZrC system, the sintering temperature has been observed to influence the final sample composition and the vacancy distribution. Similarly, slow cooling of Nb_4AlC_3 post-fabrication has been observed to produce Nb_4AlC_3 with ordered carbon vacancies (o-Nb_4AlC_3) which were observed to exist alongside the α-Nb_4 AlC_3 phase with a ‘disordered’ vacancy distribution [68]. The order to disorder transition temperature for carbon vacancies was observed to be from 1400 to 1500°C by TEM investigations [68]. This is similar to the order to disorder transition observed in the

V_4AlC_3 MAX phase which occurs between 1300 to 1500°C. The larger lattice constants a = 5.423and c = 24.146 Å [68] of the o-Nb_4AlC_3 phase provide the basis for distinguishing it from the α-Nb_4AlC_3 phase.

1.2.1 General objectives and thesis structure

This thesis is organised into 5 chapters. This subsection provides an overview and the general objectives that are to be achieved within each chapter.

Chapter 1 initially introduces ZrC and Nb_4AlC_3 as potential nuclear materials and describes the uncertainties in the composition and structure of ZrC_{1-x} and Nb_4AlC_3. The remainder of this chapter describes the experimental techniques used throughout this thesis such as ^{13}C NMR, carbon analysis, SEM, XRD and Raman spectroscopy and the fabrication of the ZrC samples.

Chapter 2 is the first experimental chapter and focuses on understanding how the sintering temperature and the stoichiometry of reactively hot-pressed unirradiated/pristine ZrC affect the carbon content and distribution within the sample by using complementary analysis techniques. The objective is to compare the total carbon content of the fabricated ZrC samples that have been quantified using the current gold standard technique of combustion carbon analysis with ^{13}C NMR based techniques. The NMR technique can also potentially reveal distributions of vacancies that can be compared to previous computational molecular dynamics studies that have found theoretically stable phases.

Chapter 3 aims to discover the effect of incremental radiation damage on ZrC as a function of stoichiometry for samples sintered at 2000 ºC (nominal carbon contents of C/Zr= 0.60, 0.80, 1.00) by comparing results from pristine analysis in Chapter 2.

Chapter 4 aims to use the ^{13}C NMR and Raman techniques developed in earlier chapters for ZrC to examine non-stoichiometry in the Nb_4AlC_3 layered carbide MAX phase.

Finally, Chapter 5 will present the conclusions from this thesis and recommendations for future work.

1.2.2 Outline of the main thesis results

Methods that are typically used to assess and report the carbon content, primarily nominal and combustion analysis measurements, were observed to overestimate the carbon content of ZrC. A new method, using ^{13}C NMR, was found to provide a more accurate carbon content value and revealed consistently lower values than the nominal and combustion analysed values. This result implies that ZrC values of carbon contents reported in the literature, which are subsequently used to reference physical property data may be inaccurate.

The carbon within ZrC samples was found to be comprised of Zr-C bonded carbon, amorphous carbon and graphitic carbon – the latter two were independently confirmed by Raman spectroscopy. The relative abundance of these carbon environments was observed to vary non-systematically with both sintering temperature and carbon content. At higher sintering temperatures, the distribution of carbon atoms within the sample was observed to obey a random distribution whilst at lower sintering temperatures they obeyed a more ordered distribution. The NMR, corrected carbon contents were observed to be in close agreement with computationally stable phases. No deviation from the NaCl structure as determined by XRD was observed.

Investigations into the effects of radiation damage revealed that ZrC was observed to be radiation tolerant, resisting amorphisation and maintaining its crystal structure up to 2.4 dpa. Vacancies were observed to be created within the ZrC structure, and this was observed to increase with increasing dose. Lattice parameter swelling was observed in samples at higher doses. In addition, the concentration of carbon was observed to increase in inter and intra granular regions – indicating that carbon dislocated from the ZrC lattice sinks at grain boundaries.

Carbon analysis of Nb_4AlC_3 samples revealed that approximately 1/3 of carbon atoms were missing from the structure. Examination of the short-range order showed that within the sample studied, carbon atoms obey an avoidance distribution. More detailed conclusions can be found in Chapter 4.

1.3 Methods

This section aims to introduce the techniques used in this thesis, the basic working principles underpinning these techniques and the operational protocols used in this PhD project. Additionally, an overview of basic radiation damage theory can be found at the start of Section 3.1 and is followed by the methods in which radiation damage was computationally simulated prior to irradiations.

1.3.1 Sample Fabrication

To minimise contamination and maintain oxygen-free conditions, the ZrC powders were prepared in a glove box under an argon atmosphere. Precursor powders of ZrH_2 (453330317, 2.4 μm, Rockwood Lithium GmbH, Germany) and graphite powder (282863, <20 μm, synthetic, Sigma-Aldrich, USA) were mixed in nominal C/Zr = 1.00, 0.80 and 0.60 ratios to a target mass of 50 g.

Homogenous pre-sintering powder mixtures were obtained in two mixing steps. Initially, the samples were mixed in a nylon jar with a stainless-steel spatula by hand in the glove box. A greater degree of homogeneity was achieved by further dry milling these powders, as described in the following steps. 50 ZrO_2 balls (~1.0 cm in diameter) were added to the jar, and the jar was then sealed via a three-bolt clamp and removed from the glove box. The mass of the pot was weighed, and this value was used to offset the centrifugal counterweight in a Retsch 80 PM100 planetary miller (Resch, Han, Germany). The pot was milled/mixed for 30 minutes at 150 rpm with milling/mixing direction reversal occurring every 5 minutes. The jar was then removed from the planetary miller and placed back in the glovebox (undergoing 3 vacuum purge cycles before entering the glove box). Milling balls were extracted individually to reduce any sample loss. The remaining mixed powders were distributed into glass vials which were then sealed, labelled with the corresponding target C/Zr, and stored in the glove box.

Uniaxial hot pressing is a technique usually used to produce dense pellets for characterisation. This technique involves the uniaxial compression of powder constrained within a mould and concurrent heating. This fabrication method consists of several processes that occur

simultaneously. Firstly, the soft Zr creeps and plastically deforms around the hard carbon phase and the Zr bonds with the carbon. Secondly, the pressure exerted by the press aids in the densification of the final product.

To create the ZrC pellets, the mixed ZrC powders were loaded into a graphite die that was lined circumferentially with Grafoil™ *(Erodex (*UK) Ltd, UK) 0.05 cm in thickness to stop the samples bonding to the side of the die and facilitate easy removal. Grafoil™ was used in the present study, instead of a release agent such as boron nitride, to limit contaminant species that can otherwise arise through ingression of boron or nitrogen into the sample during fabrication.

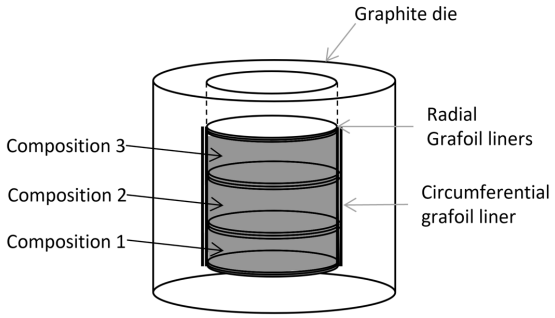

Figure 4 Schematic of the graphite die used in the hot press

The different compositions of feed stock ZrC powder(s) were also separated from one another in the graphite die using Grafoil™ sheets within the graphite die to stop sample mixing (Figure 4). Reactive hot-pressing (FCT Systeme GmbH, Germany) was conducted under a vacuum atmosphere in the Materials Department of Imperial College London.

A two-phase reactive hot-pressing protocol was used to fabricate the dense ZrC pellets. The first phase is the reaction phase (see equation (1.3)) and the second is the densification and further stage [22].

$$ZrH_2 + C \rightarrow ZrC + H_2\,. \qquad (1.3)$$

Sintering temperatures of 2000, 1700 and 1500°C were used to study the evolution of the final ZrC pellet with sintering temperature. The powders were heated at a rate of 10°C /minute to 1400°C at a contact load of 5 kN. Once at 1400°C, this temperature was maintained for 1 hour at 21.3 kN. The samples were then heated to the desired sintering temperature at a rate of 10°C /minute under 30 kN and remained at the sintering temperature for 1 hour. Next, the load was reduced to 5 kN and the heaters were turned off to allow the samples to cool down.

Post-hot-pressing, cooled samples were removed from the graphite moulds using a hydraulic press and punch. The thin graphite lining that had bonded to the pellet from the mould was detached using a Stanley knife. A grit 120 disk (water-cooled Phoenix Beta Grinder/Polisher) was used to remove the weakly bonded Grafoil^{TM} layer from the surface of each pellet. In addition to this, 0.25 cm was removed from all faces to remove any residual carbon from the fabrication process.

To achieve a uniform thickness of sample for irradiation, with a requirement of parallel faces, a horizontal rastering grinder was used. Samples were adhered to level metal plates using clear resin. This plate was then attached to a horizontal raster grinding machine (2880 revolutions per minute), which was manually operated to remove any variations in surface height using adjustment wheels of varying resolution. This process was repeated for both pellet faces to ensure parallel faces. Samples were then removed from the pellet and cleaned in an ultrasonic bath with acetone.

Due to time restrictions at irradiation facilities, the samples sintered at 2000°C with nominal C/Zr = 0.6, 0.8, 1.0 were used for the irradiation studies. These stoichiometries were chosen as their C/Zr ratios are at the centre and the bounds of the homogeneity region in the phase diagram. The irradiation facility specifications required the samples to be in a specific form hence two 0.5cm x 0.5cm x 200 μm blocks were cut from the centre of each pellet using electrical discharge machining in the Engineering department at the University of Cambridge. The blocks were cleaned after the cutting process and were polished to a mirror finish with

colloidal silica polishing paste of decreasing particulate size with the 0.25 μm polishing paste being used in the final step. A mirror finish on the sample surface was important for analysing the samples when conducting SEM and EBSD analysis. The remainder of the pellet that had not been cut into blocks was powdered and used in carbon analysis and NMR spectroscopy. As ZrC is an incredibly hard material, the pellet was initially broken down into small pieces using a metal hammer and a punch. Subsequently, these pieces were ground into smaller particle sizes using an agate mortar and pestle.

1.3.2 Non-Dispersive Infrared combustion carbon analysis

1.3.2.1 Introduction

Non-Dispersive Infrared combustion carbon analysis (carbon analysis) is an essential tool in determining the total carbon content of a material. As ZrC has a clear carbon content dependence, combustion carbon analysis is the de facto analysis technique for determining carbon content in the literature. Carbon analysis is also undertaken in this study to provide a basis for comparison between samples produced in this study to those produced in the literature.

1.3.2.2 Basic working principle

The total carbon content of a material is obtained by the complete combustion of a sample – the proportion of CO_2 (carbon dioxide) and CO (carbon monoxide) gas that is released from the sample is measured via absorption of infrared light.

To measure the total carbon content of the ZrC sample combustion analysis was conducted using a HORIBA EMIA-320 V2 Carbon and Sulphur chemical analyser. This analyser uses a 20 Megahertz (MHz) high-temperature induction furnace with a plate current of up to 500 mA and an anode output of up to 2300 watts (W), with O_2 carrier gas for combustion. Upon combustion, CO_2 and CO are released from the sample. The gas passes in front of an infrared light source (not pre-filtered) [71]. As this light passes through the sample, the gas that has been released causes the absorption of specific wavelengths of light (see Figure 5). This light is then incident on an optical filter and finally the IR detector. The optical filter eliminates all

other wavelengths except those of carbon oxides. Since CO and CO_2 have very specific absorption frequencies, two detectors can be used to measure the IR absorption and provide the concentration of carbon in the sample.

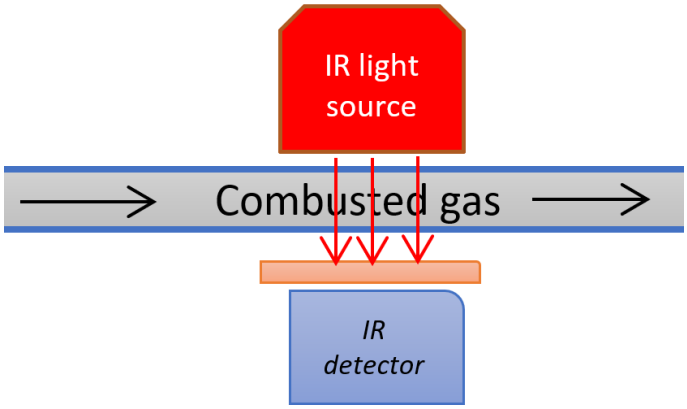

Figure 5 diagram showing the combustion analyser measurement process.

1.3.2.3 **Procedure**

The calibration procedure was run by analysing three blank crucibles followed by three calibration runs (with accelerant) to determine the residual carbon present in the ceramic crucible and the accelerant, respectively. An accelerant is required to enhance the process of combustion at lower temperatures and thus release carbon. For the accelerant, a combination of copper (0.64 g) and iron pellets (0.48 g) were used. The accelerant was supplied by HORIBA and the copper and iron pellets were added in layers on top of one another. The oxygen (carrier gas, 0.30-0.33 Mpa) and nitrogen (operating gas, 0.35 Mpa) lines into the analyser were turned on – the flow sequence is shown in Figure 6.

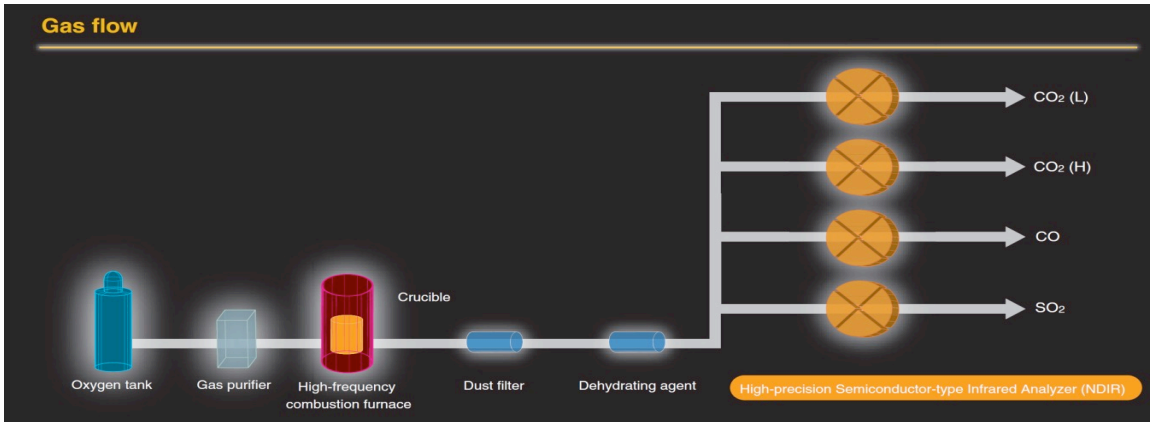

Figure 6 flow of oxygen through the carbon analysis machine [72].

Three blank runs and three calibration runs were run. For the blank runs, the masses were entered at 0 grams into the system. Subsequently, the calibration was run with a crucible containing the standard powder Tungsten Carbide (Purchased from HORIBA) (30 mg - BSC – CRM No. 352/1 from The Bureau of Analysed Samples) as the total carbon content of the tungsten carbide is known to a high degree of accuracy. A measure (0.1g) of the sample was added to the crucible, and the mass of the sample was then recorded in the software and the run queued. Copper followed by iron accelerant pellets were layered on top of the sample. The execution routine was initiated. Once three standard runs and three blank runs had been completed, a calibration curve was produced, and the known total carbon content of the standard was entered. The calibration was produced by fitting the recorded measurements vs the calibration:

$$y = A(x - C)10w + B. \quad (1.4)$$

The following coefficients were obtained from the calibration: A = 1.19060, B = 0.000294, C = 0.038247. The calibration results were saved to the software and samples were run. Each sample was analysed three times and the average value of the measurements was calculated with the error being calculated from the standard error on the mean from a range of three measurements.

1.3.3 X-ray diffraction (XRD)

1.3.3.1 Introduction

XRD is a powerful technique that can be used to assess the long-range order of a crystalline material and obtain information including, but not limited to, lattice parameters and microstrain. These parameters are particularly useful in studying the effect of vacancies and radiation damage on ZrC. In addition, in carbide fabrication, XRD is often used as a tool for determining if the synthesis was successful, with the absence of precursor powder diffraction peaks being used as confirmation of a successful reaction. Diffraction peaks can be indexed, and crystalline phases present in the material can be identified, with the help of a peak search database.

1.3.3.2 Working principle

In XRD x-rays generated, via electron bombardment of a target, are used to probe the crystal structure of a material that in turn acts similarly to a multidimensional diffraction grating. A set of parallel planes can be drawn through a set of atoms in a crystal that is equally spaced – so-called Bragg planes [73]. X-rays incident on these planes are scattered through interactions with the electrons of the atoms in the plane [74] which in turn act as secondary sources [75]. The waves from these sources then interfere with each other, either incoherently (out of phase and they destructively interfere) or coherently (in-phase and they constructively interfere- known as Bragg reflections). The criterion of coherency is described by Bragg's law (equation (1.6)) which is only satisfied when the phase difference between X-rays scattered by the separate planes are n integer wavelengths apart[73]. Both the X-ray source and detector are rotated whilst the sample is fixed. The intensity of the constructively reflected X-rays from the sample is recorded with respect to the 2θ diffraction angle is recorded (angle between source and detector).This can be summarised by Bragg's law:

$$n\lambda = 2d\,sin(\theta). \tag{1.5}$$

Where n is an integer, λ is the wavelength of radiation used, d is the spacing between the planes and θ is the angle of incidence.

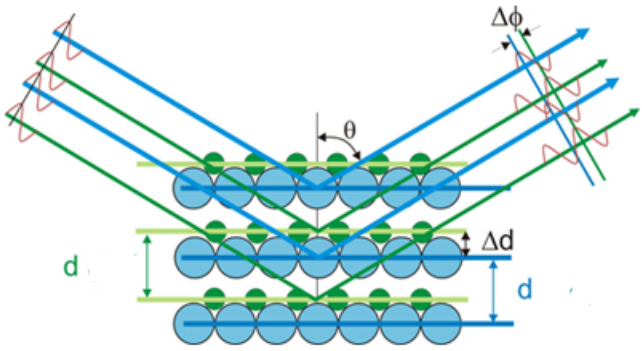

Figure 7 wave diagram showing the diffraction of X-rays in XRD analysis between crystal planes. [76]

The locations of the diffraction peaks in a diffraction pattern are dependent on the spacing of the lattice planes and hence the dimension of the unit cell (via Braggs law – equation (1.5)). The intensity of an XRD peak is related to the type of atoms in the target material, the positions of the atom and the multiplicity of the scattering planes (via the structure factor).

It follows that we can calculate the lattice parameter of a unit cell from the planar spacing for a cubic crystal via the following equation:

$$d = \frac{a}{\sqrt{h^2 + k^2 + l^2}}. \tag{1.6}$$

Where h, k, l are the miller indices, a is the lattice parameter and d is the spacing between the planes.

Fitting of the XRD diffraction patterns was undertaken using the TOPAS Academic V6 software for Rietveld refinement to determine information about the crystal structure. XRD patterns and the structure of peaks can provide a multitude of information about the material under investigation. For example, changes that may occur due to physical (for example sintering temperature, the energy imparted by irradiation) or chemical (stoichiometry) factors.

Rietveld refinement is a least-squares method of matching a theoretical crystallographic model to XRD pattern experimental data. The crystal structure of ZrC was retrieved from *The Inorganic Crystal Structure Database* (ICSD) [77], [78].

The peak profiles and background were modelled with a Thompson-Cox-Hastings pseudo-Voigt and a Chebyshev polynomial function, respectively, which were refined by TOPAS during the fitting process. Corrections of diffraction peak shift contributions resulting from zero error and specimen displacement were made by identifying the positions of known standard compound peaks. To obtain accurate lattice parameters, a single parameter for specimen displacement was used while the silicon lattice parameters were kept constant throughout the Rietveld refinement.

Physical and chemical factors can also affect the material's crystallinity and manifest in peak broadening. Deconvolution of these factors required the subtraction of instrumental broadening. Standards of silicon powder (powdered samples) and a corundum wafer (solid sample blocks) were used as internal standards to model and subtract the instrumental broadening contribution in the TOPAS academic software.

The crystal size values are not reported for some samples in this study as they were found to be over 1000 nm. When the crystal size is large, its contribution toward peak broadening is negligible, the crystal size cannot be estimated, and the crystal size parameter was thus removed from the refinement in these cases. The microstrain broadening β_e was fitted using a full pattern matching Pawley refinement. Unlike Rietveld refinement, in a Pawley refinement, the calculated peak position depends on the phase lattice parameters and symmetry, but the calculated peak intensities are free to vary independently and do not depend on a structural model.

The microstrain (ε) then follows from the angular dependence of β_e with θ [79] :

$$\beta_e = 4\varepsilon \tan\theta. \tag{1.7}$$

In the refinements, the contribution to microstrain was modelled using Gaussian functions.

1.3.3.3 Experimental details

XRD on the pristine powdered samples sintered at different temperatures was undertaken on a Bruker D8 operating in a theta-theta configuration, with a CuKα source ($\lambda = 1.5406$ Å) and a Vantec PSD detector through angles of 2θ = 10 – 50˚ with a 0.01˚ step size. A Si powder internal standard was used to model and deconvolute experimental broadening. 15mg of sample and 5mg of the standard were mixed and placed on a glass slip which was mounted onto a zero-background XRD stage. The powder was levelled by adding 0.5 ml of acetone onto the sample stage and mixing the sample using a stainless-steel needle, which was then allowed to dry and set.

As the machine used to run the powder samples was decommissioned, the solid sample XRD on the samples sintered at 2000°C both pre and post-irradiation was conducted on a Theta-theta Bruker D8 probe using MoKα ($\lambda = 0.70930$ Å) source. This was coupled with a Bruker Lynxeye XE-T position-sensitive detector. XRD was undertaken through an angular range of 2θ = 10 – 45˚ with a 0.01˚ step size. The solid samples were fixed in place by a mouldable adhesive on a zero-background stage alongside the corundum standard – this setup is shown in the diagram below.

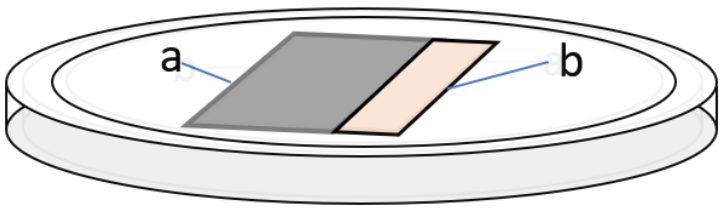

Figure 8 diagram showing the configuration of the ZrC the Corundum blocks, labelled a, and b respectively, used in solid XRD experiment.

This process was repeated for the pristine and irradiated solid sample blocks. The angular offset between the corundum tile and the sample was also accounted for in TOPAS to improve the accuracy of the fitted lattice parameters.

1.3.4 Scanning electron microscopy (SEM)

1.3.4.1 Introduction

SEM was utilised to examine the microstructure of the solid samples. SEM is a high-resolution technique for probing the microstructure of a sample. This technique facilitates the pre- and post-irradiation characterisation of the surface of the samples, as well as comparing those that have different stoichiometries. Average grain size can also be obtained using EBSD analysis and post-processing analysis.

1.3.4.2 Basic working principle

SEM uses a focused electron beam to image samples and obtain information about the microstructure of the sample including, but not limited to, the topology, crystallinity, texture and phase composition [80], [81].

High energy electrons in an SEM can be generated as a result of thermionic heating of either a tungsten filament, lanthanum/cerium hexaboride or tungsten field emission gun [Schottky/cold] (as was the case in the SEM used in this study) [80], [82], [83]. The electrons are collimated and focused onto the sample via a set of electromagnetic lenses [84]. Objective lenses are used to focus the beam on the sample, and the condenser lenses are used to produce the correct spot size (area of the beam on the sample). High energy electrons have several interaction modes. When they are incident on a sample, electrons do not pass through the sample but instead interact with a volume of material – known as the volume of interaction. The following modes and their detectors are described below.

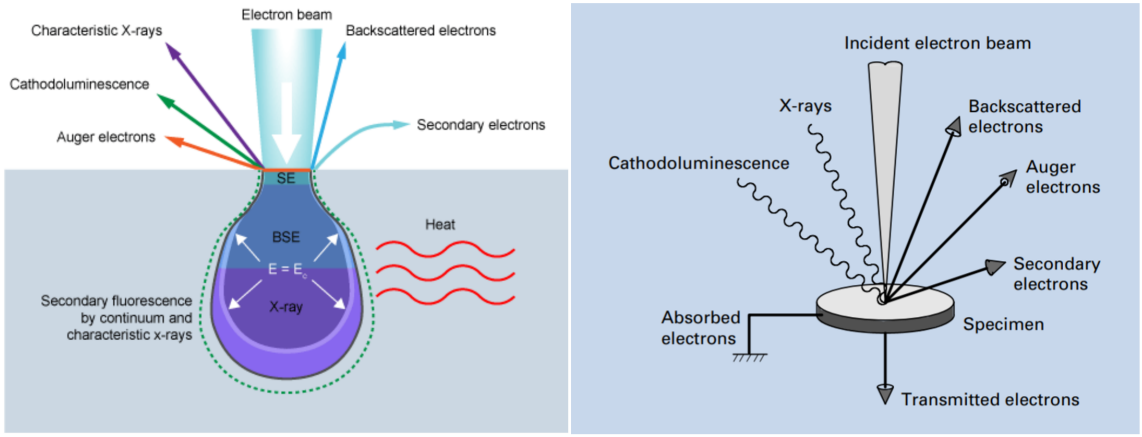

Figure 9 diagram showing the interaction volume of an electron beam (left) [85] and the various interaction modes (right) [83]

Inelastic collisions of the incident electrons with the electrons of the sample cause the ionisation of surface atoms. These ejected electrons are termed secondary electrons. As the SE ejection only occurs at ~1µm of the surface depth, changes in sample topology produce contrasting signals due to the angle of incidence between the sample and the incident electron beam [86].

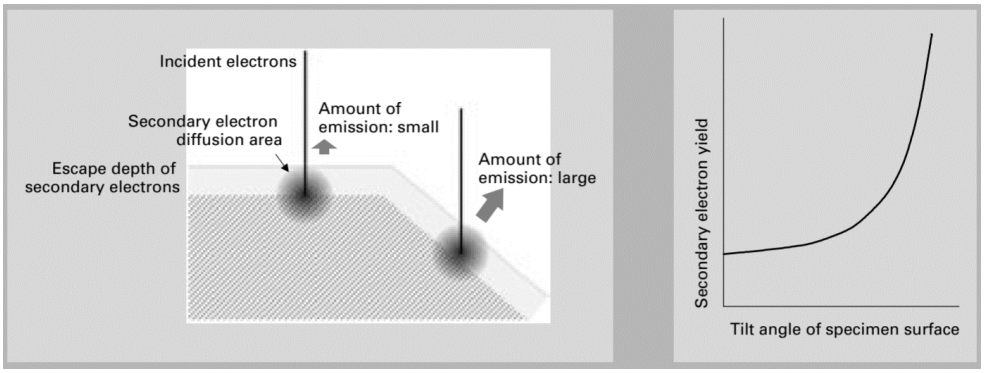

Figure 10 secondary electron production as a function of topological tilt [83]

Secondary electrons can be detected using an Everhart-Thornley detector [87]. The detector is comprised of a scintillator located in a Faraday cage. The cage is charged with a positive voltage (~v) to attract the secondary electrons and, the position-sensitive signal generated from the scintillator can be used to construct an image of the sample on a computer screen.

Back scattered electrons are electrons produced in high energy elastic collisions of the incident electron beam electrons with nuclei in the sample. As heavier elements have larger nuclei, they deflect electrons back to the detector with greater intensity, with the opposite true for lighter nuclei [88]. The above technique provides the basis for the discrimination of elements within a sample [89].

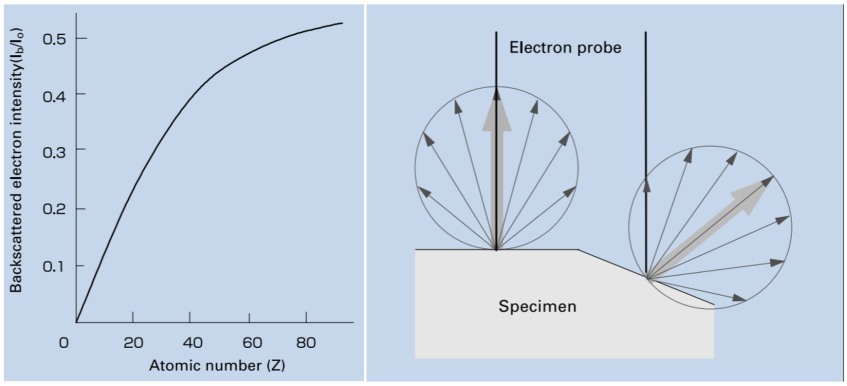

Figure 11 backscattered electron production as a function of the atomic number (left) and surface angle topology [83]

Backscattered electrons were measured using a detector that is located concentrically around the entrance hole of the electron beam into the sample chamber. The signal generated by the detector is reconstructed by the computer to yield an image.

Energy dispersive X-ray spectroscopy is a crucial technique of the SEM suite as it is used to obtain semi-quantitative data on the elemental composition of a sample. X-rays are emitted from a sample when the incident electron beam ionises an inner shell electron, creating a hole that is filled by an outer shell electron. To conserve energy of the system, a characteristic x-ray is emitted whose energy corresponds to the difference between the two energy states. An EDS detector is at a very basic level comprised of a cooled crystal. The x-rays incident on the ionise electrons in the detector producing a charge bias – hence x-ray energies can be discriminated between. If the electron beam is swept across the sample an EDS map can be created – otherwise, the electron beam can be used to analyse certain regions (spot EDS).

1.3.4.3 Experimental Details

Scanning electron microscopy was conducted on the samples using a Quanta-6F0F SEM. Backscattered and secondary electrons were collected using an Everhart Thornley detector and a Circular Backscatter Detector, respectively. To collect SE and BSE images, solid samples were mounted on metal stubs using carbon tape. Samples were imaged at a working distance of 13 mm using SE and BSE detectors with a beam current of 5 keV in a high vacuum with a spot size of 4.5. The SEM was operated in a high vacuum mode to reduce the effects of charging on the conductive samples. In order to differentiate between different elements, EDX was carried out with the Bruker 6130 XFlash and the ESPIRIT microanalysis software [90].

1.3.5 Raman spectroscopy

1.3.5.1 Introduction

Raman spectroscopy is a non-destructive, semi-quantitative in-situ technique that can be used to investigate a sub-set of vibrational modes of a material. This can be used to supplement other techniques and complements data established from additional experimental techniques. Raman spectroscopy was undertaken on the samples in this study to understand the speciation of carbon dissociated from the ZrC unit cell, such as graphite and 'free' carbon. Perfect ZrC itself has no Raman signal due to the high point symmetry of the rock salt structure. This makes Raman spectroscopy ideal for studying the evolution of exsolved carbon as a function of stoichiometry and irradiation dose.

1.3.5.2 Principle

Raman scattering is a relatively rare, inelastic photonic scattering process, occurring every $1/10^6$-10^8 photons [91]. If a photon that has equivalent energy to the energy band between the ground and excited vibrational state is incident on a material, then an atom can absorb this energy and be promoted to this excited state. After a period, the atom deexcites to a lower energy state that is either in a higher or lower vibrational state than its original state and in accordance with energy conservation a photon is emitted as a result of de-excitation.

In this study, the wavelength of vibrations we are interested in occur within the visible light region (400 -700 nm), thus we can use a visible laser to provide the excitation energy.

In an applied setting, Raman spectroscopy uses a laser to produce monochromatic photons. When these photons are incident on a material, they cause polarisation of the electron cloud, causing the atom to enter an excited state. The polarisability (α) of an atom can be thought of as the ease of distortion of the electron cloud and hence its local electric field (E). It is this distortion that results in the induction of a dipole moment (μ_{ind}).

$$\mu_{ind} = \alpha E. \tag{1.8}$$

Different molecules have different polarisabilities that depend on factors including the number of electrons and the distribution of electrons.

The de-excitation of the electron cloud from this transient state to a lower energy state results in photonic emission due to the conservation of energy. Rayleigh scattering occurs when the emitted photon is of the same energy as that of the incident photon - an elastic process. In contrast, Raman scattering occurs when the emitted photon is of a different energy to that of the incident photon - an inelastic process. Within Raman scattering, we can further define two more processes, Stokes and anti-Stokes shifts.

A Stokes shift occurs when an atom in a material in its ground vibrational state is excited into a higher energy state. After a period, this atom de-excites into a vibrational state higher than its initial state before excitation and emits a photon whose energy and frequency is lower than the incident photon energy. An anti-Stokes shift occurs when an atom in a higher vibrational state than its ground state before excitation is excited into a higher excited state. After a period, this molecule will de-excite into a lower vibrational state than it was initially in before excitation.

An atom can occupy this higher initial state due to its thermal energy [91]. After a period, the atom de-excites into the ground vibrational state. In this case, the emitted photon has larger energy and frequency than the absorbed incident photon. These processes are demonstrated with more clarity in Figure 12.

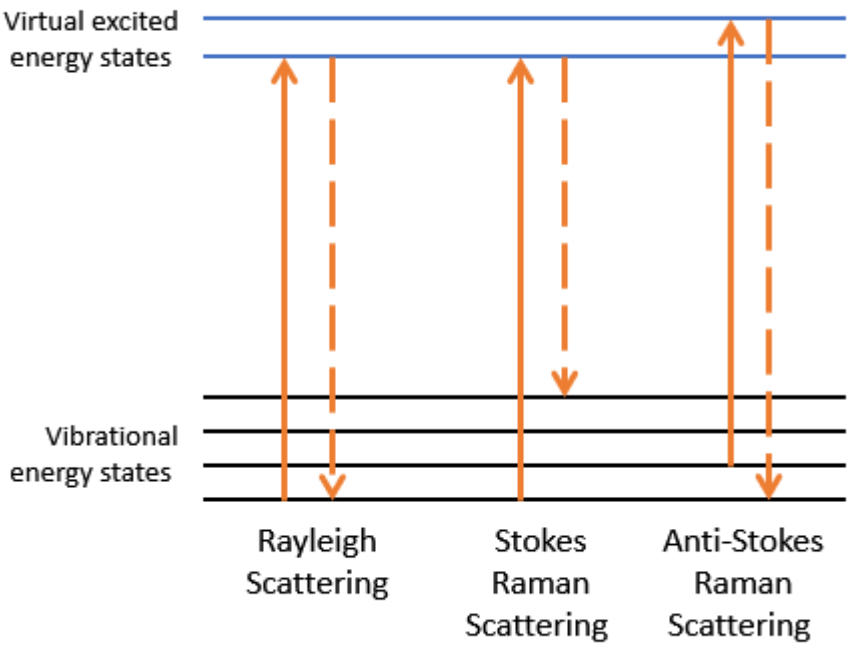

Figure 12 diagram showing the different excitation effects an incident photon can have on a molecule – incident photons are denoted by the dashed arrow, whilst emitted photons are denoted by a solid arrow.

It then follows that the difference between the incident photon energy and the emitted photon energy corresponds to the difference between the virtual state and the ground vibrational state. In Raman spectroscopy, the spectrum of intensity and the change in the frequency of scattered photonic emission is measured (with respect to the incident photon).

The units of wavenumbers are used in Raman spectroscopy a wave number ν (cm^{-1}), can be simply thought of as the number of waves per unit length:

$$v = \frac{f}{c}. \tag{1.9}$$

where f is the frequency, and c is the speed of light. We can substitute in the following expression which involves the wavelength λ:

$$f = c/\lambda. \tag{1.10}$$

Substitution of (1.10) into (1.9) gives:

$$v = \frac{f}{c} = \frac{1}{\lambda}. \tag{1.11}$$

In the Raman spectroscopy of carbon materials, including graphene, sooty carbons, sp^2 and sp^3 carbons, we are interested in the D and G resonances that occur in the Raman spectra. The sensitivity to different molecular vibrations makes Raman suitable for discriminating between these forms of carbon. The G resonance, typically centred at ~1582 cm^{-1}, arises due to the presence of in-plane stretching of carbon-carbon bonds – this is characteristic of sp^2 carbon or graphite [51], [92]. The D resonance (centred ~ 1620 cm^{-1}) occurs due to the out of plane vibrations arising from partially destroyed graphite and amorphous carbon [51], [92]. The structural units of different forms of carbon and how they affect the structure of the D and G peaks are summarised in Figure 13.

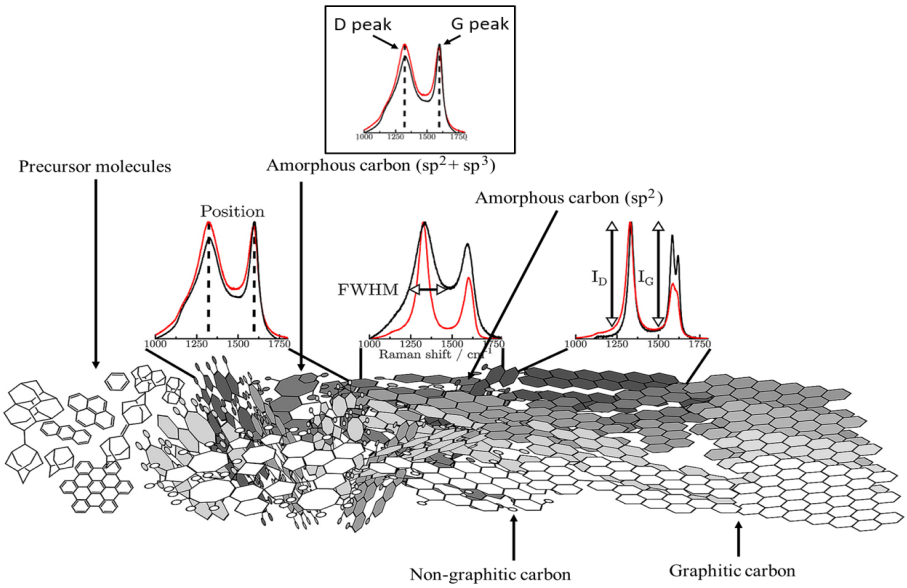

Figure 13 diagram showing the structural units of different forms of carbon and how they affect the D and G resonance peaks [93].

1.3.5.3 Experimental details

Raman spectroscopy was undertaken on a Horiba Jobin Yvon LABRam300 spectrometer using a green solid-state laser of wavelength 532 nm at a power of 100 mW. For signal collection, an Olympus 50 x objective lens was used in conjunction with a Peltier cooled detector (CCD). The spot size on the sample was ~ 2 μm making Raman suitable for analysing small features in grain boundaries.

The LabRAM has the advantage of having an interchangeable Raman and optical sensor (in axis optical microscope) that can be switched by changing the shutter position. The acquisition of data was conducted using the Lab spec software provided with the spectrometer. The laser beam focus was optimised by using a white light and an inline optical detector; the focus adjustment handles were used to focus the beam such that an image was visible on the LabSpec software being run on the computer. Fine adjustment of the focus was completed by using the motorised wheel whose input was modulated by a joystick configuration connected to the microscope. Once the optimum focus was achieved, the LabRam was switched back into Raman mode, using the laser as the light source.

The Raman spectrometer was calibrated using a silicon wafer that has a characteristic Raman resonance peak located at ~520 cm^{-1} (Figure 14).

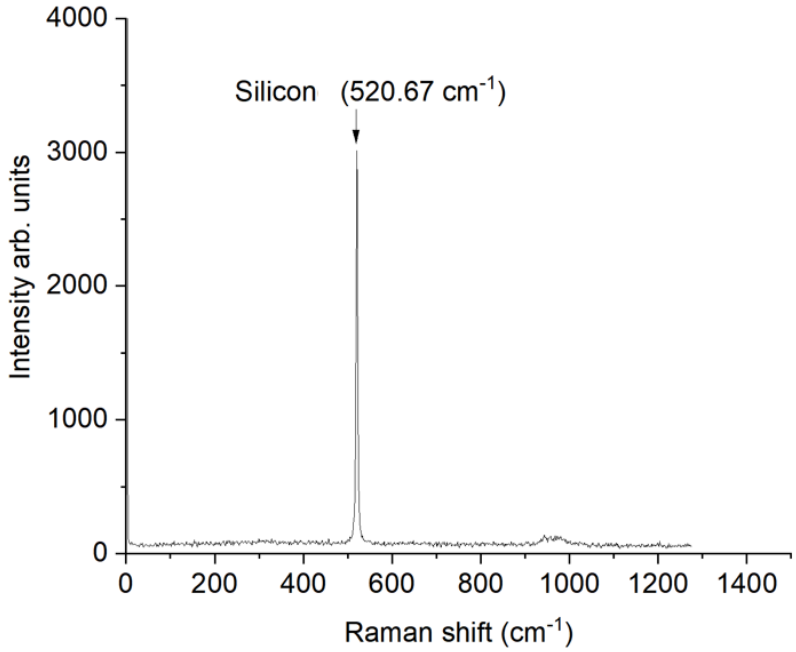

Figure 14 Raman spectrum of silicon standard used in Raman spectrometer calibration – the silicon band is marked.

All Raman spectroscopy presented in this thesis was undertaken on the solid ZrC blocks sintered at 2000°C, in order to image similar regions of interest in the pre and post irradiated samples. As the penetration depth for Raman is of the order of microns, this was in the range of interest for the study. In order to fix the solid samples and position them in the same place for all samples, a sample stage was constructed, shown in Figure 15 below.

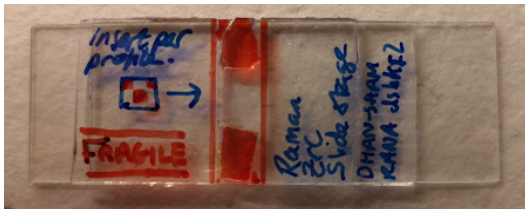

Figure 15 glass sample stage constructed for holding ZrC blocks for Raman spectroscopy.

Spectral peaks were fitted using IGOR pro [94] and Origin Pro software [95].

1.3.6 Carbon 13 Nuclear Magnetic Resonance (^{13}C NMR)

1.3.6.1 Introduction

The non-monotonic variations in the physical properties with carbon content make investigating the distribution and the short-range order of carbon environments important. NMR, provides a powerful method of studying the distribution of these environments on a bulk volume of samples as opposed to a localised area observed by microscopy, which may not be entirely representative. ^{13}C (~1% abundance) is the only carbon NMR active nuclei. ^{13}C NMR allows the differentiation of ^{13}C nuclei present in unique chemical environments. For example, graphitic carbon can be differentiated from carbon that is present in the ZrC lattice. Similarly, ^{13}C nuclei that are in an altered chemical environment due to the presence of a vacancy, say, can be differentiated from those that are in a perfectly stoichiometric sample with no vacancies. It is this sensitivity to perturbations of local carbon environments that make NMR a powerful tool for analysing the ordering of carbon environments.

As the NMR signals from ^{13}C nuclei are directly observed - the integral intensity of a ^{13}C NMR resonance is proportional to the number of ^{13}C nuclei producing it. This allows the relative abundance of different environments to be quantified and makes it possible to correct the measurements by other techniques such as combustion carbon analysis.

1.3.6.2 Basic working principle

It is not possible to discuss NMR without introducing the quantum and classical components which underpin the occurrence and the measurement of an NMR signal. Quantum mechanical spin angular momentum (I) is the phenomena that underpins NMR spectroscopy. Each nucleon (protons and neutrons) which form each atomic nucleus possess an individual spin equal to ½ ($I = \frac{1}{2}$). NMR active nuclei arise due to uneven numbers of protons or neutrons in a nucleus, and hence the nucleus possesses nuclear spin (denoted by angular momentum quantum number I) which can be half-integer or integer dependent on the nucleon numbers [96]. ^{13}C for example has six protons and seven neutrons arranged in nuclear angular momentum energy levels

resulting in a spin of a half or $I = \frac{1}{2}$. Not all nuclei are NMR active. Nucleons are filled such that they have the lowest possible energy configuration, the nucleus is then said to be in its ground state where the spin up and spin down nucleons are paired, obeying the Pauli Exclusion Principle. Non-NMR active nuclei have spin vectors that superimpose to produce a net spin of 0 ($I = 0$).

The projection of the angular momentum vector I onto the z-axis I_z is defined below:

$$I_z = m\frac{h}{2\pi} = m\hbar. \tag{1.12}$$

We can define the multiplicity of m:

$$m = I, I-1, I-2 \ldots -I+1, -I. \tag{1.13}$$

For ^{13}C I_z has 2I+1 possible orientations $I_z = \pm\frac{1}{2}\hbar$ the graphical representation is shown in Figure 16.

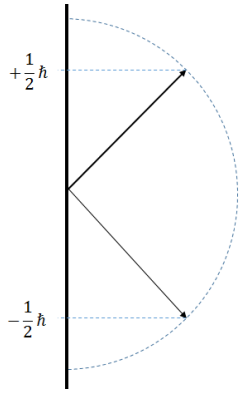

Figure 16 C-13 I_z spatial quantisation

The spin of a nucleus (I) can also be related to its classical magnetic moment (μ) by each element's gyromagnetic ratio γ:

$$\mu = \gamma I. \tag{1.14}$$

When ^{13}C atoms are placed in the external magnetic field (B_0), such as one generated by an NMR magnet, the energy degeneracy of the 2I+1 states are broken (Figure 16). The energy levels in a magnetic field are then equally spaced by $\hbar\gamma B_0$ – this is called the Zeeman effect.

The energy of μ on the z-axis now oriented applied field direction can be described, classically, by equation (1.15).

$$E = -\mu.B = -\mu_z B_0 = -m\hbar\gamma B_0. \quad (1.15)$$

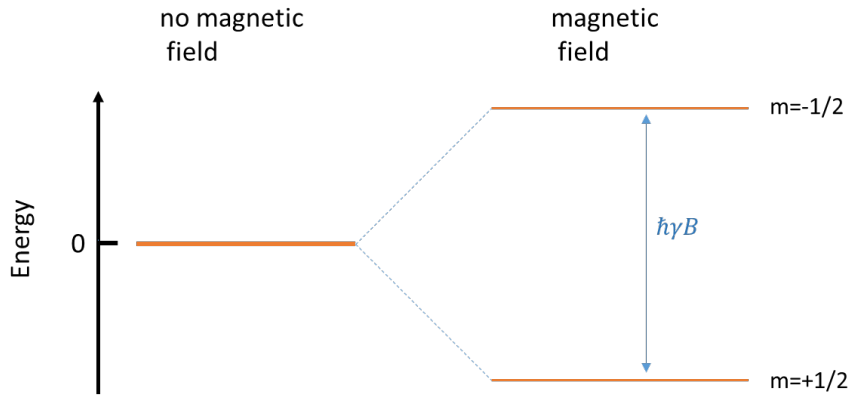

Figure 17 Splitting of energy states in a magnetic field as opposed to no magnetic field. Adapted from [97]

The transition energy of the magnetic moment of the nucleus when it is placed in an external field of strength B_0 is proportional to several factors: the strength of the magnetic field, the magnetisation (and hence I_z), and the gyromagnetic ratio (γ). As the selection rule for an NMR transition is $\Delta m = \pm 1$ between energy levels, the electromagnetic frequency needed to cause a transition is given by equation (1.16).

$$\Delta E = h\nu = \hbar\gamma B_0. \quad (1.16)$$

$$\nu_f = \frac{\gamma B_0}{2\pi}. \quad (1.17)$$

Equation (1.17) – the Larmor frequency (the frequency of dipolar precession around the magnetic field), can then be defined as:

$$\omega_0 = -\gamma B_0 = \nu_f 2\pi. \quad (1.18)$$

An ensemble of spins in a material produces a macroscopic magnetisation. Applying an RF (radio frequency) pulse via an RF coil at the Larmor frequency specific for ^{13}C rotates the macroscopic moment, exciting a proportion of the spins into a higher energy state [98].

When the RF pulse is turned off the spins within a material relax into a lower energy state – this consists of two processes, longitudinal (z) and transverse (x-y) spin component relaxation of the nuclear spin magnetisation, which can be quantified by relaxation periods T_1 and T_2. These are also known as spin-lattice (T_1) and spin-spin (T_2) relaxation periods. The T_1 relaxation time can be different for each sample and knowledge of it is essential to determine the quantitative contribution of each carbon resonance to the spectrum of the sample. The Larmor frequency (resonance position) and hence the NMR spectrum is affected by two factors: the first is the local field induced in the local electronic bonding environment and the second is the contribution of additional nuclear spins [99].

It is the dephasing of x-y components of the magnetisation that is measured in an NMR experiment as the decaying x-y magnetisation induces a voltage in the NMR coil. Since bonding between atoms is a purely electronic interaction, different bonding arrangements produce different electronic configurations; hence the atoms experience different local magnetic fields. As a result, the differently shielded atoms absorb different RF frequencies [43]. This shift is measured in parts per million (ppm [δ]) with respect to a standard (in this case TMS, by a secondary reference to solid adamantane) [15]– [17], [19], [20].

It is in the above way that unique carbon environments can be distinguished from one another. The abundances of these different carbon environments can be quantified by the integral of these resonance peaks which correspond to the proportion of carbon sites represented by that peak (with respect to the total spectrum integral).

1.3.6.3 Magic angle spinning (MAS) 13C NMR

Conducting experiments on solid-state samples can often be complicated by broad spectral linewidth as compared to spectra obtained in solution-state NMR. In solution-state NMR, the transition frequencies of differently oriented molecules are averaged due to the rapid isotropic tumbling of the molecules in the samples, which results in the orientation of the electron distribution being averaged [100].

This is not the case in solid-state NMR, as powders consist of molecules that have random orientations and are locked in place. The chemical shift anisotropy and the dipole-dipole interactions which are of the form $3\cos^2\theta - 1$, are also spatially locked with the orientation of the molecules. Spinning the rotor at an angle of $\theta = 54.74°$ with respect to B_0 averages the anisotropies to 0 [101].

As discussed previously, the ZrC samples were crushed into a fine powder – so that solid-state NMR can be used to probe the bonding structure for different C/Zr. Magic angle spinning is used to counteract this and mimics isotropic tumbling; a MAS rotor schematic is shown in Figure 18 below.

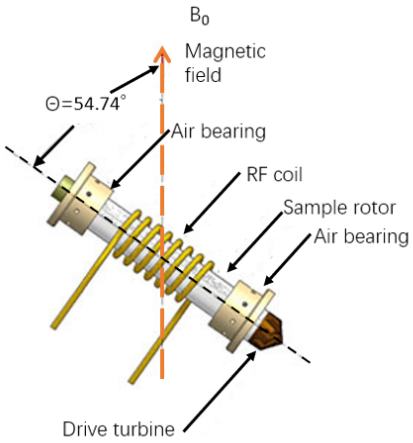

Figure 18 MAS experiment [102] a rotor containing the powdered sample is rotated about the rotation axis at an angle with respect to the magnetic field of $\theta_R = 54.74^o$. The sample at position in the rotor such that it is in the field of the coil.

The result of employing this technique is better resolved peaks in the spectra. Issues with MAS occur when the sample is not spun fast enough about the rotation axis. The spinning rate of the sample must be 3-4 times greater than the chemical shift anisotropy in order to produce single narrow peaks [103]. At lower rotation speeds, spinning sidebands are observed in the NMR spectrum. These appear as sharp lines which are spaced at integer multiples of the spinning frequency apart from the isotropic resonance line [101], [103].

1.3.6.3.1 Chemical shifts

In addition to the interaction of an NMR active nucleus with the external magnetic field, the electrons surrounding a nucleus can also interact with the external magnetic field. Hence as the electronic spins are polarised in B_0 they act as current loops and generate an additional induced magnetic field B_{ind} experienced by the nucleus.

As chemical bonding is an electronic interaction, different bonding configurations induce different B_{ind} which is the basis for differentiating between nuclei in different chemical environments. In an NMR spectrum ^{13}C nuclei in different chemical environments can be identified as different resonance peaks as they have different amounts of chemical shielding (σ). This results in a measurable frequency shift (δ) called the chemical shift. Thus, the effective magnetic field experienced by a nucleus B_{eff} can be written as follows (equation (1.19)):

$$B_{eff} = B_0 + B_{ind} = B_0(1-\sigma). \tag{1.19}$$

Equation (1.19) can be combined with equation (1.17) to give (1.20) below:

$$\nu = \frac{\gamma B_0(1-\sigma)}{2\pi}. \tag{1.20}$$

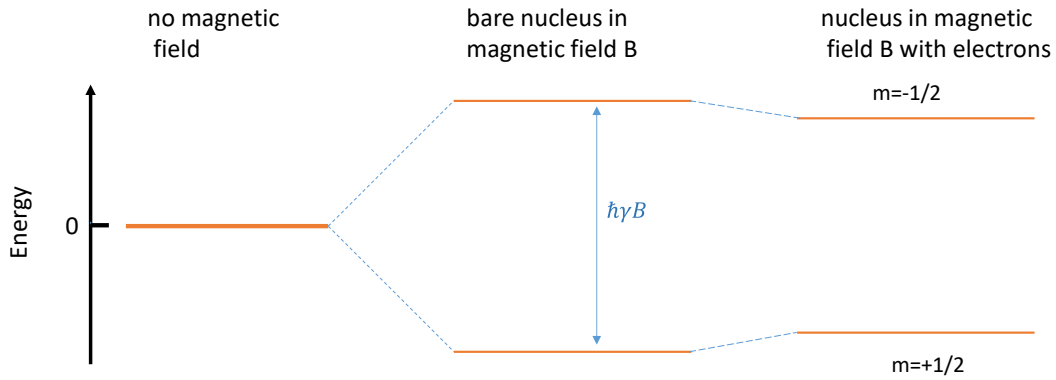

Figure 19 illustration of the effect of nuclear shielding on energy levels adapted [42].

As NMR shifts are proportional to B_0 , the instrumental magnet field, it is useful to define a chemical shift such that it is independent of an instrumental setup and the results can be reproduced – this can be done using a standard – in this case, Tetramethylsilane (TMS). It follows that NMR spectra can be referenced to TMS by equation (1.21).

$$\delta = \frac{\omega^0 - \omega^0_{TMS}}{\omega^0_{TMS}} \, 10^6 \text{ ppm.} \tag{1.21}$$

1.3.6.3.2 The Knight shift

In a metallic or semi-metallic material, an additional consideration is the interaction between the nucleus and the delocalised electrons. These delocalised electrons cause an additional magnetisation, generally greater than the chemical shift, which acts to further shift the effective field observed by the nucleus. If no external magnetic field, $B_0 = 0$, is present then the electrons are paired in accordance with the Pauli exclusion principle and occupy electronic states, as per the Fermi distribution, to the Fermi level. In the presence of an external magnetic field, $B_0 \neq 0$, the electrons will experience a separation of the up and down spin states. As the electronic and nuclear magnetic moments interact with one another this interaction induces a dipole and hence an induced magnetisation. The Knight shift can be measured by changing the temperature at which NMR is conducted and measuring the NMR response at different temperatures.

1.3.6.4 Pulse sequences

Depending on the composition of the sample to be probed by NMR, different pulse sequences are used. The width of the NMR spectrum, whether the line is heterogeneously or homogeneously broadened, and the relaxation time influence the choice of the pulse sequence. In this study, the Hahn spin-echo pulse sequence, adapted by Carr and Purcell, is used [104]. This technique is used to counteract the dead time - a period at the beginning of the signal in which data cannot be collected as the signal contains artefacts – this is a function of the probe ringing, pre-amplifier ringing and the receiver recovery time. The Hahn echo pulse sequence consists of a $\pi/2$ – delay – π – delay. The $\pi/2$ pulse flips the net magnetic moment, by 90°, into the x-y plane and the π pulse rotates the net magnetic moment by 180°.

Over time, spins making up this macroscopic moment begin to de-phase as different local magnetic environments with different frequencies dephase at different rates. Applying a π pulse acts to flip and refocus the spins so more slowly dephasing spins are leading the more rapidly dephasing spins, now – after a period, the faster spins are in the same position as the slower spins – causing an echo signal. This pulse sequence was used for static NMR experiments in the 7.5 mm rotor.

Spinning NMR experiments were conducted using the CPMG (Carr–Purcell–Meiboom–Gill) pulse sequence. The CPMG pulse sequence is an extension of the Hahn echo pulse sequence. In the case of the CPMG pulse sequence, a $\pi/2$ pulse is followed by a number of π pulse sequences. As with the Hahn echo, the $\pi/2$ pulse acts to focus the net magnetic moment in the x-y plane. After a time, the individual spins begin to dephase, hence dephasing the net magnetic moment. As a result, some of the carbon environments that relax more rapidly (for example those of graphite) de-phase faster. Applying a series of π pulses flips the magnetisation such that the slower spins, are now at the front. Hence all the spins refocus at the same time resulting in the formation of an echo for each π pulse. These echoes can be co-added and Fourier transformed to increase the signal to noise ratio of the spectrum in the case of a limited sample quantity or long T_1 relaxation times.

1.3.6.5 Experimental procedure

1.3.6.5.1 Loading an NMR rotor

Powdered samples were loaded into 7.5 mm rotors using the rotor packing tools. In order to limit contributions from the rotor to the NMR signal, the 7.5 mm zirconia rotor with aluminium nitride spacer inserts were used. Polymeric spacers which are typically employed in NMR spectroscopy were not used as they contain carbon [24].

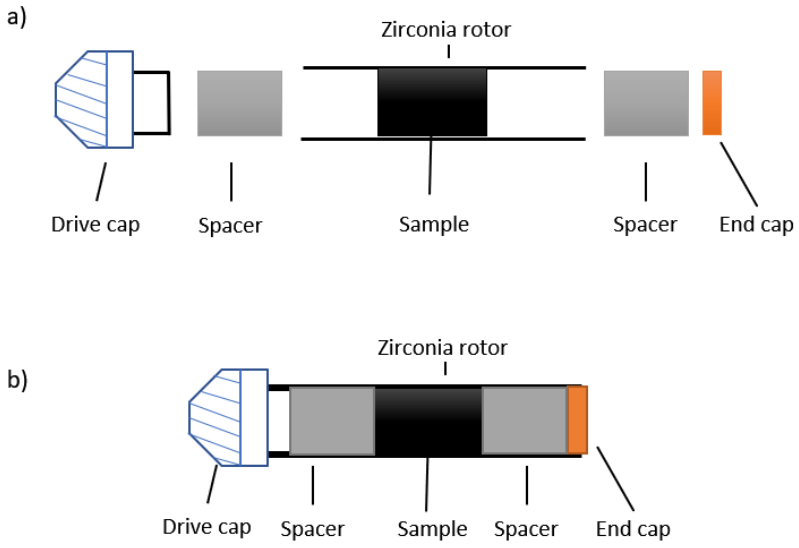

Figure 20 a) exploded and b) packed diagram of the 7.5 mm rotor configuration.

The 7.5 mm rotor packing configuration is shown in Figure 20. The 1.3 mm rotor used for MAS experiments has the same configuration as the 7.5 mm rotor, however, it does not require spacers as it is smaller in size and its volume sits within the NMR RF coil. When loading the rotors, samples were compacted as much as possible inside the rotor to maximise the quantity of sample in the rotor and hence the number of ^{13}C nuclei. In the fast MAS NMR rotor, a compacted densely-packed sample also ensures that there is a homogenous weight distribution across the rotor whilst spinning, which is essential when utilising high rotational frequencies.

1.3.6.5.2 Tuning and matching the probe

To set up each probe for measurements, the match and the tune had to be iteratively and interchangeably adjusted to obtain a sharp power reflection dip a the 1 V level. As ZrC is a semi-metallic material, insertion of the packed rotor into the probe coil causes a considerable (~MHz) shift in the resonance of the circuit. The probe was matched by adjusting the matching capacitor, which adjusts the real impedance of the tuned circuit to be 50 Ohms. The tune capacitor adjusts the Larmor frequency of the ^{13}C nucleus, which is shifted from the frequency of insulating, diamagnetic ^{13}C samples that the probe was designed for. Final matching and tuning were completed using an oscilloscope set at the tuning frequency of the ^{13}C nucleus for the 9.4 Tesla magnet (100.6 MHz). In practice, the tuning of circuit components may change with the voltage (power) of the RF pulse. Hence, further matching and tuning is required to minimise the reflected power (at the resonance frequency) at the 100-400 V level. This process acts to achieve the maximum forward/reflected power ratio.

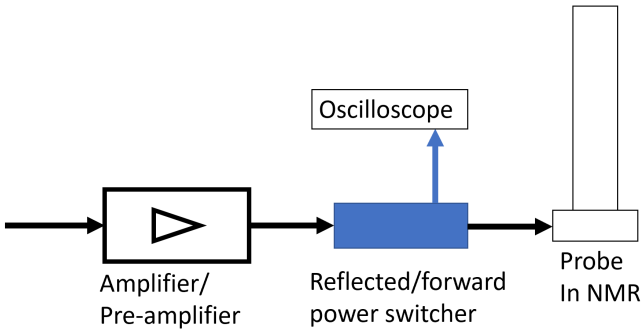

Figure 21 optimising the reflected power to the transmitted power

1.3.6.5.3 Calibration of the NMR spectrometer

The NMR spectrometer was calibrated by running the powdered adamantane standard. In the adamantane structure, there are two carbon environments. The first carbon environment consists of one carbon atom bonded to two other carbons, and two hydrogens observed seven times (environment A). The second environment is one carbon atom bonded to the three other carbons and one hydrogen – observed three times (environment B). In theory, the NMR

spectrum should be split into two distinct lines each denoting the unique carbon environment with the more abundant carbon environment having an integral intensity under its respective peak. A ^{13}C NMR spectrum of adamantane (Figure 22) shows two sharp peaks, as expected. These peaks correspond to chemical shift values of 37.85 ppm and 28.46 ppm [105]. The absolute resonance frequency of the 37.85 ppm peak was recorded to be 1 Hz in 10^8 Hz as a secondary reference on the tetramethylsilane (TMS) scale conventionally used for ^{13}C.

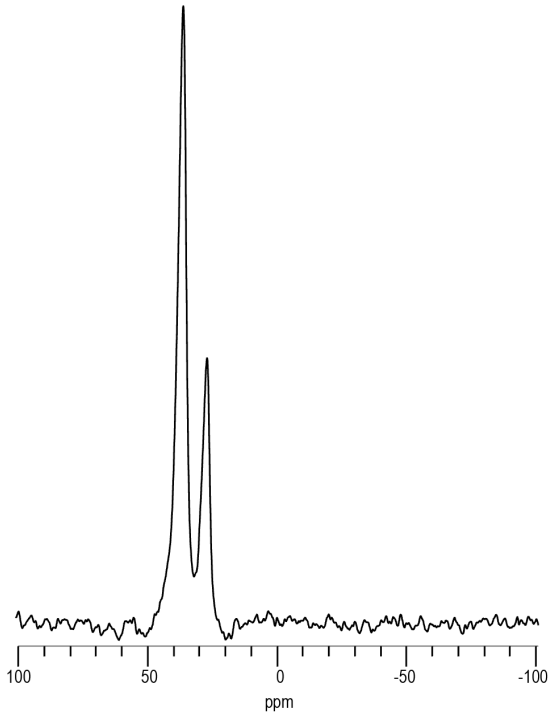

Figure 22 Adamantane reference MAS ^{13}C NMR on the 7.5 mm probe – left peak = 37.85, right peak =29.47 [106].

1.3.6.5.4 Pulse length calibration – nutation experiment

To ensure the correct 90˚ (and hence 180˚) pulse for the 7.5 mm and 1.3mm probes, a nutation experiment was conducted using the single pulse Bloch decay pulse sequence with variable pulse lengths. This was completed using adamantane. In this experiment, the period of the applied pulse was varied in an array. The maximum signal occurs when the spins are projected into the x-y plane (90˚ flip) – hence the time required for the RF pulse to achieve rotation can be determined (as pulse power is held constant). The results of this experiment are shown in

Figure 23. For the 7.5 mm probe, the 180-degree pulse was found to be 11 microseconds; thus the optimal pulse was 5.5 microseconds. For the 1.3 mm fast MAS probe the 180-degree pulse was found to be 7 microseconds – hence the optimal pulse was 3.5 microseconds.

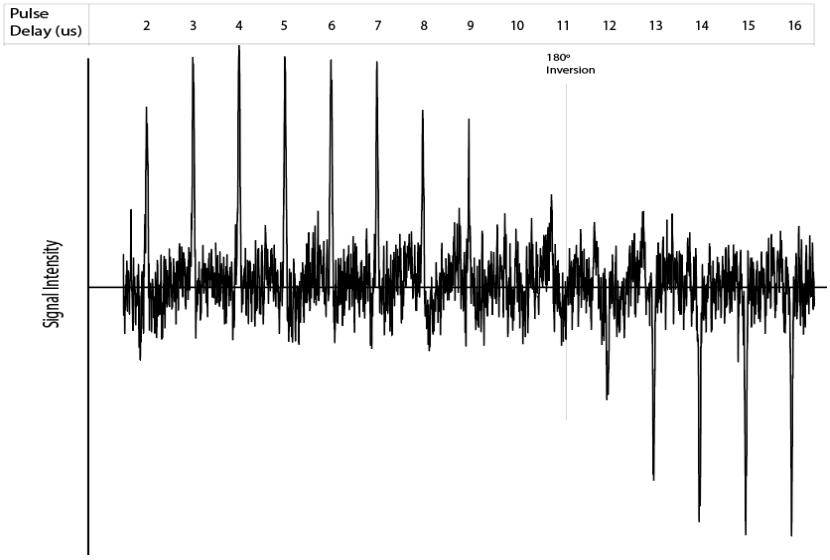

Figure 23 Variable 90-degree pulse duration spectrum of adamantane taken using the one pulse Bloch decay technique – for the 7.5 mm static probe.

1.3.6.5.5 Minimising the skin depth of the samples for NMR spectroscopy

RF waves are used in the NMR pulse to excite the spins of resonant nuclei. In metals, the skin depth effect, which occurs due to the conductivity of the sample, becomes an important factor when using RF waves to probe semi-metallic NMR samples. For volumes larger than the skin depth, the RF field travels through the conductor as a surface wave [107] not exciting the spins of carbons deep within the volume of the material.

To mitigate this and excite all the spins in the sample, the particulate size can be reduced to below the skin depth. The skin depth (δ) [108] is related to the material conductivity (σ), the speed of light (c^2), and the permittivity of free space (ε_0) is given by :

$$\delta = \sqrt{\frac{2\,\varepsilon_0\,c^2}{\sigma\,\omega}}\,. \tag{1.22}$$

As the relationship between the conductivity (σ) and the resistivity (ρ) is given by:

$$\sigma = \frac{1}{\rho}. \tag{1.23}$$

And the angular frequency (ω) is related to the ordinary frequency (f) given by:

$$\omega = 2\pi f. \tag{1.24}$$

Substitution of (1.23) and (1.24) into (1.22) gives:

$$\delta = \sqrt{\frac{2\,\varepsilon_0\rho\,c^2}{2\pi f}}\,. \tag{1.25}$$

We can introduce the permeability of free space (μ_0):

$$c^2 = \frac{1}{\mu_0\varepsilon_0}. \tag{1.26}$$

Substitution of (1.26) into (1.25) gives:

$$\delta = \sqrt{\frac{2\,\varepsilon_0\rho}{2\pi f\mu_0\varepsilon_0}}. \tag{1.27}$$

This can then be simplified to the following:

$$\delta = \sqrt{\frac{\rho}{\pi f\mu_0}}. \tag{1.28}$$

As resistivity is a function of carbon content [13] we have the following empirical equation originally formalised by Storms and Wagner [12], [17], [109]:

$$\rho = \frac{1}{0.00382 + \left(\frac{1}{55 + 950(x)}\right)}. \quad (1.29)$$

This provides us with a simplified approximation to the skin depth profile with respect to C/Zr. Thus, using the above relationship, for the RF signal penetrate fully into a particle, its skin depth needs to be reduced below 66 μm. To achieve this samples were crushed in an agate mortar and pestle and passed through a sieve with a 26 μm nominal opening (#500 Mesh, SS316 Grade, The Mesh Company). The process was repeated until all the material was below 26 μm in diameter.

1.3.6.5.6 Determining and optimising the pulse delay of an NMR experiment

Before the signal acquisition, the Hahn echo pulse sequence was used to determine the pulse delay that would result in the maximum signal. This is the time after which all the carbon spins have relaxed – as a result, quantitative analysis is possible. In order to collect the NMR spectra, the spin-lattice/longitudinal relaxation (T_1) time needs to be determined. This quantity is important in pulse repetition rates to ensure that the maximum signal is collected. In the duration of free induction decay the signal and hence the z-component of the net magnetisation in (M_z), recovers according to:

$$M_z = \left(1 - e^{\left(-\frac{pulse\ delay}{T_1}\right)}\right) \quad (1.30)$$

$$M_z = \left(1 - e^{(-5)}\right) = 0.99326. \quad (1.31)$$

From equations (1.30) and (1.31) it is shown that the loss of the magnetisation in the Z direction is asymptotic. Although the maximum signal will be collected at infinite time, due to the exponential nature of the function, this is by no means practical. It is therefore reasonable to assume that that maximum signal is recovered at 99.32%. Thus, the pulse delay for a given sample can be taken to be $5T_1$. With a metal, one would expect that the relaxation would be relatively rapid due to the delocalised conduction electrons.

If the carbon deficient samples have multiple sites – these might have different T_1 relaxation times. The pulse delay must respect the longest relaxation environments to ensure the maximum signal of each chemical environment is collected. This experiment was conducted by filling a 7.5 mm rotor with the finely milled powder. The rotor was inserted into the 7.5 mm NMR probe and tuned using an oscilloscope to the resonant frequency of ^{13}C in a field of 9.4 T (100.59 MHz) - tuning the probe with the sample inserted was crucial as inserting a conducting sample changes the tuning of the probes. The probe was then inserted into the NMR magnet and a simple one-pulse experiment was run. The match and the tune were adjusted to maximise the forward to reflected power.

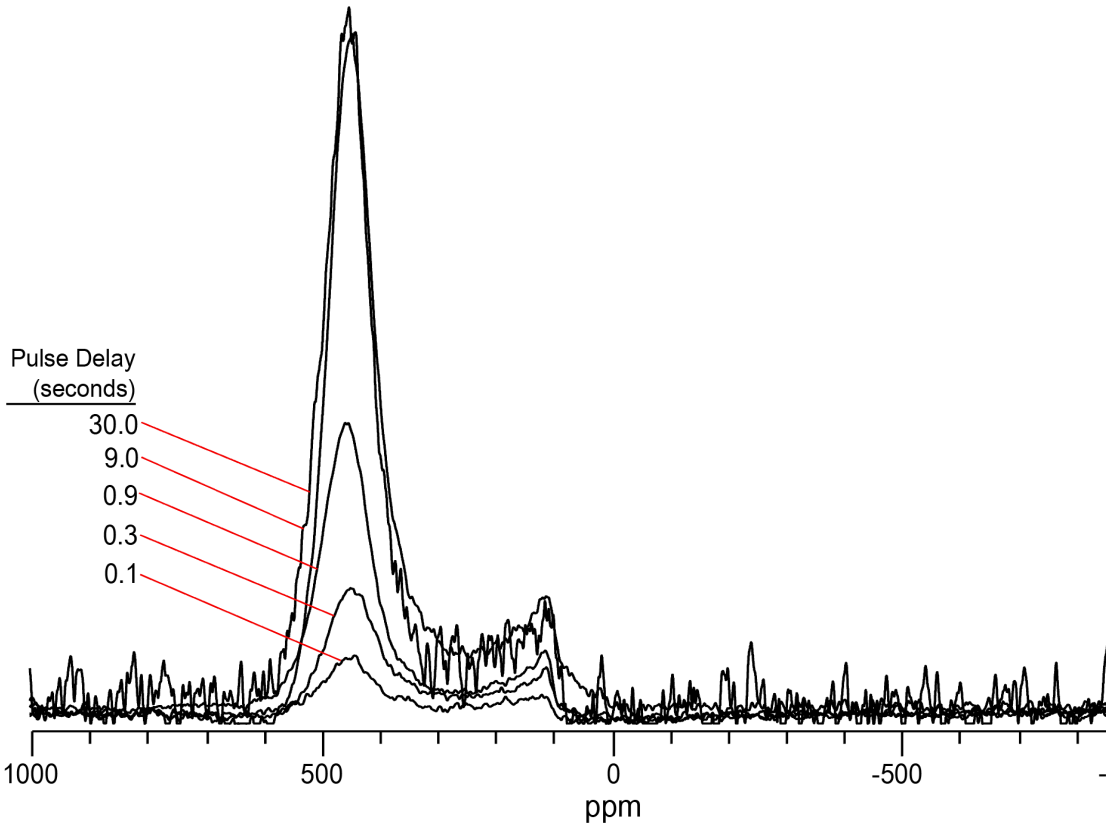

Figure 24 Varying the pulse delay for sample C/Zr = 0.70 (nominal) sintered at 1700C

Figure 24 shows that many sub-environments within the ZrC resonance structure are relaxing over the course of several seconds, with maximum signals obtained for delays of 9s and 30s. This indicates a ^{13}C T_1 (for the ZrC component) of the order of 1.8 s (T_1= pulse delay/5) for >99% relaxation.

By comparison, the carbon environments in the Nb_4AlC_3 showed a more rapid signal saturation relaxation time (~1 second) than the ZrC. As the longer pulse durations were not observed to increase the signal intensity, it was sufficient to collect the ^{13}C NMR signal with smaller pulse delay periods.

1.3.6.5.7 The effect of magnetic material on the NMR signal

Although every effort was taken to reduce contamination in the processing steps, it was the case that stainless-steel fragments were present in some samples. This was apparent in the NMR spectra of the aforementioned samples.

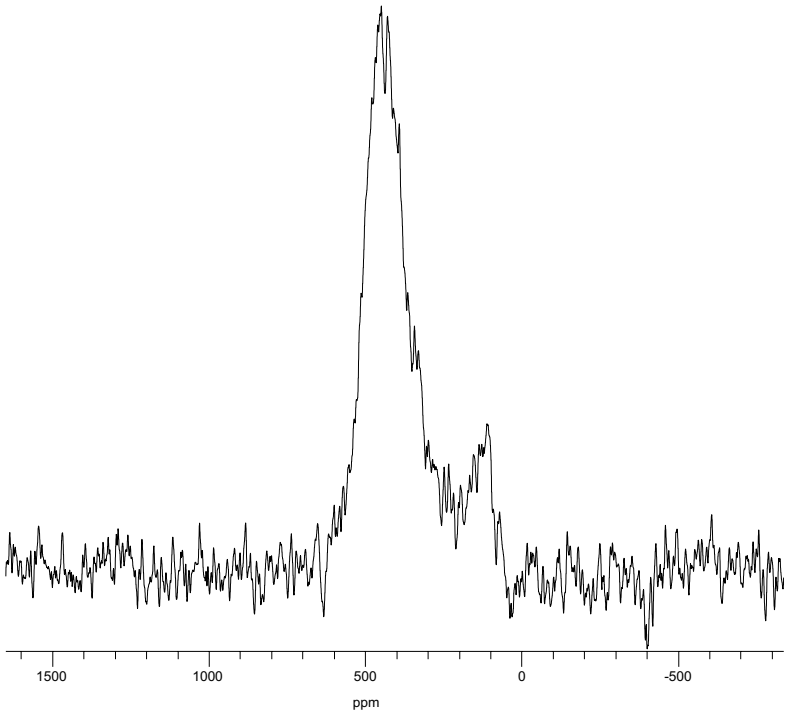

Figure 25 NMR spectra of a sample with nominal carbon content C/Zr = 0.60 sintered at 1700°C

Figure 25 shows one such NMR spectra of the nominal C/Zr = 0.60 sample sintered at 1700°C. As the NMR response of a signal is determined by the relaxation of multiple carbon environments in a magnetic field, the inclusion of foreign metallic material in powdered samples can interfere with the NMR. ^{13}C NMR spectra are very sensitive to the presence of ferromagnetic particles, the presence of which will create a dispersion of local magnetic fields destroying magnetic field homogeneity, spectral resolution and lowering the signal to noise ratio. To filter out these inclusions, magnetic particles were separated from the samples using a very high magnetic field (9T). The results of this are displayed in Figure 26.

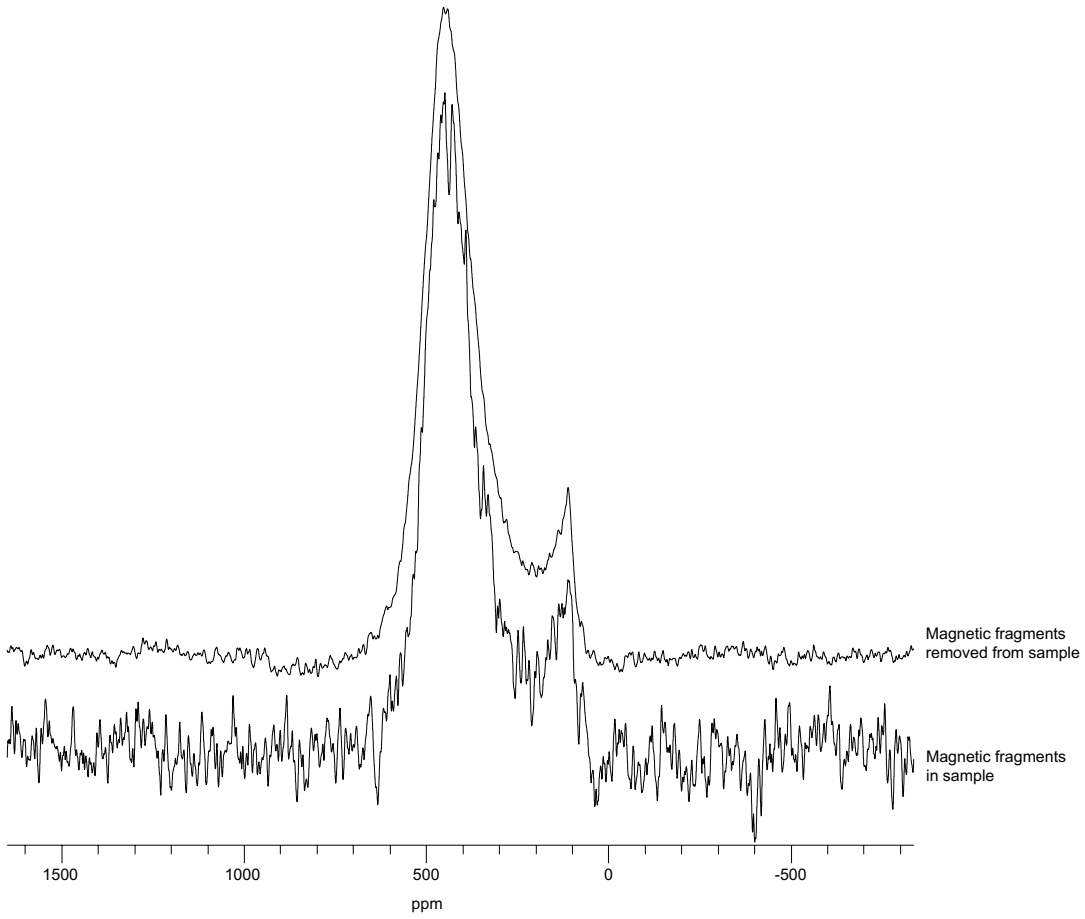

Figure 26 stacked NMR spectra of sample with nominal carbon content C/Zr = 0.60 sintered at 1700°C. The top spectrum shows the NMR spectrum with the magnetic fragments removed from the sample. The lower spectrum shows the NMR response with the magnetic fragments in the sample.

Figure 26 shows the ^{13}C static NMR spectra of the unfiltered and filtered nominal C/Zr = 0.60 sample sintered at 1700°C. The filtered sample, with the stainless-steel fragments removed, produces a higher signal to noise ratio as compared to the spectra of the sample before the fragments were removed.

Chapter 2 Pristine ZrC

2.1.1 Section aims and objectives

This section systematically explores how stoichiometry and sintering temperature affect the long- and short-range order within the ZrC samples fabricated[2].

The objectives of the chapter are the following: to characterise the samples fabricated in this study with NMR, SEM, XRD and Raman spectroscopy techniques; to understand how varying the sintering temperature and carbon content influences the distribution of carbon environments within a given sample. Additionally, this chapter will determine a protocol for determining the carbon content for ZrC such that trends in the physical properties with composition can be examined with confidence.

The total carbon contents of the ZrC samples are measured using the standard carbon combustion analysis method. The range of carbon environments in these samples are then probed using static room temperature ^{13}C NMR. The structure in the line shape of the ZrC bonded and dissociated local carbon environments are also explored with respect to sintering temperature and stoichiometry. Additionally, systematics in the resonance line shapes corresponding to a change in the local ZrC carbon environments such as sintering temperature and carbon content are investigated. SEM is undertaken on samples to probe the microstructural variation between stoichiometries. The lattice parameter and relevant values are calculated from XRD analysis to determine if there are any changes in long-range order between samples sintered at different temperatures and/or with different stoichiometries. The nature of the dissociated carbon within the sample is explored using Raman spectroscopy for the samples sintered at 2000°C.

[2] *The majority of the findings presented in this chapter describe results published in the following paper: "Rana, D.B.K., Solvas, E.Z., Lee, W.E. and Farnan I. An investigation of the long-range and local structure of sub-stoichiometric zirconium carbide sintered at different temperatures. Sci Rep 10, 3096 (2020)*

In addition, the analysis of the pristine samples examined in this chapter act as a point of reference when examining the effects of proton and Xe irradiation on the samples. Pristine samples sintered at 2000°C are analysed by combustion carbon analysis, SEM, XRD, static ^{13}C NMR and Raman spectroscopy and are discussed in comparison with results presented in the literature. The samples sintered at 2000°C are further characterised by carbon analysis, solid sample XRD, ultrafast ^{13}C MAS-NMR and Raman spectroscopy.

2.2 Combustion carbon analysis of ZrC

In this section, the results of combustion carbon analysis are presented. Table 2.1 shows the total carbon content from carbon analysis measurements (with their associated errors) of the post-fabrication ZrC for all samples fabricated referenced to their sintering temperatures and stoichiometry.

Table 2.1- Nominal and carbon analysed values for ZrC samples. Error on the carbon analyser measurements is presented as one standard deviation calculated from the triplicate measurements, as the variability in the measurements was deemed to be the dominant source of error.

Sintering temperature (°C)	Nominal C/Zr	Measured C/Zr ± error
2000	1.00	1.00 ± 0.01
	0.80	0.85 ± 0.00
	0.60	0.64 ± 0.00
1700	1.00	0.96 ± 0.00
	0.80	0.73 ± 0.01
	0.60	0.64 ± 0.00
1500	0.95	0.95 ± 0.01
	0.70	0.73 ± 0.01
	0.65	0.64 ± 0.00

A more straightforward illustration of the samples fabricated can be seen by plotting the tabulated data with a reference line to denote a perfect fabrication outcome. Such a configuration is plotted in Figure 27, where the black dashed line (x=y) indicates the perfect fabrication scenario where the targeted stoichiometry matches the analysed carbon content. Data points that are above or below this line denote samples whose analysed carbon contents are greater or less than the nominal carbon contents, respectively.

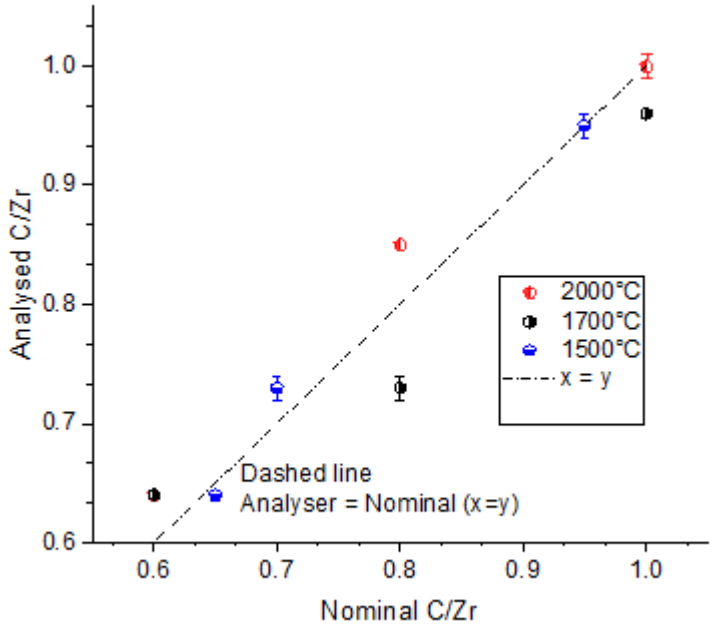

Figure 27 Carbon analyser values plotted against nominal values for ZrC samples of different stoichiometries sintered at 2000, 1700 and 1500°C.

The analysed carbon content of samples sintered at 2000°C were observed to deviate from their targeted stoichiometries. The maximum deviation from nominal carbon content was observed in the nominal C/Zr = 0.80 sample whose total carbon content was analysed to be 0.05 C/Zr higher.

The 1700°C samples were observed to have, on average, lower analysed carbon contents as compared with the nominal carbon content. The nominal C/Zr = 0.60 was the only sample that

showed an increase by C/Zr = 0.04 in the analysed carbon content as compared with the targeted carbon content. The samples of higher nominal carbon content showed a decrease in the total carbon content from the nominal, with the nominal C/Zr = 0.80 sample deviating the most by C/Zr = 0.07.

In the samples sintered at 1500°C, the highest nominal carbon content was seen to match the total analysed carbon content. The analysed carbon content of the nominal 0.70 sample was observed to increase by C/Zr = 0.03. Finally, the analysed carbon content of the nominal C/Zr 0.60 sample was seen to decrease as compared to the targeted value.

Overall, the majority of the samples showed a decrease in the total carbon content from their nominal values: three of the nine samples, sintered at mixed temperatures, showed an increase in the analysed carbon content as compared with their nominal values.

2.3 Quantification of carbon phases by static ^{13}C NMR analysis

In the following section and the constituent sub-sections, the results of the static ^{13}C NMR analyses are presented. The associated and dissociated carbon phases are identified and separated by a combination of peak fitting and several mechanistic NMR experiments. Key features and systematics are highlighted that relate to the identification of each unique carbon environment. Further, changes in the line shape between samples of different carbon contents and different sintering temperatures are presented. The results of ultrafast ^{13}C MAS-NMR experiments undertaken on the pristine samples sintered at 2000°C are also presented in this chapter to investigate any changes in the ZrC sub-peak structure.

2.3.1 Identifying the ZrC carbon environment using static 13C NMR

Figure 28 shows static ^{13}C NMR spectra for all samples, with samples sintered at different temperatures displayed on a common axis. Spectra are normalised to the same ZrC peak intensity (located at approximately 400 ppm) to facilitate quantitative comparisons between changes in peak width and peak intensity.

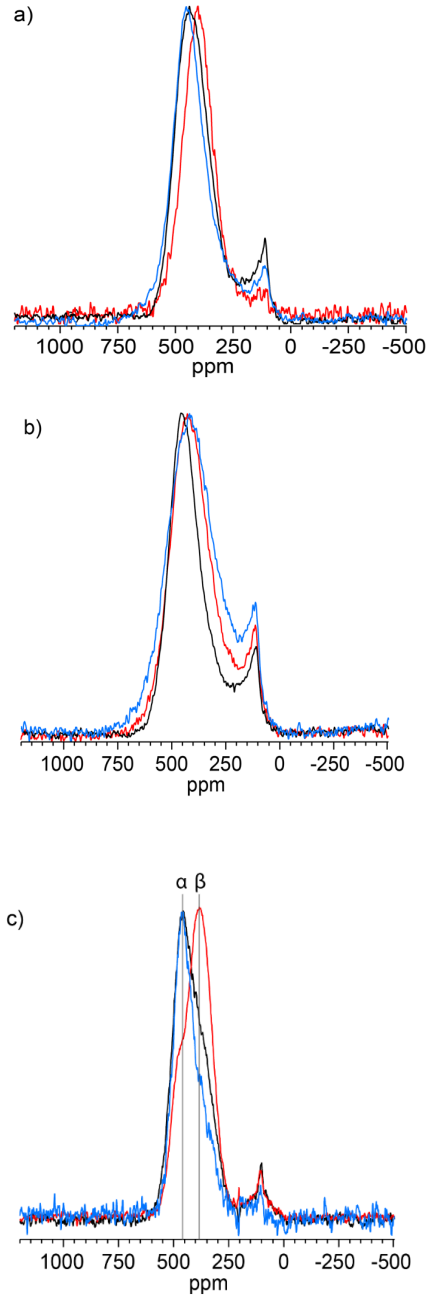

Figure 28 ^{13}C NMR spectra with normalised peak intensities for different stoichiometries sintered at (a) 2000°C, (b) 1700°C and (c) 1500°C. Red, black and blue spectrum traces correspond to nominal C/Zr = 1.00, 0.80, 0.60 for the 2000°C and 1700°C sintered samples, and nominal C/Zr = 0.95, 0.70, 0.65 for 1500°C sintered samples. α and β denote resolved peaks in the 1500˚C spectra.

The graphite resonance was observed to be centred around 113 ppm across all sample spectra. However, the ZrC resonance exhibits a dynamic behaviour with carbon content and sintering temperature. The ZrC resonance of samples sintered at 2000°C (Figure 28a) showed a noticeable shift in its centre of gravity (CG) from 404 to 434 ppm. The ZrC resonance CG, of samples with lower carbon contents, are located at lower ppm whilst the higher carbon content sample is located at higher ppm shifting the peak asymmetrically.

The ZrC resonance shift of samples sintered at 1700°C (Figure 28b) showed an asymmetric peak shift Δ~23 ppm. Contrary to the trend seen in the 2000°C sintered samples, the peak CG was seen to shift from 411 to 434 ppm with higher carbon content samples located at lower ppm and lower carbon content samples located at higher ppm. The ZrC resonance of the samples sintered at 1500°C (Figure 28c) was seen to comprise of two sub-environments within the central ZrC peak. These sub-environments are assigned as α and β in samples sintered at 1500°C, with tracer lines indicating the chemical shift of the peak CG which evolve as a function of the carbon content. As the sample becomes less metallic (carbon content increases) the carbon in the α sub-resonance position evolves into that of the β– and the overall peak structure changes. The intensity of α is present in NMR samples of nominal C/Zr = 0.65 and 0.70, whereas β is seen predominantly in the nominal 0.95 samples.

2.3.2 Identifying the ZrC carbon environment using static ^{13}C NMR

Figure 29a shows the static ^{13}C NMR spectrum of the nominal C/Zr = 0.60 sample sintered at 2000°C. Two main resonance features were observed within this spectrum; a sharp resonance located at approximately 113 ppm and a broader resonance observed at approximately 430 ppm. To decompose and attribute carbon environments to each resonance, static ^{13}C NMR was undertaken on the graphite carbon precursor (Figure 29b). Both samples are plotted on a common axis in Figure 29. Comparing Figure 29 (a) and (b) shows that the sharp graphite resonance and its location is common in both spectra – indicating the presence of free graphite in the ZrC sample, which implies the second resonance is ZrC. The portion of the graphite resonance in Figure 29a located at chemical shifts greater than 113 ppm before the ZrC peak

shows less of a sharp peak compared to the graphite precursor spectrum; potentially indicating the presence of an additional resonance. Evidence supporting that the broad peak ~430 ppm in Figure 29 (a) can be attributed to ZrC, can be seen by inspecting the compiled ^{13}C NMR sample spectra in Figure 28.

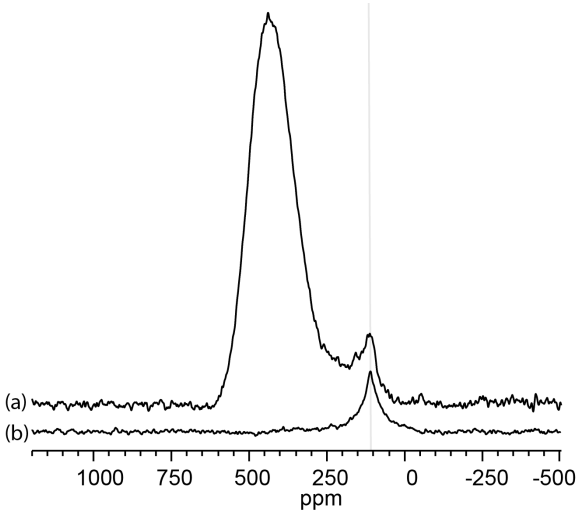

Figure 29 Static ^{13}C NMR spectra (a) of ZrC, nominal C/Zr = 0.60, sintered at 2000°C and (b) of precursor graphite located at approximately 113ppm. Spectra are scaled to emphasise the common position and presence of the graphite peak between the two spectra.

2.3.3 Identifying the ZrC carbon environment and a broad carbon phase using static ^{13}C NMR

As well as the 'sharp' graphite resonance located at approximately 113 ppm, evidence for an additional resonance, and therefore an additional carbon local environment in these ^{13}C NMR spectra, emerges in the range of 120 to 300 ppm.

Quantification of the spectral resonances was achieved by peak fitting appropriate Gaussian or Voigt profiles to the features observed in the spectra. The graphite resonance was fit in each spectrum using a Voigt peak profile, as this was determined to encompass the characteristics of the graphite precursor graphite powder. In all cases, the ZrC peak was fit using a Gaussian profile, and the fit was optimised using non-linear regression in Igor Pro. Figure 30 shows the nominal C/Zr = 0.80 sample spectrum with the fit ZrC and graphite resonances labelled a and

b respectively. An additional broad resonance is observed in the residual spectrum (Figure 30 top spectrum) labelled c, which is positioned at approximately 120 to 300 ppm. Difficulty arose in fitting the broad structure as fitted peaks were seen to infringe on both the ZrC and the graphite resonances. As such, quantification of the broad peak structure was determined by subtracting the sum of the graphite and the ZrC resonances from the total signal integral.

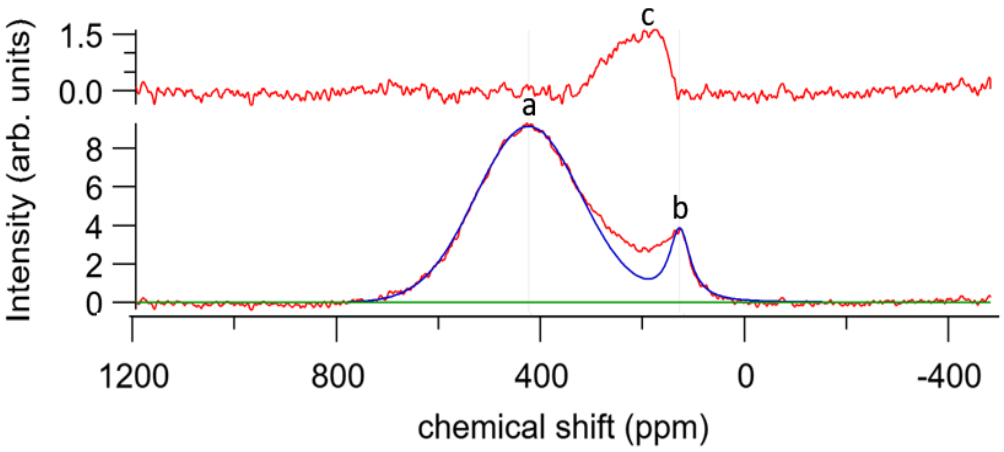

Figure 30 Deconvolution of the ^{13}C NMR peaks in a sample sintered at 1700°C with nominal C/Zr = 0.80. The bottom spectrum shows the Gaussian peak fitted to the ZrC carbon resonance at 419ppm (a) and a Voigt peak at 113 ppm to the resonance of graphite carbons (b) (blue) fit to the original spectrum (red). The top profile shows the residual when (a) and (b) are subtracted from the original line shape, revealing an additional resonance labelled (c).

A compilation of the carbon contents obtained from the different methods used are presented in Table 2.2 alongside quantification of the carbon environments as determined from the peak fitting.

Table 2.2 - Compilation of the analysed and NMR corrected carbon contents. Errors on the NMR fits are propagated from errors on the peak fits, and the error (±1σ) on the carbon analyser was calculated from the triplicate measurements.

Sintering temperature (°C)	Nominal C/Zr	Analysed C/Zr ± error	Corrected C/Zr from NMR ± error	Corrected Graphite content from NMR ± error	Corrected broad carbon content from NMR ± error
2000	1.00	1.00 ± 0.01	0.95 ± 0.01	0.03 ± 0.01	0.03 ± 0.03
	0.80	0.85 ± 0.01	0.75 ± 0.01	0.03 ± 0.01	0.07 ± 0.01
	0.60	0.64 ± 0.01	0.50 ± 0.01	0.04 ± 0.01	0.09 ± 0.01
1700	1.00	0.96 ± 0.01	0.81 ± 0.01	0.07 ± 0.01	0.17 ± 0.03
	0.80	0.73 ± 0.01	0.56 ± 0.01	0.09 ± 0.01	0.03 ± 0.01
	0.60	0.64 ± 0.01	0.50 ± 0.01	0.05 ± 0.01	0.08 ± 0.01
1500	0.90	0.95 ± 0.01	0.88 ± 0.02	0.06 ± 0.02	0.01 ± 0.11
	0.70	0.73 ± 0.01	0.69 ± 0.01	0.03 ± 0.01	0.01 ± 0.22
	0.65	0.64 ± 0.01	0.60 ± 0.01	0.00 ± 0.01	0.04± 0.13

2.4 Pre-irradiation XRD

In this section results from XRD analysis and Rietveld refinement are presented. The corresponding lattice parameter values are analysed, and their various values are presented in the context of the carbon contents of each sample. Plots are stacked by sintering temperature to aid with inter-sintering temperature comparisons.

2.4.1 ZrC powdered XRD on samples sintered at 2000, 1700 and 1500°C

Figure 31, Figure 32 and Figure 33 show powdered XRD diffractograms for samples sintered at 1500, 1700, 2000°C, respectively. In order to identify phases, CIF files were generated from the *Inorganic Crystal Structure Database* (ICSD) [77], and the XRD patterns were simulated using Mercury software produced by the Cambridge Crystallographic Data Centre. Phases are labelled in the legend and assigned vertical tick marks which are labelled at their appropriate diffraction angles on the diffractograms. The silicon standard peaks are identified using an

asterisk * above the top diffraction pattern. The location of the graphite peak is also labelled above the bottom diffraction pattern with a triangle marker. XRD patterns for all samples showed the fully indexable ZrC NaCl peaks whose corresponding crystallographic (hkl) planes are labelled at the top of each figure.

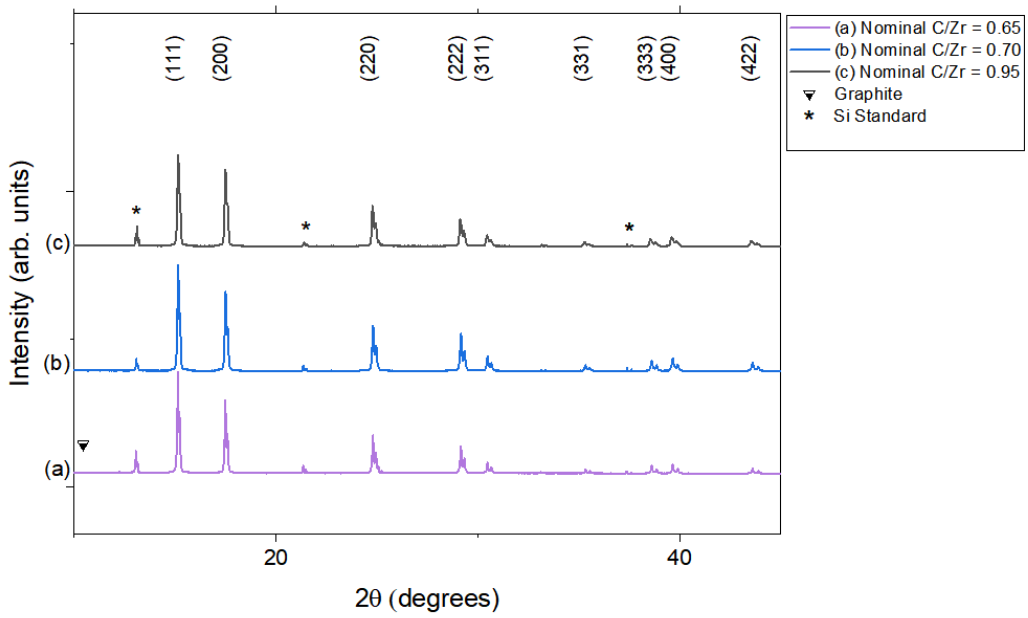

Figure 31 Stacked diffractograms of samples sintered at 1500°C for nominal C/Zr= 0.65, 0.70, 0.95 labelled (a), (b), (c) respectively – ZrC peaks are indexed and identified in the legend alongside additional phases.

No evidence of graphite was observed in any of the diffractograms; similarly, no unreacted Zr was observed. In addition, no diffraction peaks belonging to crystalline zirconia were observed.

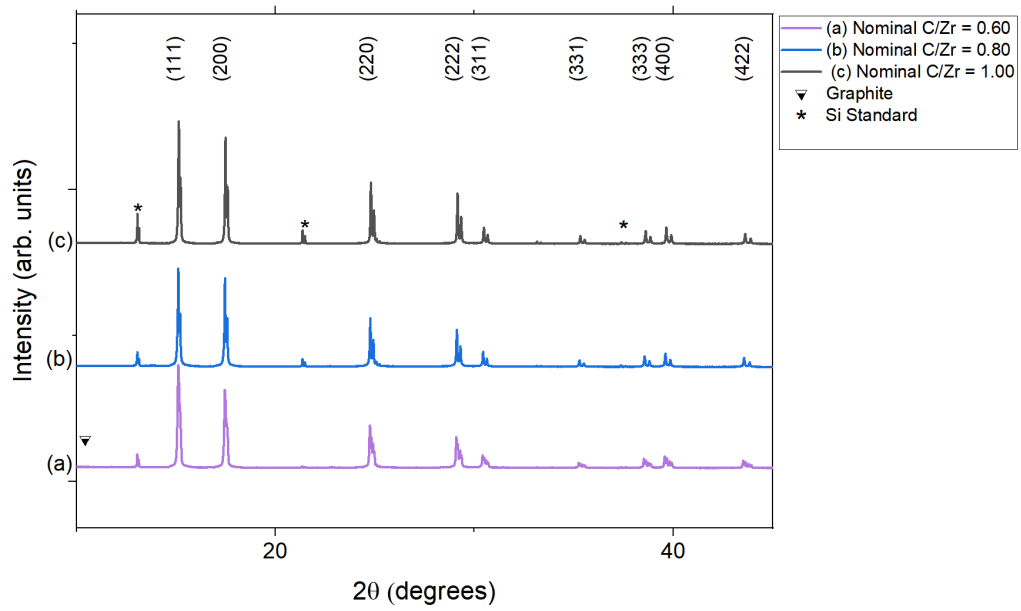

Figure 32 Stacked diffractograms of samples sintered at 1700°C for nominal C/Zr= 0.60, 0.80, 1.00 labelled (a), (b), (c) respectively – ZrC peaks are indexed and identified in the legend.

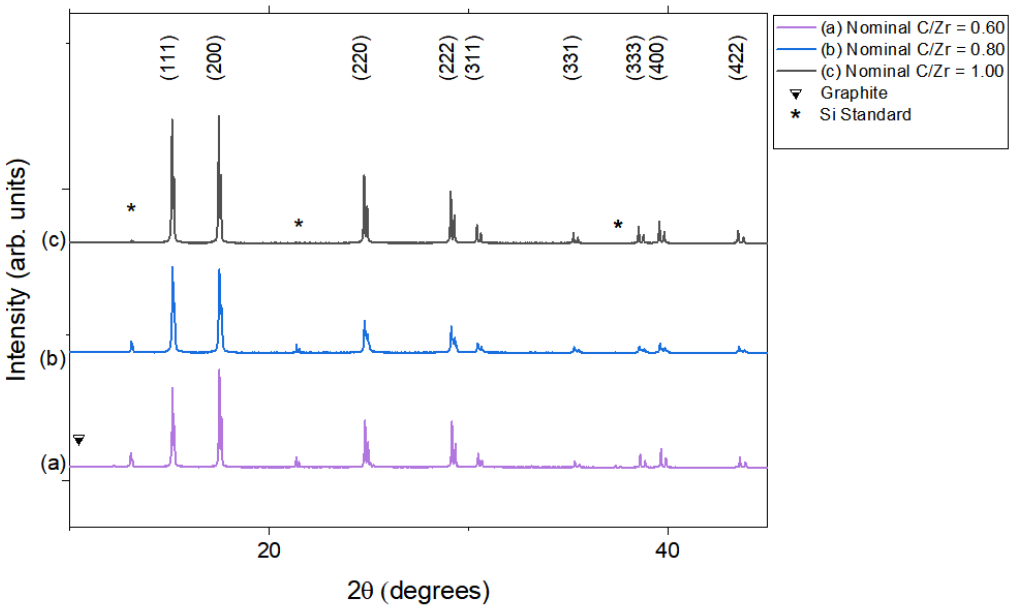

Figure 33 Stacked diffractograms of powdered samples sintered at 2000°C for nominal C/Zr= 1.00, 0.80, 0.60 labelled (a), (b), (c) respectively – ZrC peaks are indexed and identified in the legend alongside additional phases.

The NaCl ZrC structure was maintained, independent of sintering temperature. In addition, no diffraction peaks belonging to zirconia, oxygen or graphite were observed in any of the XRD patterns.

2.4.1.1 The lattice parameter of powdered samples

Figure 34 shows the lattice parameters obtained from Rietveld refinement of the XRD diffractograms plotted with respect to the carbon content as determined by different methods. An isolated plot of the lattice parameters plotted against nominal carbon content is included in the top right of Figure 34 for clarity.

Two main trends were observed in this data: an increase in the lattice parameter with carbon content and an increase in the lattice parameter with the sintering temperature. Although lines have been drawn between each datapoint, this does not necessarily describe the correct trend for individual sets of samples at each sintering temperature. These lines have been drawn to highlight potential trends between sintering temperatures and carbon content assignments.

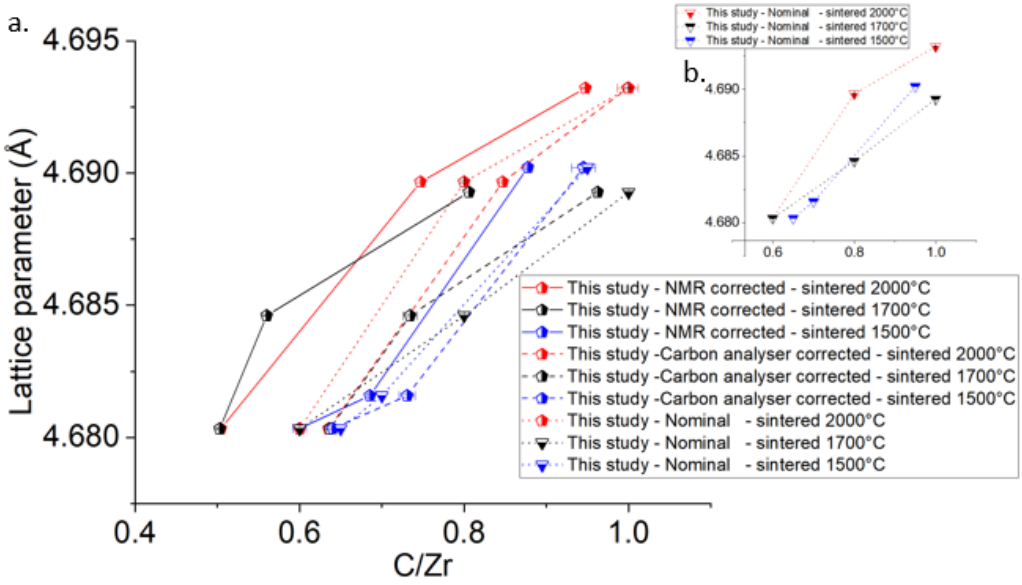

Figure 34 a. Lattice parameters of the powdered samples as obtained from Rietveld refinement plotted with respect to carbon content determined through the different carbon analysis methods. b. lattice parameters plotted with respect to the nominal carbon content.

Examining the small graph of the isolated nominal carbon content with respect to temperature reveals that all samples show an increase in the lattice parameter with increasing carbon content. The nominal graph shows that the sample sintered at 2000°C on average has a larger

lattice parameter than the samples sintered at lower temperatures for a given carbon content. The 1500, 1700 and 2000°C sintered samples appear to show an almost linear increase in the lattice parameter.

Referencing the lattice parameters to NMR corrected carbon content, as expected, shows that the values for the lattice parameter shifted negatively in the x-direction as compared to the nominal values.

2.4.2 ZrC XRD on solid samples sintered at 2000°C

To compare changes in the XRD diffractograms and associated properties – XRD was undertaken on the solid blocks cut from each pellet sintered at 2000°C. Figure 35 shows unirradiated offset XRD patterns for the solid samples sintered at 2000°C for the nominal C/Zr = 1.00, 0.80 and 0.60.

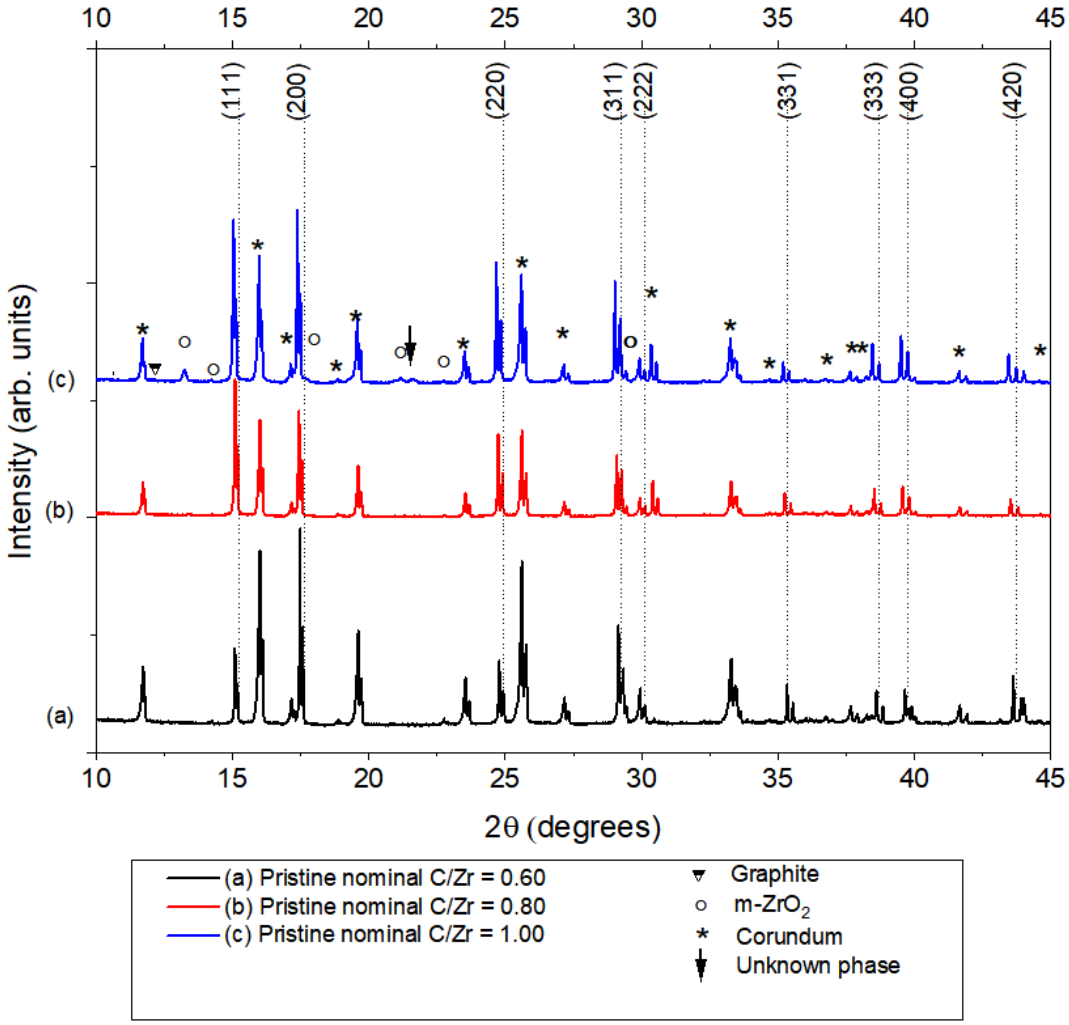

Figure 35 Stacked diffractograms of the samples sintered at 2000°C nominal C/Zr= 1.00, 0.80, 0.60 labelled (a), (b), (c) respectively – ZrC peaks are indexed and identified in the legend.

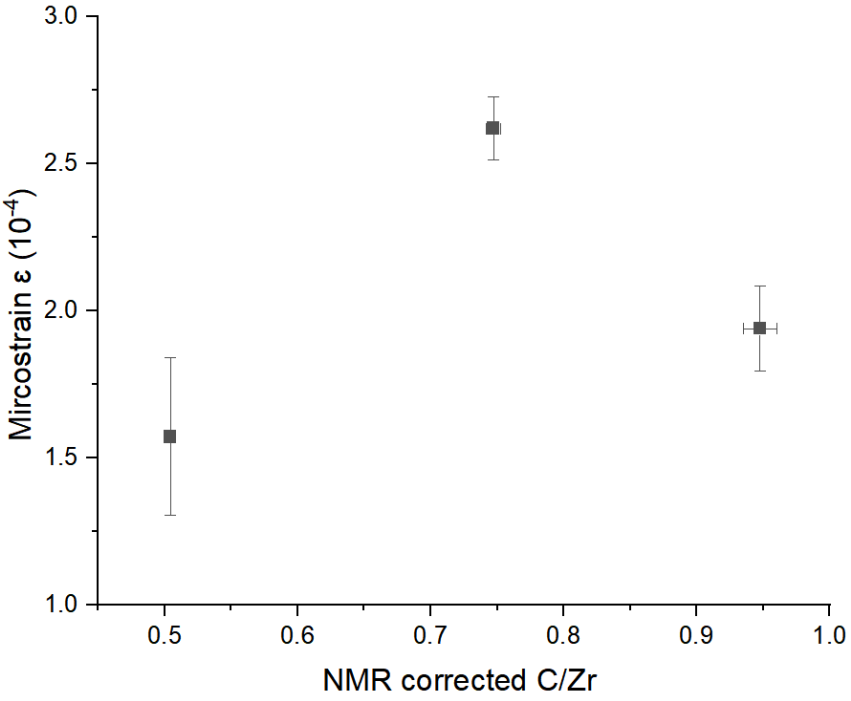

Figure 36 the crystallite microstrain of solid ZrC samples sintered at 2000°C plotted with respect to the NMR corrected carbon content.

Figure 36 shows the microstrain of the ZrC solid samples. The mean microstrain values of the nominal C/Zr = 0.6 and 1.00 samples were observed to be within error of one another. The nominal C/Zr= 0.80 sample was observed to have the highest microstrain values.

2.5 Pristine SEM of 2000°C sintered samples

This section presents the results of SEM (SE, BSE and EBSD) imaging on the pristine ZrC samples.

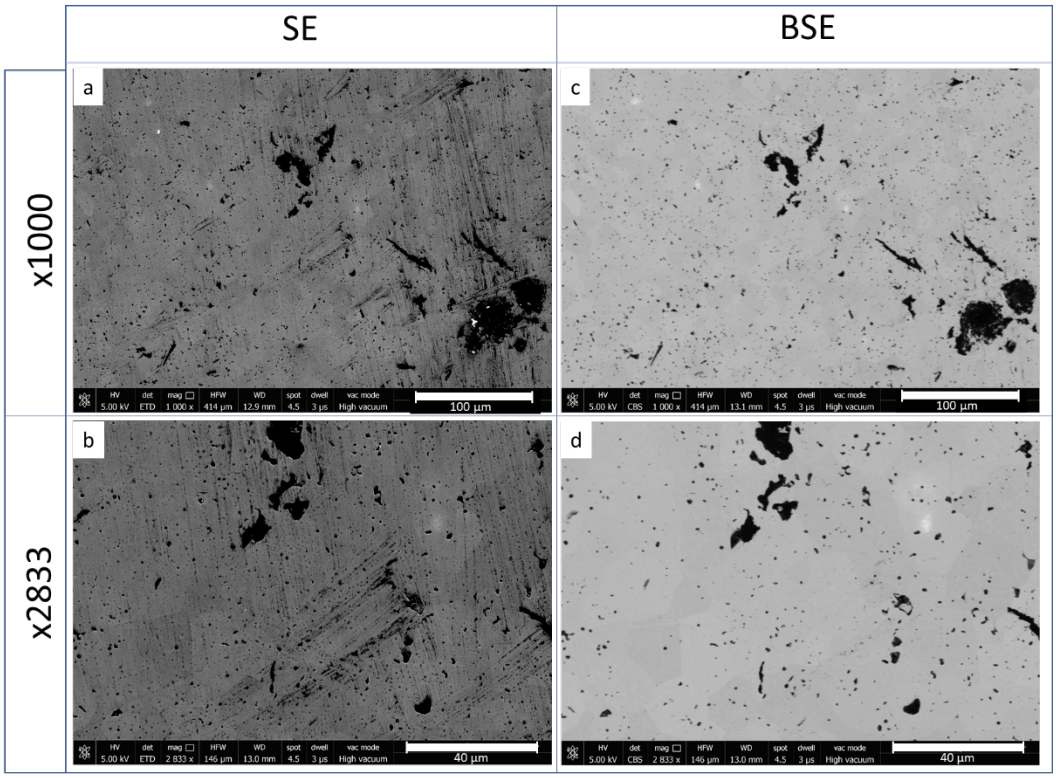

Figure 37 BSE and SE images of sample sintered at 2000°C with nominal C/Zr = 1.00, BSE images are on the right-hand side and SE images are on the left-hand side. Images on the top and bottom row have been taken at 1000x and 2833x magnification, respectively.

Figure 37 shows BSE and SE (left and right) images taken on the SEM at x1000 and x2833 magnification (top and bottom) for nominal C/Zr = 1.00 sintered at 2000°C. SE and BSE images showed a resolvable grain structure accompanied by inter-and intra-granular black structures. The width of these black structures was observed to range from approximately 1 to 10 µm, with larger structures preferentially located at grain boundaries. Inter-granular features were seen to be elongated in shape, as they extended along the grain boundaries, whilst intra-granular features appeared to be more circular.

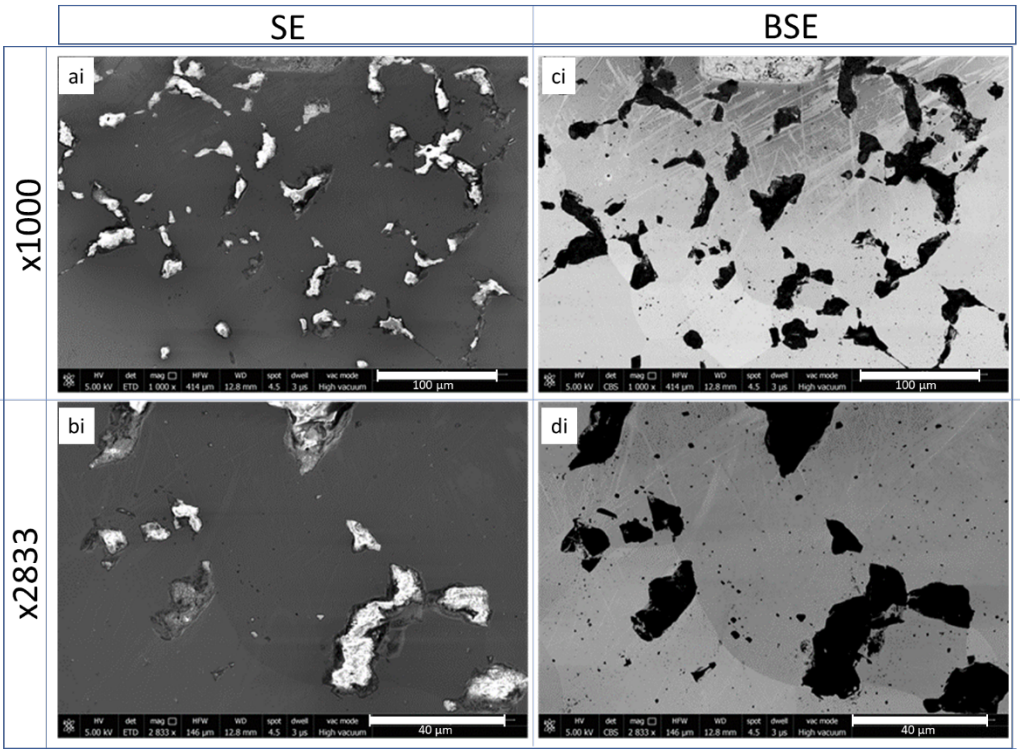

Figure 38 BSE and SE micrographs of the nominal C/Zr = 0.80 sample sintered at 2000°C. sintered sample (NB: image locations have the same significance as Figure 37).

The nominal C/Zr = 0.80 sample SEM images (Figure 38) also showed the large elongated dark (from here on referred to as black structures) which were observed to be preferentially located along grain boundaries. Smaller structures (~µm in diameter) were again seen to be located intra-granularly.

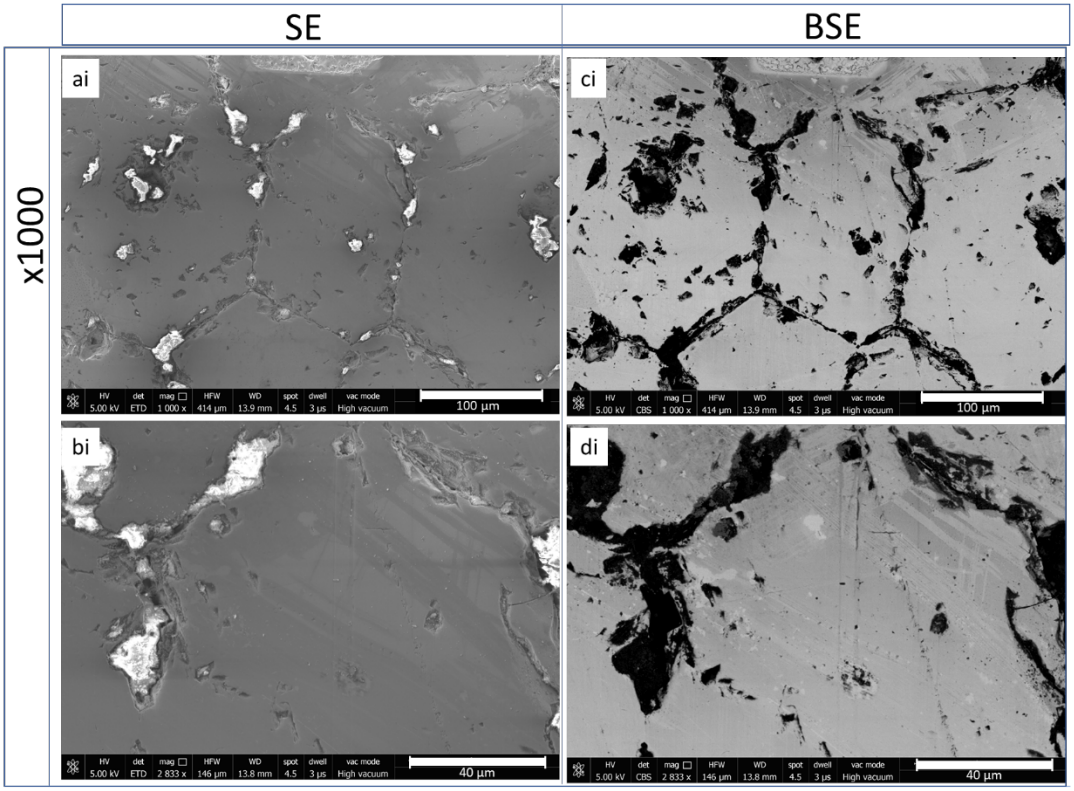

Figure 39 BSE and SE micrographs of the nominal C/Zr = 0.60 sample sintered at 2000°C. sintered sample (NB: image locations have the same significance as Figure 37).

BSE and SE micrographs of the nominal C/Zr = 0.6 sample (Figure 39) revealed a well-developed connected network of elongated, asymmetric, inter-granular structures. As with the other samples, the intra-granular black structures were also observed.

a)

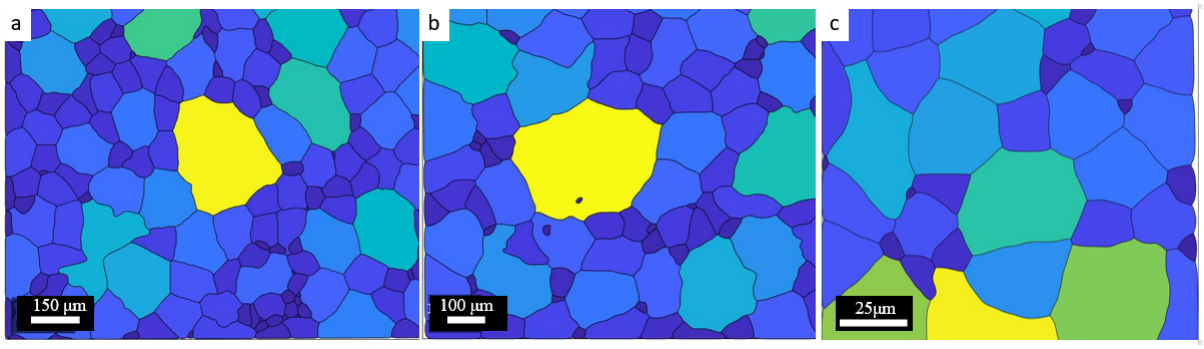

b)

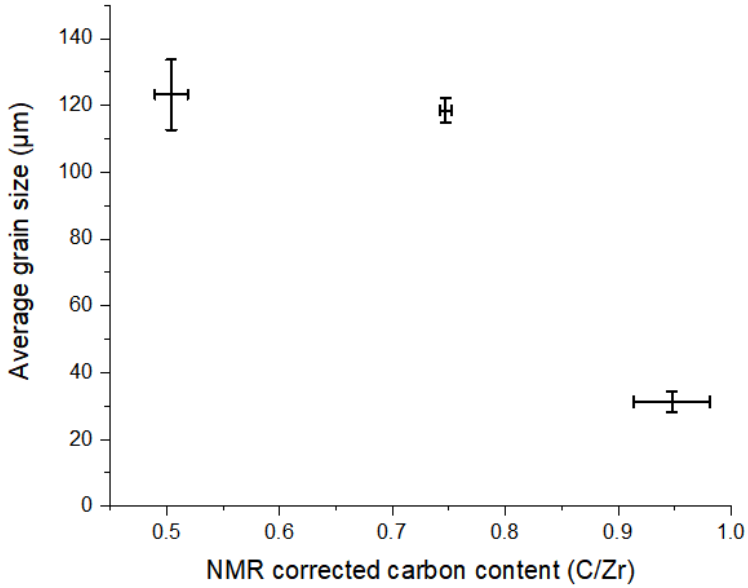

Figure 40 a) representative SEM EBSD for solid irradiated samples of nominal a. 0.60, b 0.80, c 1.00 sintered at 2000°C. b) average pristine grain size of pristine pre-irradiation ZrC samples to the NMR corrected carbon content. Average grain size errors are plotted to two standard deviations.

The results of the EBSD analysis and processing in the MTEX package in MATLAB are shown in Figure 40 shows an apparent decreasing average grain size with increasing carbon content. This data is presented in Figure 40 b), which shows the average grain sizes plotted with respect to the NMR corrected carbon content. The average grain size of the nominal C/Zr = 0.60 and 0.80 samples (123.2 ± 10.5 and 118.5 ± 3.5 µm) were observed to be within two standard deviations of one another. In contrast, the nominal C/Zr = 1.00 sample was observed to have a significantly lower average grain size (31.2 ± 3.2 µm), than the lower carbon content samples.

It is possible that the nominal C/Zr = 0.80 sample is an anomaly as it is markedly different from the decreasing trend in the grain size observed.

2.6 Pre-irradiation Raman

In this section, the results of the Raman spectra of the irradiated samples are presented for the samples sintered at 2000°C. Features of interest are highlighted in each spectrum as well as between samples.

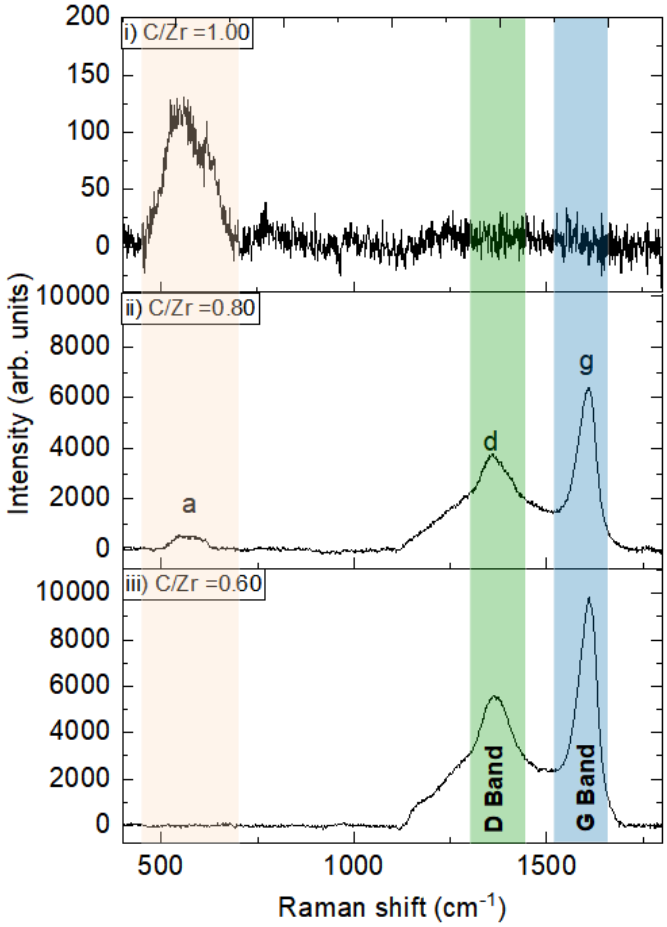

Figure 41 Raman spectra for the nominal C/Zr = 1.00 (i), 0.80 (ii) and 0.60 (iii) samples sintered at 2000°C. Raman spectra were baselined using a manually selected, user-defined baseline.

Figure 41 shows the baseline-corrected Raman spectra of the samples of nominal C/Zr =1.00, 0.80 and 0.60 sintered at 2000°C labelled i, ii and iii, respectively. The three observed Raman active modes labelled a, d and g are located above spectrum ii at their respective positions.

Mode a, centred around 600 cm^{-1}, has been previously attributed to amorphous carbon [92], [110]. The peaks labelled d and g can be attributed to graphite centred around 1359 cm^{-1} and 1600 $cm^{-1,}$ which are called the D and G bands respectively [16], [51], [111]–[113].

The signal intensities of the Raman active modes were observed to increase with decreasing carbon content. Thus, the nominal C/Zr = 0.60 exhibited the highest signal intensity of the D and G bands, followed by the nominal C/Zr = 0.80 sample and then finally by the nominal C/Zr = 1.00 sample in which the D and G bands are absent.

The presence of the D band in the Raman spectra of nominal C/Zr = 0.80 and 0.60 samples was accompanied by a broader component located below the sharp peak. The spectra of the nominal C/Zr = 0.80 sample also revealed the activation of the amorphous carbon mode labelled ‘a’ which was absent from the nominal C/Zr = 0.60 sample. The D and G bands were not seen to be active in the nominal 1.00 sample; instead, the amorphous band was seen to be the only active mode present.

The D and G modes were fitted using the Igor Pro software in a similar manner to the NMR spectral fitting detailed earlier. It was evident from visual inspection of the nominal C/Zr = 1.00 and 0.80 samples that the D band was comprised of two components: a broad Gaussian component and a sharper Lorentzian component. Contrastingly, the characteristics of the G band could be captured by a single, sharp Voigt function. Fitting peaks to these active modes confirmed these observations. Difficulty in fitting these peaks often arose due to small asymmetries in the spectral peak. The broad and narrow peak characteristics of the D band for the nominal C/Zr = 0.80 sample were seen to be captured by narrow Lorentzian profiles, and a broad Gaussian centred around 1361 ± 1 cm^{-1} and 1370 ± 1 cm^{-1} with FWHM of 53 ± 1 cm^{-1} and 298 ± 4 cm^{-1} respectively. The G band characteristics were determined to be suitably captured by a single Voigt profile centred at 1609 ± 1 cm^{-1} with FWHM of 58 ± 1 cm^{-1}.

For the nominal C/Zr = 0.60 sample, the D band characteristics were similarly captured by a broad Gaussian and narrow Lorentzian profile centred at 1361 ± 2 cm $^{-1}$ and 1409 ± 1 cm $^{-1}$ with FWHM of 284 ± 1 cm $^{-1}$ and 74 ± 4 cm $^{-1}$ respectively. The characteristics of the G band were determined to be suitably captured by fitting a single Voigt profile centred around 1607 ± 1 cm^{-1} with FWHM of 56 ± 1 cm^{-1}. The locations of the D and G band narrow components were seen to shift by 1 and 3 cm^{-1} respectively and the FWHM was seen to vary by 20 and 2 cm^{-1} respectively between the nominal C/Zr = 0.80 and 1.00 samples. The broad peak was seen to vary in position by 10 cm^{-1} with the FWHM varying by 2 cm^{-1} between these samples.

Another component of the spectra that requires consideration is the 'a' mode that appears at lower wavenumbers in the nominal C/Zr = 1.00 and 0.80 samples. From visual inspection of the spectra, the amorphous band appears to be comprised of two convoluted active bands – this phenomenon is more apparent in the nominal C/Zr = 1.00 sample. For both samples, it was determined that two peaks could be fitted, and this was undertaken using the Igor Pro software package. For the nominal C/Zr 1.00 sample; two Gaussian functions were fitted at 549 ± 1 cm^{-1} and 633 ± 2cm^{-1} with FWHM of 96 ± 3 cm^{-1} and 54 ± 3 cm$^{-1,}$ respectively. In the nominal C/Zr = 0.80 sample, the best fit was achieved using a Lorentzian and Voigt profile located at 574 ± 1 cm^{-1} and 692.99 ± 5.08 cm^{-1} with FWHM of 62 ± 3 cm^{-1} and 301 ± 4 cm^{-1} for the narrow and broad contributions respectively. For the fitting of the G band, a Lorentzian function was found to be the most suitable.

2.7 Discussion of pre-irradiation results

A range of unique chemical environments were revealed by the analysis of the ^{13}C NMR spectra which were determined to vary both as a function of carbon content and sintering temperature. The quantitative distinction between these carbon phases cannot be accurately captured by carbon analysis.

Analysis of the static ^{13}C NMR spectra provides quantitative corrections for the values as determined by carbon analysis. Three distinct carbon phases were observed in each ZrC

sample: carbon associated with the ZrC structure, carbon in the broad environment and graphitic carbon. The total carbon content, as measured by the carbon analysis method, which is commonly used use determine the C/Zr in the literature, is a sum of the contributions of each environment.

The distinctive ZrC resonance is observed in all samples; however, the asymmetry and centre of gravity were observed to change with the carbon content of the sample. In almost all cases a separate broad resonance of unknown origin accompanied the ZrC and graphite resonances. It was hypothesised that an anisotropy could be associated with a second nearest neighbour atom in the ZrC environment. This seemed plausible as different crystallite orientations, with respect to the applied spectrometer magnetic field, of a vacant structure could present an additional unique chemical environment that would be present as broad resonance structures in an NMR spectrum. By contrast, a perfect stoichiometric C/Zr =1.00 NMR spectrum would present a singular resonance with no associated anisotropy due to the high point symmetry of the perfect cubic structure.

An investigation into the nature of the broad peak was conducted using incremental pulse delay experiments. A pulse delay of 9.0 seconds (T_1 = 1.8 seconds) was determined to be the time for maximal signal acquisition which was set by the slow relaxation period of the ZrC peak. The broad carbon peak was seen to reach the equilibrium signal at 3.0 seconds (corresponding to a T_1 = 0.6 seconds). Thus, the unique carbon environment associated with the broad carbon peak is determined to be closer, chemically, to carbon in the graphite environment than carbon in the ZrC environment as evidenced by nutation experiments. Comparison of the broad peak location with literature values reveals that this resonance peak can be attributed to sp^2 type carbon which is similar to the black fullerenes and amorphous carbon structures [56], [57], [61], [62], [63].

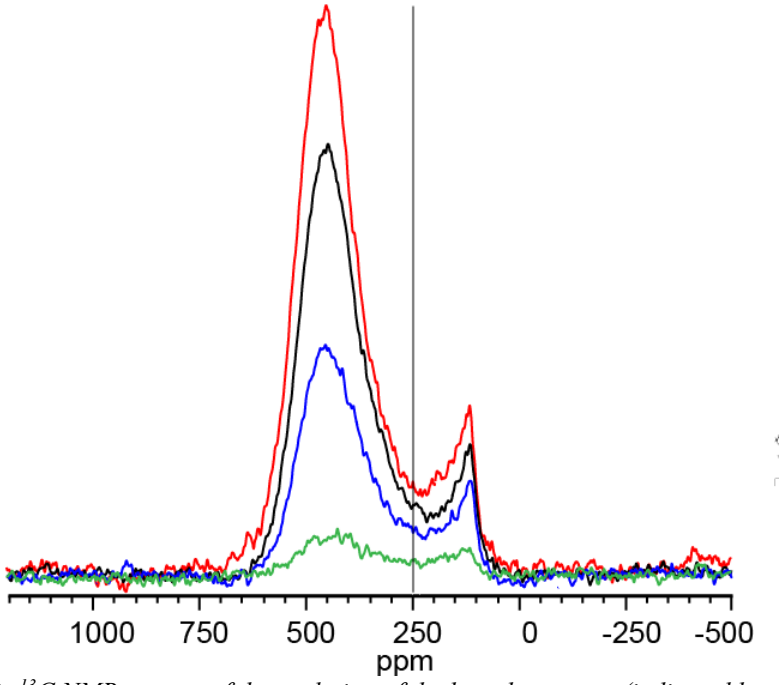

Figure 42 Static ^{13}C NMR spectra of the evolution of the broad structure (indicated by grey line) with respect to the pulse delay for the nominal C/Zr = 1.00 sample sintered at 1700°C. Red, black, blue and green spectral traces correspond to pulse delays of 9.0, 3.0, 1.0 and 0.1 seconds respectively.

The graphite (113 ppm) resonance was observed in all samples. The C/Zr of the samples produced lie within the homogeneity zone (0.55 > C/Zr > 1.00) highlighted in red in the ZrC phase diagram in the literature review Figure 1. An ideal and pure ZrC material whose composition lies within this region should be comprised of pure ZrC with no additional phases present [13], [117]. Thus, assuming the phase diagram is correct, the fabrication procedure could be the predominant source of the extra phases observed within the sample.

One possible explanation as to the source of this graphite could be due to the presence of a carbon diffusion gradient between the Grafoil™ and the vacancy rich ZrC. The presence of high temperatures could enhance the rate at which graphite ingresses into ZrC. The dissociation of this resonance from the ZrC structure would imply that although the graphite exists within the sample, it was not incorporated into the vacant carbon sites. Furthermore, the time to reach the equilibrium NMR signal of the graphite peak was observed to be 3.0 seconds, whereas the

unreacted precursor graphite equilibrium signal time was 0.1 seconds. The relaxation behaviour confirms that unreacted graphite, which has a very short T1 relaxation, is not present in the sample. The chemical shift position of the broad peak resonance in the ^{13}C NMR spectra, as indicated in the literature, exhibits an NMR response of sp^2 type carbon similar to that seen by black fullerenes and amorphous carbon structures [118]–[120]. It is possible that this peak may have an anisotropic characteristic contributing to its broad structure.

Static NMR conducted on the samples sintered at 1500°C revealed the presence of two sub-environments, α and β. This apparent sub-environment structure was not seen in the spectra of samples sintered at different temperatures. Figure 43 shows the CG of the ZrC resonance, determined from fitting Gaussian functions, for all samples plotted against the corrected stoichiometry as determined from NMR analysis. The Gaussians fitted to the α, and β resonances are located at approximately 460 ppm and 370 ppm, respectively. Computing the average CG of each of the 1500°C samples weighted by intensities of the α and β peak shows a trend similar to the variation of CG samples sintered at different temperatures.

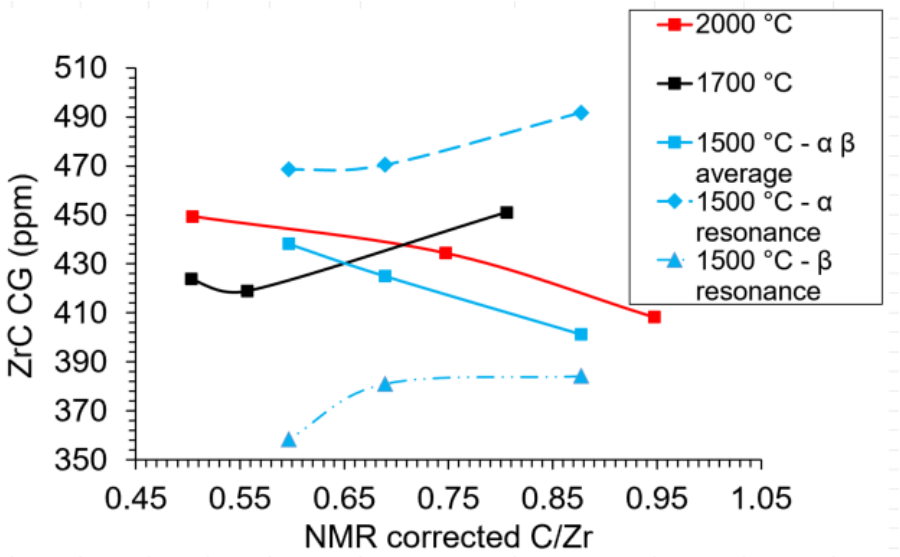

Figure 43 CG of the ZrC peak as determined from NMR spectrum peak fitting plotted with respect to NMR determined C/Zr for samples sintered at 2000°C, 1700°C and 1500°C.

It was possible that the 1500°C peak may have an element of anisotropy associated with it due to random crystal orientations. However, at first glance this did not seem to be the case as a

clear systematic evolution of the α to β environment was seen with carbon content. The number of carbon atoms that were, proportionally, in the α and β environments were seen to decrease and increase respectively with increasing carbon content. This indicated the evolution in preferential occupancy changed from the more metallic, based on paramagnetism of conduction electrons, vacancy rich α environment to the less metallic, carbon-rich β environment. The percentage of carbons present in the ZrC resonance for the nominal C/Zr = 0.95, 0.70, 0.65 samples (sintered at 1500°C) were for the α resonance 16%, 49%, 72% and for the β resonance 84%, 51%, 28% respectively.

The fitting of a single Gaussian function was sufficient to capture the characteristic structure of the ZrC resonances of the samples sintered at 2000°C and 1700°C. The CG of the samples sintered at 2000°C are seen to decrease in position with increasing carbon content in accordance with the trend seen in the 1500°C samples.

In sub-stoichiometric ZrC, the carbon atoms can be envisaged to adopt a number of arrangements around a Zr matrix [121], [122]. As NMR is sensitive to probing the local structure around a carbon atom, it is sensitive to the environments of both first and second carbon nearest neighbours. Thus, a change in the distribution of the first and second nearest neighbour carbons would alter the local magnetic field induced at a carbon atom. A second effect is the peak position shifting in metallic or semi-metallic systems as the carbon content of ZrC is increased due to the local density of states at the Fermi level (at carbon) i.e., a Knight shift component. A sub- stoichiometric structure with vacancies could affect both factors.

Zhang *et al.* [123] and Xie *et al.* [21] recently investigated and identified several stable ZrC stoichiometries of ZrC. The NMR corrected carbon content can be compared to the computationally determined phases as a means of validating them. Comparing the stoichiometries of the stable samples as determined in the two studies mentioned above with the NMR corrected C/Zr, as determined by this study, reveals common results as shown in Table 2.3.

Table 2.3 - Comparison of static ^{13}C NMR evaluated NMR C/Zr as compared with stable Zr_yC_z phases computed by Zhang et al. (†) [123] Xie et al (‡) [21].

Experimentally determined			Computationally determined
Sintering temperature (°C)	Nominal C/Zr	Corrected C/Zr from NMR ± error	Stoichiometry
2000	1.00	0.95 ± 0.01	NA
	0.80	0.75 ± 0.01	Zr_4C_3 †
	0.60	0.50 ± 0.01	Zr_2C_1 † ‡
1700	1.00	0.81 ± 0.01	$Zr_{32}C_{28}$ †
	0.80	0.56 ± 0.01	$Zr_{32}C_{18}$†
	0.60	0.50 ± 0.01	Zr_2C_1 † ‡
1500	0.95	0.88 ± 0.02	Zr_8C_7 †
	0.70	0.69 ± 0.01	NA
	0.65	0.60 ± 0.01	NA

In contrast to the results reported by Zhang *et al.* [123] no departure from the stoichiometric FCC symmetry was determined via XRD experiments. The computationally determined phases may exist dispersed throughout the samples or exist on a scale that is not detectable by XRD.

Several ordering schemes can be considered for the multiple peaks found in the static NMR spectra for the samples sintered at 1500°C, which could be used to explain the systematic evolution and inhomogeneity in the line NMR shape. As the NMR chemical shift is modulated by the change in the local bonding environment, the following analysis considers the change in the chemical environments.

The first model we can consider is a 3x3x3 ZrC supercell populated by 108 carbon atoms. Considering the central carbon atom; it is surrounded immediately by 12 nearest neighbour carbon atoms (NN_C) that are located at $\sqrt{2}\ d_{Zr\text{-}C}$ (where change the Zr-C $d_{Zr\text{-}C}$ is the zirconium carbon distance). The second NN_C are 6 carbon atoms positioned at a distance of $2d_{Zr\text{-}C}$ from the central atom. Finally, the 24 third NN_C are positioned at a distance of $3/2\ d_{Zr\text{-}C}$ from the central atom.

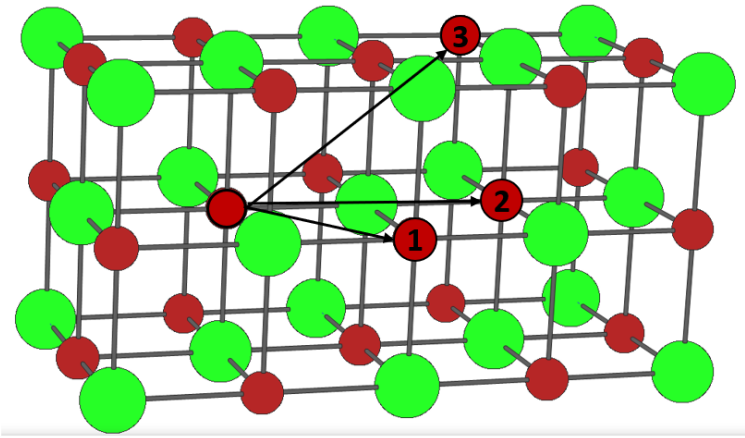

Figure 44 Vacancy positions relevant to near-neighbour effects that could be present in the NMR spectrum, shown in a 2x1 cell where the carbon and zirconium atoms are identified by the red and green atoms, respectively. Examples of first, second and third NN_c atoms are labelled by their corresponding numbers. An arrow is drawn from a resonant carbon atom outlined in black to each numbered NN_c.

One can consider several vacancy models to explain the systematic changes in the 1500°C NMR spectra with carbon content. Considering the vacation of the 24 third NN_C sites resulting in a C/Zr = 0.79, vacating the next 6-second NNc sites would result in a C/Zr = 0.72. As mentioned previously, the β peak is only observed in the sample which has an NMR corrected carbon content of C/Zr =0.88; the distinct α peak is first seen in the sample with an NMR corrected carbon content of C/Zr = 0.69. It is reasonable to assume that if the avoidance model is correct that the transition from α to β occurs at an NMR corrected C/Zr ~ 0.79 due to a change in the local chemical environment caused by the number of vacancies to moving from requiring third NNc to second NNc carbon atoms being absent.

For the samples sintered at 2000°C and 1700°C, it was not possible to resolve the ZrC peak structure in both the static ^{13}C NMR and the ultrafast ^{13}C MAS-NMR. This homogeneous peak structure may be due to the high sintering temperatures which would, in turn, lead to a higher carbon atom mobility – resulting in a more stochastic filling of vacant sites as opposed to a more ordered filling.

A simple binomial model can be used to model the stochastic distribution over the first and second NNc vacancies for the 108-atom cell as used previously. The binomial distribution may describe the underlying stochastic mechanism that produces a change in the peak centre of gravity for the samples sintered at 2000°C and 1700°C.

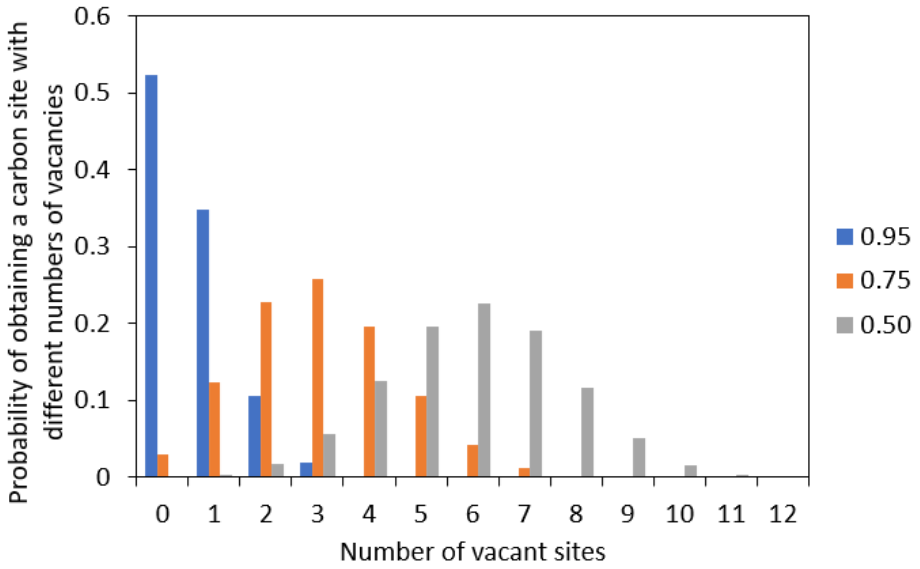

Figure 45 Binomial distribution of having a carbon site with different numbers of vacancies for the samples sintered at 2000°C for the NMR corrected carbon content for the 12-site carbon neighbour model.

The binomial distribution shown in Figure 45 presents the probabilities of obtaining carbon sites with different numbers of vacancies, for samples of different carbon content sintered at 2000°C. The individual bars in Figure 45 belonging to a particular sample, and hence carbon content, can be thought of as individual Gaussian functions, which then sum to produce a broader Gaussian. From the experimental NMR results for the 2000°C samples, lower carbon content samples produced an NMR spectrum centred at higher frequency (higher ppm). This

would match the progression of the binomial distribution calculated in Figure 45, of lower carbon content ZrC resonating at higher frequencies, as observed for the higher temperature ^{13}C NMR spectra of ZrC.

This is markedly different from the previous vacancy ordering model, which describes the preferential liberation of certain carbon atoms or ordering of vacancies. Both schemes reflect the results observed in the corresponding NMR spectra, however further computational analysis would need to be taken to understand this comprehensively.

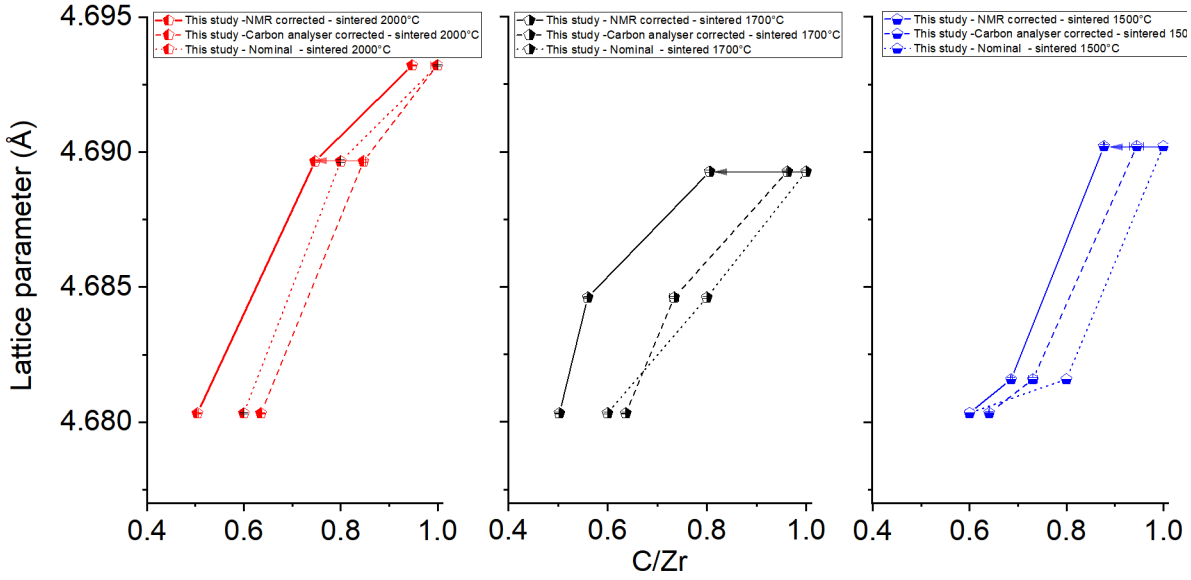

Figure 46 shows the change in position of the lattice parameter when the samples are referenced with respect to the different carbon determination values.

Figure 46 shows the lattice parameter values for all samples, determined by Rietveld analysis of XRD, plotted with respect to C/Zr determined by the three different carbon determination methods. Referencing the lattice parameter to carbon content as determined by various methods results in a spread of data originating from the accuracy of each method to the true carbon content. Previously, lattice parameter correlations have been used in the literature to determine the carbon content of the samples [41] which the above results deem to be inaccurate. It is proposed that the change in the C/Zr arises due to the mis-referencing of the carbon content -

whilst the change in the lattice parameter value is influenced by fabrication parameters that may promote the inclusion of interstitial gas species (e.g. oxygen) [12], [13], [44].

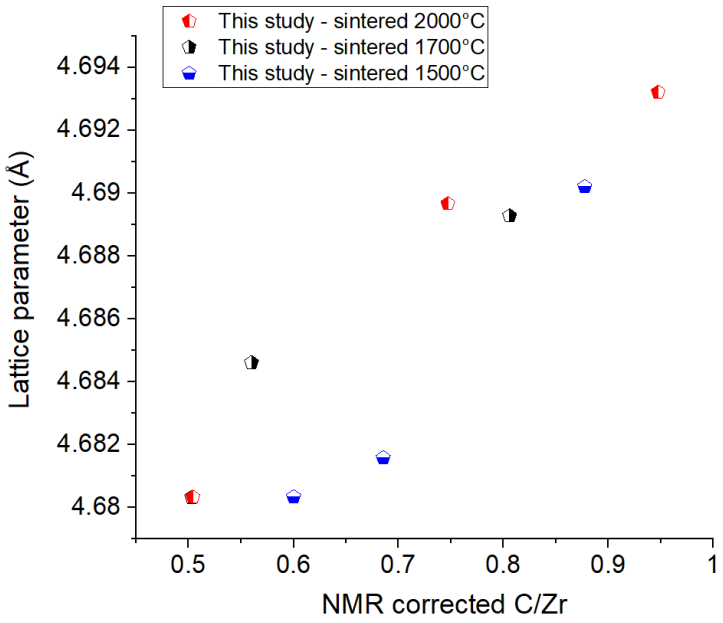

Figure 47 The lattice parameters of samples sintered at different temperatures plotted with respect to the NMR corrected carbon content.

The Lattice parameter of the samples sintered at 1500°C (Figure 47) was observed to have two of the lowest values of all the samples at lower carbon contents. Due to the structure in the NMR peak of the 1500°C, this may hint at the presence of ordering within the carbon environments within the ZrC structure. One interpretation of this result may be that samples with a greater degree of carbon atom ordering may have a lower lattice parameter value.

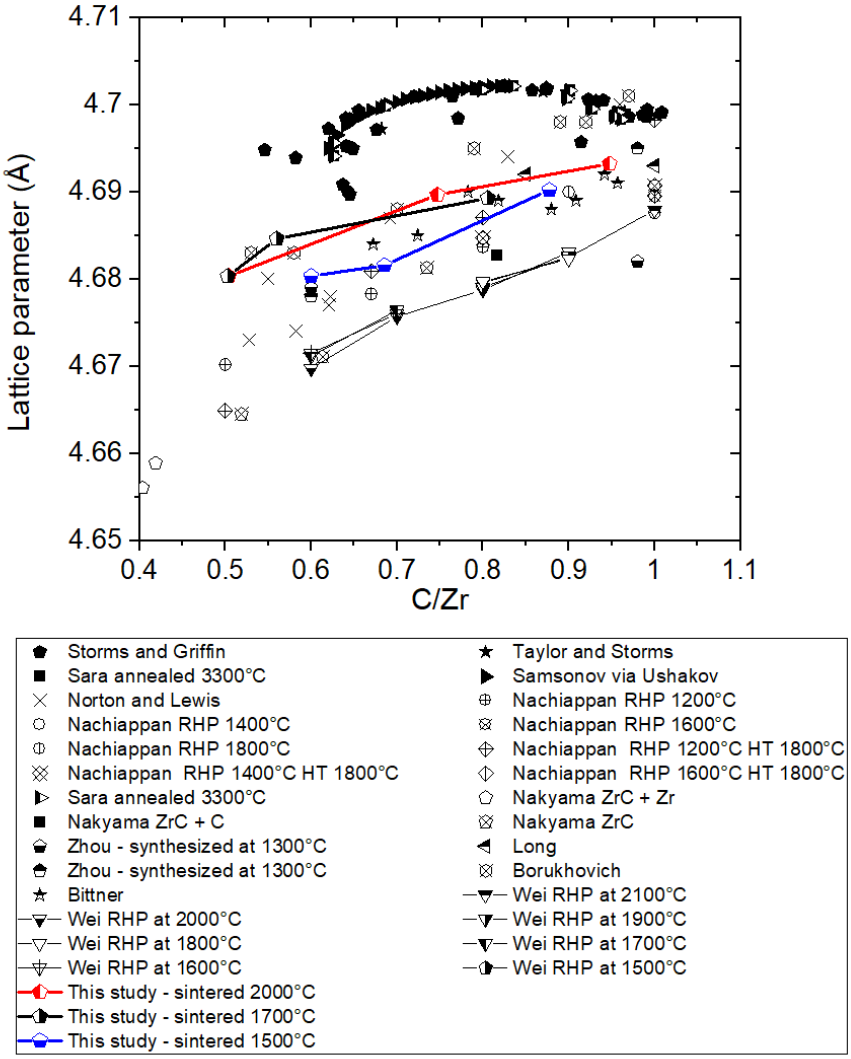

Figure 48 Lattice parameter of samples sintered at 1500, 1700 and 2000°C plotted with respect to the NMR corrected carbon content. Lattice parameter values from the literature are also plotted with respect to their reported carbon contents.

Figure 48 shows the data in the literature for the lattice parameters and the carbon content. Lattice parameter values reported in the literature with their referenced carbon content (including this study) reveal two distinct trends. The first trend is the parabolic lattice parameter [124], [125] which has a maximum value of 4.702 Å at C/Zr ~0.83 [18], [109] and decreases thereafter. The second trend, observed in this study and other recent studies [48], [126], [127],

shows an approximately linear trend as stoichiometry is approached. This highlights the variability in the data which can arise due to carbon content.

XRD analysis on the pristine samples reveals that they crystallise in the rock salt type structure up to approximately 50% vacancy concentration (NMR corrected) on the carbon sites. XRD patterns showed no evidence of the excess graphite that was detected in non-negligible quantities in the static ^{13}C NMR spectra. One theory is that the free carbon is not seen as it is dispersed, in small quantities, predominantly in grain boundaries. Previously, it has been proposed by several studies, that XRD was unable to detect the presence of excess free carbon and TEM analysis revealed the carbon existed in an amorphous form on the ~100 nm scale [128][129]. No unreacted phases were determined to be present in the XRD patterns. The ZrC phases were indexed to a powder spectrum generated by Crystal Maker and matched the ICD accessible in TOPAS.

Increasing the carbon content of the sample resulted in microstructural changes such as a decrease in the average grain size of the sample sintered at 2000°C. As the samples were fabricated together, at the same time and under the same conditions, it was deemed unlikely that other factors would affect the grain size. Thus, the change in the carbon content was the dominant contributing factor in the change in the grain size.

The average microstrain of the solid samples was seen to have the highest value in the nominal C/Zr = 0.80 sample. Overall the microstrain values reported in this study were seen to be smaller than the values reported in the literature [47], [54], [55]. One possible explanation for this trend could be that the small grain sizes in the C/Zr = 1.00 sample act to reduce the microstrain in the sample. In the nominal C/Zr = 0.60 sample, the large intergranular dark structures in addition to the presence of vacancies act to reduce the strain of ZrC.

Analysis of grain size and stoichiometry is not well documented in the literature and has not been studied with corrected stoichiometry values. However, if the general trend of decreasing

grain size with increasing carbon content holds for all ZrC samples this could explain the increase in the values of mechanical properties observed in the literature [13], [18]. One such example is the yield strength and hardness that are related to grain size via the Hall-Petch relationship [79], [80], [81].

Probing the microstructure via SE and BSE imaging revealed two features: the sample grains themselves and the presence of intra- and inter-granular dark structures. It was initially hypothesised from the BSE images that these structures were carbon phases that had not been incorporated into the ZrC structure. However, SE imaging showed that these were depressions from the bulk surface height. Identification of structures in the samples was initially conducted by EDS mapping. Due to the uneven surface of the black structures, EDS was determined to be unreliable due to X-ray absorption and secondary emission, giving false-positive results.

Raman spectroscopy was used to probe the composition of these structures and gain compositional information on the carbon in the solid samples. No signal was observed from the grains of the ZrC samples. The spectra of the black structures were found to contain 'partially destroyed' graphite, pristine graphite, and amorphous carbon. In addition, probing similar 'black' structures in the sample revealed that not all these structures produced a Raman signal and that the location of graphite phases not incorporated in the ZrC structure were not preferentially located in those regions. Nevertheless, the activation of the G mode was attributed to the presence of in-plane carbon sp^2 pristine carbon vibrations – which corresponds to the graphite peak, verifying the sharp graphite resonance (~113 ppm) observed in all NMR spectra.

The activation of the D mode was determined to correspond to partially destroyed carbon and amorphous carbon [51], [92] and the out of plane vibrations that occur as a result. This result complements the rapid relaxation findings of both the graphite and broad resonances from NMR pulse delay saturation experiments. The activation of these modes was also seen by Wang *et al.*, Ang *et al.* and Dong *et al.* [112], [133], [134].

The decrease in the intensity of the overall Raman spectral signal appears to be a function of the carbon content of the sample. As the carbon content of the sample is increased the number of structural vacancies is reduced. It is, therefore, reasonable to assume that the quantity of stoichiometric ZrC present in the sample increases. Thus, active modes which are activated by defects, such as the D and G mode, will become less active – which is consistent with experimental results from this study. The validity of fitting a Voigt profile to the G band of the nominal C/Zr 0.60 and 0.80 is explored by Puech *et al.* [135] and most recently by Mallet-Ladeira *et al.* [136]. The fitting of a double Lorentzian profile to the D mode is also suggested by Mallet-Ladeira *et al.* However, in the case of the spectra obtained in this study the fitting, of a Lorentzian followed by a broad Gaussian appeared to capture the profile better than a double Lorentzian.

Since graphitic carbon is present in the samples sintered at 2000°C but appears to be dispersed throughout the sample in small quantities (evidenced by NMR spectra XRD results respectively), it is possible to use some of the insights used from studies on graphene that have used Raman analysis to further confirm these findings. To better understand the scale of the carbon seen in the samples, we can examine the position of the G peak in the context of the amorphisation trajectory as detailed by Ferrari *et al.* [137]. Both the nominal C/Zr = 0.60 and the nominal C/Zr = 0.80 samples, as stated previously, were observed to have peaks centred around 1607 and 1605 cm^{-1} respectively which correspond to nano-crystalline graphite on the amorphization trajectory [51], [137]. These would explain why the graphite is undetectable by XRD but can be detected by NMR.

A large quantity of work exists in understanding the significance of active Raman modes through graphene and graphene oxide materials. One such relationship is the change in the relative peak height of the D and G peaks [51], [136]. Due to the specific location of these peaks, differences in the intensity can be related to the crystallite size of the sp^2 component for point defects via the modified Tuinstra and Koenig relation as proposed by (2.1) [50], [138], [139].

$$L_a(nm) = (2.4\ x\ 10^{-10}).\lambda_l^4 \left(\frac{I_D}{I_G}\right)^{-1} \quad (2.1)$$

where:

I_D= *The intensity of the D peak*

I_G= *The intensity of the G peak*

λ_l= *The wavelength of the laser (532 nm)*

L_a= *The sp^2 crystallite size*

Thus, the calculated sp^2 crystal crystallite size was determined to be approximately 33 nm for the nominal C/Zr = 0.80 and 0.60 samples.

2.8 Conclusions

A systematic range of nominal stoichiometry samples have been successfully fabricated at different sintering temperatures. The sample stoichiometries have been tested using academic and industrial standard combustion carbon analysis techniques. This chapter has shown that these techniques are not accurate for determining the carbon content of a sub-stoichiometric carbide sample. This could be the source of a large amount of scatter in physical property values that exist in the literature with one such example being the lattice parameter. Different sintering temperatures were seen to affect the incorporation of dissociated carbon into the sample for the same precursor powder composition. Systematic evolution in the structure of the ZrC resonance with carbon content was observed in the 1500°C samples. Similarly, systematic shifts in the centre of gravity of the samples sintered at 2000°C and 1700°C were also observed. The rock salt structure was seen to be constant throughout the samples, regardless of the stoichiometry and contrary to the predictions by several theoretical studies. Traces of ZrO and ZrO_2 were seen to be present in the sample evidencing the affinity of the Zr to bond with not only carbon but also oxygen – which could also lead to a difference in the lattice parameter. The structure of the carbon that is unincorporated in the sample has been confirmed to be a combination of

partially destroyed and amorphous carbon - the intensity of these active bands were seen to decrease as stoichiometry is approached.

Chapter 3 The irradiation of ZrC

This chapter presents the results of heavy-ion and proton irradiations on the pristine ZrC samples sintered at 2000°C as characterised in Chapter 2.

This chapter is divided into the following sections to better reflect the accumulated damage dose. Section 3.1 details basic radiation damage theory and the radiation damage modelling that was undertaken prior to irradiation. Section 3.2 presents the 5 MeV proton irradiations on ZrC samples to a fluence of 3.20 x 10^{17} protons/cm^2 or 0.015 dpa on ZrC samples (dose 1). Section 3.3 presents the 5 MeV proton irradiations on ZrC samples to a fluence of 6.42 x 10^{17} protons/cm^2 or 0.031 dpa on ZrC samples (dose 2) . Finally, section 3.4 presents the irradiation of 158 MeV on ZrC Xe ions to a fluence of 1.00 x 10^{15} ions/cm^2 or 2.4 dpa. Each section contains an introduction, experimental, discussion, and conclusion sections. This is followed by a general discussion regarding the key results from the entire chapter.

3.1 Calculation of heavy-ion and proton damage on ZrC

Components close to nuclear fuel need to withstand a range of harsh and diverse conditions, this can include high radiation flux, mechanical and thermal stresses and gradients [117], [140], [141]. Commonly protons and heavy-ions are used to simulate the radiation damage of reactor environments. Proton and heavy-ion irradiations offer a lower cost and lower activation alternative to neutron irradiation. Particle accelerators can be used to achieve these requirements.

As the goal is to study the irradiation damage as a function of stoichiometry, the irradiation temperature will be at room temperature/beam heating temperature – and will not be heated to the operating conditions that this material would operate at (~700°C) as there is potential for damage to be annealed out. In addition to this, irradiations at very high temperatures are practically difficult as sample cooling becomes a significant issue.

When an ion is incident on a material, it produces a damage cascade as kinetic energy from the incident particle is transferred to the target lattice. As ions move through the target material, they experience a loss in energy initially through interaction with the target atoms' electron clouds. When the ions have lost enough energy, they are slowed down by nuclear elastic collisions. These nuclear collisions cause damage cascade(s) as the incident ion hits the first atom in the target (termed the primary knock-on atom – PKA). The energy of the incident ion determines penetration depth in the material, along with the charge and the density composition of the target material.

The stopping of the impinging particle in the material can be defined as below:

$$\left(\frac{\partial E}{\partial x}\right)_{total} = \left(\frac{\partial E}{\partial x}\right)_{nuclear} + \left(\frac{\partial E}{\partial x}\right)_{electronic}. \quad (3.1)$$

Once the PKA is displaced, it proceeds to transfer its energy to other atoms in the target. This causes multiple other cascades that result in damage. Consequently, this process produces defects, which are introduced into the structure.

3.1.1 Modelling of radiation damage using TRIM/SRIM

SRIM is an ion transport software that utilises Monte Carlo methods to simulate charged particle damage in materials [142]. In this project, SRIM was used to determine the appropriate stopping distance for proton irradiation. From this simulation, several useful parameters can be obtained - the most relevant for designing the experiments for the specified constraints (see below) are stopping range, and dose rates.

The 'quick Kinchin Pease' model mode is used in SRIM [143], contrary to what the name would suggest, it provides the most accurate damage calculations [144]. Post irradiation analysis requirements inform and constrain the irradiation energy and radiation exposure time. In the case of this project, pre- and post-irradiation NMR will be compared – hence creating sufficient irradiated material in the damage campaigns to analyse the 1.3 mm rotor is essential.

Assuming a constant beam flux over a fixed sample surface area, the only way to produce a greater volume of irradiated material is to increase the energy of the impinging particle. The sample capacity of the 1.3 mm rotor is 0.0015 cm^3 with the end caps inserted. As the blocks cut from the samples fabricated have a fixed cross-sectional surface area of 0.25 cm^2. It is, therefore, the depth of the penetrating particles that is the variable in determining the volume of material produced. The penetration depth of a particle is determined by a particle's energy. Figure 49 shows a graph of the proton projectile energy with respect to the penetration depth in ZrC (density 6.73 g/cm^3).

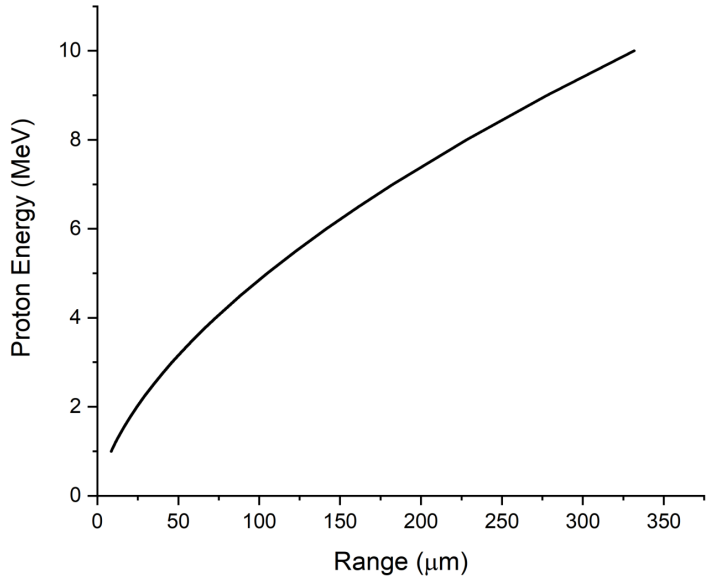

Figure 49 The variation of proton energy with respect to the penetration depth in ZrC (ideal density 6.73 g/cm2) calculated using SRIM.

The graph shows that the penetration depth of the proton increase with increasing proton energy. Since the volume of the 1.3 mm rotor used in the post-irradiation NMR is 0.004 cm^3, this corresponds to a depth of 60 μm.

When comparing the radiation damage induced by different irradiation particles, it is standard practice to use displacements per atom or dpa as these units are independent of the impinging particle. To meaningfully interpret the results from irradiations the dpa must be calculated. The method in which dpa is calculated is shown in (3.2) and (3.3).

$$\frac{dpa}{sec} = \phi . VACANCY_{SRIM\ by\ ions} . \frac{1}{\rho_N} . C \tag{3.2}$$

$$= \left(\frac{ions}{\sec . cm^2}\right) . \left(\frac{displacements}{ion . Å}\right) . \left(\frac{cm^3}{atoms}\right) . \left(\frac{Å}{cm}\right)$$

$$= \frac{displacements}{atoms\ .sec} = dpa/sec\ .$$

$\phi =$ *Proton flux*

$\rho_N =$ *Atomic density of the target* (3.3)

$C =$ *Conversion factor angstroms/cm*

For SRIM calculations we assume the following:

1. *Rastering can be neglected (as is common in these calculations)*
2. *We can assume the beam current is uniform both temporally and spatially*
3. *Incident energetics are constant*
4. *The target material ZrC is treated as a homogenous slab of material*

In the VACANCY.txt file SRIM outputs "VACANCIES by IONS" and the "VACANCIES by RECOILS" ($VACANCY_{SRIM\ by\ ions}$) with respect to depth into the target- these two quantities are summed to the total damage quantity seen by the material.

a.

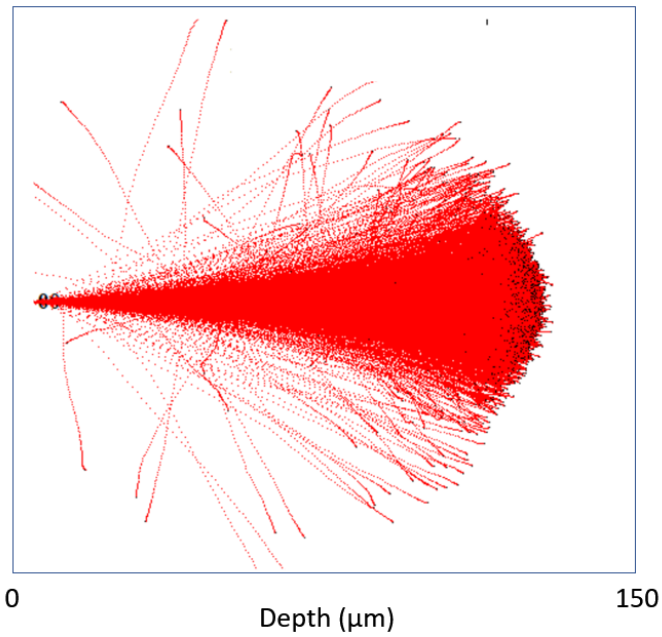

b.

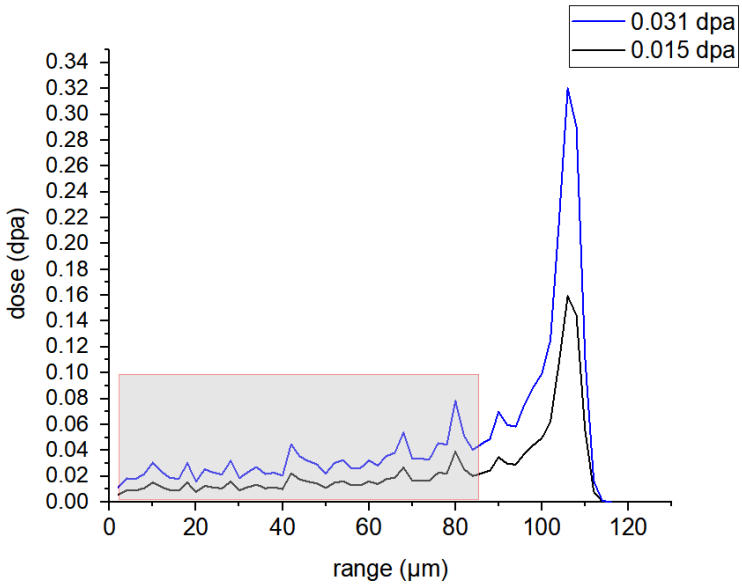

Figure 50 a. Penetration of protons trajectories in ZrC (ideal density 6.73 g/cm^2) the variation of the depth with proton irradiation energy for a. ion trajectories b. proton range for doses of 0.015 dpa and 0.031 dpa.

Figure 50 a. shows the simulated proton tracks if the beam were to impact at one point on a ZrC target material of ideal theoretical density. A single red tracer represents one proton, Figure 50 b. shows the dpa with respect to the penetration depth for ZrC of ideal density (6.73 g/cm^2)

for both irradiations that were carried out to 0.031 dpa and 0.015 dpa. The region that will be used for analysis is the uniform region, ranging from 0 to ~80 μm, highlighted in the grey box in Figure 50 b located before the Bragg peak (92 to 115 μm). Choosing this uniform region allows us to study relatively constant damage over an extended region, as opposed to the Bragg peak that has a large damage over a much shorter distance. It must be noted that experimental techniques such as Raman spectroscopy, are undertaken on samples with a lower dose where the penetration depth of these techniques is smaller than the larger dose averaged depth range sampled by NMR.

Similar simulations can be undertaken for the 158 MeV Xe particles where the Bragg peak in ZrC is located between 8 to 10 μm. The highly energetic and massive (compared with protons) xenon ions interact strongly with the material; hence their travel path is of the order of ~ μm. As the penetration depth of the Xe ions is not sufficient to produce a greater depth of irradiation (due to the energies used), NMR will not be undertaken on the irradiated sample, as the volume of irradiated material generated would be insufficient to fill the 1.3 mm NMR rotor.

In calculating the average dpa, consideration must be given to the penetration depth of XRD analysis. When comparing the lattice parameter to that of other studies, the dpa must be averaged over the approximate range of the XRD penetration depth. In practice, the penetration depth of x-rays is difficult to compute because of factors such as material inhomogeneity that need to be accounted for. However, an approximation can be made using the beer lambert law, the mass attenuation coefficient of Zr, and the ideal density of ZrC, which results in a penetration depth for Mo radiation of approximately 7.2 μm. Averaging the dpa up to this point provides an approximation (given the more complex factors) of ZrC (ideal density 6.73 g/cm^2) to be 2.4 dpa. This region is highlighted in the grey box in Figure 51.

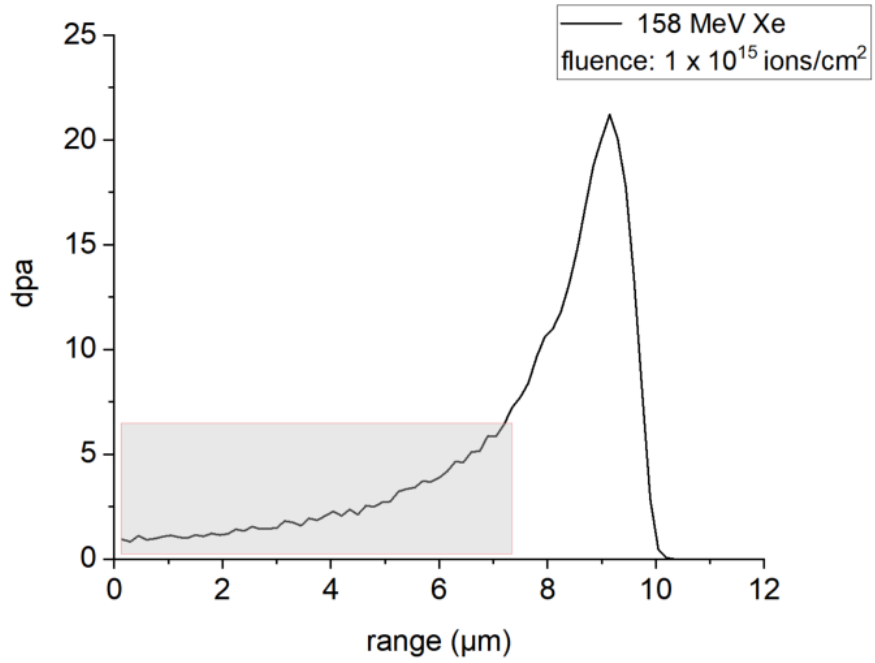

Figure 51 The variation of damage (dpa) with respect to the penetration depth for 158 MeV Xe ions - calculated using the SRIM package and the ideal density of ZrC was used (6.73 g/cm^2).

Heavy-ion irradiations were carried out at the Joint Institute for Nuclear Research at Dubna, Russia using 158 MeV Xenon ions up to a fluence of 1 x 10^{15} ions/cm^2 taking approximately four weeks to complete.

Proton irradiations were carried out at the Dalton Cumbria Facility, operated by the University of Manchester located in Cumbria, England. The irradiation using 5 MeV protons was broken up into short and long irradiation campaigns due to beamline availability and technical difficulties that were experienced with stable beam production. This provided the basis for determining the effect that varying doses had on the samples, allowing an understanding of how the carbon environments change with varying dose rates.

3.2 Irradiation of ZrC with 5 MeV protons to a fluence of 3.20 x 10^{17} protons/cm^2 – 0.015 dpa (dose 1)

3.2.1 Introduction

The aim of this section is to present and discuss the effects that proton irradiations had on the solid ZrC samples. These samples were sintered at 2000 ºC for nominal C/Zr = 1.00, 0.80 and 0.60. In this section, these samples were irradiated with 5 MeV protons to a fluence of 3.20 x 10^{17} protons/cm^2. This corresponds to an average dose of 0.015 dpa in the uniform region of the damage production curve (see methods section 1.3) – this dose will be here on referred to as dose 1. Note: that due to equipment malfunctions and accelerator unavailability, the irradiations presented in this chapter are to a lower dose than was originally desired ~1 dpa.

Most proton irradiation studies in the literature that investigate the irradiation response of ZrC do not consider the material response over a systematic range of stoichiometries [35], [65], [145]. The objectives for the section are outlined in the following paragraph below: to characterise the changes that the dose 1 proton irradiation had on the ZrC samples by using Electron backscatter diffraction (EBSD), Scanning electron microscopy (SEM), X-ray diffraction (XRD) and Raman techniques. To compare the extent to which these irradiation changes vary between different stoichiometries for dose 1 and pristine samples; to determine if any evolution of material properties occur by comparing the stoichiometries for pristine and dose 1 samples. To discuss these results in the context of previous literature, and to provide recommendations for future work.

These objectives have been achieved by determining the changes in lattice parameter, microstrain by XRD for dose 1 samples and these are compared to the pristine sample values. SEM and EBSD are undertaken on all irradiated samples to characterise if any changes in the microstructure or phase separation exist post-irradiation. Raman spectroscopy is undertaken on irradiated samples, to determine if any change in speciation occurs within the dissociated carbon environments as compared with the pristine samples.

3.2.2 Experimental results: Irradiation of ZrC with 5 MeV protons to a fluence of 3.20 x 10^{17} protons/cm^2 (dose 1)

3.2.2.1 XRD

This section presents the post-irradiation XRD results for the dose 1, 5 MeV proton irradiated to a total fluence of 3.20 x 10^{17} protons/cm^2 samples that were undertaken on the pristine ZrC samples that were produced in Chapter 2.

Figure 52 shows XRD diffractogram of the solid (a) pristine nominally stoichiometric ZrC sample sintered at 2000°C with nominal C/Zr = 1.00 [black trace] sample and (b) the dose 1, 5 MeV proton irradiated nominal C/Zr = 1.00 [red trace] sample. The nominal C/Zr = 0.80 and the 0.60 samples are shown in Figure 53 and Figure 54 respectively and adhere to the layout of the nominal C/Zr= 1.00 sample as described above.

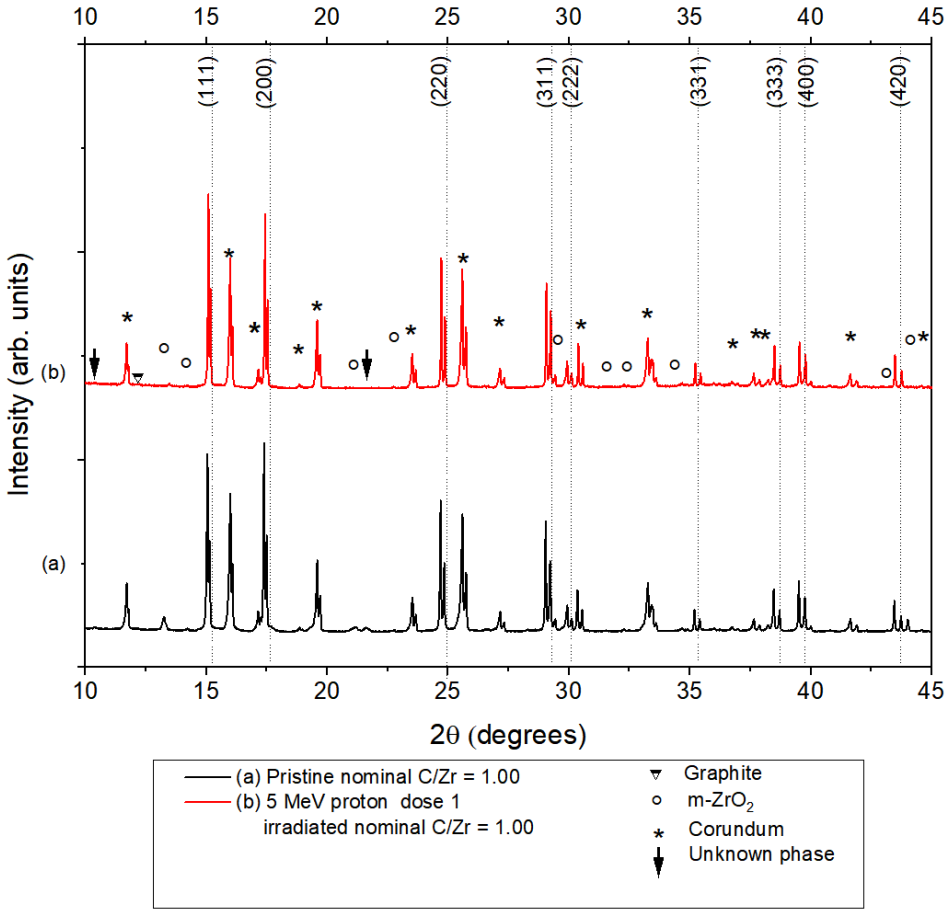

Figure 52 vertically offset XRD patterns of ZrC (nominal C/Zr = 1.00) for (a) pristine and (b) dose 1, 5 MeV proton irradiated samples.

The irradiated nominal C/Zr = 1.00 (Figure 52) sample diffractogram showed that the NaCl structure of ZrC was maintained after the dose 1 proton irradiation. The intensity of the (200) ZrC diffraction peak was seen to decrease with respect to the (111) diffraction peak in the irradiated sample as compared to the pristine sample diffractogram. Weak ZrO_2 diffraction peaks were also observed and assigned, from Rietveld refinement, in the irradiated spectrum to m-ZrO_2 (monoclinic zirconia). The diffraction peak belonging to the unknown phase that was observed in the pristine nominal C/Zr = 1.00 sample located at 21.6° (2θ) was not observed in the irradiated sample.

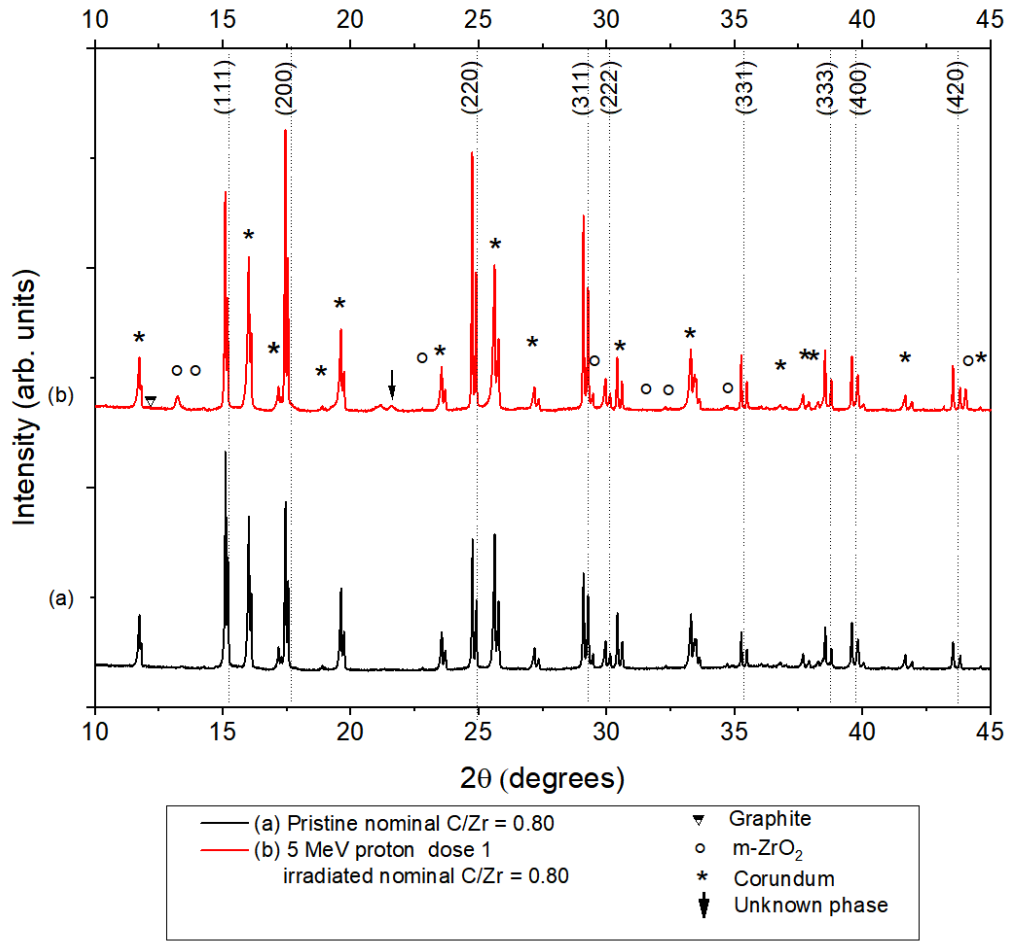

Figure 53 vertically offset XRD patterns of ZrC (nominal C/Zr = 0.80) for (a) pristine and (b) dose 1, 5 MeV proton irradiated samples.

The nominal C/Zr = 0.80 XRD patterns (Figure 53) show that the irradiated sample maintained its NaCl crystal structure after irradiation. Furthermore, a decrease in the relative intensity of the (111) peak compared to the (200) ZrC diffraction peak was observed with irradiation. The (220) diffraction peak was also observed to increase in the dose 1 sample diffraction pattern as compared to the pristine sample pattern. As with the nominal C/Zr = 1.00 sample, m-ZrO_2 attributable diffraction peaks were observed in the irradiated nominal C/Zr = 0.80 sample. One weak diffraction peak located at approximately 21.6 ° (2θ) belonging to an unknown phase was also seen in the dose 1 diffractogram.

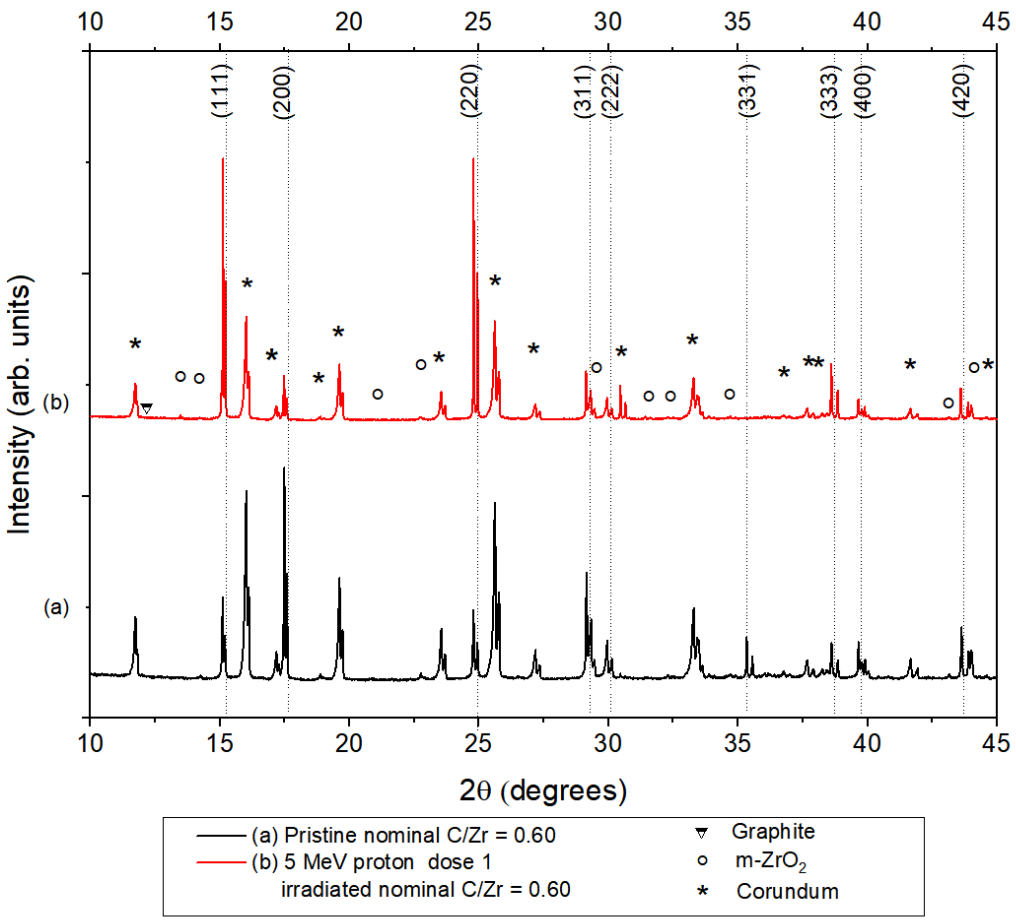

Figure 54 vertically offset XRD patterns of ZrC (nominal C/Zr = 0.60) for (a) pristine and (b) dose 1, 5 MeV proton irradiated samples.

Following the trend from previous samples, the nominal C/Zr =0.60 XRD patterns (Figure 54) showed no evidence of graphite in the irradiated or the pristine sample. The irradiated sample diffractogram produced a more intense (111) peak as compared to the (220) diffraction ZrC peak intensities.

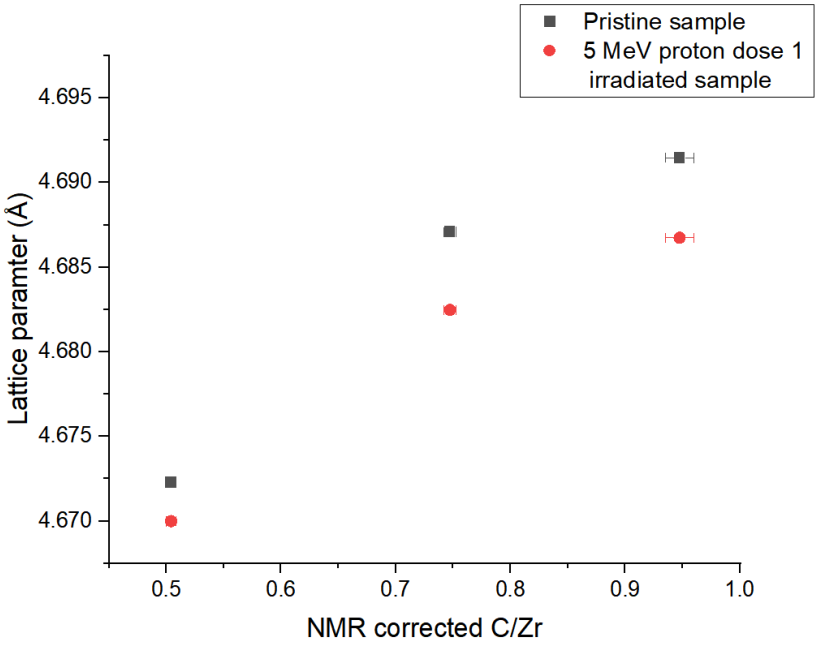

Figure 55 Pristine and dose 1, 5 MeV proton irradiated lattice parameters for samples sintered at 2000°C plotted with respect to the NMR corrected C/Zr.

Lattice parameters, as determined by Rietveld refinement, of the 5 MeV proton irradiated ZrC samples plotted with respect to the NMR corrected C/Zr for samples sintered at 2000°C are shown in Figure 55 (tabulated in Table 3.2). The lattice parameters of the irradiated samples were observed to have, on average, lower values as compared to the pristine sample lattice parameter values. The lattice parameter of the irradiated samples showed an increasing trend with respect to carbon content that was also seen in the pristine samples. The lattice parameter was seen to decrease in the irradiated samples by approximately 0.10, 0.10 and 0.05 % for the nominal C/Zr = 1.00, 0.80 and 0.60 samples.

Table 3.1- Lattice parameters of the pristine and 5 MeV proton dose 1 irradiated samples.

Nominal C/Zr	NMR corrected C/Zr	±error	Pristine Lattice parameter	±error	Proton dose 1 Lattice Parameter	± error
1.00	0.95	0.01	4.692	0.001	4.688	0.001
0.80	0.75	0.01	4.688	0.001	4.683	0.001
0.60	0.50	0.01	4.672	0.001	4.670	0.001

The microstrain contribution was determined using the full pattern fitting Pawley method. To increase the accuracy of this method, the offset between the standard tile and the sample was accounted for and the instrumental broadening was characterised using a corundum standard.

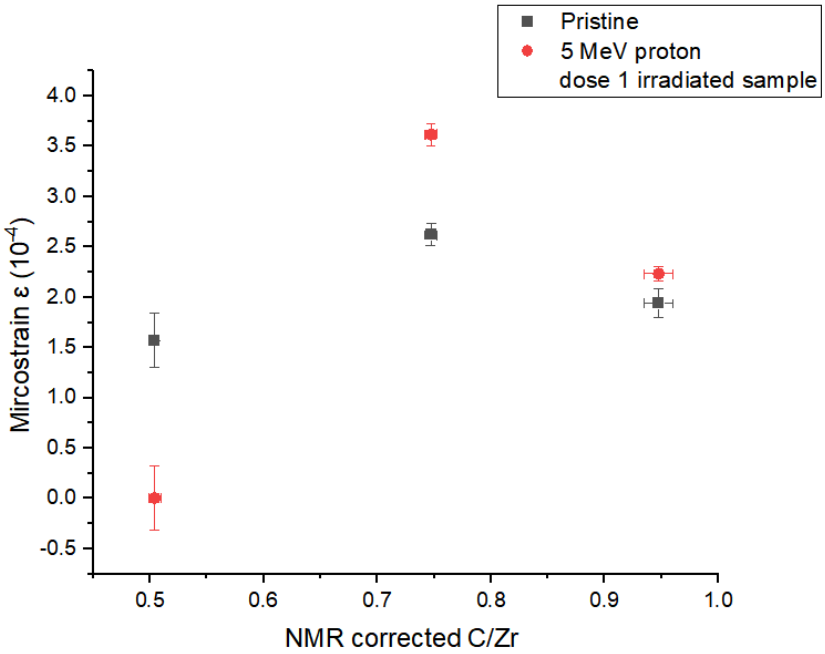

Figure 56 Pristine and 5 MeV proton irradiated microstrain values for ZrC samples plotted with respect to the NMR corrected C/Zr.

Figure 56 shows the irradiated microstrain of the pristine and the irradiated 5MeV proton dose 1 samples (tabulated in Table 3.2). The microstrain of the irradiated samples showed a similar non-monotonic response to the pristine samples. For both the irradiated and unirradiated samples, the lowest, highest and intermediate microstrain values were observed in the nominal

C/Zr = 0.60, 0.80 and 1.00 samples, respectively. The microstrain of the nominal C/Zr = 0.60 sample was seen to decrease as compared to the unirradiated samples, whereas the nominal C/Zr = 1.00 and 0.80 sample microstrains were seen to increase with irradiation.

Table 3.2 - Microstrain of pristine and the 5 MeV proton irradiated dose 1 samples.

Nominal C/Zr	NMR corrected C/Zr	± error	Pristine microstrain (ε)	± error	Proton dose 1 microstrain (ε)	± error
1.00	0.95	0.01	1.94	0.15	2.23	0.07
0.80	0.75	0.01	2.62	0.11	3.62	0.11
0.60	0.50	0.00	1.57	0.28	0.00	0.32

The GOF (goodness of fit) values from the Rietveld refinement, which was used to determine the lattice parameters, were observed to be 4.24, 6.22 and 6.23 for samples of nominal C/Zr = 1.00, 0.80 and 0.60, respectively. The GOF/chi-squared (goodness of fit) from the Pawley fit was determined to be 1.90, 3.70 and 4.00 for samples of nominal C/Zr = 1.00, 0.80 and 0.60, respectively. The variation of the GOF was seen to be due to the presence of additional phases, in addition to the marginal offset between the corundum standard and the sample tiles. As the difference in the offset was assumed to be zero, the peak centring, which was important for determining the lattice parameter, was checked by visual inspection of the residual spectrum.

3.2.2.2 **SEM**

The following sub-section presents the results of SEM microscopy undertaken on the 5 MeV dose 1 irradiated samples of ZrC. Where possible, the same areas have been imaged. However, this was not possible for some samples because of the short turnaround time (1 day) between receiving the samples and having to transport them to the accelerator facility. Figure 57, Figure 58, Figure 59 show the SE and BSE SEM images for nominal C/Zr = 1.00, 0.80, 0.60 pristine and dose 1, 5 MeV proton irradiated samples, respectively.

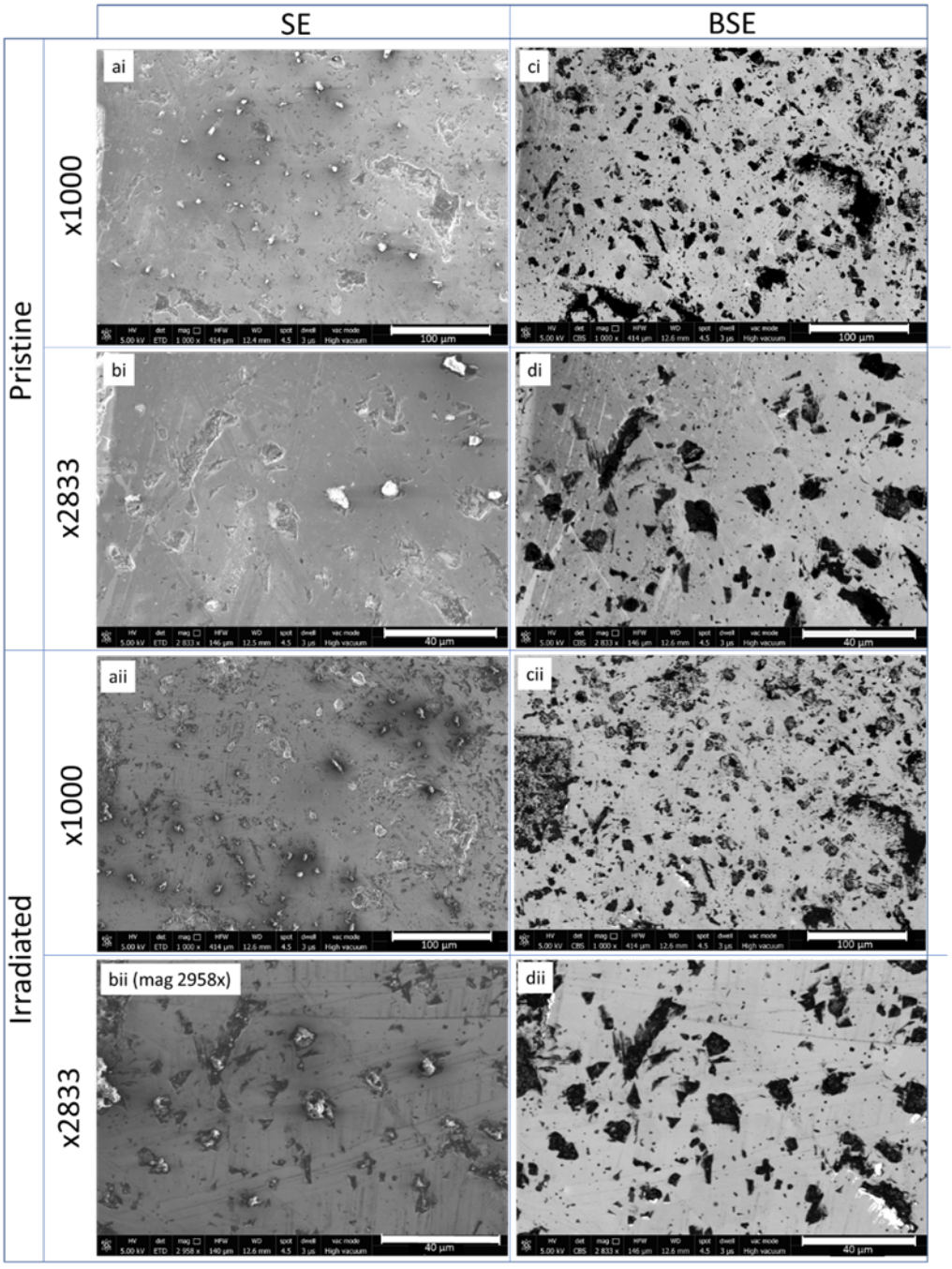

Figure 57 BSE and SE images of (nominal C/Zr = 1.00 sintered at 2000 °C) pristine and dose 1, 5 MeV proton irradiated ZrC samples. Samples are classified as per the dividers specified in the table above. Images that are labelled with a letter followed by a i and ii (e.g. ai and aii) denote images that have been taken in the same area before and after irradiation. SE and BSE images are displayed in the left and right columns respectively – labels starting with a and b denote SE images whilst labels starting with c and d denote BSE. Image labels starting with the letters 'a' 'c' are images that have been taken at x1000 magnification and those starting with labels starting with 'b' or 'd' are taken at x2833 magnification.

The irradiated nominal C/Zr = 1.00 showed no significant difference in the microstructure as compared with the pristine material. The black structures appear sharp in the irradiated material - as with the pristine material. A slight difference in contrast was observed around the side of the laser-ablated reference points that was attributed to the burn marks from the rastering of the beam to create the reference points (see di and dii). These darker areas were not seen in the irradiated samples. In addition, a roughening of the microstructure was observed in SE images of the samples after irradiation (bii as compared to bi). No phase separation was observed in the BSE images.

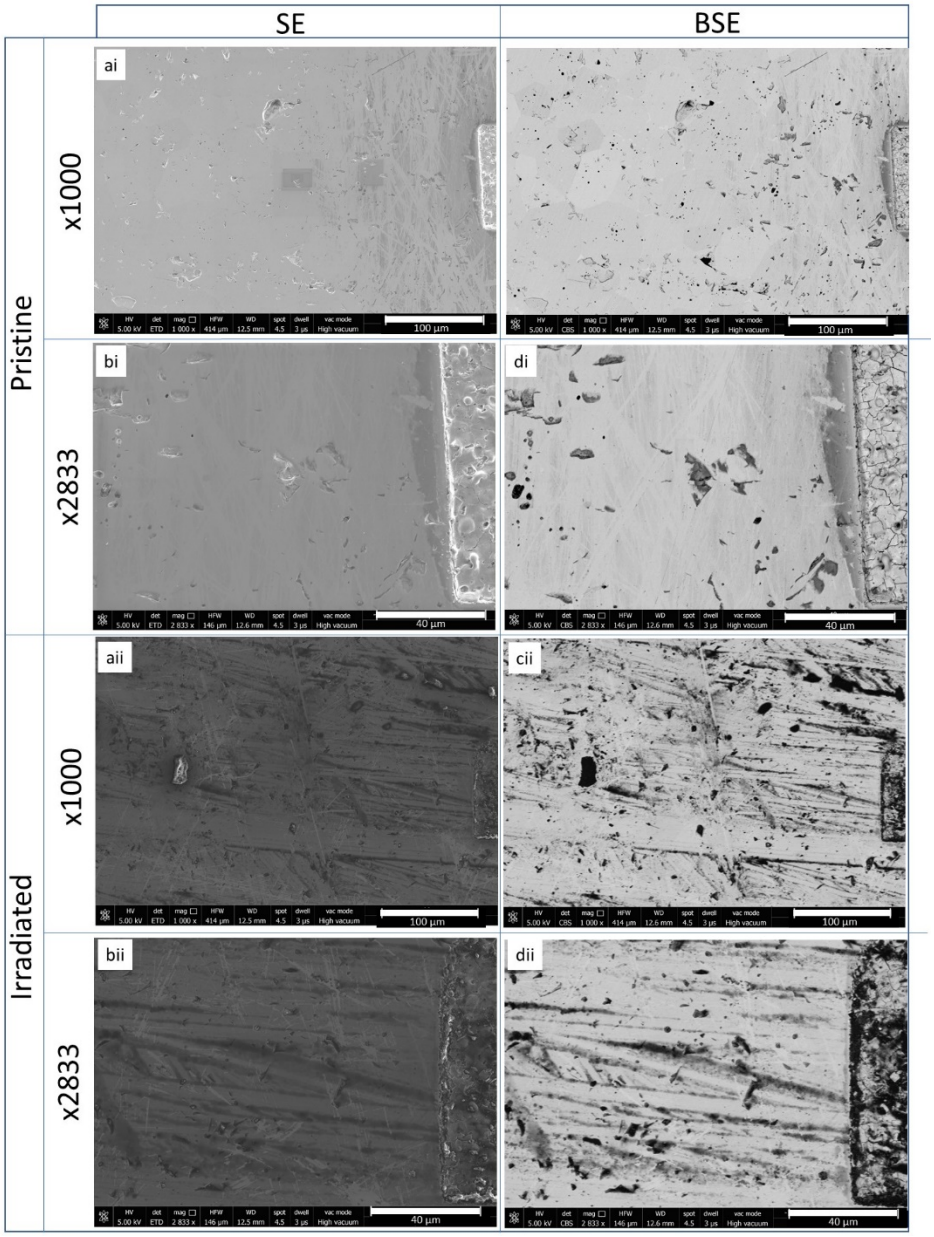

Figure 58 *BSE and SE images of (nominal C/Zr = 0.60 sintered at 2000 °C) pristine and dose 1, 5 MeV proton irradiated ZrC samples. Samples are classified as per the dividers specified in the table above. Images that are labelled with a letter followed by a i and ii (e.g. ai and aii) denote images that have been taken in the same area before and after irradiation. SE and BSE images are displayed in the left and right columns respectively – labels starting with a and b denote SE images whilst labels starting with c and d denote BSE. Image labels starting with the letters 'a' 'c' are images that have been taken at x1000 magnification and those starting with labels starting with 'b' or 'd' are taken at x2833 magnification.*

No phase separation was observed in the irradiated BSE images. The irradiated nominal C/Zr = 0.80 sample (Figure 58) similarly showed a roughening of the surface microstructure as compared to the representative pristine nominal C/Zr = 0.80 samples. As with the nominal C/Zr = sample, the burn marks located around the square reference marker were absent in the irradiated samples. Microstructural roughening was observed in the irradiated samples as compared to the representative pristine samples – this can be seen by the dark streaks seen in the irradiated SE images (aii and bii).

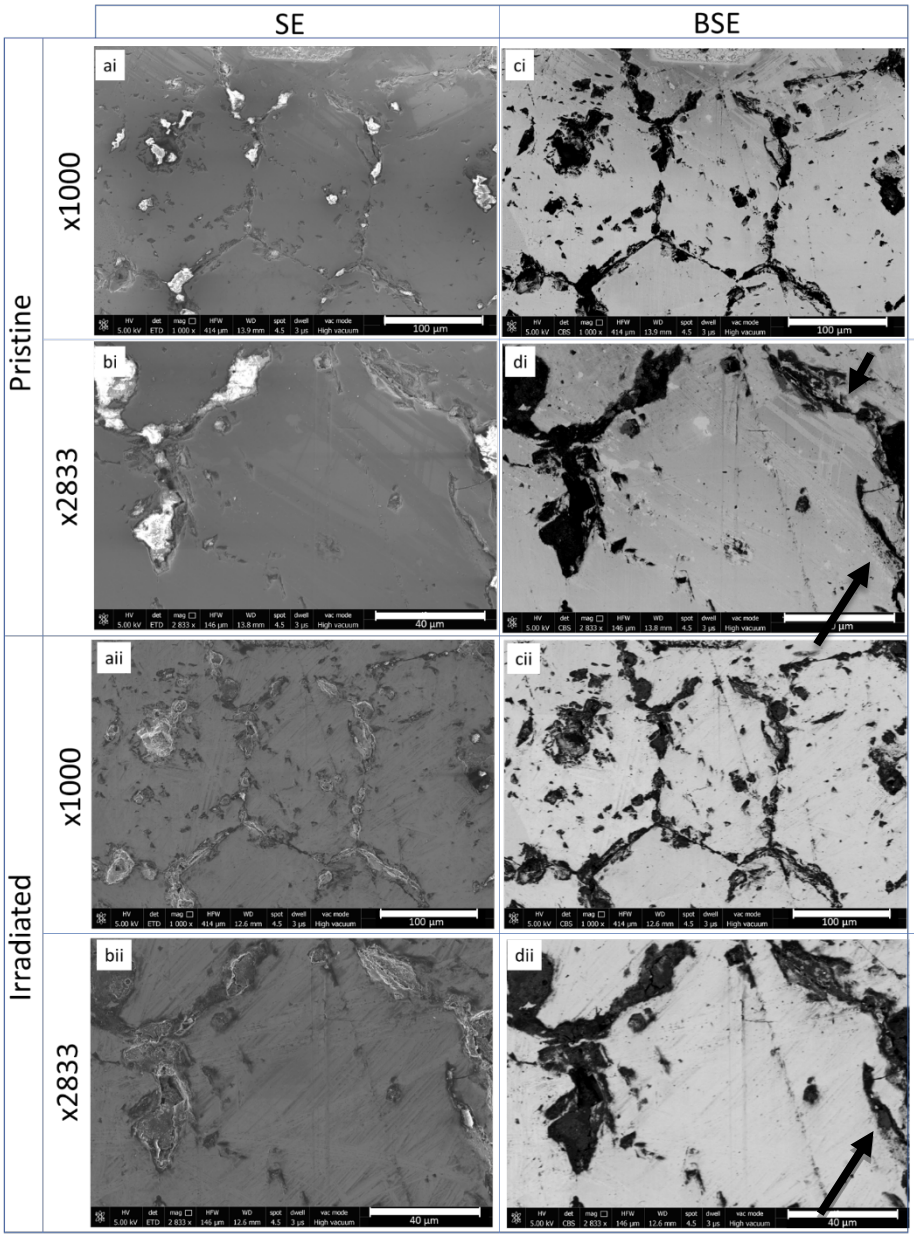

Figure 59 BSE and SE images of (nominal C/Zr = 0.60 sintered at 2000 °C) pristine and dose 1, 5 MeV proton irradiated ZrC samples. Samples are classified as per the dividers specified in the table above. Images that are labelled with a letter followed by a i and ii (e.g. ai and aii) denote images that have been taken in the same area before and after irradiation. SE and BSE images are displayed in the left and right columns respectively – labels starting with a and b denote SE images whilst labels starting with c and d denote BSE. Image labels starting with the letters 'a' 'c' are images that have been taken at x1000 magnification and those starting with labels starting with 'b' or 'd' are taken at x2833 magnification.

The irradiated nominal C/Zr = 0.60 (Figure 59) samples showed the same connected inter- and intra-granular black structural network as in the pristine sample. An increase in the apparent area of the black structures (see arrow in Figure 59 di and dii) was observed in the irradiated samples compared to the pristine samples. Despite this, no large-scale changes in the microstructure were observed post-irradiation.

EBSD analysis was undertaken on the irradiated samples to determine the grain size post-irradiation. As with the pristine samples, the average grain size of the irradiated samples was analysed using the MTEX package.

a)

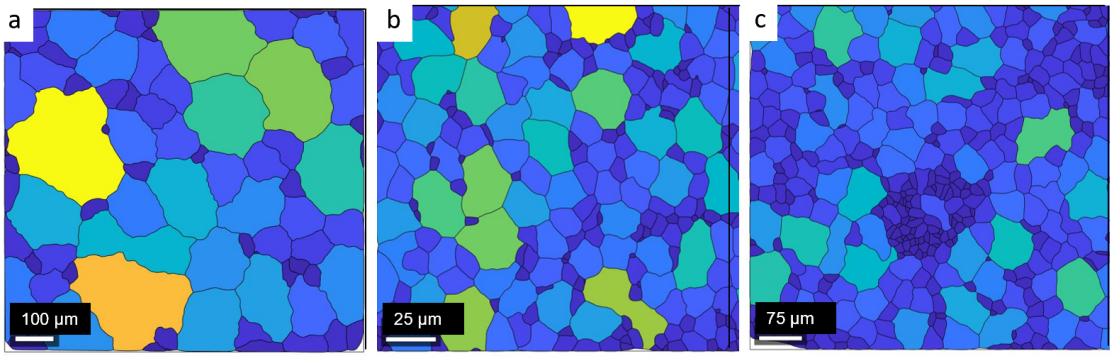

b)

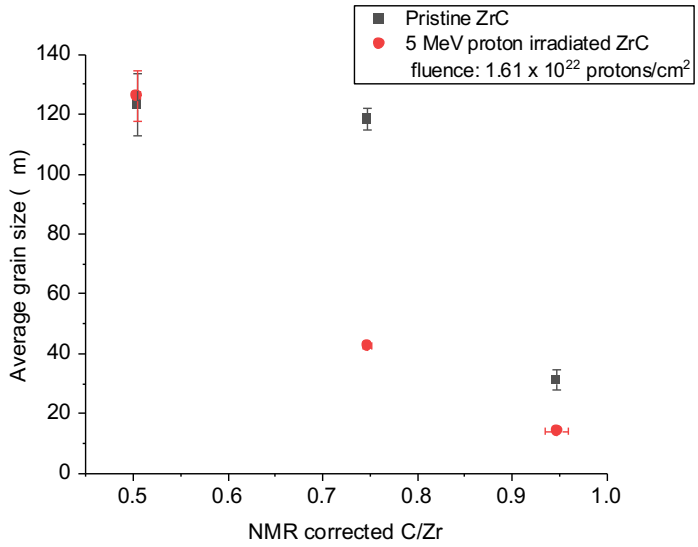

Figure 60 a) representative SEM EBSD for solid irradiated samples of nominal a. 0.60, b 0.80, c 1.00 sintered at 2000°C. –, b) average pristine grain size of pristine pre-irradiation ZrC samples and average grain size of dose 1, 5 MeV proton irradiated samples plotted with respect to the nominal carbon content.

The results of the grains traced in the analysis are presented in Figure 60. Figure 60 a) shows that the irradiated samples presented with decreasing grain size with increasing carbon content, a trend that was previously seen in the pristine samples.

Quantitatively, Figure 60 b) shows the average grain size for the pristine ZrC samples and dose 1, 5 MeV proton irradiated samples plotted against the NMR corrected carbon content. The grain size of the irradiated samples was determined to be 14.1 ± 0.3 μm, 42.6 ± 0.9 μm and 126.2 ± 8.4 μm for the nominal C/Zr = 1.00, 0.80 and 0.60 samples, respectively. The nominal C/Zr= 1.00 sample showed approximately a 55% grain shrinkage from 31 ± 3 μm, in the pristine sample, to 14 ± 1 μm in the irradiated sample.

The average grain size of the nominal C/Zr = 0.80 was seen to shrink by approximately 64% from 118 ± 4 μm to 43 ± 4 μm for the pristine to irradiated samples, respectively. In addition, this composition showed the largest difference between the pristine and irradiated grain size amongst all the samples. It is also possible that the value of the pristine nominal C/Zr = 0.80 may be an anomalous result.

The grain size of the nominal C/Zr = 0.60 irradiated sample (126 ± 8 μm) was seen to be within the error of the pristine sample value (123 ± 11 μm)..

3.2.2.3 **Raman spectroscopy**

This subsection presents the results obtained from Raman spectroscopy investigations on dose 1, 5 MeV irradiated ZrC. The dark structures were selected as sampling spots for the irradiated Raman characterisation because as they exhibited a clear Raman signal in the pristine sample, as opposed to the other sample regions. It was determined in Chapter 2 that studying these regions provides a method for understanding how the speciation of carbon changes within the

sample. The physical interpretation behind the spectral resonance widths, from the fitted peak functions, and the location of these peaks are further interpreted in the discussion section of this chapter.

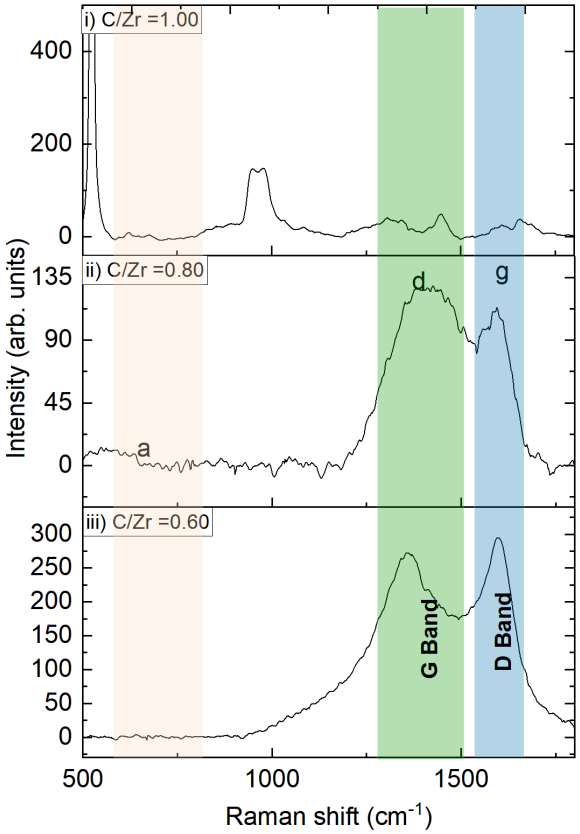

Figure 61 Raman spectra for the 5 MeV dose 1 proton irradiated samples of nominal C/Zr = 1.00 (i), 0.80 (ii) and 0.60 (iii) sintered at 2000°C. Spectra were baselined using a manually selected, user-defined baseline.

Figure 61 shows the Raman spectra of the dose 1 proton irradiated ZrC samples. Overall, the Raman spectra of the irradiated samples show a decrease in signal intensity of the D and G bands for samples of higher carbon content. The irradiated nominal C/Zr = 0.80 and 0.60 samples showed, but adjoined, clear D and G resonances, whilst this signal was unresolvable in the nominal C/Zr = 1.00 sample spectrum.

Several additional features were observed in the nominal C/Zr = 1.00 sample that were not observed in the lower C/Zr samples. Most notably, a broad structure was observed in the

irradiated sample spectrum, centred at approximately 963 cm^{-1}. This structure was seen to contain two overlapping double resonances located at around 949 and 979 cm^{-1}. Additionally, at lower wavenumbers, another previously unobserved sharp peak was observed to be centred at approximately 525 cm^{-1} in the irradiated sample spectrum.

The Raman spectrum of the irradiated nominal C/Zr = 0.80 sample shows the largely overlapped structure of the D and G resonances. The intensity of the D band was seen to be higher than the G band with the difference in the peak height being 134 counts. The characteristics of the D and G bands are seen to be appropriately fitted by a Gaussian and Lorentzian function, respectively. The fitting and optimisation of these functions were made difficult due to the asymmetry associated with the peaks, hence as before, initially fitting was conducted using manual adjustment - a function to a resonance minimising the residual signal. Unconstrained fitting parameters were then optimised.

The broad Gaussian function used to fit the D resonance in the irradiated nominal C/Zr = 0.80 sample was seen to be centred around 1410 ±1 cm^{-1}, with FWHM = 234 ± 2 cm^{-1} and the intensity to be 125 ± 1 counts. The Voigt function used to fit the G peak was determined to be centred around 1596 ± 1 cm^{-1}, with FWHM = 77 ± 2 cm^{-1} and height 93 ± 1 counts. The D and G peaks in the irradiated samples were seen to have a greater overlap than was seen in the pristine sample spectra, however, the line shape was seen to be suitably captured by fitting two functions, and a third was not necessary. The irradiated nominal C/Zr = 0.80 spectra also showed a broad resonance located at lower wavenumbers that was centred around 570 ± 4 cm^{-1}.

The Raman spectrum of the irradiated nominal C/Zr = 0.60 showed the presence of the D and G bands as was observed previously in the pristine sample. The average signal intensity from these bands is lower than that seen in the pristine sample. The G and D band from visual inspection had comparable intensities to one another with the difference in peak height being approximately 20 counts. This result is contrary to the pristine sample spectra where the

intensity of the G peak is seen to be larger than the D peak. The D and G bands were seen to be less distinct in their structure as compared with the pristine samples. A Voigt function was fitted to the D band was seen to be located at 1358 ± 1 cm^{-1} with FWHM = 199 ± 3 cm^{-1} with the intensity of 294 ± 2 counts. The Lorentzian profile fitted to the G peak was centred around 1595 ± 2 cm^{-1} with FWHM = 93 ± 1 cm^{-1} and intensity of 295 ± 1 counts.

3.2.3 Discussion: Irradiation of ZrC with 5 MeV protons to a fluence of 3.20 x 10^{17} protons/cm^2 – 0.015 dpa

SE and BSE images showed no discernible changes in the microstructures of the samples following irradiation to a fluence of 3.20 x 10^{17} protons/cm^2 or 0.015 dpa. Furthermore, no phase separation was observed in the BSE images. A noticeable roughening of the microstructure was observed in the irradiated samples as is to be expected, however little evolution of the black structures was observed from the pristine microstructure.

Post irradiation SEM showed an absence of the laser ablation burn marks used to mark the reference points on the pre-irradiation sample. The absence of these marks could result from ~μm removal of surface layers or simply a re-organisation of the microstructure due to irradiation. No phase separation was observed in the dose 1 proton irradiated samples. An increase in the uneven surface height was observed in all samples after irradiation.

All irradiated ZrC samples were observed to maintain their crystalline cubic rock salt structure after irradiation irrespective of carbon content. Changes in intensity of the (111) and the (200) diffraction peaks indicate that irradiation has caused damage to the crystal structure. Previous proton studies do not include XRD patterns; thus, no information is available regarding the change in the relative peak intensities. However, a relative change in the intensity of ZrC diffraction peaks has been observed in heavy-ion damage studies on materials [61]. The dissimilar relative changes in peak intensity between the pristine and irradiated samples is indicative of ZrC with different carbon contents having different irradiation responses. Weak

diffraction peaks belonging the m-ZrO_2 zirconia phase were also identified in the XRD spectra, as this polymorph is stable at room temperature up to 1170°C [146]–[148] (see discussion). In addition to this, no diffraction peaks belonging to the graphite phase were observed for any of the irradiated samples. As discussed previously, XRD is not always capable of showing the presence of graphite, especially when it is nanocrystalline in size; which was previously confirmed by Raman spectroscopy undertaken on pristine samples and independently confirmed by C-13 NMR.

Proton irradiations undertaken in this study were observed to cause a decrease in the lattice parameter by 0.10, 0.10 and 0.05 % for the nominal C/Zr = 1.00, 0.80 and 0.60 irradiated samples respectively with respect to their pristine values. This is unexpected and contrary to the results reported by Yang *et al.* [65] who reported an expansion in the lattice parameter, in 2.6 MeV proton irradiated ZrC (C/Zr = 1.01), increasing from their pristine values by 0.09% (4.696 Å) and 0.11% (4.697 Å) for doses of 0.7 and 1.5 dpa, respectively [65]. To separate the effects of irradiation time (fluence) from temperature, Yang *et al.* heated a control sample to 800°C for 20 hours (the duration of the 1.5 dpa irradiation). Although the percentage change was not reported, a value of 4.692 Å was assessed from the presented lattice parameter plot - which represented no significant increase in the lattice parameter post-irradiation. The lattice parameter of the annealed (and pristine) samples in Yang's study was observed to match the lattice parameter of the pristine nominal C/Zr = 1.00 sample produced in this study. Factors governing the divergence in the evolution of the lattice parameter between the two samples include the difference in irradiation dose between the two studies (this study: 0.015 dpa, Yang *et al.*: 0.7 and 1.5 dpa), the sample composition (this study C/Zr: 0.95 , Yang *et al.*:1.01) and the irradiation temperature (this study: 285°C, Yang *et al.*: 800°C).

The hyper-stoichiometry of the samples used by Yang *et al.* implies no vacant sites would be available to sink defects. As irradiation produces dislocations and point defects, the range of vacant sites in the hypo-stoichiometric samples investigated in this study could act as sinks for

defects produced during irradiation [54], [61]. Thus, as a vacancy occupies a greater volume in a lattice than a perfect crystal for ZrC [149], dislocated carbon atoms may sink in vacant sites. The higher doses undertaken by Yang *et al.* also show that radiation damage likely influences the lattice parameter as a greater concentration of defects accumulate, manifesting increased density of Frank loops with irradiation dose [65]. Further, although annealing the sample did not affect the lattice parameter of the pristine samples, the higher irradiation temperatures can affect defect recovery by enhancing mobility.

It is also possible that the irradiation damage caused by a low dose in our study is not sufficient to create extended defects, detrimental to the sample. Instead, it supplies enough energy to cause a re-arrangement of carbon atoms and anneal pre-existing defects in the samples arising from the fabrication process. In this annealing period, free oxygen present in the sample may diffuse into ZrC vacant sites that act to lower the lattice parameter [9]–[14].

A higher microstrain was observed in the pristine nominal C/Zr = 0.60 sample as compared to the proton irradiated value. As with the lattice parameter, a possible explanation for this decrease in the microstrain present in the pristine sample may be due to the annealing out of strain from EDM cutting and the polishing of the samples [155] – which can arise in sample preparation. Low dose irradiation as detailed above, may act to anneal some of the stresses resulting in lower microstrains as seen in the irradiated sample. However, if this were the dominant factor influencing microstrain response for all samples then the microstrain in the irradiated sample when compared to the pristine microstrain would consistently decrease for all samples. This is not the case, as an increase in microstrain was observed in the irradiated nominal C/Zr = 1.00 and 0.80 samples as opposed to the decrease that was observed in the nominal C/Zr = 0.60 samples.

It is possible that the vacancy concentration of the sample plays a significant role in microstructure evolution. If this were the case, then samples with higher vacancy concentrations would have a greater proportion of sink sites available to radiation damage.

This, however, does not explain the higher microstrain increase seen in the nominal C/Zr = 0.80 versus the 1.00 sample and more systematic doses at lower temperatures would be needed to explore this further.

For a consistent explanation of the change in microstrain, we can instead turn to the behaviour of grain growth as determined from SEM EBSD analysis. The nominal C/Zr = 1.00 and 0.80 were seen to decrease from 31 ± 3 μm and 118 ± 4 μm to 14 ± 1 μm and 43 ± 4 μm respectively - whilst the nominal C/Zr = 0.60 was seen to remain within error of one another, producing grain sizes of 123 ± 11 μm to 126 ± 8 μm for the pristine and dose 1 irradiated samples. It is proposed that the apparent volume of the intergranular black structures that trace out the grain boundaries in the nominal C/Zr = 0.60 samples are significantly larger (~μm) and visible on SEM images, as opposed to the nominal C/Zr = 1.00 and 0.80 samples. It is likely that these structures act as sinks for defects, instead of nucleating on the octahedral interstitial sites of the ZrC unit cell, thus reducing the overall microstrain of the material.

The decrease in the microstrain may likely be a combination of the above two effects, which act to reduce the number of defects in the system.

Since the free carbon cannot be studied via XRD, Raman spectroscopy was undertaken on the samples to better understand how the speciation of carbon in the samples evolved with proton irradiation. As with the pristine samples, the irradiated nominal C/Zr = 0.80 and 0.60 samples were seen to contain the D and G peaks, these features were not resolvable in the irradiated nominal C/Zr = 1.00 sample.

Thus, in the black structures sampled, Raman spectroscopy revealed partially destroyed and pristine graphitic carbon given by the D and G peaks, respectively. The irradiated Raman spectra of the nominal C/Zr = 0.80 and 0.60 showed a greater overlap of the D and G bands accompanied by larger FWHM as compared to the pristine sample. This indicates that the amount of disorder in the graphite has increased due to proton damage. The nominal C/Zr =

0.80 Raman spectrum shows ultra-wide line widths combined with a low signal intensity, again, indicative of disorder. The irradiated nominal C/Zr = 1.00 spectra did not show the presence of the D and G band for the areas sampled, as was the case in the pristine sample.

Two new features were observed at lower wave numbers in the nominal C/Zr = 0.60 samples, which were not observed in the pristine samples. The broad signal located at 957 cm^{-1} and 525 cm^{-1} was observed to be centred around the similar position of silica structures seen in the literature [156], [157]. This was further evidenced by the position of the sharp Raman peak located at ~520 cm^{-1} and also the position of the silicon standard used to calibrate the Raman spectrometer. It is very likely that the origin of the signal is from the 0.2 μm colloidal silica polishing paste that was used to give the samples a mirror finish that became lodged in the sampling spot used for post-irradiation Raman characterisation.

The location of the Voigt function fitted to the G resonance in the irradiated nominal C/Zr = 0.80 samples was 1598 ± 1 cm^{-1}, which according to the three-stage phenomenological model outlined by Ferrari and Robertson [51], indicates that the graphite present in the sample is nanocrystalline in size. The nominal C/Zr = 0.60 sample was also seen to contain nano-crystalline graphite. Calculation of the sp^2 crystal size, showed that the sp^2 crystal size for the nominal C/Zr = 0.80 and 0.60 samples was approximately 17 and 21 nm, respectively. This is a decrease from the 33 nm crystallite size observed in the pristine samples which could be due to recrystallisation following radiation damage.

A shift to lower wavenumbers in the centring of the G resonance was observed after irradiation in the nominal C/Zr = 0.80 sample, decreasing from 1605 ± 1 cm^{-1} to 1596 ±2 cm^{-1}. Similarly, the G-band in the nominal C/Zr = 0.60 sample was seen to shift to lower wavenumbers from its pristine value at 1609 ± 1 cm^{-1} to 1595 ± 2 cm^{-1} in the irradiated samples. A movement of the G peak to lower wavenumbers indicated bond disorder, as determined by Ferrari and Robertson [51], [158].

Both the location of the irradiated G peaks in the nominal C/Zr = 0.80 and 0.60 were seen to shift to lower wavenumbers with irradiations. This movement indicates a decrease in the amount of graphitic clustering and chains and an increase in bond disorder as would be expected from irradiations [51], [158],.

3.2.4 Conclusions: Irradiation of ZrC with 5 MeV protons to a fluence of 3.20 x 10^{17} protons/cm^2 – 0.015 dpa

The pristine nominal samples sintered at 2000°C, analysed in Chapter 2, were irradiated with 5 MeV protons to a fluence of 3.20 x 10^{17} protons/$cm^{2,}$ which corresponded to an average dose of 0.015 dpa in the uniform damage region.

All stoichiometries produced were observed to have good stability under low dose irradiation – with no separation of phases evident from SEM studies. XRD analysis showed that the NaCl structure was maintained after irradiation. The average grain sizes of irradiated samples were seen to decrease for the irradiated nominal C/Zr = 1.00 and 0.80 samples, whilst average grain size was observed to increase in the nominal C/Zr = 0.60 but remained within error of its pristine value. In addition, the lattice parameters of all samples were observed to decrease after irradiation, which was contrary to higher dose studies (on hyper-stoichiometric ZrC) in the literature. It was proposed that this could be due to the presence and availability of sinks for defects in these samples. A decrease in the microstrain of the nominal C/Zr = 0.60 sample was attributed to a combination of the large intergranular black structures seen in the SEM images and vacancies acting as mechanisms to limit nucleation of defects at this dose. The amount of disorder in graphite and disordered carbon located in the black structures of the ZrC samples were seen to increase with irradiation dose indicative of radiation damage. As a result, a decrease in the sp^2 crystallite size was observed when compared to the pristine values. To summarise, the irradiation dose did not cause sufficient irradiation damage, extended defect structures and any catastrophic effects in the ZrC samples.

3.3 Proton dose 2: Irradiation of ZrC with 5 MeV protons to a fluence of 6.42 x 10^{17} protons/cm^2 - 0.031 dpa (dose 2)

3.3.1 Introduction

The aim of this section is to present and discuss the effects that a higher dose proton irradiation had on the solid ZrC samples produced in Chapter 1. These samples, detailed earlier, were sintered at 2000 ºC for nominal C/Zr = 1.00, 0.80 and 0.60. In this section, blocks of these pristine samples were irradiated with 5 MeV protons to a fluence of 6.42 x 10^{17} protons/cm^2; approximately twice the fluence used in the previous dose 1 section. This corresponds to an average dose of 0.031 dpa in the uniform region of the damage production curve– this dose will be referred to as dose 2 throughout this section. NB: this is a separate irradiation and not a cumulative irradiation of dose 1 samples. Doubling the radiation dose from the previous section makes it possible to systematically study the evolution of the radiation response across a range of sample stoichiometries.

These irradiations were also subject to equipment malfunctions and accelerator downtime issues at the Dalton Cumbrian Facility (DCF). Thus, the irradiations presented in this chapter are higher than dose 1 but still to a lower dose than was originally desired of ~1 dpa. It was initially desired that irradiations could be carried out to a higher dpa as to simulate nuclear material damage integrated over the application lifetime. In addition, due to the effects of COVID-19 on departmental facilities, it was not possible to collect the dose 1 NMR spectra for the nominal C/Zr = 0.80 and 0.60 samples to compare with NMR measurements on these dose 2 samples.

The objectives of this section are to; characterise the changes that the dose 2 proton irradiation had on the ZrC samples by using EBSD, SEM, XRD and Raman techniques, to determine if any evolution of material properties occurred by comparing the irradiation response of the different stoichiometries between the pristine, dose 1 and dose 2 samples and to discuss these results in the context of previous literature and provide recommendations for future work.

The above objectives were achieved by the following actions. Changes in lattice parameter, microstrain are investigated by XRD for dose 2 samples and these are compared to the pristine sample values. SEM and EBSD are undertaken on dose 2 irradiated samples to characterise if any changes in the microstructure or phase separation exist in the samples. Fast MAS ^{13}C NMR is used to probe the nuclear structure of the ZrC samples to provide a basis for discussing the changes in carbon sub-environments of ZrC resonance. Raman spectroscopy is undertaken on irradiated samples to investigate the disordering of carbon located in the black structures located in the sample.

3.3.2 Experimental results: Irradiation of ZrC with 5 MeV protons to a fluence of 6.42 x 10^{17} protons/cm^2 - 0.031 dpa (dose 2)

3.3.2.1 XRD

X-ray diffraction experiments were undertaken (with a Mo anode) on ZrC samples following proton irradiations. Figure 62 shows XRD diffractograms of the solid (a) pristine nominal ZrC sample sintered at 2000^{o}C with nominal C/Zr = 1.00 (black trace) and the solid nominal C/Zr = 1.00 irradiated with (b) dose 1, 5 MeV protons (red trace) and (c) dose 2, 5 MeV proton (blue tracer). The nominal C/Zr = 0.80 and the 0.60 samples are shown in Figure 63 and Figure 64, respectively, and conform to the layout of the nominal C/Zr= 1.00 sample as described above. As in the previous section, the Corundum internal standard diffraction peaks are labelled with * and the potential position of the first graphite peak is indicated by the half-shaded triangle pointer. Where monoclinic ZrO_2 diffraction peaks are identified, they are denoted by an open black marker above the specific diffraction peak. Diffraction peaks belonging to a phase or phases, which were unidentified are denoted by an arrow above the respective diffraction peaks.

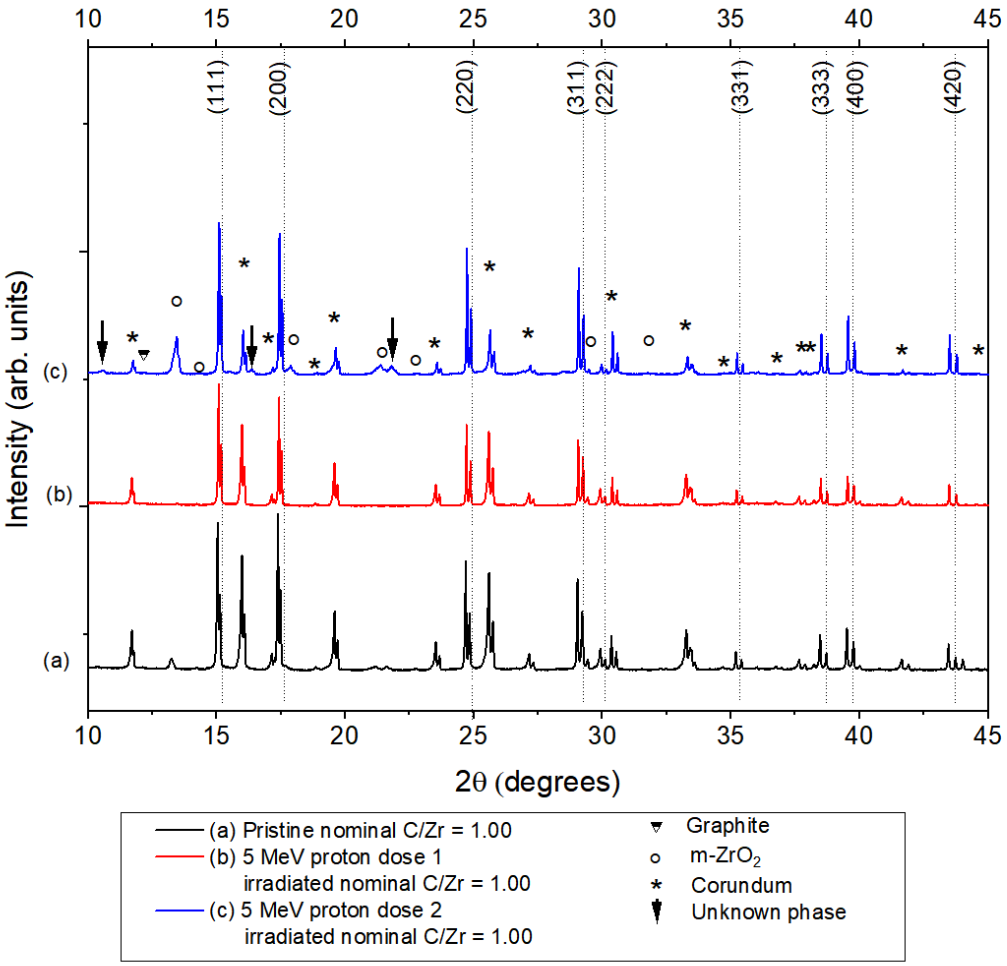

Figure 62 Vertically offset XRD patterns of ZrC (nominal C/Zr = 1.00) for (a) pristine and the 5 MeV proton irradiated (b) dose 1, (c) dose 2 samples.

In Figure 62, the nominal C/Zr = 1.00 dose 2 sample diffraction pattern is consistent with a NaCl structure for ZrC, as seen in both the pristine and dose 1 samples. The intensity of the (200) diffraction peak was observed to be less intense relative to the (111) diffraction peak for the dose 2 sample, which was in good agreement with the dose 1 sample diffraction pattern and opposite to that in the pristine diffraction pattern. Several monoclinic ZrO_2 peaks were observed in the X-ray diffraction pattern, confirming the presence of monoclinic ZrO_2 in the sample. An unknown peak located at 21.88 ° (2θ) that was present in the pristine pattern, but absent from the dose 1 pattern, was observed again in the dose 2 sample. Two previously

unseen diffraction peaks were also observed in the dose 2 sample pattern located at 10.55 and 16.42 ° (2θ), but these could not be identified. A database search of the potential phases (Zr, that these diffraction peaks could belong to was not able to identify or attribute with any certainty the origin of the diffraction peak.

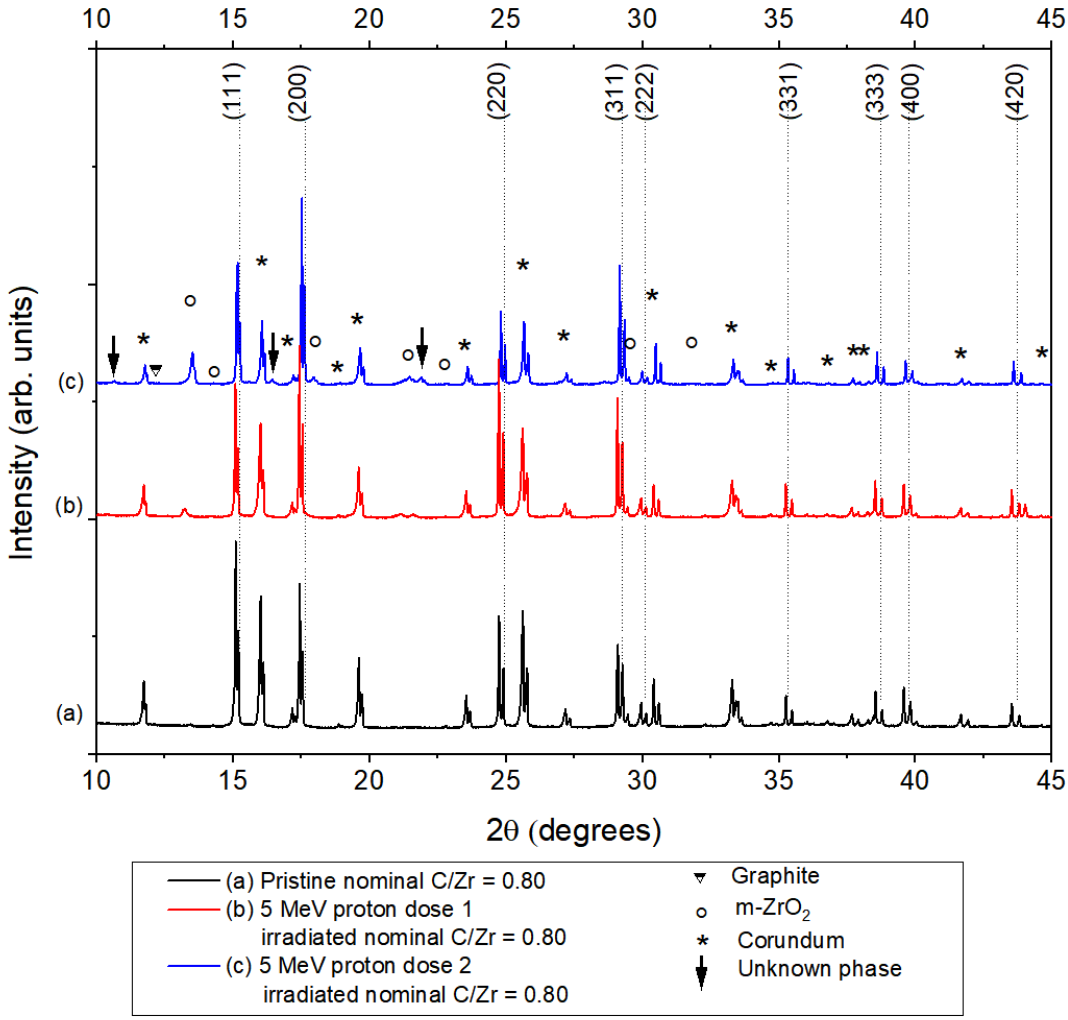

Figure 63 Vertically offset XRD patterns of ZrC (nominal C/Zr = 0.80) for (a) pristine and the 5 Me0V proton irradiated (b) dose 1, (c) dose 2 samples.

Figure 63 shows that the irradiated nominal C/Zr = 0.80 sample also maintained its cubic NaCl structure after the dose 2 irradiation, as agreed with XRD results in the pristine and dose 1 sample. The (200) diffraction peak was observed to be more intense relative to the (111) peak

in the dose 1 and dose 2 diffraction patterns, while the pristine diffraction pattern showed the opposite trend. The apparent intensity of multiple diffraction peaks belonging to zirconia was seen to increase in the dose 2 samples relative to the ZrC diffraction peaks as compared with the dose 1 and pristine sample diffraction patterns. In addition, two unknown diffraction peaks were observed in the pristine, dose 1 and dose 2 sample located at 10.55 and 21.88 ° (2θ). Further, an additional unknown peak located at 16.42 ° (2θ) was observed to develop in the dose 2 sample diffractogram. Locations of these peaks matched those of the unknown phases seen in the nominal C/Zr = 1.00 dose 2 pattern.

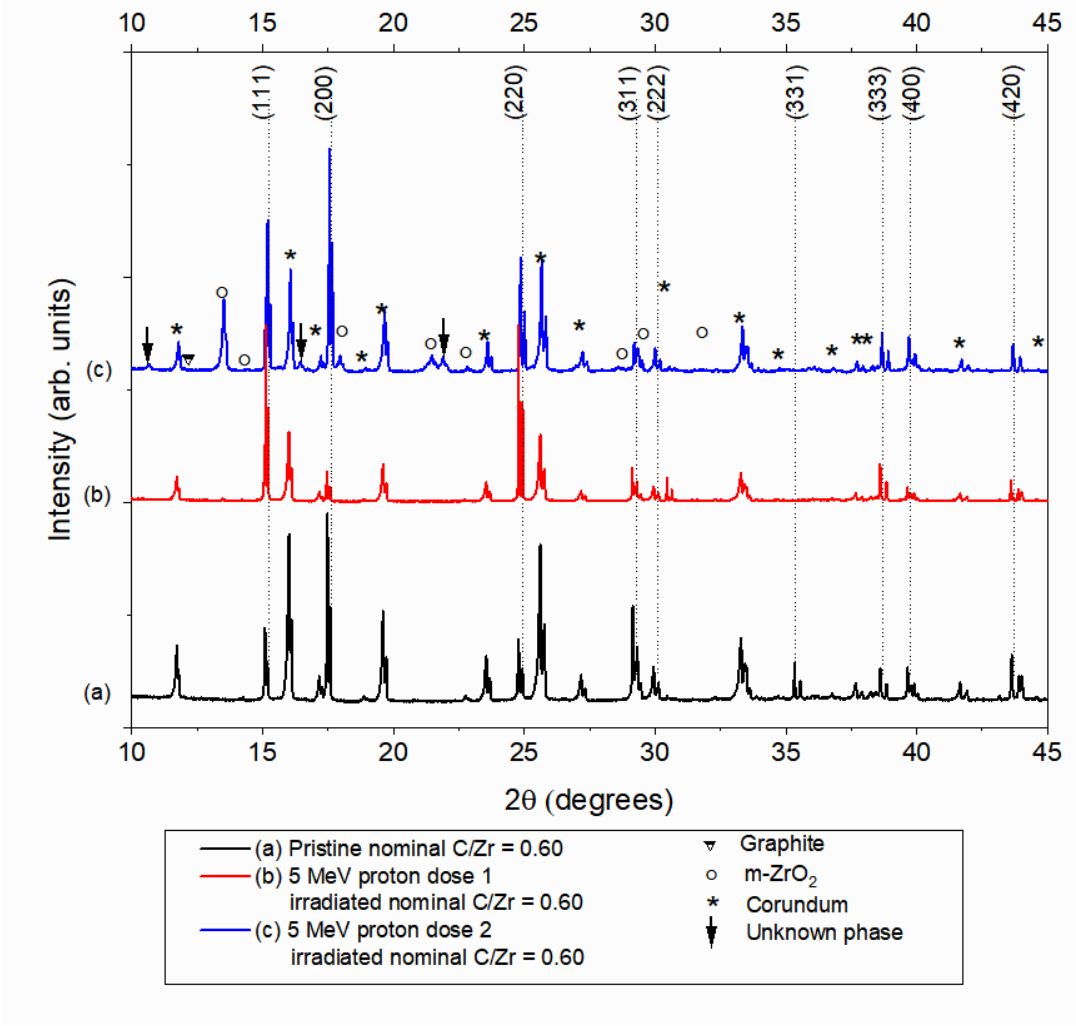

Figure 64 Vertically offset XRD patterns of ZrC (nominal C/Zr = 0.60) for (a) pristine and the 5 MeV proton irradiated (b) dose 1, (c) dose 2 samples.

The diffraction pattern of the nominal C/Zr =0.60 sample (Figure 64) showed that this sample also maintained its cubic structure post-irradiation. The (331) reflection that was present in the pristine sample pattern was absent from the dose 1 and 2 sample diffraction patterns. No graphite phase was observed in the dose 2 irradiated pattern, which was consistent with the trends seen in the dose 1 and pristine samples. XRD diffraction peaks belonging to a m-ZrO_2 phase were observed in the dose 2 diffraction pattern – the intensity of these peaks, relative to the other peaks, was seen to increase as compared to the dose 1 XRD pattern. Consistent with the dose 2 nominal C/Zr = 1.00 and 0.80 samples, the dose 2 nominal C/Zr = 0.60 sample pattern showed three diffraction peaks belonging to an unknown phase. These peaks were not observed in the pristine and the dose 1 diffraction pattern of the nominal C/Zr = 0.60 sample.

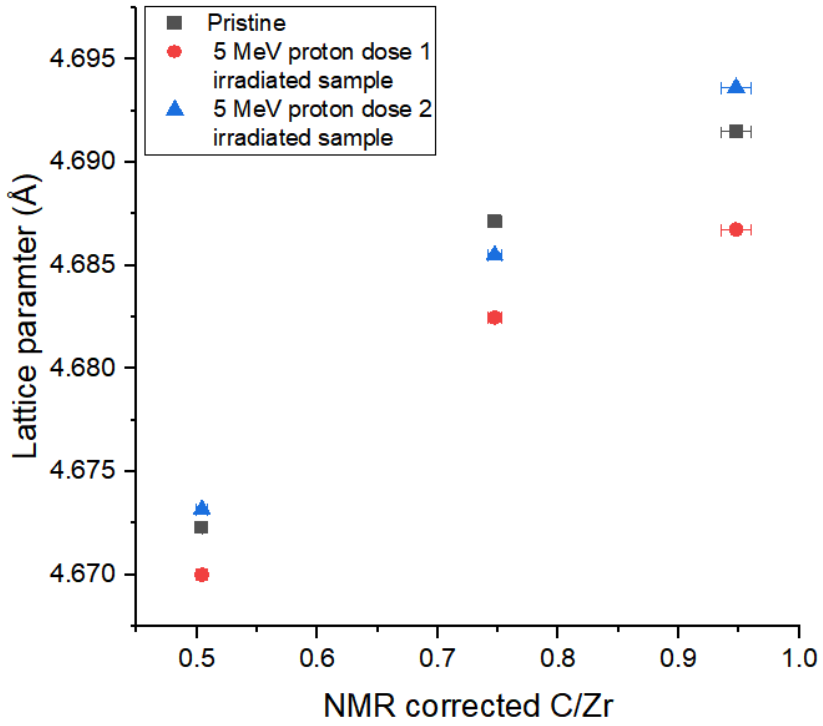

Figure 65 Pristine (black), 5 MeV proton irradiated dose 1 (red) and 5 MeV proton irradiated dose 2 (blue) lattice parameters for samples sintered at 2000 C plotted with respect to the NMR corrected C/Zr.

Figure 65 shows the lattice parameters as determined from Rietveld refinement plotted with respect to the NMR corrected carbon content Table 3.3). The dose 2 samples were observed to

follow the same decreasing trend in lattice parameter values with decreasing carbon content - consistent with the pristine and the dose 1 lattice parameter behaviour. The lattice parameter values of the dose 2 samples were seen to be consistently higher than those of the dose 1 samples, and higher than the pristine sample values with the exception of the pristine nominal C/Zr = 0.80 sample.

Table 3.3 - Lattice parameter of pristine vs 5 MeV proton dose 1 irradiated values.

Nominal C/Zr	NMR corrected C/Zr	NMR corrected error	Pristine lattice parameter (Å)	± error (Å)	Proton dose 1 Lattice Parameter (Å)	± error (Å)	Proton dose 2 Lattice Parameter (Å)	± error (Å)
1.00	0.95	0.01	4.692	0.001	4.688	0.001	4.69361	0.001
0.80	0.75	0.01	4.688	0.001	4.683	0.001	4.6855	0.001
0.60	0.50	0.01	4.672	0.001	4.670	0.001	4.67317	0.001

The goodness of fit (GOF) values from the Rietveld structural refinement, used to determine the lattice parameters, were observed to be 3.77, 5.25, 5.73 for the dose 2 samples of nominal C/Zr = 1.00, 0.80 and 0.60, respectively. The GOF from the Pawley fit was determined to be 3.61, 5.09 and 5.42 for the dose 2 samples of nominal C/Zr = 1.00, 0.80 and 0.60, respectively. The variation of the GOF was seen to be due to the presence of additional phases in addition to the marginal offset between the corundum standard and the sample tiles. As the difference in the offset was assumed to be zero, the peak centring, which was important for determining the lattice parameter, was checked by visual inspection of the residual spectrum.

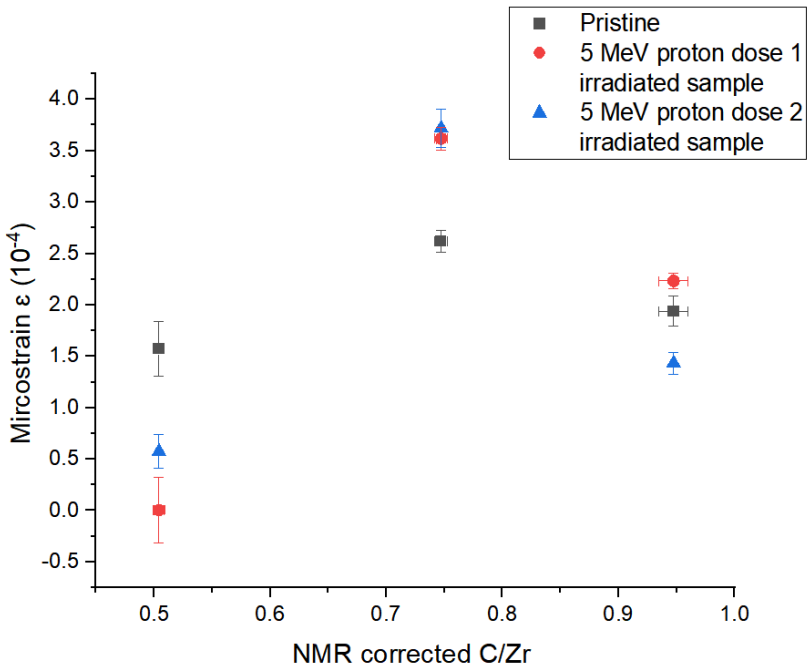

Figure 66 Pristine, dose 1 and dose 2 5 MeV proton irradiated lattice microstrain for samples sintered at 2000 °C *plotted with respect to the NMR corrected C/Zr.*

Figure 66 presents the pristine, 5 MeV proton dose 1 and dose 2 sample microstrain (Table 3.4). In the pristine case, the average microstrain values of the nominal C/Zr= 0.60 and 1.00 samples were within error of one another.

The dose 2 irradiated nominal C/Zr = 0.60, 0.80 and 1.00 samples were seen to have the lowest, highest and intermediate average microstrain values respectively, similar to those of the dose 1 samples. The nominal C/Zr = 0.60 dose 2 sample showed an increase in the microstrain from the dose 1 sample, with both samples observed to have a lower microstrain than the pristine sample. The mean value of the microstrain seen in the dose 2 nominal C/Zr = 0.80 sample showed an increase from the pristine and dose 1 sample values, however, the estimated standard deviation for both samples show that the measurements are within range of one another. The dose 2 nominal C/Zr = 1.00 sample was the only value to show a decrease from the pristine and the dose 1 sample microstrain values which, after the dose 1 irradiation, were higher than the pristine sample.

Table 3.4 - Microstrain of pristine, 5 MeV dose 1 and dose 2 proton samples.

Nominal C/Zr	NMR corrected C/Zr	± error	Pristine microstrain (ε) $x10^{-4}$	± error $x10^{-4}$	Proton dose 1 microstrain (ε) $x10^{-4}$	± error $x10^{-4}$	Proton dose 2 microstrain (ε) $x10^{-4}$	± error $x10^{-4}$
1.00	0.95	0.01	1.94	0.15	2.23	0.07	1.43	0.10
0.80	0.75	0.01	2.62	0.11	3.62	0.11	3.7	0.19
0.60	0.50	0.00	1.57	0.28	0.00	0.32	0.57	0.17

3.3.2.2 **SEM**

The following subsection presents the results of SEM microscopy of the dose 2, 5 MeV proton irradiated samples. The SEM images of the irradiated nominal C/Zr = 1.00, 0.80, 0.60 samples are presented in Figure 67, Figure 68 and Figure 69, respectively. The BSE and SE images of each set (left and right) were taken at 1000X and 2833X magnification (top and bottom). Due to time constraints – the two-day turnaround time between the samples arriving back in the UK from Dubna and the DCF irradiation – it was not possible to laser mark and image areas on the pristine sample. This meant that the same area could not be imaged before and after irradiation to directly compare changes in the microstructure as there was no reference marker. Nevertheless, as samples irradiated in the dose 2 irradiation campaign were cut from the same sintered pellet, it is acceptable to compare the dose 2 irradiated samples with the pristine micrographs of the same nominal stoichiometry displayed in the dose 1 section.

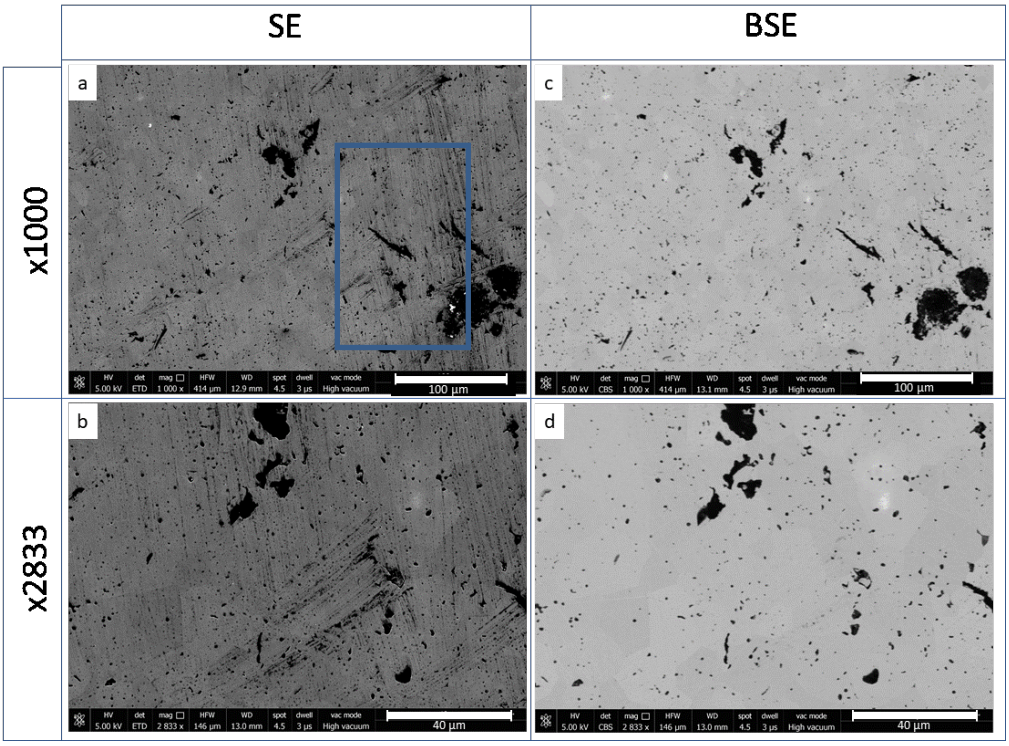

Figure 67 BSE and SE images of proton irradiated samples sintered at 2000°C with nominal C/Zr = 1.00, (a,b) SE images are on the right-hand side and (c,d) BSE images are on the left-hand side. Images on the top (a, c) and bottom (b,d) row have been taken at 1000x and 2833x magnification respectively.

The dose 2 irradiated nominal C/Zr = 1.00 (Figure 67) sample shows the same inter and intra-granular black structures as was seen in the pristine and dose 1 irradiated samples, with no significant changes in the microstructure observed as compared to the dose 1 samples. In addition, no phase separation was observed in the BSE images. Black structures remained distributed inside (intragranular) and between grains (intergranular), as observed in the dose 1 and pristine samples. SE images showed evidence of the microstructural roughening of the surface after the dose 2 irradiation: a result which was also observed in the dose 1 samples (blu e box Figure 67 a).

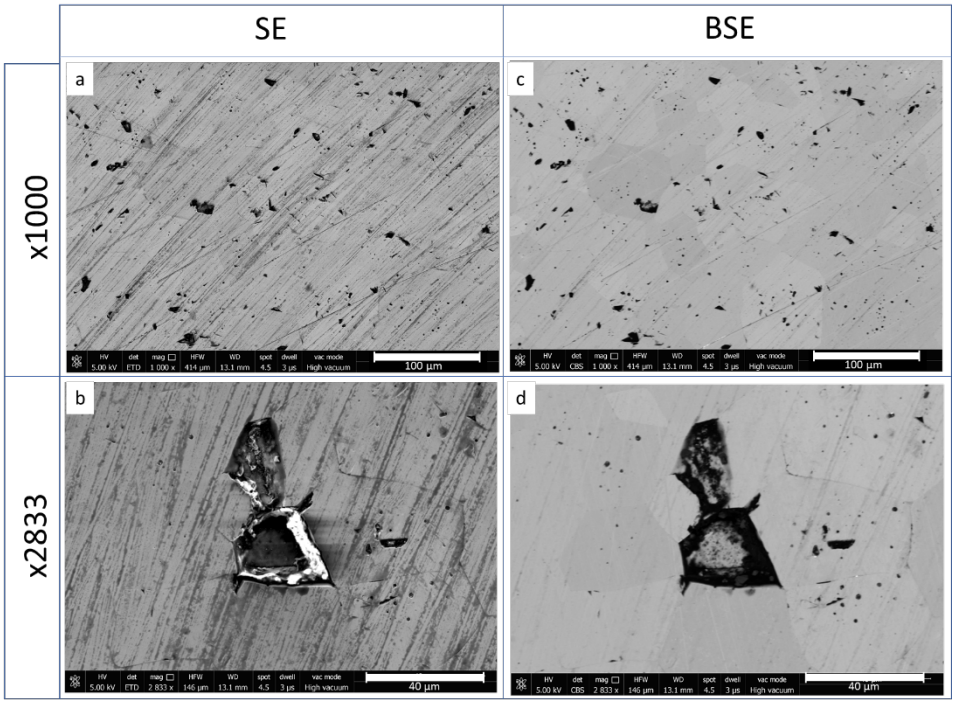

Figure 68 *BSE and SE images of proton irradiated samples sintered with nominal C/Zr = 0.80, (a,b) SE images are on the right-hand side and (c,d) BSE images are on the left-hand side. Images on the top (a, c) and bottom (b,d) row have been taken at 1000x and 2833x magnification respectively.*

Consistent with the dose 1 samples, the nominal C/Zr = 0.80 dose 2 irradiated sample shows the presence of intra and intergranular black features (Figure 68). The nominal C/Zr = 0.80 dose 2 irradiated sample shows a significantly smaller grain structure than samples of lower carbon contents, which are apparent in the BSE image. The presence of dark streaks across the surface was observed in the dose 2 sample, which was similar to the features that were present in the dose 1 sample and again, is indicative of roughening of the microstructure due to irradiation. BSE images did not show any phase separation.

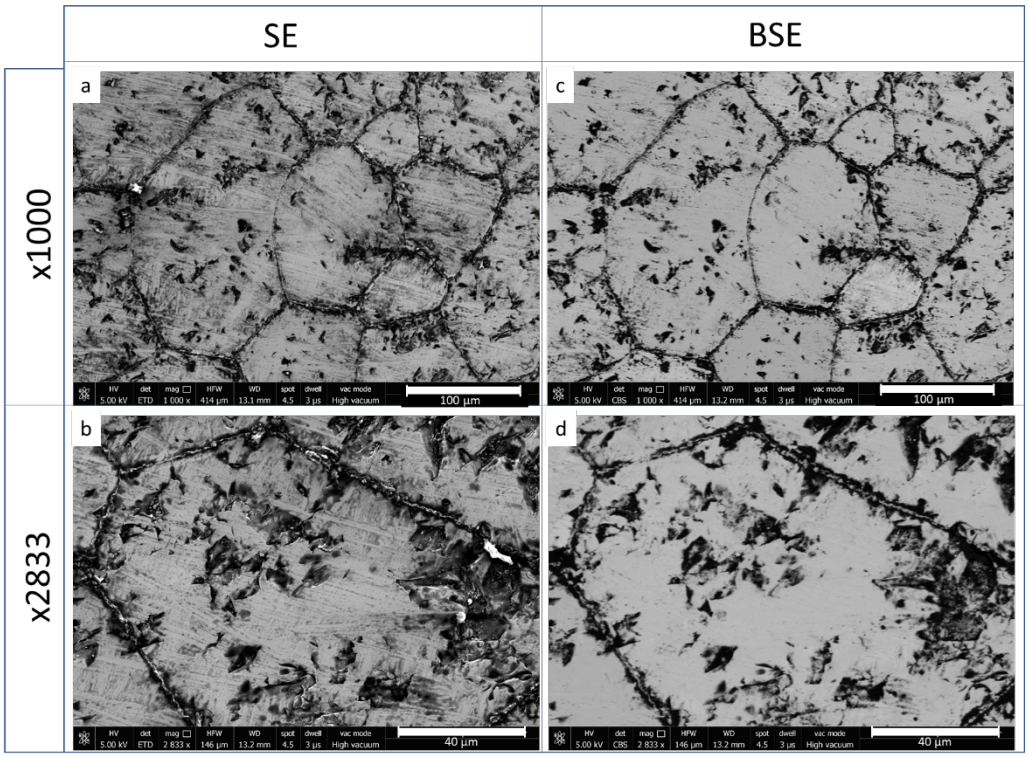

Figure 69 BSE and SE images of proton irradiated samples with nominal C/Zr = 0.60, (a,b) SE images are on the right-hand side and (c,d) BSE images are on the left-hand side. Images on the top (a, c) and bottom (b,d) row have been taken at 1000x and 2833x magnification respectively.

The nominal C/Zr = 0.60 dose 2 irradiated sample (Figure 69) revealed the presence of inter and intragranular black structures, consistent with the dose 1 and irradiated samples. The connected inter-granular features make the boundaries visible, as was seen in the unirradiated and the dose 1 micrographs. A significant roughening of the microstructure was observed in SE images as compared to the pristine and dose 1 microstructures as seen in the previous sub-section. Intergranular black structures in the dose 2 sample appear to be more uneven around the edges of the black structure as compared to the dose 1 and pristine samples. A greater concentration of the intragranular black structures was also observed for the dose 2 irradiated samples as compared to their dose 1 and pristine counterparts. No separation of phases was observed in the BSE images.

EBSD analysis was undertaken on the irradiated solid samples to determine the grain size post-irradiation. As with the pristine samples in Chapter 2, the average grain sizes of the irradiated samples were analysed using the MTEX package with scripts written in MATLAB.

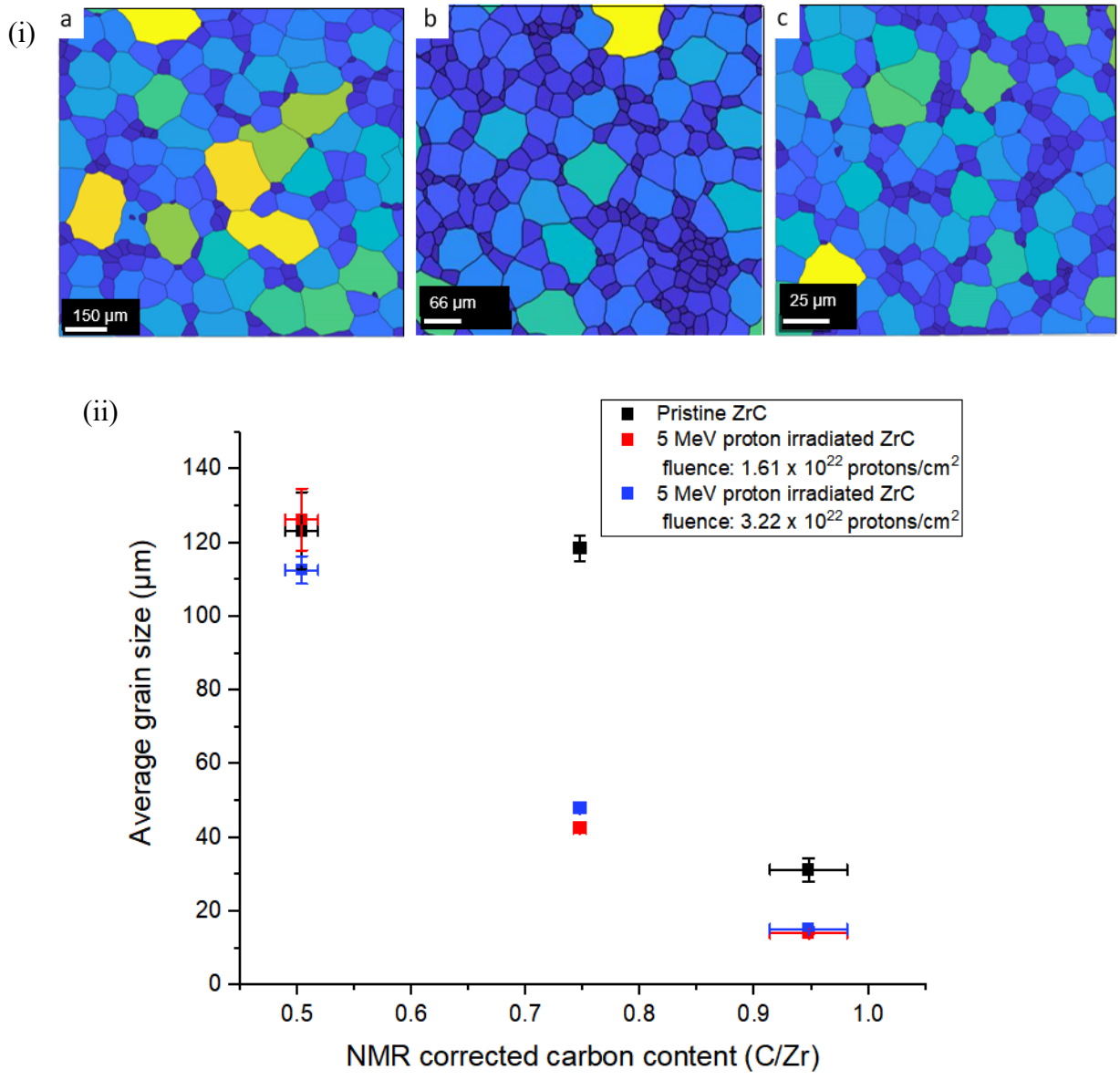

Figure 70 (i) (a) Grain trace diagrams for the irradiated nominal C/Zr = 0.60 (a), 0.80 (b), 1.00 (c) samples – the darker blue the smaller the grain size larger grains are yellow in colour. (ii) The grain size of the pristine, dose 1 and dose 2 samples with average grain error plotted to 2 standard deviations.

The results of the grains traced in EBSD analysis are presented in Figure 70 (i). The average grain size of the nominal C/Zr = 1.00, 0.80 and 0.60 samples was determined to be 15.2 ± 0.4 µm, 48.0 ± 0.5 µm and 112.6 ± 3.7 µm, respectively. Figure 70 (ii) shows the graph of the average grain size of the pristine, 5 MeV proton irradiated dose 1 and dose 2 samples plotted with respect to the NMR corrected C/Zr. The error bars on the grain size are plotted to two standard deviations in order to capture the range of grain sizes that exist within each sample – a typical grain size distribution of the 5 MeV proton, dose 2 irradiated sample is displayed in Figure 71.

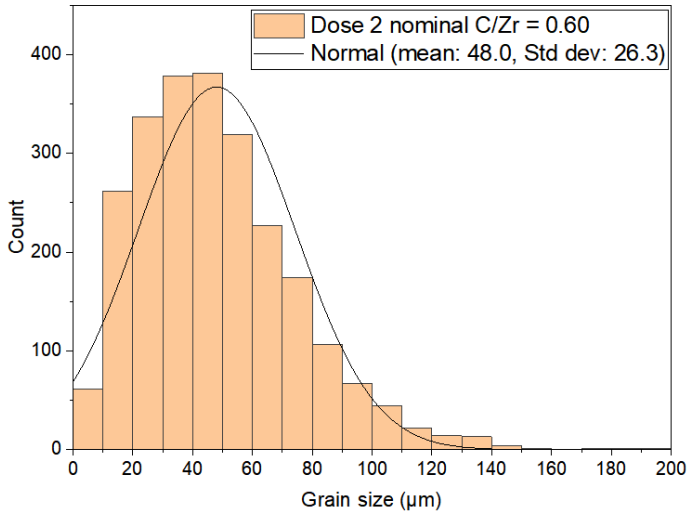

Figure 71 Histogram showing the grain size of the nominal C/Zr = 0.60, 5 meV proton irradiated dose 2 sample. A normal distribution is fitted to histogram to determine the mean.

All irradiated samples maintained the trend of decreasing average grain size with increasing carbon content. The nominal C/Zr = 1.00 samples were observed to have the smallest overall average grain size, with respect to all other samples, both before and after irradiation. The dose 1 and dose 2 mean grain sizes were observed to be within two standard deviations of one another at 14.1 ± 0.6 µm and 15.0 ± 0.8 µm respectively – indicating that both samples have a proportion of common grain sizes between them. Both irradiated values showed a decrease from the mean pristine value of 31.2 ± 6.3 µm.

The nominal C/Zr = 0.80 samples were seen to have the joint highest grain size, with the nominal C/Zr = 0.60 sample average grain size value. The irradiated samples showed the largest decrease of all samples produced from the pristine value; the average grain size of the dose 1 and dose 2 proton irradiated samples were determined to be 42.6 ± 1.8 μm and 48.0 ± 1.0 μm respectively, decreasing from their pristine value of 118.5 ± 6.86 μm. Doubling the irradiation dose was seen to increase the average grain size by approximately 6.0 μm. As was noted in the dose 1 section it may be the case that the pristine nominal C/Zr = 0.80 sample is an outlier and thus may give the impression that the grain size has dramatically decreased.

The average grain size of the dose 2 irradiated nominal C/Zr = 0.60 sample showed the lowest value (112.6 ± 7.3 μm) - compared to the value for the pristine sample and dose 1 irradiated samples 123.2 ± 20.6 μm and 126.2 ± 16.5 μm, respectively. The dose 1 sample resulted in an increase in the average grain size, compared to its pristine value. Doubling the irradiation dose resulted in a decrease in the average grain size from the pristine value. However, both the dose 1 and dose 2 average grain size measurements were observed to be within the two standard deviations of one another.

3.3.2.3 **Raman spectroscopy**

This sub-section presents the results from the Raman spectroscopy investigation on the dose 2, 5 MeV proton irradiated samples. Similarly to the pristine and dose 1 sample Raman spectroscopy, the sampling spots were the black structures, as sampling on other regions produced no Raman response.

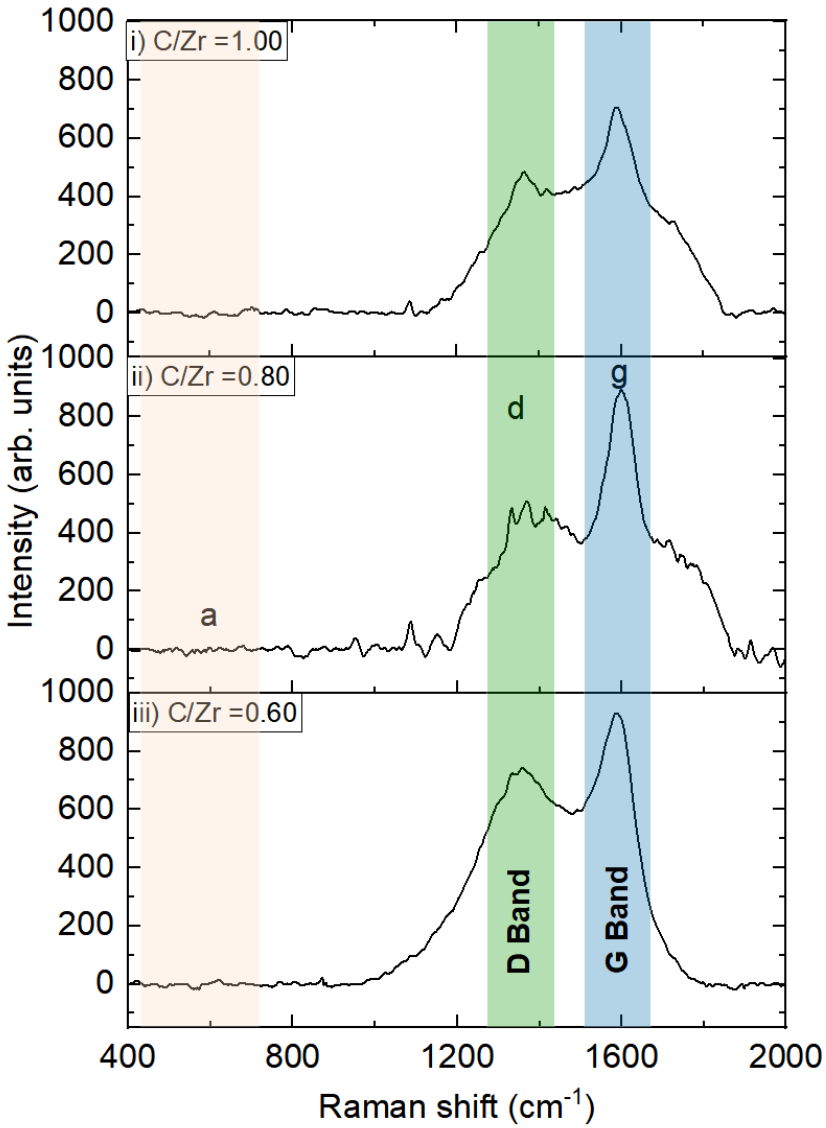

Figure 72 Raman spectra of nominal C/Zr = 1.00 (i), 0.80 (ii) and 0.60 (iii) samples sintered at 2000°C and irradiated with dose 2, 5 MeV proton irradiated samples. Spectra were baselined using a manually selected, user-defined baseline.

Figure 72 shows the baseline-corrected Raman spectra of the dose 2, 5 MeV protons irradiated samples (nominal C/Zr =1.00, 0.80 and 0.60 sintered at 2000°C labelled (i), (ii) and (iii) respectively). The three observed Raman active modes are labelled a, d and g above spectrum (ii) at their respective band location regions.

All dose 2 sample spectra showed the presence of the D and G bands [50], [51], [54], [58], [92]. The D and G band peak structure was seen to be increasingly convoluted in the irradiated samples, compared to the pristine sample. No resonances were present in the 'a' band in any of the dose 2 samples. On average, as with the noticeable trend in the previous sections, the measured Raman signal decreased with increasing nominal carbon content.

The nominal C/Zr = 1.00 sample shows characteristic D and G peaks that were not seen in the nominal C/Zr = 1.00 pristine or the dose 1 proton irradiated samples. The sharp structures of both peaks were seen to be captured using two Lorentzian profiles. The Lorentzian fitted to the D peak was seen to be centred around 1362 ± 2 cm^{-1} with a FWHM of 83 ± 1 cm^{-1} – the resonance intensity was observed to be 483 ± 1 counts. The Lorentzian function fitted to the G peak was seen to be centred around 1596 ± 1 cm^{-1} with a FWHM of 96 ± 3 cm^{-1} – the resonance intensity was observed to be 706 ± 2 counts. Additional structures were visible in the residual spectrum once the D and G peaks were fitted. Two additional Gaussian peaks were fitted to the residual spectrum to capture the profile of these features. The first Gaussian profile fitted captured that exists between the D and G peaks; this fitted peak was centred around 1467 ± 2 cm^{-1} with the FWHM = 325 ± 1 cm^{-1} and intensity 196 counts. The G peak was seen to be flanked by a shouldering resonance on the right-hand side - which was fitted by a Gaussian function – centred around the 1727 ± 2 cm^{-1}, and FWHM = 130 ± 2 cm^{-1} and intensity 196 counts.

As with the nominal C/Zr = 1.00 sample the nominal C/Zr = 0.80 sample was seen to have a better defined and sharper G peak structure, whereas the D peak appears to be broader and less well defined but still resolvable. Both peaks were seen to be appropriately fitted using Gaussian functions. The Gaussian function fitted to the D peak was centred around 1385 ± 1 cm^{-1} with FWHM = 224 cm ± 2 cm^{-1} and intensity 490 counts. The Gaussian function fitted to the G peak was seen to be centred around 1599 ± 1 cm^{-1} with FWHM = 95 cm ± 2 cm^{-1} and intensity 820 ± 2 counts. A further resonance was observed to be present shouldering on the right-hand side of the G peak. This was captured by fitting a Gaussian function centred around 1731 ± 2

cm $^{-1}$, with FWHM 144 ± 2 cm $^{-1}$ and intensity 334 ± 2 counts. An additional Gaussian function was required to fit the additional resonance between the D and G peaks in order to optimise the spectral fit, this was located around 1733 ± 2 cm $^{-1}$ with a FWHM = 95 ± 2 cm $^{-1}$ and intensity 344 ± 7 counts.

The Raman spectra of the nominal C/Zr = 0.60 sample shows the presence of the characteristic D and G bands but does not show any evidence of the 'a' band. The tops of the peaks are clearly resolvable: whilst the base of the peaks appear to be convoluted. Two Voigt functions were seen to capture the behaviour of the D and G peaks. A Gaussian function was fitted to the D peak, which was seen to be centred around 1355 ± 2 cm^{-1}, with FWHM = 258 ± 2 cm^{-1} and intensity = 712 ± 1 counts. The G peak was fitted with a Voigt function that was centred around the 1591 ± 1 cm^{-1}, FWHM = 107.5 ± 1 cm^{-1} and intensity = 868 counts. A third peak was required to optimise the peak fit and capture the middle region between the D and G peaks – this was located at 1503 ± 1 cm^{-1} with FWHM = 67 ± 1 cm^{-1} and height 111 ± 2 cm^{-1}. The sample spectrum did not show any additional shouldering resonances at higher wavenumbers.

3.3.2.4 **NMR**

The following sub-section presents the results of fast MAS ^{13}C NMR experiments on the dose 2, 5 MeV proton irradiated samples. ^{13}C MAS NMR was undertaken on the pristine and dose 2 samples to investigate changes in the ZrC resonance with increasing radiation dose.

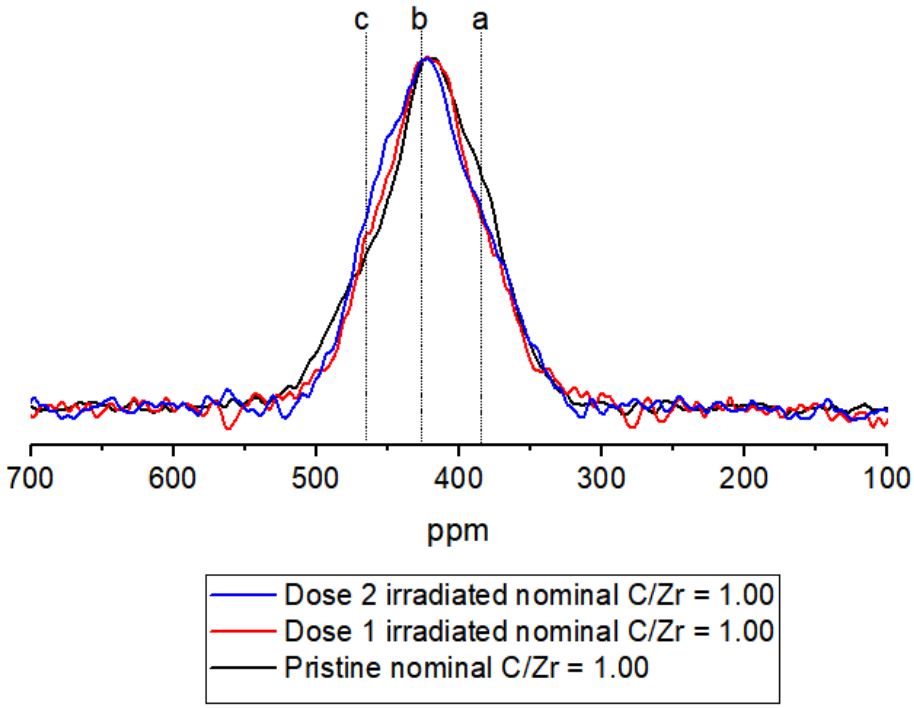

Figure 73 Overlain 39 kHz spinning ^{13}C MAS-NMR spectra of nominal C/Zr = 1.00 pristine (black tracer) sintered at 2000°C, 5 MeV proton irradiated ZrC samples to a fluence of dose 1 (red) and dose 2 (blue).

Figure 73 shows the overlain, 39 KHz spinning, ^{13}C NMR spectra for the nominal C/Zr = 1.00, pristine (black), 5 MeV proton dose 1 (red) and 5 MeV proton irradiated dose 2 (blue) samples. Both the irradiated and the pristine peaks studied were broad and asymmetrical in shape. The centre of gravity of the pristine, dose 1 and dose 2 samples was observed to be approximately 423 ppm. The line shape of the NMR spectrum was seen to change with increasing dose. A shoulder, located at approximately 368 ppm, labelled 'a' was observed in the pristine sample, after dose 1 irradiation the 'a' structure was seen to decrease in intensity. On the other hand, another shoulder located at approximately 450 ppm was observed to be more prominent, labelled the 'c' peak and was seen to gradually increase in intensity, with increasing dose.

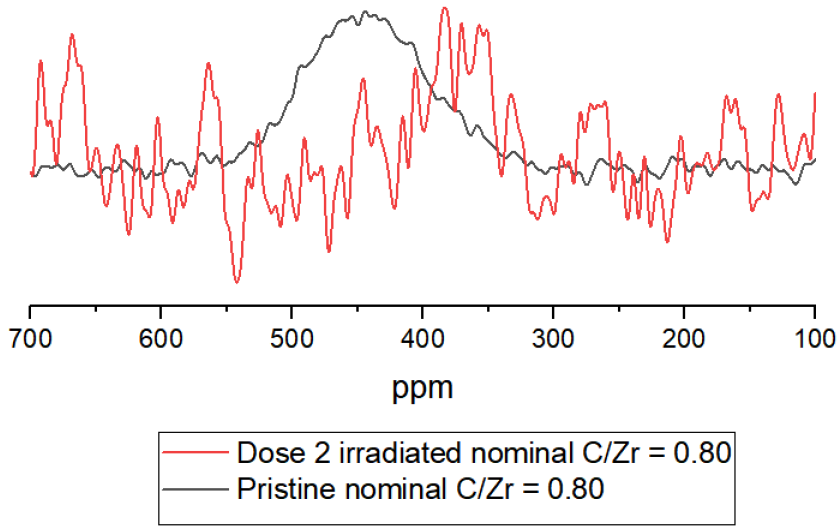

Figure 74 Overlain 39 kHz spinning ^{13}C MAS-NMR spectra of nominal C/Zr = 0.80 pristine (black tracer) sintered at 2000°C, 5 MeV proton irradiated ZrC samples to a fluence of dose 1 (red) and dose 2 (blue).

Figure 74 shows the overlain, 39 KHz spinning, ^{13}C NMR spectra for the nominal C/Zr = 0.80, pristine (black), 5 MeV proton irradiated dose 2 (red) samples. The centre of gravity of the pristine peak was determined to be approximately 426 ppm. The poor signal to noise of the irradiated sample spectra made it difficult to determine if any signal was present.

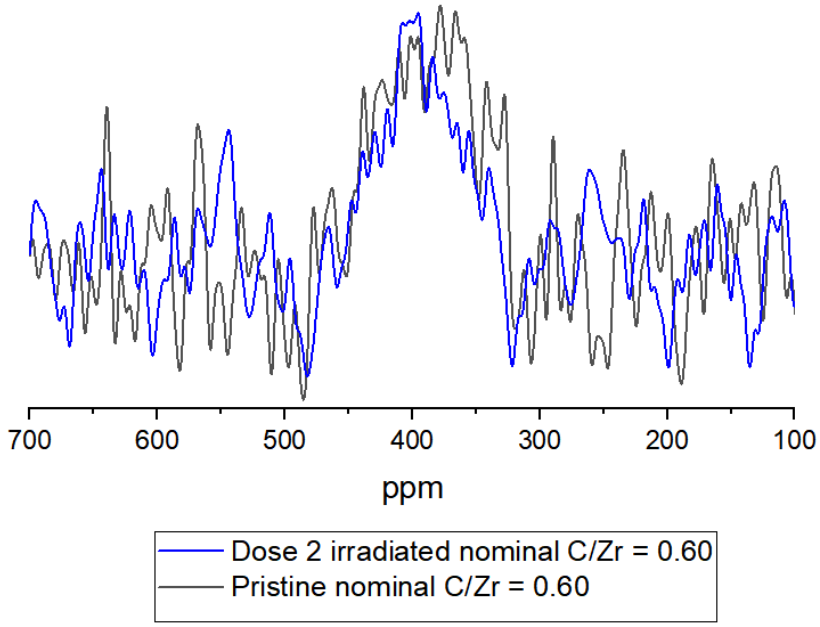

Figure 75 Overlain 39 kHz spinning ^{13}C MAS-NMR spectra of nominal C/Zr = 0.60 pristine (black tracer) sintered at 2000°C, 5 MeV proton irradiated ZrC samples to a fluence of dose 1 (red) and dose 2 (blue).

Figure 75 shows the overlain, 39 kHz spinning, ^{13}C NMR spectra for the nominal C/Zr = 0.60, pristine (black), 5 MeV proton irradiated dose 2 (blue) samples. A minor shift in the centre of gravity of the ZrC peak was observed in the dose 2 sample. A single Gaussian function was seen to fit the characteristic line shape of the pristine and irradiated NMR spectra. The centre of gravity of the pristine and irradiated samples were determined to be around approximately 387 and 395 ppm respectively, indicating that the peak centre of gravity shifted to higher ppm after irradiation. This result agreed with the dose 2 proton nominal C/Zr = 1.00 sample results.

The NMR signal to noise ratio is smaller in this sample and may be due to the lower proportion of carbons present in the sample, which inevitably would produce a lower NMR response. As the random noise is proportional to the square root of the number of scans, acquiring the same S/N as $ZrC_{0.95}$ for this sample ($ZrC_{0.50}$) would require 4 times the acquisition time, which would be approximately a month [159] due to the unexpectedly long ^{13}C relaxation times.

3.3.3 Discussion: Irradiation of ZrC with 5 MeV protons to a fluence of 6.42 x 10^{17} protons/cm^2 - 0.031 dpa (dose 2)

Doubling the irradiation dose showed no significant changes in the microstructure of the SEM of the nominal C/Zr = 1.00 and 0.80 samples. However, the inter-/intra-granular black structures observed in the dose 2 irradiated nominal C/Zr = 0.60 sample were rougher and more jagged in appearance, in contrast to the smoother edges observed in the pristine and the dose 1 samples. No phase separation was detected in the irradiated samples, highlighting the resistance of the sample to radiation damage. The trend of decreasing sample grain size; as determined by EBSD analysis, with the increasing carbon content of the samples, was in good agreement with the pristine and the dose 1 irradiated sample results. Smaller grain sizes in the dose 2 sample also indicate that the yield strength of the material should increase with carbon content via the Hall-Petch relationship [130], [132].

The NaCl rock salt structure was maintained for all the irradiated samples, which was consistent with the pristine and dose 1 proton irradiated samples. The monoclinic ZrO_2 phase diffraction peaks were also observed in the dose 2 diffraction patterns, a result which was again in agreement with the dose 1 results.

As with the pristine and dose 1 sample, no diffraction peaks belonging to graphite were observed in the dose 2 irradiated sample spectrum. This result indicates that the irradiations did not act to increase the coherence of the scattering domains; suggesting free carbon remains dispersed throughout the sample or at grain boundaries on the nanoscale, as indicated by Raman spectroscopy.

The microstrain values of the dose 2 sample were seen to follow the same trend as seen in the dose 1 sample, with microstrain being the highest, intermediate, and lowest values for the nominal C/Zr = 1.00, 0.80 and 0.60 samples, respectively. As proposed in the previous section: the combination of large intergranular black structures in the nominal C/Zr = 0.60 sample increased the vacancy sink efficiency of the sample [54], [61]. This, in turn, results in a lower

microstrain value, with respect to the samples of higher carbon content. The increase in the microstrain of the nominal C/Zr = 0.60 dose 2 sample as compared to the dose 1 sample value could indicate that defects are starting to accumulate in the sample [54], [160]. The nominal C/Zr = 0.60 dose 1 and dose 2 samples were observed to be within two standard deviations of the pristine grain size value, indicating that irradiations did not cause a significant change in the average grain size.

At the other stoichiometric extreme, the C/Zr = 1.00 sample shows the second-lowest microstrain values, with respect to the other dose 2 sample values, in conjunction with the lowest grain size. The dose 2 nominal C/Zr = 1.00 sample again showed a decrease from its pristine value. The small grain size acts to increase the sink efficiency of the grain boundaries by decreasing the distance a defect needs to travel to get to a grain boundary, with vacant sites in the sample augmenting the defect sink capabilities. The microstrain of the nominal C/Zr = 1.00 dose 2 sample was observed to decrease from its pristine and higher dose 1 value, while the lattice parameter was observed to increase. It is proposed that the small grain size of the samples and proximity to grain boundaries act to reduce microstrain in the sample by sinking interstitial carbon atoms; however, the vacancy produced from the liberation of carbon from its original site again acts to increase the lattice parameter [149]. The dose 1 and dose 2 average grain size values were observed to be within two standard deviations of one another, indicating dose 2 irradiations did not significantly affect the grain size from their dose 1 values.

In the case of the nominal C/Zr = 0.80 sample, the dose 1 and 2 microstrains showed the highest microstrain values of all samples. The dose 1 and dose 2 microstrain values were observed to be within two standard deviations of one another. Extending the above hypothesis, it is proposed that the defects produced in this sample have a longer migration path to travel to reach grain boundaries, due to larger grain sizes, in addition to the volume of the intergranular black features lower in volume (SEM images) and thus less efficient sinks. In turn, interstitial carbon atom defects liberated from their original pristine lattice positions due to irradiation may nucleate within the grains creating microstrain, which is augmented by a reduced number

of vacant sites for the defects to sink into as compared to the nominal C/Zr =0.60 sample. Again, this increase in the vacant sites due to irradiation, results in an increase in the lattice parameter that is consistent with DFT computational simulations by Mellan *et al.* [149].

The largest decrease in the grain size of pristine, dose 1 and dose 2 samples was seen in the nominal C/Zr = 0.80 sample. This result, accompanied by a higher microstrain, may indicate that a subdivision of grains is occurring as a result of irradiation-induced defects. The phenomena of grain subdivision or polygonization in the nuclear context has also been observed in high burn-up UO_2 (uranium dioxide) fuel. However, the instance of UO_2 may be considered a more complicated system [161]–[163], due to the potential role played by fission product nucleation as well. As the average grain sizes of the pristine samples were determined to vary with respect to carbon content, another possibility could be that carbon atoms liberated from their interstitial sites are sunk at grain boundaries, and hence change the stoichiometry of the sample and the sample grain size.

Additional detail regarding the change in the carbon sub-environments within the ZrC lattice can be determined from ^{13}C MAS NMR. The changes in the line shape of the nominal C/Zr = 1.00 sample showed the evolution of an additional structure at higher ppm to the central ZrC peak when comparing the pristine spectrum to the dose 1 and dose 2 samples. The movement of the peak structure was also observed in the pristine static NMR spectra of the samples sintered at 2000°C and the samples sintered at 1500°C, which both show a similar movement in the line shape to higher ppm with increasing vacancy concentration.

In the 1500°C samples (discussed in the earlier chapter), the α peak located at lower ppm was observed to disappear and the β shouldering peak at higher ppm for more metallic samples was seen to increase in intensity with increasing dose. The liberation of carbon atoms from their octahedral interstitial sites within the ZrC lattice as a result of irradiation would indeed create a more metallic ZrC structure, and this behaviour is likely to be the reason why the NMR line shape evolves systematically with irradiation dose. Similar behaviour is observed in the dose

2 nominal C/Zr = 0.60 sample spectra, where irradiation causes a shift in the peak structure to higher ppm. Spinning the sample at 39 kHz did not increase the resolution of individual sub-environments within the ZrC resonance, which suggests that a range of environments are present within the ZrC resonance. Samples likely need to be spun at much higher rotational frequencies to resolve these environments –this is practically difficult as ZrC is a semi-metallic material.

The above results clearly show microstructural alterations even with low doses of irradiation – a result contrary to the literature. Motta *et al.*[43] reported no damage at 0.1 dpa when using TEM to investigate the effects of proton irradiation nominal C/Zr = 0.8 and 0.9 ZrC samples, for the temperature range of 26 to 800°C. Black dot damage was reported to occur between 0.1 and 0.3 dpa, an order of magnitude higher than the dose used in this study. Motta *et al.* also observed the presence of graphite in the zone refined, commercially purchased, samples. Unfortunately, no XRD patterns or lattice parameters were reported in these studies.

Raman investigations into the black structures seen in the dose 2 samples revealed the presence of the D and G peaks corresponding to disordered and pristine graphite. This was consistent with the pristine and the dose 1 samples. An additional shouldering peak was observed in the nominal C/Zr = 1.00 and 0.80 located at approximately 1727 and 1733 cm^{-1}. This shouldering peak has not been previously observed in previous studies of ZrC [164], [165] and more generally in carbon-based systems [50], [92], [165], [166]. The broad FWHM of the extra resonance may indicate that this feature could be an amorphous feature however, its origin is ambiguous.

Increasing irradiation doses caused the location of the maximum of the G resonance the nominal C/Zr = 0.60 to shift to lower wavenumbers (approximately 1609, 1595, 1586 cm^{-1} for the pristine, dose 1 and dose 2 samples respectively). The shift to lower wavenumbers suggests an increasing bond disorder within the graphite present in the sample [51] and a decrease in the chains and graphitic clustering. This phenomenon was also observed in the G peak of the

nominal C/Zr = 0.80 samples. The sp^2 crystallite size within these black regions was calculated to be approximately 28, 34 and 24 nm for the nominal C/Zr = 1.00, 0.80 and 0.60 dose 2 samples; this was an increase from the crystallite size seen in the dose 1 samples.

3.3.4 Conclusion: Irradiation of ZrC with 5 MeV protons to a fluence of 6.42 x 10^{17} protons/cm^2 - 0.031 dpa (dose 2)

The dynamic behaviour of the microstrain, grain size and lattice parameter with irradiation dose showed that dose 2 irradiations caused a change in the structure of the material as a result of irradiations. It was proposed that carbons displaced from their original lattice sites are sunk at grain boundaries and vacant sites (sub-stoichiometric ZrC) and that this sink efficiency is supplemented by grain boundary width and grain size.

NMR results signified a change in the ZrC resonance sub-environment with irradiations. This manifested as the growth of shouldering resonances emerging at higher ppm for irradiated samples. This result was seen to be consistent with ZrC resonance evolution from less metallic to more metallic samples sintered at 2000°C and 1500°C as presented in the pristine chapter. This shows that vacancies are caused in the samples due to irradiation. The NaCl structure of ZrC was maintained after irradiation. Diffraction peaks belonging to monoclinic ZrO_2, and an unknown phase were also observed in the dose 2 sample.

3.4 Irradiations with 158 MeV Xe to a fluence of 1 x 10^{15} ions/cm^2 - 2.4 dpa

3.4.1 Introduction

This section aims to present and discuss the effects of Xenon (Xe) irradiation on the ZrC samples produced in this research project. Irradiation was undertaken on ZrC samples with 158 MeV Xe ions to a fluence of 1 x 10^{15} ions/cm^2 on the nominal C/Zr = 1.00, 0.80 and 0.60 samples sintered at 2000 ºC to simulate heavy-ion damage.

Most heavy-ion irradiation studies in the literature, like the proton studies before them, focus on the irradiation response of near stoichiometric ZrC but do not consider the material response over a systematic range of stoichiometries.

The objectives of this section are the following: to characterise the changes that Xe heavy-ion irradiations have had on the ZrC samples by using SEM, XRD, EBSD and Raman spectroscopy techniques, to compare the extent to which the irradiation has altered the properties of the ZrC samples of varying stoichiometries, to discuss the possible underlying mechanisms that could contribute to the irradiation response seen and finally, to discuss these results in the context of previous literature and provide recommendations for future work.

The above objectives are achieved by the following actions. Changes in the relative abundances of the phases and the lattice parameter are investigated by XRD. SEM is undertaken on all irradiated samples to characterise if any changes in the microstructure or phase separation exist post-irradiation. EBSD is utilised to determine if any changes in the grain size occur as a result of irradiation. Raman spectroscopy is undertaken on irradiated samples to probe the changes in the black structures determine the response of the graphite and the amorphous carbon in pristine samples.

3.4.2 Experimental Results: Irradiations with 158 MeV Xe to a fluence of 1 x 10^{15} ions/cm^2

3.4.2.1 XRD

The following section presents the results of the XRD diffraction experiments undertaken on the irradiated ZrC samples. Figure 76 shows XRD diffractograms of the solid (a) pristine nominal ZrC sample sintered at 2000ºC with nominal C/Zr = 1.00 (black tracer) and the offset (b) the solid irradiated nominal C/Zr = 1.00 sample up to to a fluence of (1 x 10^{15} ions/cm^2) with 158 MeV Xe (red tracer). The nominal C/Zr = 0.80 and the 0.60 samples are shown in Figure 77 and Figure 78, adhering to the layout of the nominal C/Zr= 1.00 sample as described above.

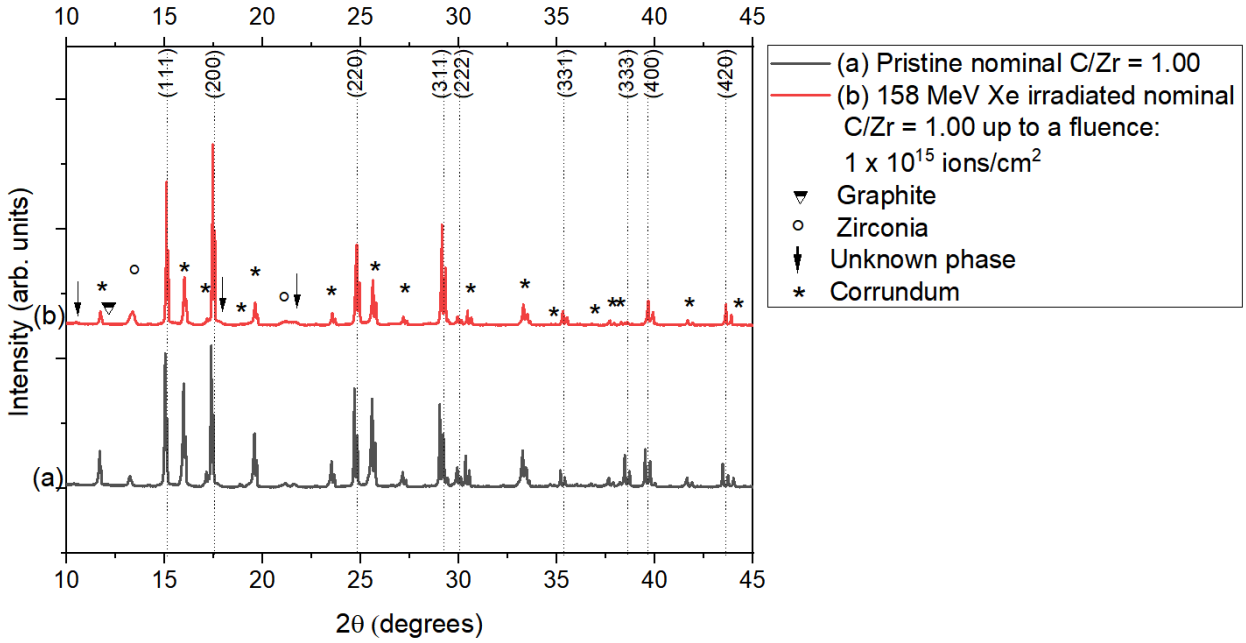

Figure 76 Vertically offset XRD patterns of pristine (a) and irradiated with 158 MeV Xe to a fluence of (1 x 10^{15} ions/cm^2) at room temperature (b) ZrC of nominal C/Zr = 1.00 sintered at 2000°C.

Figure 76 shows that the nominal C/Zr = 1.00 pristine sample patterns are consistent with a NaCl structure for ZrC. The intensity of the (111) diffraction peak was seen to decrease with respect to the (200) peak as a result of irradiation. No graphite phase was observed in the irradiated pattern. The growth in intensity of three diffraction peaks attributable to Zirconia as compared to the corresponding peaks in the pristine pattern. These were located at approximately 13.4 ° and 21.0 ° 2θ. The growth of diffraction peaks associated with one or more unknown phases was also seen in the irradiated sample at approximately 10.5 °, 17.6 ° and 21.0 ° (2θ).

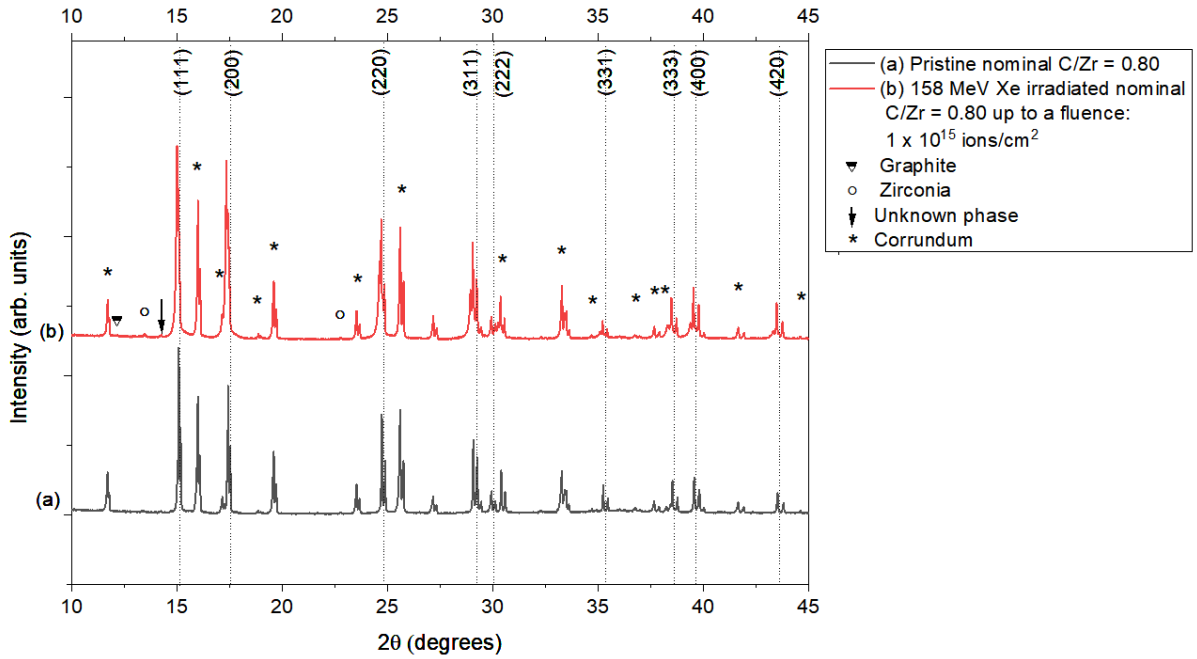

Figure 77 Vertically offset XRD patterns of pristine (a) ZrC of nominal C/Zr = 0.80 sintered at 2000°C (b) and irradiated with 158 MeV Xe to a fluence of (1 x 10^{15} ions/cm^2) at room temperature

Figure 77 shows that the irradiated nominal C/Zr = 0.80 sample maintained its cubic NaCl structure after irradiation. Two weak diffraction peaks belonging to zirconia located at approximately 13.5 ° and 22.8 ° (2θ) were observed to grow in intensity after irradiation. A broadening of the peak width was also observed for the irradiated ZrC samples. A weak diffraction peak belonging to an unknown phase was also seen to grow with irradiation located

at approximately 14.3 ° (2θ). Similar to results from previous samples, no evidence of diffraction peaks associated with graphite were observed.

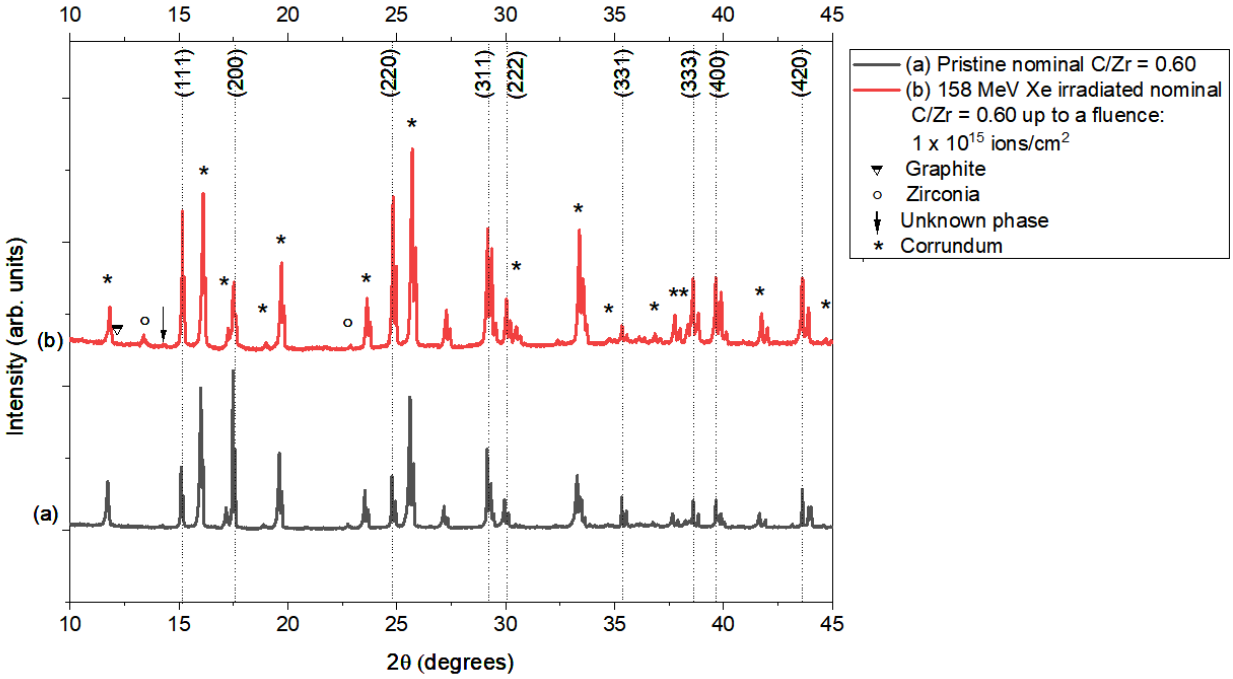

Figure 78 Vertically offset XRD patterns of pristine (a) ZrC of nominal C/Zr = 0.60 sintered at 2000 ° (b) and irradiated with 158 MeV Xe to a fluence of (1 x 10^{15} ions/cm^2) at room temperature

The diffraction pattern of the nominal C/Zr =0.60 sample (Figure 78) showed that this sample also maintained its cubic structure post-irradiation. However, a shift to lower 2θ was observed for diffraction peaks in the irradiated sample. Several diffraction peaks belonging to the zirconia were seen to grow in intensity with irradiation, but still maintained a very weak peak intensity located at approximately 13° and 22.9° (2θ). As with the previous samples, a weak unknown peak was seen to be present in the pristine and irradiated sample located at approximately 14.3° (2θ). As with all other samples, diffraction peaks belonging to graphite were not observed.

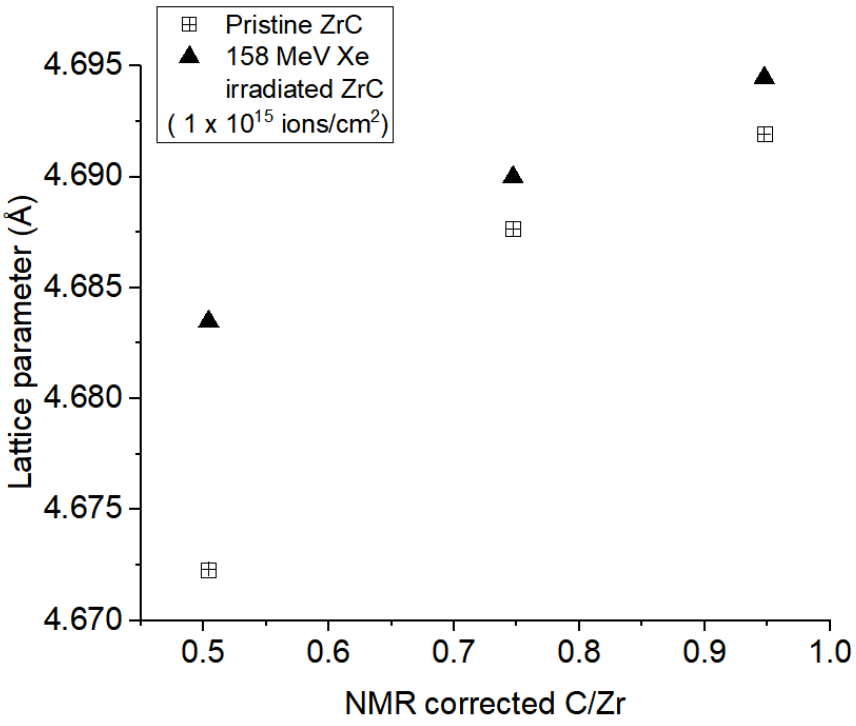

*Figure 79 Pristine and 158 MeV Xe (*1 x 10^{15} ions/cm^2*) irradiated lattice parameters for samples sintered at* 2000 °C *plotted with respect to the NMR corrected C/Zr.*

Figure 79 shows the lattice parameter of the 158 MeV Xe irradiated to *a* fluence 1 x 10^{15} ions/cm^2 at room temperature and pristine ZrC samples plotted with respect to the NMR corrected C/Zr for samples sintered at 2000°C, as determined from Rietveld refinement.

The lattice parameter of Xe-irradiated ZrC was seen to increase for all samples except for the nominal C/Zr = 1.00 sample. The irradiated lattice parameters showed the same general trend of increasing lattice parameter with carbon content. All Xe irradiated lattice parameter values were seen to increase from their pristine values. The nominal C/Zr = 0.60 sample showed the largest increase in lattice parameter after irradiation, increasing from 4.672 ± 0.001 to 4.683 ± 0.001 Å. Furthermore, the nominal C/Zr = 0.80 sample showed the smallest increase in the lattice parameter post-irradiation, increasing from 4.688 ± 0.001 to 4.689 ± 0.001 Å. Finally,

the lattice parameter of the nominal C/Zr = 1.00 sample expanded from 4.692 ± 0.001 to 4.694 ± 0.001 Å.

The GOF values from the Rietveld refinement were observed to be 5.33, 3.84, and 4.19 for samples of nominal C/Zr = 1.00, 0.80 and 0.60. The variation in the GOF was determined to be a combination of the marginal offset between the corundum standard and the sample tiles and the growth of the unknown phases, which made fitting difficult. As the difference in the offset was assumed to be zero, the peak centring (essential for the accuracy of lattice parameter determination) was checked carefully by visual inspection of the residual spectrum.

3.4.2.2 **SEM**

The following subsection presents the results of SEM microscopy on the irradiated samples. The SEM images of the irradiated nominal C/Zr = 0.60, 0.80 and 1.00 samples are presented in Figure 80, Figure 81 and Figure 82, respectively. The micrographs belonging to pristine samples and irradiated samples are at the top and bottom with four images, respectively. The BSE and SE images of each set (left and right) were both taken at 1000X and 2833X magnification (top and bottom).

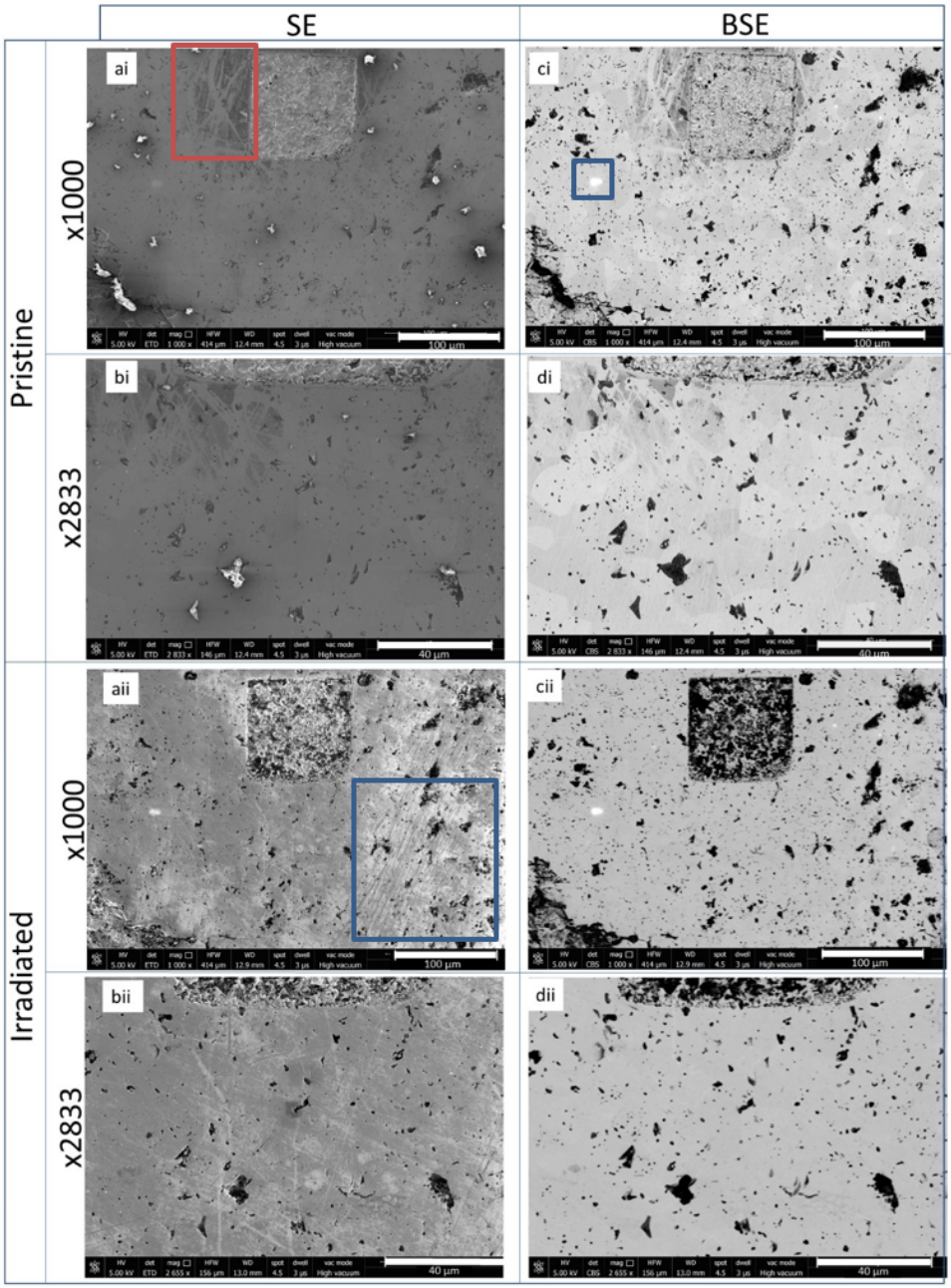

Figure 80 BSE and SE images of nominal C/Zr = 1.00 sintered at 2000°C pristine and 158 MeV Xe irradiated ZrC samples up to a fluence of 1.00 x 10^{15} ions/cm^2. Samples are classified as per the dividers specified in the table above. Images that are labelled with a letter followed by a i and ii (e.g. ai and aii) denote images that have been taken in the same area before and after irradiation. SE and BSE images are displayed in the left- and right-hand columns respectively – labels starting with a and b denote SE images whilst labels starting with c and d denote BSE. Image labels starting with the letters 'a' 'c' are images that have been taken at 1000X magnification and those starting with labels starting with 'b' or 'd' are taken at 2833X magnification.

The irradiated nominal C/Zr = 1.00 (Figure 80) showed a noticeable (~µm) exfoliation of the surface structure in the irradiated sample as compared to the pristine sample. This is illustrated by the dark patches surrounding the square reference markers (highlighted in the red box in Figure 80 ai) where the laser used to mark reference points ablated the surface of the sample when rastering. In the irradiated sample, these marks are not present, which signals the removal of material from the surface. The SE images of the irradiated sample, highlighted by the blue box in Figure 80 aii, also shows a change in the surface roughness due to irradiation, reflected by the significant change in contrast. The grain structure appeared less evident in the irradiated BSE images than in the pristine BSE images. However, such an effect may be intensified by contrast differences between the two images.

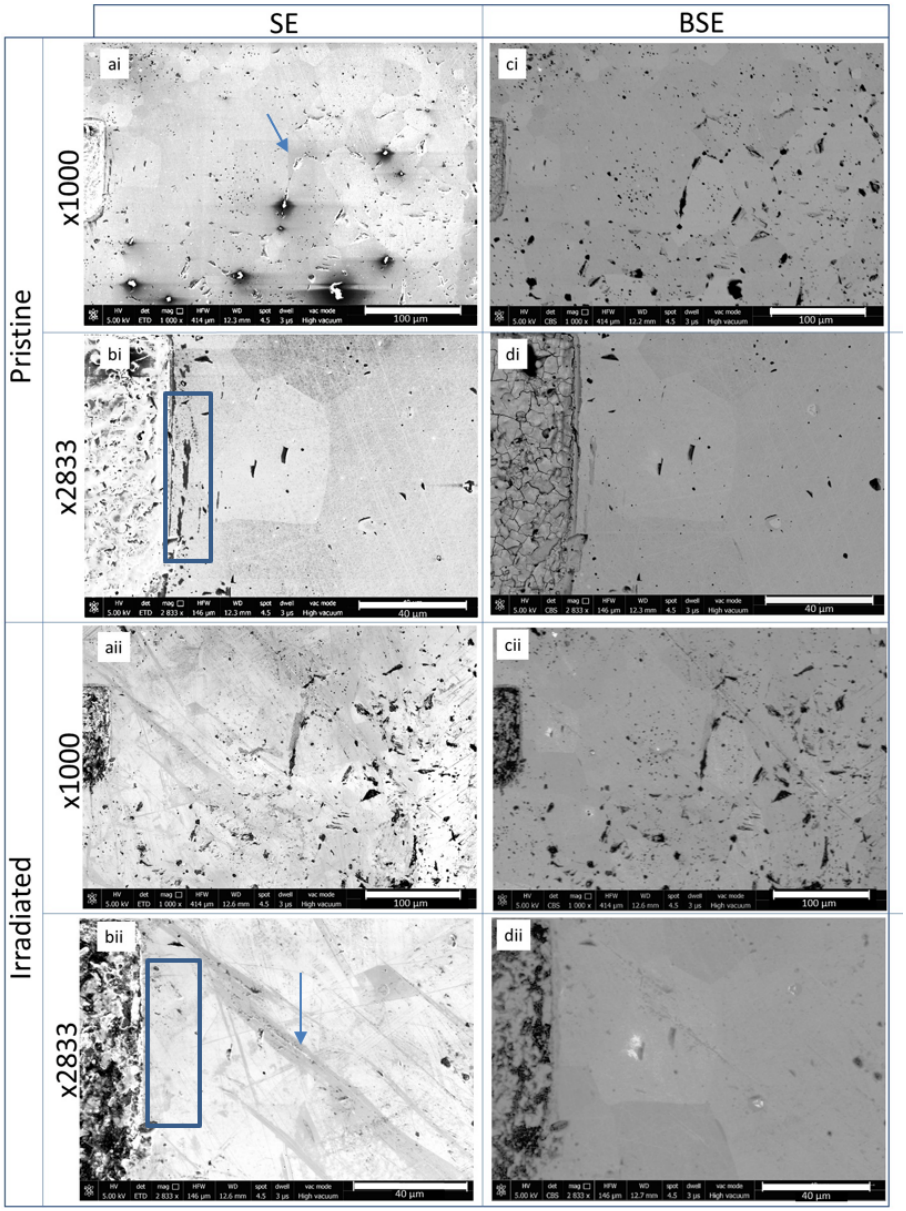

Figure 81. *BSE and SE images of nominal C/Zr = 0.80 sintered at 2000°C pristine and 158 MeV Xe irradiated ZrC samples up to a fluence of 1 x 10^{15} ions/cm^2. Samples are classified as per the dividers specified in the table above. Images that are labelled with a letter followed by a i and ii (e.g. ai and aii) denote images that have been taken in the same area before and after irradiation. SE and BSE images are displayed in the left- and right-hand columns respectively – labels starting with a and b denote SE images whilst labels starting with c and d denote BSE images. Image labels starting with the letters 'a' 'c' are images that have been taken at 1000X magnification and those starting with labels starting with 'b' or 'd' are taken at 2833X magnification.*

To compare the pre- and post-irradiation images, the histograms of all SE and BSE images were matched to ensure brightness was consistent across all images using the Image J software. The reference histograms used were Figure 81 aii for the SE images and Figure 81 di for the BSE images. A ~μm-scale exfoliation of the surface was observed, as evidenced by the disappearance of the burnt surface marks (highlighted in the blue box in Figure 81 bi) left by laser ablating square marker points. The pristine samples SE images show less pronounced intergranular (blue arrow in Figure 81 ai) depressions as compared to the irradiated sample. Whilst the observed increase in the darkness of these structures implies that their depth increases with irradiation, this could also be due to changes in contrast that histogram matching cannot account for. Although samples were cleaned after irradiation, dark streaks are seen in the surface sample. In addition, large streaks are seen in Figure 81 bii (blue arrow), which have contrast that would be expected to be seen in a depression from the bulk surface height. The BSE images do not show any phase separation – however, on equalising the histograms, an increase in the number of bright spots is observed, which is an artefact of image manipulation. A small bright spot ~1 μm in diameter (arrow Figure 81 ci) was seen in both the SE and BSE images before histogram matching. Since this is seen in SE images, it is likely that this a raised feature and not an extra phase.

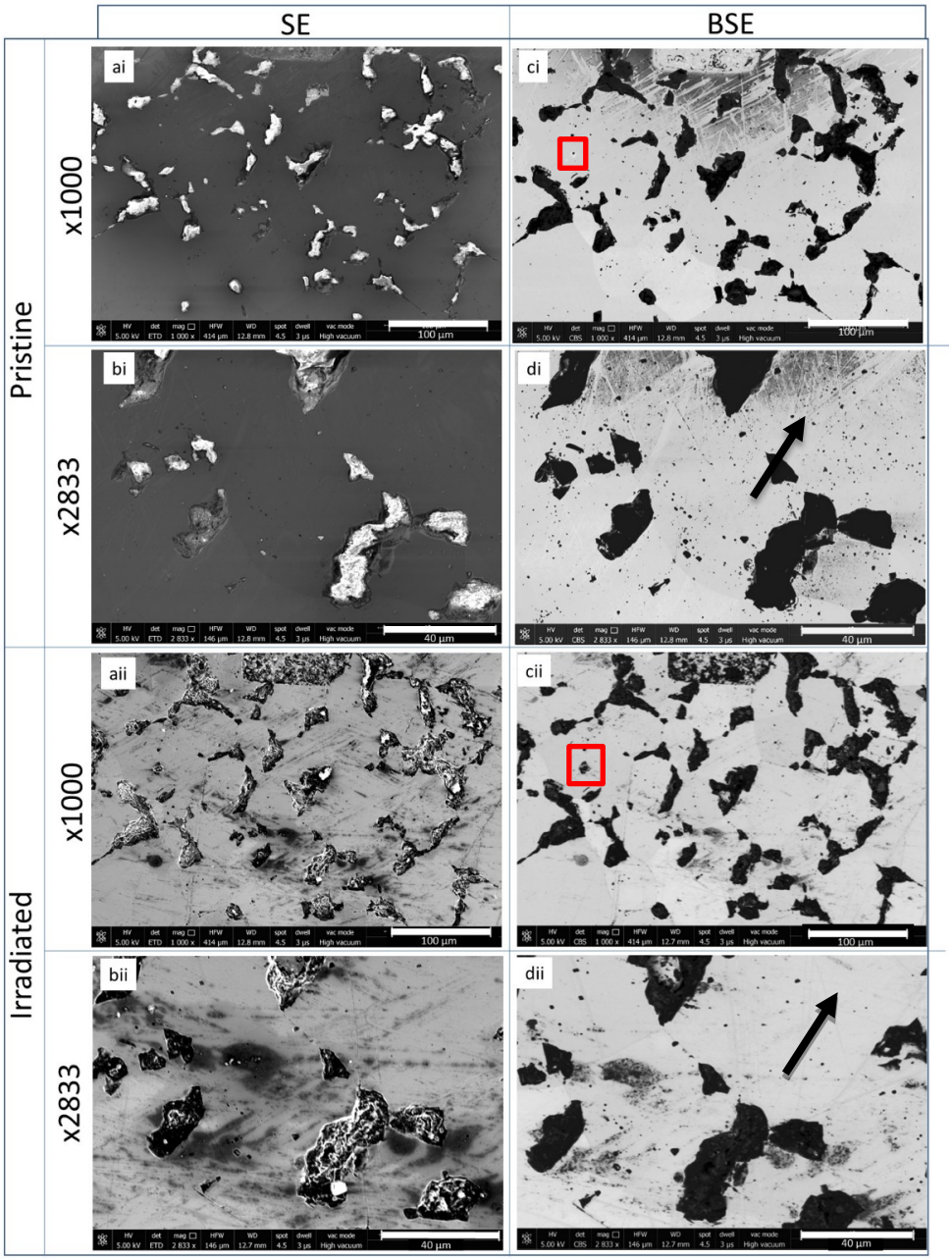

Figure 82. BSE and SE images of nominal C/Zr = 0.60 sintered at 2000°C pristine and 158 MeV Xe irradiated ZrC samples up to a fluence of 1.00 x 10^{15} ions/cm^2. Samples are classified as per the dividers specified in the table above. Images that are labelled with a letter followed by an 'i' and 'ii' (e.g. ai and aii) denote images that have been taken in the same area before and after irradiation. SE and BSE images are displayed in the left- and right-hand columns respectively – labels starting with 'a' and 'b' denote SE images whilst labels starting with 'c' and 'd' denote BSE images. Image labels starting with the letters 'a' 'c' are images that have been taken at 1000X magnification and those starting with labels starting with 'b' or 'd' are taken at 2833X magnification.

BSE images histograms were matched using Figure 82 cii as a reference histogram for easier comparison of features. The SE images were left in their original histograms, as histogram matching did not add any additional information or enhance any features of interest. The SE images of the irradiated nominal C/Zr = 0.60 (Figure 82) show a similar surface microstructure as was seen in the pristine samples. As with the nominal C/Zr = 1.00 sample, the ablation marks cause by the laser were not present in the irradiated sample (seen by comparing Figure 82 di and dii black arrows). Several features are seen to develop with irradiation – for example the small circular feature in the red box Figure 82 ci developed in size significantly after irradiation (red box- Figure 82 cii). Post-irradiation black features were seen on the sample surface that can be seen in both SE and BSE images. BSE images showed no phase separation due to the irradiation.

EBSD analysis was undertaken on the irradiated solid samples to determine the grain size post-irradiation. As with the pristine samples in Chapter 2, the average grain sizes of the irradiated samples were analysed using the MTEX package.

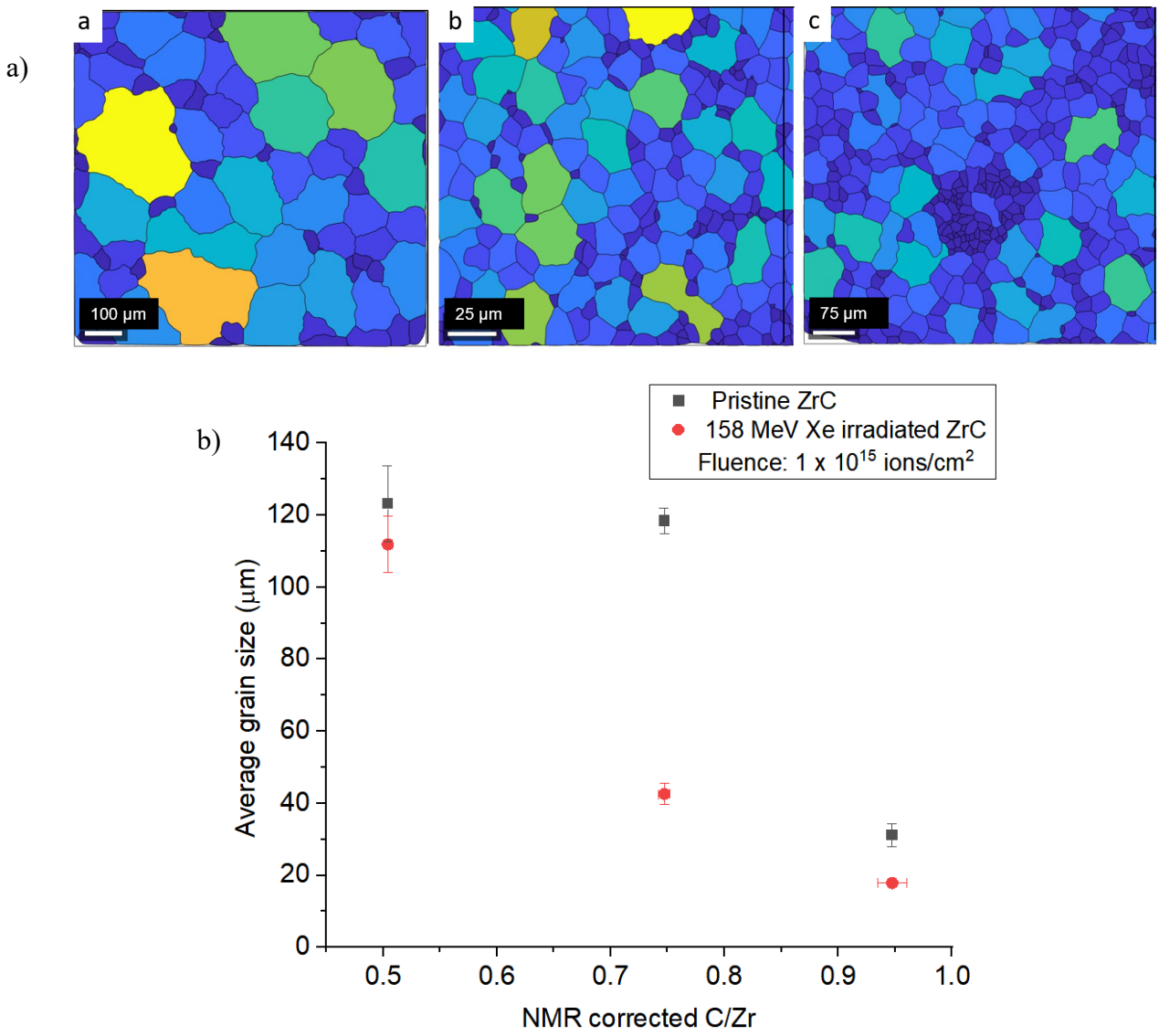

Figure 83. Average pristine grain size of pristine ZrC samples and average grain size of 158 MeV Xe irradiated samples to a fluence of 1 x 10^{15} ions/cm^2 plotted with respect to the NMR corrected C/Zr (b).

The results of the grains traced in EBSD analysis are presented in Figure 83.(a). Figure 83.(b) shows a graphical representation of the grain sizes. Errors on the grain size are plotted to two standard deviations, 95% of the data range. The average grain size of the nominal C/Zr = 1.00 and 0.80 Xe irradiated samples was seen to shrink as compared to the pristine values, and a trend of decreasing grain size with increasing carbon content, whilst the nominal C/Zr = 0.60 irradiated value was observed to be within two standard deviations of its original value.

The irradiated nominal C/Zr = 0.60 sample showed from 123 ± 10 to 111 ± 8 µm. The largest decrease in grain size was seen in the C/Zr = 0.8 0 sample, which decreased from 118 ± 4 to 42 ± 3 µm. The smallest decrease was observed in the nominal C/Zr = 1.00 sample that was seen to decrease from 31 ± 3 to 17 ± 1 µm.

3.4.2.3 Raman spectroscopy

This sub-section presents the results from the Raman spectroscopy investigation on Xe irradiated ZrC.

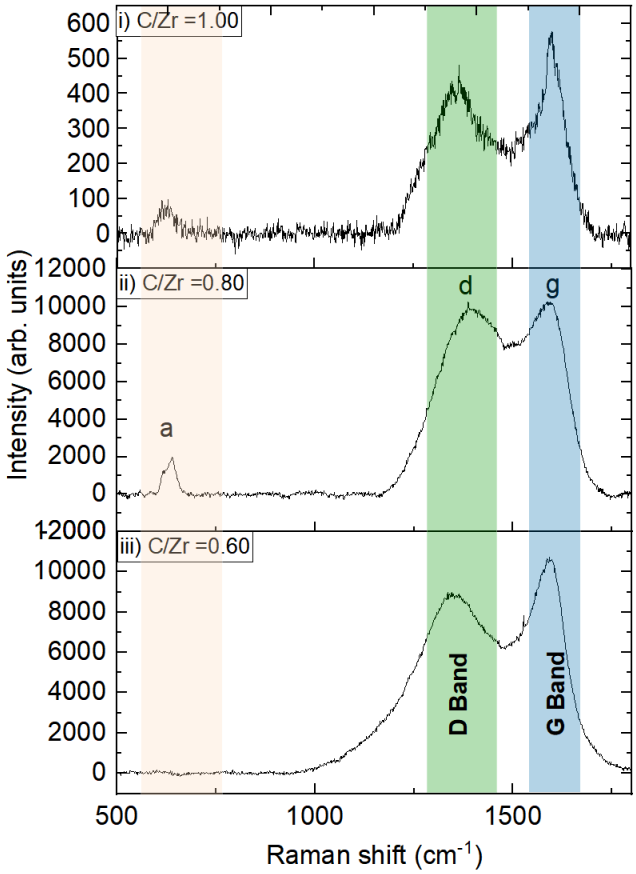

Figure 84. Raman spectra for nominal C/Zr = (i) 1.00 , (ii) 0.80 and (iii) 0.60 158 MeV Xe irradiated samples to a fluence of 1 x 10^{15} ions/cm^2. Raman spectra were baseline corrected using a user defined baseline.

Figure 84. shows the baseline-corrected Raman spectra of the 158 MeV Xe irradiated (1 x 10^{15} ions/cm^2) samples of nominal C/Zr =1.00, 0.80 and 0.60 sintered at 2000°C labelled (i), (ii)

and (iii) respectively. The three observed Raman regions corresponding to the analysis in the pristine chapter are labelled ‘a’, ‘d’ and ‘g’ above spectrum (ii) centred at their respective positions.

All stoichiometries showed the presence of well-defined but adjoined D and G resonances. The signal intensity of the G mode was higher in samples of lower stoichiometry – with the nominal C/Zr = 0.60 being the highest overall signal followed by the C/Zr = 0.80 and finally the C/Zr = 1.00 samples. A similar trend was also observed in the intensity of the D band, with the exception that the irradiated nominal C/Zr = 1.00 sample showed a lower D band intensity than the nominal C/Zr = 0.80 sample.

The D and G bands were fitted using the IGOR pro software. For the irradiated nominal C/Zr = 1.00 sample, a Voigt and a Lorentzian function best captured the profile of the D and G peaks, respectively. An additional component was seen to be present in the residual spectra after the D and G peaks had been fitted, and an additional Gaussian peak was determined to best capture this feature. The Lorentzian fitted to the D peak was centred around 1360 ± 3 cm^{-1} with a FWHM of 171 ± 2 cm^{-1} and a height of 399 ± 2 counts, whilst the Voigt function fitted to the G peak was centred around 1600 cm^{-1}, with a FWHM of 70 cm^{-1} and a height of 565 counts. The additional Gaussian function fitted between the D and G peaks was centred around 1513 ± 3 cm^{-1}, FWHM = 87 ± 1 cm^{-1} and had a height of 153 ± 1 counts.

In the irradiated nominal C/Zr = 0.80 sample, Voigt and Lorentzian function were seen to best capture the main behaviour of the D and G peaks, respectively. As with the nominal C/Zr = 1.00 sample an additional Gaussian function was fitted between the D and G peaks to fully capture the profile of the spectra. The Lorentzian function used to capture the D peak was centred around 1400 ± 2 cm^{-1}, FWHM =221 ± 1 cm^{-1} and height = 10100 ± 1 counts which as an increase in the signal from the nominal C/Zr = 1.00 samples above. The Voigt function capturing the G peak was seen to be centred around 1596 ± 2 cm^{-1}, FWHM = 106 ± 1 cm^{-1} and height = 9239.4 ± 1 counts. The additional Gaussian function between the D and G peaks was

seen to be centred around 1515 ± 2 cm^{-1}, FWHM = 197 ± 1 cm^{-1} and with height = 5577 ± 1 counts.

The irradiated nominal C/Zr = 0.60 sample was observed to have the most distinct D and G peak structure. The D and G peaks were seen to be partially captured by a Lorentzian and Voigt function, respectively. The addition of a Lorentzian peak between the D and G peaks was seen to better capture the overall structure of the D and G spectral range, as was the case with the additional Gaussian peak for the other samples. The intensity of the G peak was seen to be higher than that of the D peak. The main characteristics of the D resonance was seen to be suitably captured by a Lorentzian function that was centred around 1350 ± 2 cm^{-1}, with a FWHM of 230 ± 2 cm^{-1} and height of 8686 ± 1 counts. The G resonance was suitably captured by a Voigt function centred around 1593 ± 4 cm^{-1} with a FWHM of 96 ± 3 cm^{-1} and a height of 10336 ± 1 counts. The additional Lorentzian function which captured the overlapping region was centred around 1513 ± 2 cm^{-1} with a FWHM of 93 ± 4 cm^{-1} with a height of 2436 ± 2 counts.

The a resonance observed in the nominal C/Zr = 1.00 and 0.80 pristine samples changed in structure after irradiation. This resonance was seen to be absent in the irradiated nominal C/Zr = 0.60 sample as with the irradiated sample. The irradiated nominal C/Zr = 1.00 sample was observed to have a broad peak and thus, was fit with a Gaussian function. The fitted Gaussian was centred around the 627 cm^{-1} with FWHM = 57 cm^{-1} with 77 counts. This is a change from two peaks that were fitted to the amorphous structure in the pristine chapter. The nominal C/Zr = 0.80 sample showed evidence of a more intense peak structure located at higher wavenumbers, which was shouldered by a less intense peak at lower wavenumbers. These two peaks were seen to be suitably captured by two Voigt functions centred around 618 ± 2 and 639 ± 1 cm^{-1} with FWHM of 17 ± 3 and 8 ± 4 cm^{-1} and with intensities of 843 ± 3 and 1961 ± 5 counts.

3.4.3 Discussion: Irradiations with 158 MeV Xe to a fluence of 1 x 10^{15} ions/cm^2

SEM micrographs revealed that the dark burn marks surrounding the laser-etched reference points in the pristine samples were absent in the irradiated samples. It is possible that a restructuring of the microstructure could occur during irradiation leading to this observation or that radiation caused the fractional (~μm scale) removal of surface layers. The microstructure of the irradiated samples showed no significant changes in either the BSE or SE images compared to those of the pristine samples. Furthermore, no phase separation was observed in the irradiated BSE imaged microstructures. This suggests that all samples of ZrC produced in this study have good stability under heavy-ion radiation, which is consistent with several previous studies [17], [18], [60], [63].

The average grain size for the nominal C/Zr = 1.00 and 0.80 samples was seen to decrease after irradiation as compared to their pristine values. The nominal C/Zr = 0.60 sample average grain size value was observed to be within the range of its pristine value. The largest grain shrinkage was observed in the C/Zr = 0.80 sample. A potential underlying cause of this apparent grain shrinkage could be due to the polygonization of grains resulting from the accumulation of defects or dislocations, which in turn, may cause grains to divide to produce a lower energy configuration [167], [168] - this would be realised as a decrease in the average grain size.

Microscopy of the black structures in the irradiated sample showed little noticeable difference in their size, as compared to the pristine sample. Raman spectroscopy was used to further probe the compositional changes of the carbon located in the black structures of the irradiated samples, previously identified in the pristine samples. The G band of the irradiated samples with lower carbon content exhibited a higher Raman scattering intensity than the higher carbon content samples that occurs due to the presence of graphite.

A higher D resonance intensity was observed, with respect to the G resonance, in the irradiated C/Zr = 0.80 sample as compared to nominal C/Zr = 0.60 indicating an increase in the proportion

of disordered graphite and a decrease in the graphitisation of the sample, likely due to radiation damage which, as these results indicate, act to disorder graphite. A higher integral intensity of the fitted G resonance, with respect to the D resonance, in the irradiated nominal C/Zr = 1.00 sample indicates a higher degree of graphitisation.

An increase in the relative integral intensity of the D resonance with respect to the G resonance was observed in the irradiated samples for the nominal C/Zr = 0.80 and 0.60 samples as compared to their respective pristine samples. This increase in the D resonance height intensity indicates the clustering of disordered graphite [50]. Pellegrino *et al.* [58] observed an increase in the disordered peak relative to the pristine graphite peak with increasing fluence when irradiating nominally stoichiometric ZrC single crystals with 1.2 MeV Au ions.

The D and G resonances in the nominal C/Zr = 1.00 sample, which were absent the pristine spectra, were observed to be active in the irradiated spectrum. This could be due to carbon migrating through the ZrC unit cell, liberated by irradiation, and being transported to the dark regions.

The amorphisation trajectory [51] [31], [85], based on the location of the G resonance, revealed the sp^2 carbon in all irradiated samples was nanocrystalline; a result that is consistent with the pristine nominal C/Zr = 0.80 and 0.60 samples (G resonance was absent in the nominal C/Zr = 1.00 samples). For the irradiated nominal C/Zr = 1.00, 0.80 and 0.60 samples, the crystallite size was calculated to be approximately 27, 17 and 22 nm respectively using the modified Tuinstra and Koenig relation [50], [138], [139]. This is a decrease from the 33 nm crystallite size observed in the pristine nominal C/Zr = 0.80 and 0.60 samples, hence radiation damage causes a decrease in the sp^2 crystallite size.

A major noticeable difference in the Raman spectra of all irradiated samples, as compared to the pristine nominal C/Zr = 0.80 and 0.60 samples, was a reduction in the ability to resolve the D and G resonance bands. Residual spectra of the fits to the D and G bands revealed an

additional structure in the region between the fitted D and G functions. This required an additional function to be fitted to better capture the overall line shape of the spectra. The peak fitted to this additional resonance was centred around 1513 – 1515 cm^{-1} for all samples. However, the intensity of this fitted function was seen to be the highest in the nominal C/Zr = 0.80 sample, followed by the nominal C/Zr = 1.00 sample and finally, the nominal C/Zr = 0.60 sample. This suggests that a higher degree of disorder was present in all samples after irradiation, which is consistent with Raman investigations by Pellegrino *et al.* [53].

As with the pristine samples, the 'a' band resonance was seen in the irradiated nominal C/Zr = 1.00 and 0.80 samples and absent in the nominal C/Zr = 0.60 samples. In the case of the nominal C/Zr = 1.00 samples, the double resonance structure seen in the pristine sample evolved into a single resonance structure (fitted accordingly with as many peaks). The fitted peak centred around 549 ± 1 and 633 cm^{-1} in the pristine nominal C/Zr = 1.00 sample were seen to disappear in the irradiated sample – leaving one peak centred around 627 cm^{-1}. Comparing this to results from the literature, Pellegrino *et al.* [58] observed two separate optical bands in pristine ZrC located at 530 -540 and 600 cm^{-1}– the lower of the two disappeared with 1.2 MeV Au irradiations at a fluence of 2 x 10^{13} ions/cm^2. In the pristine samples, these appeared to be well separated, but the peaks seemed to overlap with increasing irradiation dose. Again, these well-separated bands were also observed by Florez *et al.* [54] and were determined to be located at ~515 and 600 cm^{-1} in the pristine samples. Upon irradiation, with 10 MeV Au ions to a fluence of 1 x 10^{15} ions/cm^2, the well-separated peak structure was maintained and both peaks were present in the irradiated spectrum. These well-separated peak structures observed in the studies above are not entirely congruent with the peak structures in this study.

The pristine nominal 0.80 sample showed a very broad structure and was hence fitted with two bands centred around ~574 and 693 cm^{-1}. The broadness and lack of structure in the resonance hints that this could be amorphous carbon [92], however, was unclear. Upon irradiation, these fitted peaks were seen to peak centred around approximately ~618 and 639 cm^{-1}. It is also a possibility that this change in the peaks could be the zirconium oxide as seen by Moya *et al.*,

who investigated the zirconium oxide thin films and found two peaks located at approximately 638 and 616 cm^{-1} which were attributed to the presence of zirconium oxide [169]. Bellucci *et al.* found a similar result when investigating the oxidation of ZrC single crystals and they attributed the peaks observed to monoclinic zirconia [170]. This was also observed by Pezzotti *et al.* who identified this structure to be partially transformed monoclinic and tetragonal zirconia [171]. This result agrees with the XRD patterns collected in this study which shows evidence of zirconia peaks, although it is not clear why these peaks are not seen in all Raman spectra – this may be due to inhomogeneity in each sample. The weak diffraction peaks belonging to zirconia already present in the pristine samples were seen to apparently increase in intensity with irradiation.

As the penetration depth of Xe ions was ~10 um, XRD was used instead of GIXRD, which has been the de-facto technique previously due to lower heavy-ion irradiation energies and thus smaller penetration depths [22], [54], [55] of the relatively higher energy of Xe ions used in this study. As with the pristine samples, graphite diffraction peaks were absent in the post-irradiation spectra. The absence of the graphite phase implies that the damage induced by heavy-ion irradiation did not affect the distribution of graphite or increase the coherency of scattering domains sufficiently to produce an XRD response.

A likely mechanism for the apparent increase in the zirconia phase could be the Xe atoms producing vacancies. As free oxygen exists in any given sample, the presence of vacancies would promote the diffusion of oxygen already present in the sample into the octahedral interstitial sites [150], [151], [172]. This seems likely as weak diffraction zirconia peaks are seen in the pristine as-fabricated sample diffractograms. Oxygen contamination may also occur when the sample is taken out o vacuum from the accelerator; vacant sites may have a greater affinity to oxygen gettering from ambient conditions. Samples of lower carbon content were seen to have lower intensity zirconia diffraction peaks, with respect to the ZrC peaks, as compared to higher carbon content samples. One may expect that samples with lower carbon

content would display more intense zirconia diffraction peaks, with respect to the ZrC diffraction peaks after irradiation, as there are more vacant sites for oxygen to occupy.

The cubic structure of ZrC appears to be maintained post-irradiation. Furthermore, in lower stoichiometry samples, vacated carbon atoms would have a range of sites that they could recombine with if liberated – which could explain why the sample maintains its crystal structure for low carbon contents and under irradiation. In the C/Zr = 1.00 samples, two additional diffraction peaks belonging to unknown phases that were present in the pristine spectrum were seen to grow in intensity in the irradiated spectrum. It was not possible with certainty to assign these diffraction peaks to any phase in the crystallographic database.

The Xe irradiation shows that the irradiated lattice parameters follow an increasing trend with a carbon content that is consistent with the linear trend in the lattice parameter reported in the literature [13], [18]. The nominal C/Zr = 1.00 (NMR corrected C/Zr = 0.95) sample reported from this chapter was observed to have a lattice parameter value (4.694 ± 0.001 Å) lower than that reported by Florez *et al.* (C/Zr = 0.99) (4.71 Å) for samples irradiated to similar doses of 2.4 and 2.5 dpa respectively [54].

The expansion in the lattice parameter has also been observed in previous ion irradiation studies on ZrC [55], [62]. The presence of vacancies was determined, by Mellan *et al.* [149] via DFT calculations, to occupy a larger volume than the stoichiometric ZrC. Thus, the increase in the lattice parameter observed in the irradiated samples, it shows that vacancies are being created in the sample during irradiation. In addition, the dpa used in this study is higher than that used by Gosset *et al.* (1.5 dpa) above, which defects were observed to coalesce based on TEM observations by Gosset *et al.* [55].

As the heavy Xe ions bombard the sample, the target material undergoes local heating due to the kinetic energy imparted from the Xe ion to the sample. The irradiation took 4 weeks to complete this radiation-induced heating and can be likened to a long term local annealing of

the target material [64]. Enhanced mobility under irradiation-induced heating is likely to contribute to enhanced recovery of defects.

The presence of free carbon (as determined from Raman spectroscopy) is problematic in nuclear environments as they can combine to produce several detrimental products. For example: carbon monoxide or carbon dioxide [173] can deposit on fuel surfaces, causing a significant reduction in heat capacity [174] and thus, localised elevation of fuel temperatures.

3.4.4 Conclusion: Irradiations with 158 MeV Xe to a fluence of 1 x 10^{15} ions/cm^2

In this section, samples of variable stoichiometry fabricated have been irradiated with 158 MeV Xe ions to a fluence of 1 x 10^{15} ions/cm^2 to simulate heavy-ion damage in ZrC.

No significant changes in the irradiated microstructure were observed in the samples after irradiation. A combination of SE and BSE microscopy revealed a slight coarsening of the irradiated microstructure for each of the samples – with no phase separation being observed. The average grain size of the irradiated samples was seen to decrease from their pristine values for all samples except for the nominal C/Zr = 1.00 samples that were in range of the pristine value. Raman investigations into the black structures, where previous analysis had revealed carbon, again showed evidence of graphite, disordered graphite, and amorphous carbon in the majority of the pristine samples. Radiation damage was seen to cause changes in the relative proportions of graphite and disordered graphite in the nominal C/Zr = 0.80 and 0.60 samples and activate the D and G resonance in the nominal C/Zr = 1.00 that were absent in the pristine sample. The sp^2 crystallite size was observed to decrease from ~ 33 nm for the pristine nominal C/Zr = 0.80 and 0.60 samples to ~27, 17 and 22 nm for the irradiated nominal C/Zr = 1.00, 0.80 and 0.60 samples, respectively.

XRD patterns showed that the irradiated ZrC samples with varying carbon contents retained their NaCl structure after irradiation. XRD patterns also showed diffraction peaks belonging to

zirconia and a secondary unknown phase. The lattice parameters of the irradiated samples were seen to be higher than the pristine samples with the overall trend being congruent with the linear trend of lattice parameter observed in the literature.

3.5 Discussion of Proton and Xe irradiated samples

The results from this chapter and the combination of techniques used provide information about the effect that a range of damage doses has on ZrC. For the first time, a range of sub-stoichiometric ZrC samples from the same precursor powders have been irradiated and characterised for a range of damage doses.

If we begin with the lowest dose, dose 1 (0.015 dpa) proton irradiations resulted in a decrease in the lattice parameter for all three compositions compared with their pristine values. A simplistic assumption, when applied to 'standard materials' with very low levels of vacancies, would be that irradiation would lead to the creation of vacancies, some macroscopic swelling and an increase in lattice parameter. The results presented in this chapter are counter to this standard situation. As the proton irradiations were carried out at 300˚C, the idea was proposed that this level of damage causes the initial defects that may be present in the pristine samples from sample preparation to be redistributed, thus the material is effectively annealed by the introduction of additional energy to the system. The presence of oxygen has been observed to lower the lattice parameter of ZrC [64], if free oxygen is present in the sample, annealing of the sample for the period of the irradiation may cause oxygen to diffuse into vacant sites on the carbon sub-lattice resulting in a decrease in the lattice parameter from its pristine value. In addition to this, radiation damage causes the inevitable production of additional vacant carbon sites [35], [66], [67], [175] which have been observed to increase the lattice parameter [149]. From the above, it is evident that the low dose proton irradiation does not act to cause detrimental damage and that a significant amount of vacancies are not created.

Increasing the irradiation proton dose from 0.015 dpa to 0.031 dpa increased the lattice parameter from the lower dose values. The lattice parameter values of the dose 2 proton irradiated samples also remained below their pristine values, with the exception of the nominal C/Zr = 0.80 sample which was observed to be higher than its pristine value. To explain this, it was proposed that the limited swelling observed in the nominal C/Zr = 0.6 and 1.00 samples was due to a relationship of the concentration of vacant sites, the width of the grain boundaries

and the average grain size that act to limit the lattice parameter expansion by providing sinks for radiation damage. This is explained as follows. The nominal C/Zr = 0.60 was observed to have a large grain size and large grain boundaries (inter-/intra-granular black structures evident from SEM) thus it was proposed that carbon atoms that have vacated their lattice sites via irradiation can sink, or be annihilated, into a number of vacant sites in the carbon sub-lattice or migrate to the large grain boundaries. In the nominal C/Zr = 1.00 samples, carbon atoms that are vacated from their lattice sites via irradiation have fewer vacant sites on the carbon sublattice for damage to sink into; however, they have a smaller grain size and thus less distance to travel to the grain boundaries than the nominal C/Zr = 0.60 samples. Due to these defect sinking mechanisms, it was proposed that both materials can accommodate vacancies at low dpa, limiting the lattice parameter increase and thus, have similar defect sink efficiencies. The nominal C/Zr = 0.80 however has an intermediate-range grain size, a smaller number of vacancies on the carbon sub-lattice and a larger grain size than the nominal C/Zr = 1.00 samples, which means that defects have a longer distance to travel to be sunk at grain boundaries.

At significantly higher damage doses of 2.4 dpa (Xe) a greater swelling of the lattice parameter was observed compared to the pristine material and the proton irradiated material at all three compositions. This result is to be expected as increasing radiation damage is known to induce swelling in materials. Comparing the nominal C/Zr = 1.00 sample lattice expansion (0.03%) to that reported in the literature for 2.5 dpa (0.44%) and similar irradiation temperatures (C/Zr = 0.99 ,10 MeV Au) [54].

Huang *et al.* and Motta *et al.* [35], [43] showed that black dot damage (proton irradiated) was observed to first occur at 0.3 dpa. However, results from this chapter show that vacancy production initiates at 0.015 dpa.^{13}C NMR studies of the irradiated nominal C/Zr = 1.00 sample showed that an increase in the number of vacancies was produced with increasing proton radiation dose for the nominal C/Zr = 1.00 sample. This was determined by the shift of the main peak to higher ppm with increasing dose and is consistent with the evolution of the ^{13}C

NMR line shape to higher ppm seen in the pristine samples, as the carbon content was decreased. If it were possible to study the effects of Xe irradiation (using higher irradiation energies to produce a great quantity of material to fill an NMR rotor), one would expect the ^{13}C NMR signal observed to be at a higher ppm than seen in the proton irradiations, consistent with the irradiated material containing an increased number of vacancies.

It is important to note that the intensity of pristine Raman spectra cannot be compared to that of the spectra of irradiated ZrC as the laser was replaced in the period before the irradiated spectra were analysed. However, the structure and the general peak form can be compared to one another. Raman spectroscopy undertaken on the inter-and intra-granular black structures showed the presence of pristine and disordered graphite through the presence of the G and D peaks, respectively. All samples aside from the nominal C/Zr = 1.00 pristine and dose 1 samples showed evidence of D and G peaks in Raman spectra and typically the intensity (height) of the D peak remains smaller than that of the G peak aside from the dose 1 nominal C/Zr = 0.80 sample. The lack of signal in the D and G band of the pristine and proton dose 1 nominal C/Zr = 1.00 sample indicates that there is no Raman signal detectable carbon in the black structures. For the nominal C/Zr = 0.60 and 0.80, the intensity of the D and G peaks signals increase with increasing irradiation doses, with the Xe irradiated samples showing the largest D and G intensities. As ^{13}C NMR studies showed vacant sites occur through increasing radiation dose, through the movement of the main ZrC peak to lower ppm, the increase in Raman signal with increasing irradiation dose implies that carbon atoms that are dislocated from their lattice sites sink into grain boundaries. As graphite was observed in the static ^{13}C NMR spectra, it is possible that this graphite is responsible for the G band signal we see in the black structures and that carbon atoms dislocated from the ZrC lattice migrate towards grain boundaries with increasing radiation dose. If this is the case, then the origin of the disordered graphite band D may then be the carbon atoms that have been liberated from their lattice sites as a result of irradiations. It was proposed that, as both the vacant sites and the grain boundaries act as sinks for damage within the sample, the sink efficiency for damage in the sample to a first approximation is a function of the volume of the grain boundaries, the size of the grains

and the number of vacant sites. The fact that carbon atoms can move out of the ZrC structure during irradiation toward the grain boundaries, as observed in the Raman spectra, may bolster the radiation tolerance of ZrC.

Chapter 4 Future materials a preliminary investigation into carbide MAX Phases

The following section describes a preliminary investigation into Nb_4AlC_3, a layered carbide MAX phase that has been shown to exist while containing a large fraction of vacancies similar to ZrC.

4.1 Introduction

MAX phase ceramics are layered, machinable, hexagonal materials that are under consideration for Generation IV reactor component materials [7], [19], [176], [177]. The interest lies in the fact that these phases possess a desirable combination of ceramic and metallic properties. Stoichiometrically, the MAX phases have the following form: $M_{n+1}AX_n$ - where 'M' is an early transition metal, 'A' is an A = group element, X is either carbon or nitrogen and n = 1,2 or 3 [7], [11]. Alloying an 'A' group element with an appropriate MX binary system produces a ternary MAX phase compound that can provide enhanced materials properties, which have been reported previously in great detail [7], [10], [11], [19], [178]–[180] through a combination of theoretical and experimental work. Most promisingly, the metallic and ceramic properties of MAX phases coupled with the wide stoichiometric, and elemental range can produce materials that are suitable for a diverse range of nuclear applications.

^{13}C NMR is a powerful tool for understanding the carbon atom distribution in a material. So far, this technique has not been applied to Nb_4AlC_3 to probe the local structure and may provide more insight into the distribution of environments that may exist within the sample.

The objectives of this section are the following. To determine if Nb_4AlC_3 has been successfully produced, to determine if the Nb_4AlC_3 contains ordered or disordered carbon vacancies (o-Nb_4AlC_3 or α- Nb_4AlC_3), to probe the local structure and investigate the range of unique carbon

environments present in the sample and relate that back to the distribution of carbon vacancies and finally to investigate potential ordering schemes of the carbon atoms.

To achieve the above objectives XRD is used to differentiate between the different phases and determine which one is produced in this study. NMR is used to investigate the distribution of carbon vacancies in the sample. EDS is undertaken on the samples to determine if any phase separation exists.

4.1.1 Nb_4AlC_3 sample fabrication

The Nb_4AlC_3 samples were supplied by Jef Veugel's group at the Katholieke Universiteit Leuven (KU Leuven) as part of the collaboration within the CAFFE consortium. The fabrication method is summarised below [11]. Precursor powders of $NbH_{0.89}$, Al and C were used to fabricate the MAX phase. Hydrogenation of the $NbH_{0.89}$ was completed at a temperature of 800℃ (under a dynamic H_2 atmosphere) with the product subsequently ball milled for 2 hours at 200 rpm at room temperature. An additional amount of C and Al were added when preparing the Nb_4AlC_3. In order to produce a homogeneous mixture/ powder consistency, the precursor powders were milled in ethanol with ZrO_2 milling balls multi-directionally for a period of 24 hours. Post-milling, the powders were compacted into graphite dies as described above for the ZrC. The powders were then reactively hot-pressed under vacuum conditions with a heating ramp rate of 20˚C/min under 5 MPa until the temperature of 1700˚C was reached (sintering temperature). At 1700˚C the pressure was increased to 20 MPa, and these conditions were maintained for 30 minutes. After which the heaters were turned off and the samples were allowed to cool. As with the ZrC, the bonded carbon layer from the fabrication process was removed. Optically, the difference between the back-carbon layer and the metallic MAX phase was discernible. Samples were polished to a mirror finish using the same steps as the ZrC samples, as detailed in the Methods section.

4.1 Results

4.1.1 XRD

The following section presents the results of the XRD diffraction experiments undertaken on the solid MAX phase samples provided by KU Leuven.

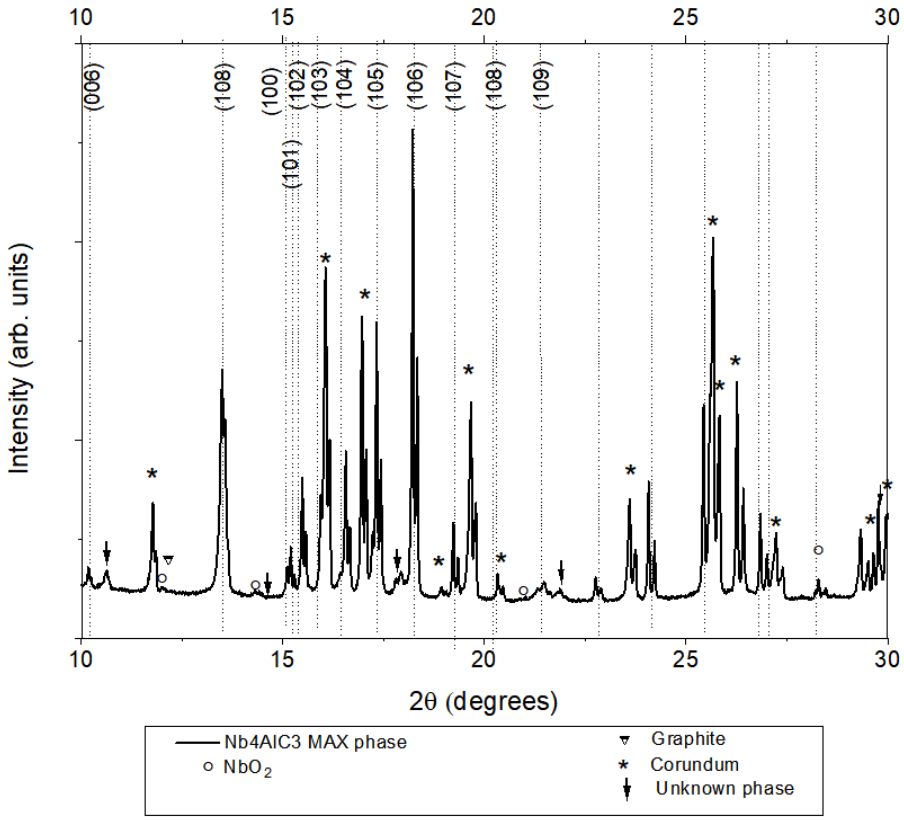

Figure 83 XRD diffraction pattern of solid Nb_4AlC_3 MAX phase (indexed) samples, corundum standard peaks are denoted by an asterisk above the respective peaks. NbO_2 is denoted by an open marker above the respective diffraction peak.

Figure 83Figure 52 shows the observed diffraction pattern of the Nb_4AlC_3 hexagonal MAX phase. The XRD pattern was analysed the using Rietveld structural refinement method, and the peaks were indexed using the phase search in the ICSD, as detailed in the methods chapter. The indexed peaks matched the Nb_4AlC_3 phase, confirming that the phase had been

successfully fabricated. The lattice parameters of the Nb_4AlC_3 phase were determined to be a = 3.134 ± 0.001 Å and c = 24.162 ± 0.001 Å with the goodness of fit = 4.886. In addition to this phase, weak peaks belonging to NbO_2 were also observed in the diffraction pattern. Finally, several diffraction peaks were present in the sample that were not possible to index. No graphite was observed in the XRD patterns.

4.1.2 NMR

^{13}C NMR was used to probe the local structure of the Nb_4AlC_3 material produced. Both static and spinning NMR was conducted on the samples at room temperature.

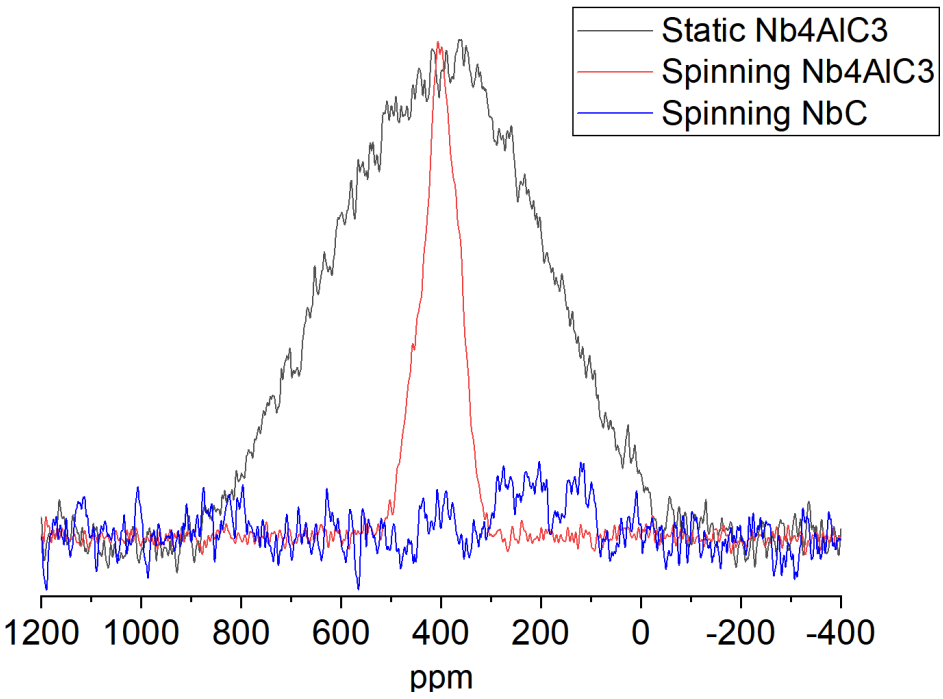

Figure 84 Overlain NMR spectra for the static and spinning NMR of Nb_4AlC_3.

Figure 84 shows the static (black trace), the fast MAS spectrum (red) ^{13}C NMR spectrum of the Nb_4AlC_3 sample and the NbC binary carbide powder spectrum. The static line profile of the Nb_4AlC_3 sample showed a broad NMR peak which significantly narrowed when the samples were spun. From visual inspection, the centre of gravity of the spinning spectrum is observed to be at a higher frequency (ppm) than the static spectrum. The centre of gravity of

the static and spinning spectra was measured to be 394 ± 5 ppm and 404 ± 2 ppm, respectively. This could be due to heating effects that occur during spinning that could act to shift the centre of gravity of the peak, as has been observed on annealed samples of uranium carbide [181]. A clear asymmetry is present in the peak structure of the spinning spectrum; Figure 85 shows the expanded range (0 to 800 ppm) of the spinning spectrum.

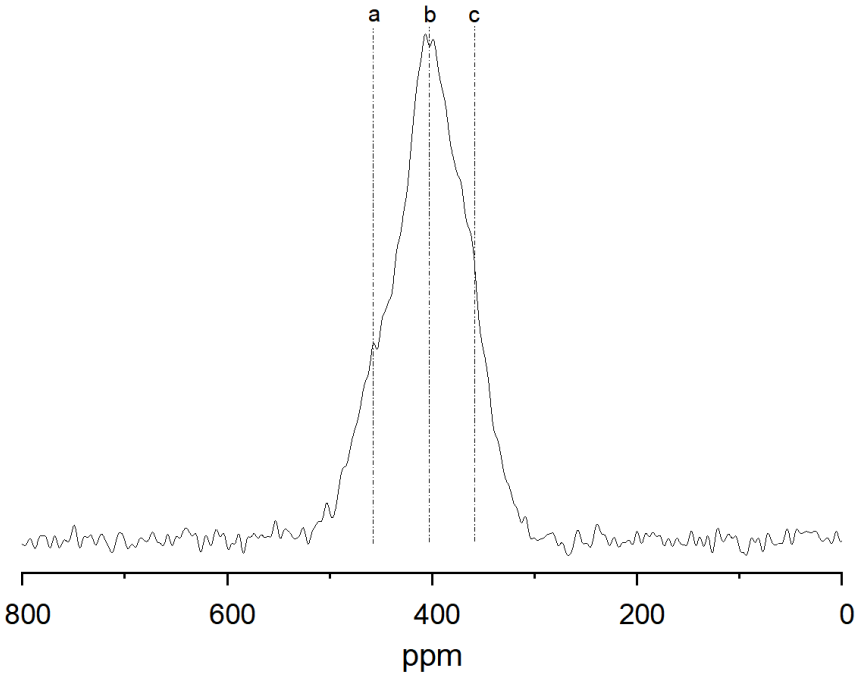

Figure 85. MAS NMR spectrum of Nb_4AlC. features of interest are labelled 'a', 'b' and 'c'.

From visual inspection, the range expanded spinning spectrum shown in Figure 85 was observed to have three distinct shoulders which contributed to the overall asymmetry of the peak. The main peak is labelled 'b' in Figure 85 and this was flanked by two additional shoulders located at higher and lower ppm, labelled 'a' and 'c' respectively. In order to deconvolute overlapping resonance peaks, IGOR pro was used to fit Gaussian functions (as they were the best fit) and minimise the residual signal – the results of this are shown in Figure 86.

Figure 86 shows the results of fitting three Gaussian functions to the spinning spectrum. The bottom spectrum shows the fitted Gaussian functions which were used as they were observed to capture the characteristics of the observed spectral line shape well (red trace middle spectrum). The fit was optimised using the least-squares regression, the residual spectrum can be seen in the top graph. The Gaussian function fitted to the 'a', 'b' and 'c' shoulders were observed to be located at 469 ± 2, 403 ± 2, and 352 ± 2 ppm.

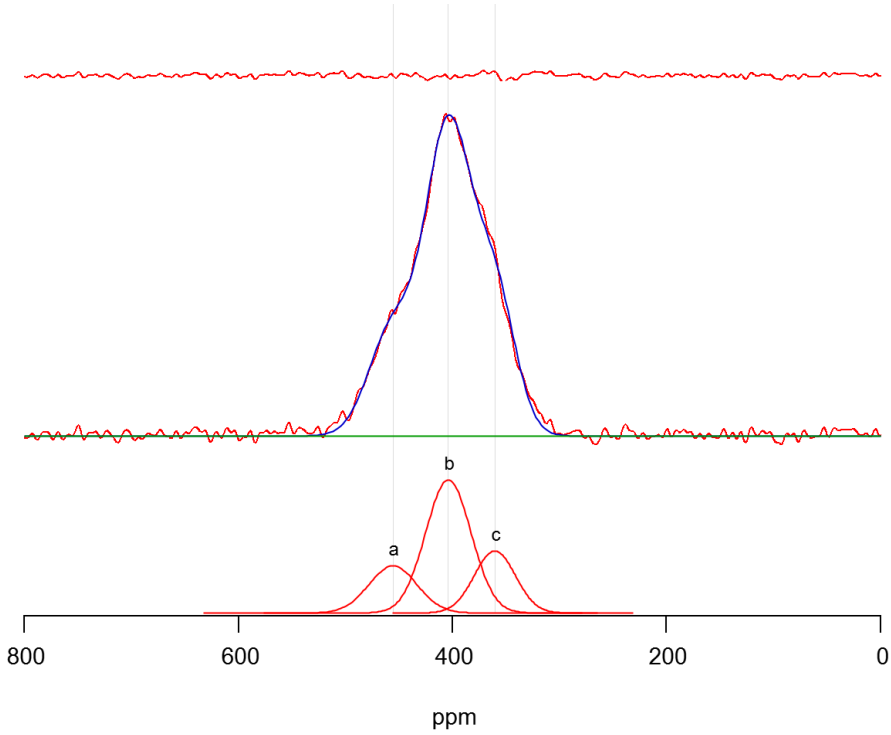

Figure 86. Peak fitting on the ^{13}C spinning NMR spectrum. The bottom spectrum shows the fitted Gaussian line shapes. The middle spectrum has overlays of; the observed spectrum (red trace), the fitted baseline (green trace) and the fitted spectrum (blue trace). The top spectrum shows the residual signal after fitting.

The fractional areas can also be calculated by taking the ratio of the fitted Gaussian to the total peak area which was calculated for the 'a', 'b' and 'c' peaks to be 23.5, 55.7 and 20.8 %, which also corresponds to the distribution of carbon nuclei in these environments.

4.1.3 EDS imaging

Preliminary EDS imaging was conducted on the sample to investigate the phase purity of the sample.

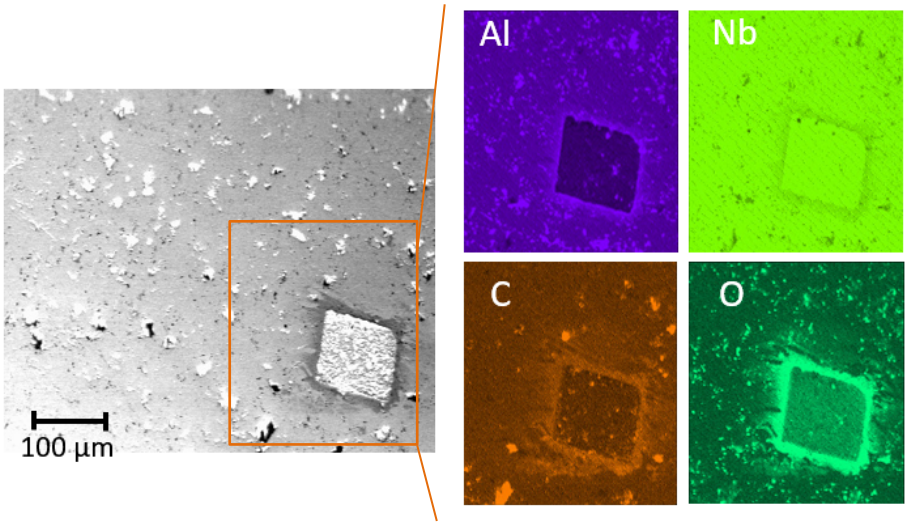

Figure 87. BSE image of the typical sample area on the MAX phase (left), and the corresponding EDS elemental maps of Al, Nb, C and O elements corresponding to the purple, light green, red and dark green images respectively.

Figure 87 shows the BSE image of a section of the Nb_4AlC_3, the square marker is a laser ablation marker, EDS mapping was conducted of elements of Al, Nb, C and O (purple, green, red and dark green respectively). EDS showed that heavier elements such as Al and Nb were distributed evenly in the sampling area. Care must be taken in interpreting the EDS images where uneven surface heights are present. Depressions in surface height can act as secondary emitters, creating unreliable results. This is the case in the carbon EDS map as all the depressions are shown as high signal areas (high brightness). In the oxygen map, the high signal regions correspond with the oxygen map and bright spots are in shallower depression regions.

Depressions from nominal surface height were observed in light and dark contrast regions, and the depression created with a laser can be used as a contrast reference to identify these regions.

4.2 Discussion

The XRD patterns collected and indexed in this study were in agreement with the indexed planes reported by Hu et al. [9], Zhang et al. [68], indicating that the sample created in this study was Nb_4AlC_3. The lattice constants measured from the samples in this study were a = 3.134 ± 0.001 Å and c = 24.162 ± 0.001 Å, which was comparable to the values reported by Hu et al. a = 3.1296 Å, c = 24.121 Å [9]. As no uncertainty was reported with these measurements, it was difficult to gauge if the values were within error of one another. As described earlier, Nb_4AlC_3 has been observed to undergo an ordered to disordered carbon vacancy transformation between 1400 and 1500°C [68], [122]. As the samples analysed by this study were synthesised at 1700°C and lattice parameters are lower than the ordered lattice parameters values seen in the literature [68], the sample was determined to be the α-Nb_4AlC_3 phase with 'disordered' carbon vacancies. The presence of NbO_2 indicated that some oxygen contamination was present during sample fabrication.

Further probing the local carbon environments using static ^{13}C NMR spectra revealed a very broad carbon resonance in which no sub-structures were identifiable. Spinning the (MAS NMR) samples caused a significant narrowing of the main resonance, revealing asymmetry in the peak structure. Peak fitting on the asymmetric resonance structure showed that the characteristics were suitably captured by three peaks, indicating that at least as many unique carbon environments exist in the sample. Using the ^{13}C NMR results as a basis, we can then try to understand what carbon atom configurations might exist.

The carbon atoms in the unit cell can be separated into C1 and C2 carbons dependent on the spacing with respect to a central C2 atom (see Figure 88). Accordingly, the distance from a C2 to a C2 is 3.13 Å and the C2 to C1 spacing is 3.18 Å. The unit cell consists of a C2 carbon located at the origin. Within a unit cell, the six carbons can be counted in terms of their constituent C1 and C2 components, of which there are four C1 carbons and two C2 carbons in a ratio of 2:1 (C1:C2).

In a Nb_4AlC_3 structure with no vacancies, the ideal NMR spectrum would then have two resonances that would occur because of carbons in the C1 and C2 environments. The proportion of integral signal intensity from each resonance in a theoretical NMR spectrum would be 67% and 33% for the C1 and C2 carbon resonances, respectively. Carbon analysis showed that 36.7 % of the carbon sites were vacant. We can correct the stoichiometric formula to reflect the analysed carbon stoichiometry which then becomes: $Nb_4AlC_{1.9}$. This approach is based on vacancies being located on the carbon sites. It is at this point we can consider a range of vacancy models with respect to the C1 and C2 carbon sites – the goal is to find a distribution model which can recreate the experimental NMR spectrum of Nb_4AlC_3. The vacancies cannot be distributed exclusively over the C2 sites as this would liberate all C2 atoms (1.1 vacancies for the single C2 site).

As the NMR is sensitive up to second nearest neighbours, we can use two polyhedra centred around a central C2 and C1 carbon atom, respectively, (Figure 88 and Figure 89) to understand better how vacancies can be distributed throughout Nb_4AlC_3. As the NMR spectra can be thought of as the summation from all the carbon sites within the sample, we must consider the ways in which carbon sites may be occupied within a complex unit cell such as Nb_4AlC_3. To this effect, we can consider the contribution of the C1 (Figure 89) and the C2 sites (Figure 88) to the NMR spectrum.

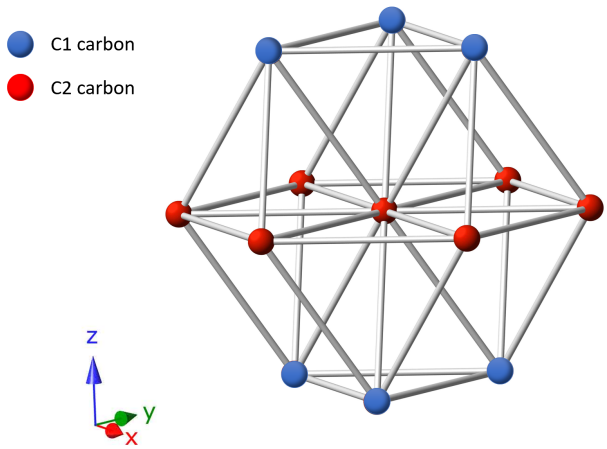

Figure 88 coordination polyhedron with the two chemically unique carbon environments listed as C1 an C2

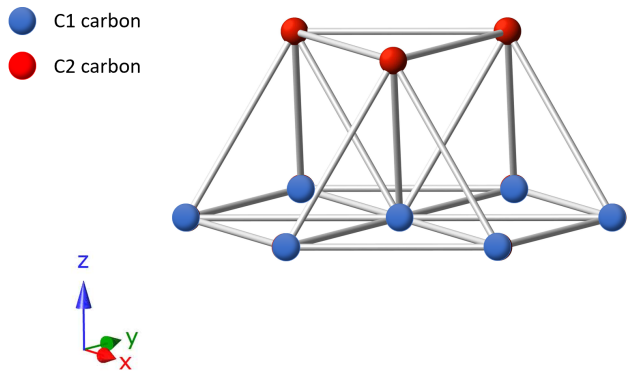

Figure 89 coordination polyhedron centred around a C1 carbon.

4.2.1 Simple model

If vacancies were distributed around a C2 central carbon atom) then 55% of the six surrounding C1 carbon atoms would be vacant, corresponding to an average of 3.33 vacant sites. This would imply that each C1 environment sees either three or four vacancies and that the relative intensity of the C1 signal would be separated into two discrete resonances in the NMR spectrum, as observed. However, the relative amounts (2:1) of C2:C1 environments are not reproduced by this model. It may be the case that the extra 5l% vacancy concentration may be distributed over the C2 carbon atoms, and this may then produce a third resonance.

A number of vacancy ordering models can be considered in an attempt to explain the NMR spectrum as observed. These are detailed in the following sub-sections.

4.2.2 Random vacancy distribution

A random distribution of carbon vacancies in the structure can be modelled by the binomial distribution. This uses the same approach used in the ZrC pristine chapter. Two vacancy stoichiometric carbon resonances should be considered as a starting point, the first would arise from a central C2 carbon (Figure 88) and the second from a central C1 carbon (Figure 89).

For the first resonance, we can consider the random distribution of vacancies over the six C1 sites and six C2 sites as per the configuration shown in Figure 88 - 12 sites in total. In the binomial model, we can account for 2:1 abundance of C1:C2 environments as a proportion of the six-carbon sites. The probability of obtaining a vacancy on a carbon site is shown in Figure 90. The most probable number of vacant sites over the 6 C2 and 6 C1 sites was observed to be three vacancies, followed by four vacancies.

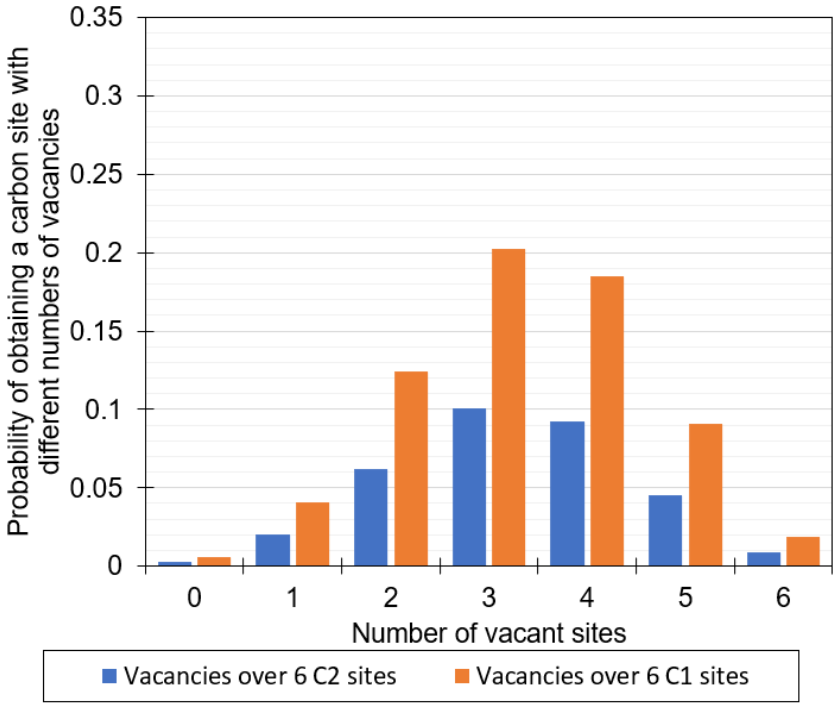

Figure 90 binomial model for the probability of vacancy creation over 6 C1 (blue) and 6 C2 sites (orange).

The next most likely vacancy concentration for the random distribution is eight vacancies over the 12 sites resulting in 33% carbon concentration. This is at the stability limit of NbC according to the phase diagram [182].

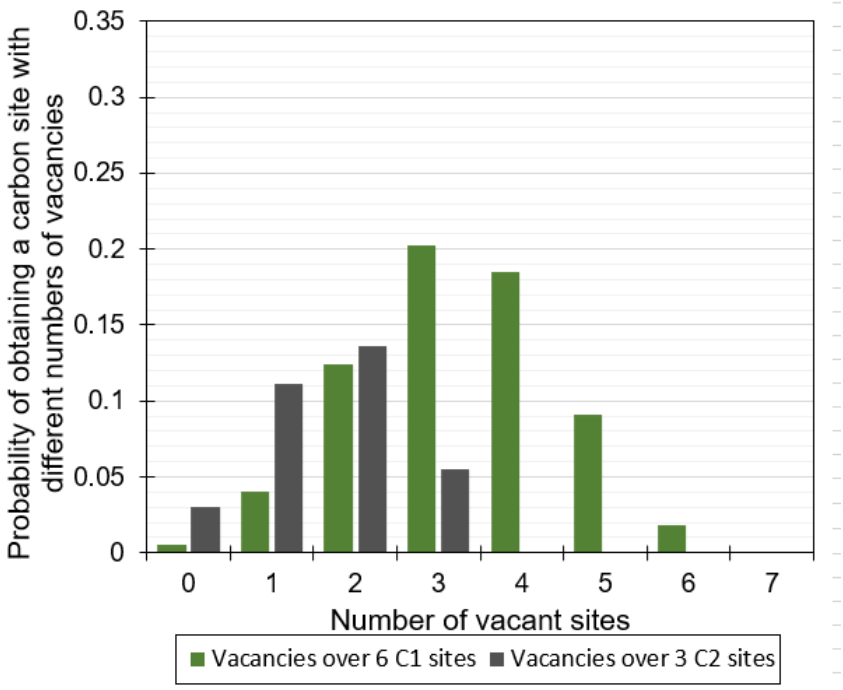

Figure 91 Binomial distribution for the probability of vacancy creation over 6 C1 (green) and 3 C2 sites (grey).

For the second resonance, we can consider the random distribution of vacancies over the nine sites (six C1 and three C2 sites) centred around a central C1 atom, as shown in Figure 89. In this resonance – 2/3 of the C1 sites were observed to be missing alongside 3/6 of the C2 carbon atoms. The resultant NMR spectrum would be the sum of these resonances discussed above.

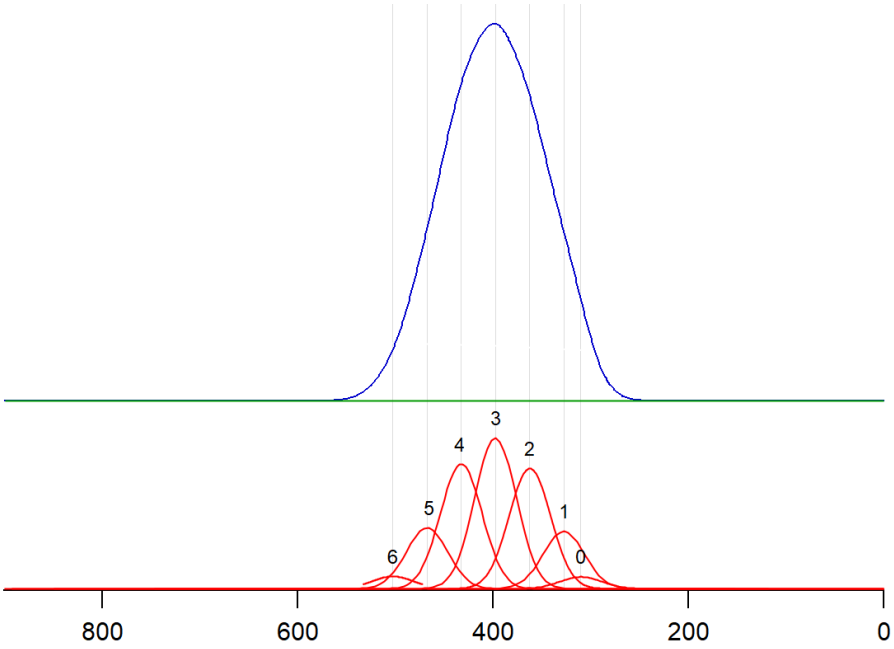

Figure 92. The theoretical NMR spectrum for a random vacancy distribution model using the binomial model. The bottom spectrum shows each contributing peak, and the top spectrum shows the sum of the peaks.

Figure 92 shows the NMR spectrum generated based on the integral peak intensities determined from the binomial distribution. The Gaussian peaks are ordered such that vacancy rich, lower carbon content peaks, are located at higher ppm following the results from the systematic studies on the pristine ZrC samples (Chapter 2). The individual peaks sum to a broad Gaussian that does not have the shouldering peak features observed in the experimental spectrum, indicating that it is unlikely that the vacancies are randomly distributed.

4.2.3 Avoidance model

The second model that can be considered is the avoidance model where carbon vacancies arrange themselves as far apart from one another as possible over the C1 and C2 sites. The proportional number of vacancies in either the C1 or C2 are the product of the number of sites (six) multiplied by the respective stoichiometric proportion (2/3 for C1 and 1/3 for C2) of the site multiplied by the vacancy concentration (1.1/3). Hence the average number of vacancies that will be distributed among the two layers is: 1.468 for C1 and 0.734 for C2.

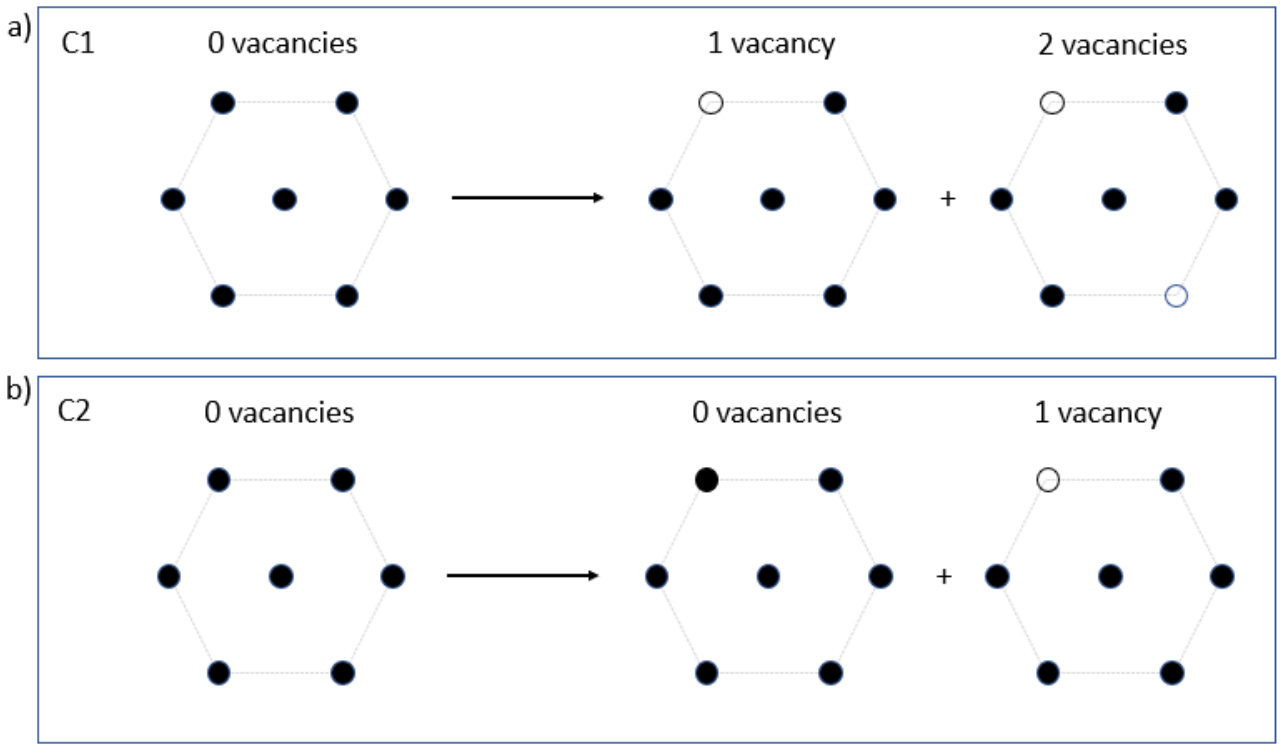

Figure 93. the arrangement of C1 and C2 sites in an avoidance model for around a) C1 and b) C2 layers.

As the number of vacancies must be an integer number, it follows that for the C1 layers a proportion of the sites will have one vacancy, and a proportion will have two vacancies (Figure 93 a)). Similarly, for C2 carbons, a proportion of C2 layers will have zero vacancies, and a proportion will have one (Figure 93 b)).

As the overall NMR spectrum of the material is a summation of the resonances produced by individual unique carbon environments, each C1 and C2 configuration (Figure 93) would produce two NMR peaks. The sum of the C1 and C2 environments in an avoidance model distribution would produce four resonances in an NMR spectrum. As the C1and C2 layers have a site with one vacancy in common, the total NMR spectrum could have three resonances with the two one vacancy resonances overlapping. Normalising these resonances and accounting for the stoichiometric ratio between the peaks results in the 0:1:2 vacancy environment that has the integral intensity ratio 27%:51%:22%. From the systematic studies on ZrC NMR spectra

in the previous chapters, we observed that carbons in less metallic environments (less vacancies/higher carbon content) are located at lower ppm. As Nb_4AlC_3 is comprised of binary carbide layers it is possible that the position of resonances in the NMR spectrum of Nb_4AlC_3 would also evolve in a similar fashion.

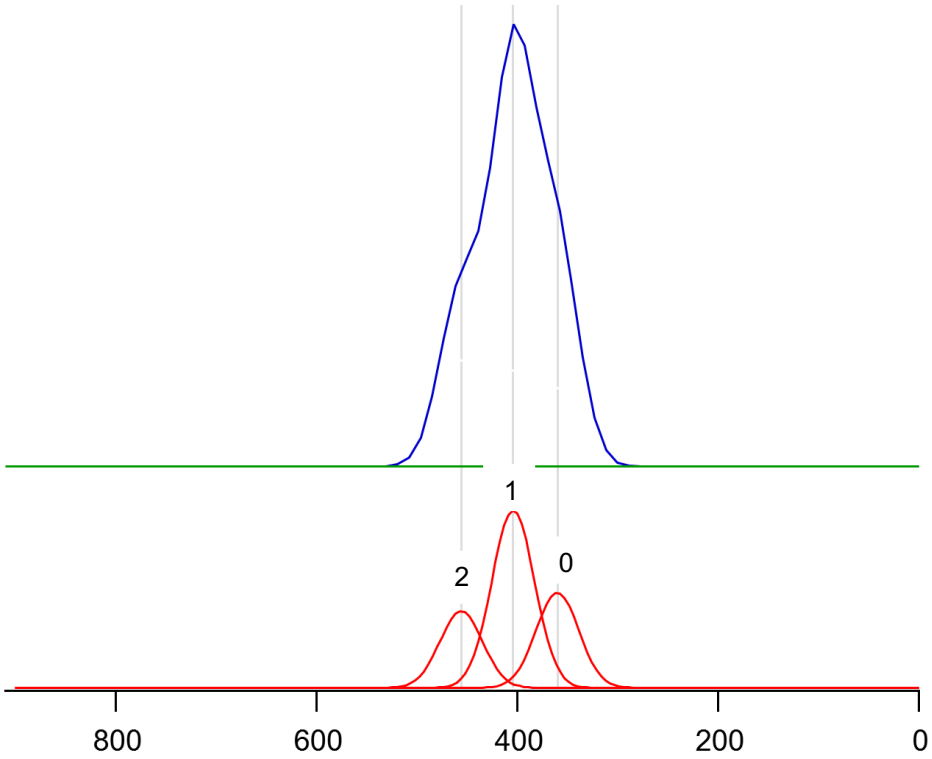

Figure 94 NMR spectrum showing the theoretical NMR spectrum for a vacancy avoidance model. The bottom spectrum shows each peak and the top spectrum shows the sum of the peaks.

Therefore, we can construct a theoretical NMR spectrum based on the above considerations placing resonances with lower vacancy concentrations at lower ppm. Figure 94 bottom figure shows the individual resonance peaks for the avoidance models as stated above, and the top figure shows the sum of the individual peaks. The fitted simulated Gaussian resonance peaks were fixed in width and position in order to construct the diagram observed.

The avoidance model approximately agrees with the experimental results on two accounts. Firstly: the integral peak intensities of each carbon resonance in the NMR spectrum as

calculated in the avoidance model are similar to that obtained from the experimental MAS spectrum. Secondly: the resonances produced in the avoidance model are ordered such that carbon layers that have fewer vacancies are located at lower ppm, and this, in turn, matches with the ordering of the resonances in the experimental MAS NMR spectrum.

Future work should focus on fabricating Nb_4AlC_3 with systematically varying carbon contents and conducting MAS ^{13}C NMR on the samples to determine if the ordering mechanism proposed in this thesis is correct. In addition, irradiation tests should be undertaken initially, at low dpa to determine stability response of the material under irradiation.

4.3 Conclusion

Nb_4AlC_3 produced at KU Leuven has been analysed using XRD and is confirmed to be the α-Nb_4AlC_3 phase. EDS analysis showed a homogenised distribution of Al and Nb elements – hinting that a near phase pure material had been produced. Spinning ^{13}C NMR showed the presence of one central resonance with two-shouldering resonances at higher and lower ppm on either side – signifying that an additional unique carbon environment had been created aside from the C1 and C2 layers. The experimental ^{13}C NMR MAS spectrum is consistent with a distribution of vacancies that corresponds to a vacancy avoidance model operating in each C1 and C2 layer.

Chapter 5 Conclusions and recommendations for future work

5.1 ZrC

5.1.1 Conclusions

A new method has been proposed by which the carbon content of ZrC can be determined with greater accuracy than techniques previously used as standard both in academia and in industry. Probing the short-range structure of the sample using ^{13}C NMR allowed for quantitative correction to the carbon analyser and hence nominal carbon content values. In some cases, these NMR corrected values were much lower than the conventional carbon determination and reporting methods (combustion carbon analysis, nominal carbon content). This result implies that ZrC values of carbon content reported in the literature, which is subsequently used to reference physical property data, may be inaccurate. The above method allows the rigorous evaluation of the effect of carbon content on the physical properties of ZrC. One of the consequences of these findings is that the homogeneity region of ZrC is extended to slightly lower carbon contents than those that appear in the phase diagram.

A few previous studies have used XRD patterns to indicate that no free carbon exists within the sample and that the synthesis of ZrC from precursor powders has been completed and was successful. Carbon dissociated from the ZrC structure was determined to be located within grain boundaries or dispersed throughout the sample in the samples studied here while a graphite phase was not observed in the XRD pattern. This was supported by SEM images that displayed dark regions in intra- and intra-granular regions.

In the dark regions, dissociated carbon existed in two forms: amorphous carbon and graphitic carbon. When these dark regions were examined by Raman spectroscopy, the presence of pristine and partially destroyed graphite was confirmed. The ^{13}C NMR spectra also revealed the presence of sp^2 amorphous carbon and graphite.

For carbon within the ZrC structure vacancy ordering was observed - multiple unique carbon environments due to the presence of vacancies were observed. The integral fraction of these environments were seen to vary systematically with carbon content in the samples sintered at the lowest temperature. At higher sintering temperatures, the carbon environments within the ZrC displayed a more random distribution. Despite this, the CG of the ZrC peak of the samples sintered at 2000°C showed a systematic movement to higher frequencies in samples with lower carbon content.

It was found that ZrC is tolerant to radiation damage up to 2.4 dpa as XRD studies showed the ZrC maintained its crystal structure after irradiations. However, during irradiation carbon atoms were observed to be vacated from the ZrC structure to grain boundaries.

Examination of the effects of irradiation on the carbons remaining within the ZrC structure suggests that the carbon content within the ZrC structure had been reduced. This was supported by high-resolution MAS ^{13}C NMR spectra of samples irradiated to higher doses that showed a systematic growth in the intensity of a shoulder at more positive ppm, a result consistent with pristine samples of lower carbon content. The migration of extra carbon atoms into the grain boundaries was based on the increase in the Raman signal within these areas with increasing irradiation dose. It was also proposed that the radiation resistance of ZrC is a function of the range of vacancy concentrations stable in the ZrC structure and the ability of ZrC to dissociate carbon from its structure.

5.1.2 Future work

Future work should be conducted, validating the trends observed in this thesis. Samples sintered at 1500°C should be annealed incrementally to 1700°C to observe the temperature at which the line shape transitions from a more ordered structure observed in the 1500°C to a more homogeneous profile as was observed in samples sintered at higher temperatures. In addition, the oxygen content and the lattice parameter of these samples should be measured

throughout the annealing process to observe if there are any systematic changes over smaller heating increments.

Long-period annealing, ~12 hours should be carried out on the samples sintered at 2000°C – to match the annealing time of the older studies in the literature to determine if this causes the parabolic lattice parameter trend [124], [183] observed in the literature [64]. The new method of carbon content determination proposed in this thesis should be applied to alternative fabrication methods used to produce ZrC such as spark plasma sintering (SPS) to determine how different fabrication routes affect the final product.

Future work should also focus on higher temperature irradiations for the same nominal stoichiometries fabricated under the same conditions, as studied in this thesis. The irradiation temperatures for these further studies should be in the range of 850 to 1350°C, typical of deep-burn pebble-bed reactor operating regimes, to doses of 10 dpa [67] – with the same techniques used in this study being used for comparative analysis. The results of these analyses should be used to extend the understanding of ZrC presented in this thesis.

5.2 Nb_4AlC_3 MAX phase

5.2.1 Conclusions

Nb_4AlC_3, studied here was observed to tolerate a large vacancy content, with the vacancies within the structure distributed in an avoidance configuration. This was supported by higher resolution ^{13}C MAS NMR in which three sub environments were visible – the intensity of these peaks matched a theoretical avoidance distribution over C1 and C2 layers. The lattice parameter of the MAX phase samples was observed to be in good agreement with literature values.

5.2.2 Future work

Future work should focus on fabricating Nb_4AlC_3 samples with higher carbon contents, and subsequently studying these to determine whether other 413 MAX phase samples can also tolerate a large degree of vacancies and adopt a similar vacancy distribution model as detailed above. Additional physical properties of Nb_4AlC_3 should also be measured, such as the ductility, as a function of carbon content in order to understand further how this varies stoichiometrically with carbon-based MAX phases.

Bibliography

[1] 'Generation IV Roadmap Description of Candidate Gas-cooled Reactor Systems Report', Generation IV forum, THE GAS-COOLED REACTOR SYSTEMS TECHNICAL WORKING GROUP, Generation IV Roadmap, Dec. 2002.

[2] B. Zohuri, 'Generation IV nuclear reactors', in *Nuclear Reactor Technology Development and Utilization*, Elsevier, 2020, pp. 213–246. doi: 10.1016/B978-0-12-818483-7.00006-8.

[3] G. Locatelli, M. Mancini, and N. Todeschini, 'Generation IV nuclear reactors: Current status and future prospects', *Energy Policy*, vol. 61, pp. 1503–1520, Oct. 2013, doi: 10.1016/j.enpol.2013.06.101.

[4] A. Bamshad and O. Safarzadeh, 'Effects of the move towards Gen IV reactors in capacity expansion planning by total generation cost and environmental impact optimization', *Nucl. Eng. Technol.*, p. S1738573320308676, Sep. 2020, doi: 10.1016/j.net.2020.09.005.

[5] K. L. Murty and I. Charit, 'Structural materials for Gen-IV nuclear reactors: Challenges and opportunities', *J. Nucl. Mater.*, vol. 383, no. 1–2, pp. 189–195, Dec. 2008, doi: 10.1016/j.jnucmat.2008.08.044.

[6] T. Allen, J. Busby, M. Meyer, and D. Petti, 'Materials challenges for nuclear systems', *Mater. Today*, vol. 13, no. 12, pp. 14–23, Dec. 2010, doi: 10.1016/S1369-7021(10)70220-0.

[7] M. W. Barsoum, *MAX Phases: Properties of Machinable Ternary Carbides and Nitrides*. Weinheim, Germany: Wiley-VCH Verlag GmbH & Co. KGaA, 2013. doi: 10.1002/9783527654581.

[8] E. Zapata-Solvas *et al.*, 'Experimental synthesis and density functional theory investigation of radiation tolerance of Zr3(Al1-xSix)C2 MAX phases', *J. Am. Ceram. Soc.*, vol. 100, no. 4, pp. 1377–1387, Apr. 2017, doi: 10.1111/jace.14742.

[9] C. Hu, Y. Sakka, H. Tanaka, T. Nishimura, and S. Grasso, 'Fabrication of Textured Nb4AlC3 Ceramic by Slip Casting in a Strong Magnetic Field and Spark Plasma Sintering', *J. Am. Ceram. Soc.*, vol. 94, no. 2, pp. 410–415, 2011, doi: 10.1111/j.1551-2916.2010.04096.x.

[10] C. Hu, F. Li, J. Zhang, J. Wang, J. Wang, and Y. Zhou, 'Nb4AlC3: A new compound belonging to the MAX phases', *Scr. Mater.*, vol. 57, no. 10, pp. 893–896, Nov. 2007, doi: 10.1016/j.scriptamat.2007.07.038.

[11] T. Lapauw *et al.*, '(Nbx, Zr1–x)4AlC3 MAX Phase Solid Solutions: Processing, Mechanical Properties, and Density Functional Theory Calculations', *Inorg. Chem.*, vol. 55, no. 11, pp. 5445–5452, Jun. 2016, doi: 10.1021/acs.inorgchem.6b00484.

[12] Y. Katoh, G. Vasudevamurthy, T. Nozawa, D.-S. Rana, I. Farnan, and L. L. Snead, 'Properties of Zirconium Carbide for Nuclear Fuel Applications', in *Reference Module in Materials Science and Materials Engineering*, Elsevier, 2020, p. B9780128035818117000. doi: 10.1016/B978-0-12-803581-8.11782-5.

[13] H. F. Jackson and W. E. Lee, '2.13 - Properties and Characteristics of ZrC', in *Comprehensive Nuclear Materials*, R. J. M. Konings, Ed. Oxford: Elsevier, 2012, pp.

339–372. Accessed: Dec. 05, 2015. [Online]. Available: http://www.sciencedirect.com/science/article/pii/B9780080560335000239
[14] 'Multidimensional multiphysics simulation of TRISO particle fuel', *J. Nucl. Mater.*, vol. 443, no. 1–3, pp. 531–543, Nov. 2013, doi: 10.1016/j.jnucmat.2013.07.070.
[15] D. Kim *et al.*, 'Microstructure evolution of a ZrC coating layer in TRISO particles during high-temperature annealing', *J. Nucl. Mater.*, vol. 479, pp. 93–99, 2016, doi: https://doi.org/10.1016/j.jnucmat.2016.06.024.
[16] 'Influence of free carbon on the characteristics of ZrC and deposition of near-stoichiometric ZrC in TRISO coated particle fuel', *J. Nucl. Mater.*, vol. 451, no. 1–3, pp. 97–103, Aug. 2014, doi: 10.1016/j.jnucmat.2014.03.045.
[17] I. L. Shabalin, *Ultra-High Temperature Materials II: Refractory Carbides I (Ta, Hf, Nb and Zr Carbides)*. Springer, 2019.
[18] Y. Katoh, G. Vasudevamurthy, T. Nozawa, and L. L. Snead, 'Properties of zirconium carbide for nuclear fuel applications', *J. Nucl. Mater.*, vol. 441, no. 1–3, pp. 718–742, Oct. 2013, doi: 10.1016/j.jnucmat.2013.05.037.
[19] W. E. Lee, E. Giorgi, R. Harrison, A. Maître, and O. Rapaud, 'Nuclear Applications for Ultra-High Temperature Ceramics and MAX Phases', in *Ultra-High Temperature Ceramics*, W. G. Fahrenholtz, E. J. Wuchina, W. E. Lee, and Y. Zhou, Eds. John Wiley & Sons, Inc, 2014, pp. 391–415. doi: 10.1002/9781118700853.ch15.
[20] D. I. Butt and T. C. Wallace, 'The U-Zr-C Ternary Phase Diagram above 2473 K', *J. Am. Ceram. Soc.*, vol. 76, pp. 1409–1419, 1993.
[21] C. Xie *et al.*, 'Effect of carbon vacancies on structural and mechanical properties of stable zirconium carbides: A first principles study', *ArXiv150900162 Cond-Mat*, Sep. 2015, Accessed: Dec. 07, 2015. [Online]. Available: http://arxiv.org/abs/1509.00162
[22] B. Wei *et al.*, 'Densification, mechanical and thermal properties of ZrC1 − x ceramics fabricated by two-step reactive hot pressing of ZrC and ZrH2 powders', *J. Eur. Ceram. Soc.*, vol. 38, no. 2, pp. 411–419, 2018, doi: 10.1016/j.jeurceramsoc.2017.09.027.
[23] C. Nachiappan, L. Rangaraj, C. Divakar, and V. Jayaram, 'Synthesis and Densification of Monolithic Zirconium Carbide by Reactive Hot Pressing', *J. Am. Ceram. Soc.*, Feb. 2010, doi: 10.1111/j.1551-2916.2010.03608.x.
[24] D. B. K. Rana, E. Z. Solvas, W. E. Lee, and I. Farnan, 'An investigation of the long-range and local structure of sub-stoichiometric zirconium carbide sintered at different temperatures', *Sci. Rep.*, vol. 10, no. 1, p. 3096, Dec. 2020, doi: 10.1038/s41598-020-59698-6.
[25] M. D. Sacks, C. Wang, Z. Yang, and A. Jain, 'Carbothermal reduction synthesis of nanocrystalline zirconium carbide and hafnium carbide powders using solution-derived precursors', *J. Mater. Sci.*, vol. 9, pp. 6057–6066, 2004.
[26] M. Doll, D. Gosset, C. Bogicevic, F. Karolak, D. Simeone, and G. Baldinozzi, 'Synthesis of nanosized zirconium carbide by a sol – gel route', *J. Eur. Ceram. Soc.*, vol. 27, pp. 2061–2067, 2007, doi: 10.1016/j.jeurceramsoc.2006.06.005.
[27] G. H. Reynolds, J. C. Janvier, J. L. Kaae, and J. P. Morlevat, 'Irradiation behavior of experimental fuel particles containing chemically vapor deposited zirconium carbide coatings', *J. Nucl. Mater.*, vol. 62, no. 1, pp. 9–16, 1976, doi: 10.1016/0022-3115(76)90279-8.

[28] K. Ikawa, 'VAPOR DEPOSITION OF ZIRCONIUM CARBIDE-CARBON COMPOSITES BY THE IODIDE PROCESS', *J. -Common Met.*, vol. 27, pp. 325–332, 1972.
[29] A. Jain, 'Synthesis and Processing of Nanocrystalline Zirconium Carbide Formed by Carbothermal Reduction', PhD Thesis, Materials Science and Engineering, 2004.
[30] A. D. Mazzoni and M. S. Conconi, 'Synthesis of Group IVB Metals Oxicarbides by Carboreduction Reactions', vol. 5, no. 4, pp. 459–466, 2002.
[31] G. Vasudevamurthy, T. W. Knight, E. Roberts, and T. M. Adams, 'Laboratory production of zirconium carbide compacts for use in inert matrix fuels', *J. Nucl. Mater.*, vol. 374, pp. 241–247, 2008, doi: 10.1016/j.jnucmat.2007.08.016.
[32] J. B. Holt and S. D. Dunmead, 'Self-Heating Synthesis of Materials', *Annu. Rev. Mater. Sci.*, vol. 21, pp. 304–334, 1991.
[33] J. Gan, Y. Yang, C. Dickson, and T. Allen, 'Proton irradiation study of GFR candidate ceramics', *J. Nucl. Mater.*, vol. 389, no. 2, pp. 317–325, 2009, doi: 10.1016/j.jnucmat.2009.02.021.
[34] A. Motta, K. Sridharan, D. Morgan, and I. Szlufarska, 'Understanding the Irradiation Behavior of Zirconium Carbide', DOE/NEUP--10-679, 1097003, Oct. 2013. doi: 10.2172/1097003.
[35] Y. Huang, B. R. Maier, and T. R. Allen, 'Irradiation-induced effects of proton irradiation on zirconium carbides with different stoichiometries', *Nucl. Eng. Des.*, vol. 277, pp. 55–63, Oct. 2014, doi: 10.1016/j.nucengdes.2014.06.001.
[36] T. Chakrabarti, L. Rangaraj, and V. Jayaram, 'On the Low Temperature Densification of Reactively Hot Pressed Non-Stoichiometric ZrC and (Zr,Ti)C', *Mater. Today Proc.*, vol. 3, no. 9, Part B, pp. 3077–3085, 2016, doi: https://doi.org/10.1016/j.matpr.2016.09.023.
[37] Y. Zhou, T. W. Heitmann, W. G. Fahrenholtz, and G. E. Hilmas, 'Synthesis of ZrCx with controlled carbon stoichiometry by low temperature solid state reaction', *J. Eur. Ceram. Soc.*, vol. 39, no. 8, pp. 2594–2600, 2019, doi: https://doi.org/10.1016/j.jeurceramsoc.2019.03.004.
[38] C. Musa *et al.*, 'Processing, Mechanical and Optical Properties of Additive-Free ZrC Ceramics Prepared by Spark Plasma Sintering', *Materials*, vol. 9, no. 6, p. 489, Jun. 2016, doi: 10.3390/ma9060489.
[39] S. Biira *et al.*, 'The role of ZrCl4 partial pressure on the growth characteristics of chemical vapour deposited ZrC layers', *Ceram. Int.*, vol. 43, no. 17, pp. 15133–15140, 2017, doi: https://doi.org/10.1016/j.ceramint.2017.08.042.
[40] K. Li *et al.*, 'Synthesis of zirconium carbide whiskers by a combination of microwave hydrothermal and carbothermal reduction', *J. SOLID STATE Chem.*, vol. 258, pp. 383–390, Feb. 2018, doi: 10.1016/j.jssc.2017.11.002.
[41] T. Chakrabarti, L. Rangaraj, and V. Jayaram, 'Effect of Zirconium on the Densification of Reactively Hot-Pressed Zirconium Carbide', *J. Am. Ceram. Soc.*, vol. 97, no. 10, pp. 3092–3102, 2014, doi: 10.1111/jace.13117.
[42] Y. Huang, B. R. Maier, and T. R. Allen, 'Irradiation-induced effects of proton irradiation on zirconium carbides with different stoichiometries', *Nucl. Eng. Des.*, vol. 277, pp. 55–63, Oct. 2014, doi: 10.1016/j.nucengdes.2014.06.001.

[43] A. Motta, K. Sridharan, D. Morgan, and I. Szlufarska, 'Understanding the Irradiation Behavior of Zirconium Carbide', DOE-NEUP 10-679, Sep. 2013. [Online]. Available: http://www.osti.gov/scitech/servlets/purl/1097003
[44] C. Gasparrini, R. J. Chater, D. Horlait, L. Vandeperre, and W. E. Lee, 'Zirconium carbide oxidation: Kinetics and oxygen diffusion through the intermediate layer', *J. Am. Ceram. Soc.*, vol. 101, no. 6, pp. 2638–2652, Jun. 2018, doi: 10.1111/jace.15479.
[45] E. Giorgi, 'Processing and Modelling of Non-Stoichiometric Zirconium Carbide for Advanced Nuclear Fuel Applications'. Aug. 2015.
[46] C. J. Ulmer, A. T. Motta, and M. A. Kirk, 'In situ ion irradiation of zirconium carbide', *J. Nucl. Mater.*, vol. 466, pp. 606–614, Nov. 2015, doi: 10.1016/j.jnucmat.2015.08.009.
[47] J. Gan, M. Meyer, R. Birtcher, and T. Allen, 'Microstructure Evolution in ZrC Irradiated with Kr ions', *J. ASTM Int.*, vol. 3, no. 4, pp. 1–7, 2006, doi: 10.1520/JAI12376.
[48] H. Nakayama, K. Ozaki, T. Nabeta, and Y. Nakajima, 'Composition Dependence of Lattice Parameter, Thermal and Electrical Properties in ZrCx Compounds', *Mater. Trans.*, vol. 58, no. 6, pp. 852–856, Jun. 2017, doi: 10.2320/matertrans.M2016283.
[49] H. Nakayama, 'Compositional and grain size dependence of the mechanical properties of ZrCx: Effect of annealing on ZrC0.45', *Ceram. Int.*, vol. 45, no. 5, pp. 6135–6142, Apr. 2019, doi: 10.1016/j.ceramint.2018.12.088.
[50] A. C. Ferrari, 'Raman spectroscopy of graphene and graphite: Disorder, electron–phonon coupling, doping and nonadiabatic effects', *Solid State Commun.*, vol. 143, no. 1–2, pp. 47–57, Jul. 2007, doi: 10.1016/j.ssc.2007.03.052.
[51] A. C. Ferrari and J. Robertson, 'Resonant Raman spectroscopy of disordered, amorphous, and diamondlike carbon', *Phys. Rev. B*, vol. 64, no. 7, p. 075414, Jul. 2001, doi: 10.1103/PhysRevB.64.075414.
[52] S. Pellegrino, L. Thomé, A. Debelle, S. Miro, and P. Trocellier, 'Damage production in carbide single crystals irradiated with MeV heavy ions', *Nucl. Instrum. Methods Phys. Res. Sect. B Beam Interact. Mater. At.*, vol. 307, pp. 294–298, Jul. 2013, doi: 10.1016/j.nimb.2012.11.091.
[53] S. Pellegrino, P. Trocellier, L. Thomé, S. Miro, J.-M. Costantini, and E. Jouanny, 'Raman investigation of ion irradiated TiC and ZrC', *Nucl. Instrum. Methods Phys. Res. Sect. B Beam Interact. Mater. At.*, vol. 454, pp. 61–67, 2019, doi: 10.1016/j.nimb.2019.02.012.
[54] R. Florez *et al.*, 'The irradiation response of ZrC ceramics under 10 MeV Au3+ ion irradiation at 800 ºC', *J. Eur. Ceram. Soc.*, p. S0955221920300352, Jan. 2020, doi: 10.1016/j.jeurceramsoc.2020.01.025.
[55] D. Gosset, M. Dollé, D. Simeone, G. Baldinozzi, and L. Thomé, 'Structural behaviour of nearly stoichiometric ZrC under ion irradiation', *Nucl. Instrum. Methods Phys. Res. Sect. B Beam Interact. Mater. At.*, vol. 266, no. 12, pp. 2801–2805, Jun. 2008, doi: 10.1016/j.nimb.2008.03.121.
[56] S. Pellegrino, J.-P. Crocombette, A. Debelle, T. Jourdan, P. Trocellier, and L. Thomé, 'Multi-scale simulation of the experimental response of ion-irradiated zirconium carbide: Role of interstitial clustering', *Acta Mater.*, vol. 102, pp. 79–87, 2016, doi: https://doi.org/10.1016/j.actamat.2015.09.004.

[57] B. S. Vasile, D. Craciun, P. Ionescu, D. Pantelica, G. Dorcioman, and V. Craciun, 'Microstructure of 800 keV Ar ion irradiated thin ZrC films', *Appl. Surf. Sci.*, vol. 442, pp. 773–777, 2018, doi: 10.1016/j.apsusc.2018.02.216.
[58] S. Pellegrino, L. Thomé, A. Debelle, S. Miro, and P. Trocellier, 'Radiation effects in carbides: TiC and ZrC versus SiC', *Nucl. Instrum. Methods Phys. Res. Sect. B Beam Interact. Mater. At.*, vol. 327, pp. 103–107, May 2014, doi: 10.1016/j.nimb.2013.11.046.
[59] D. Craciun *et al.*, 'Structural and mechanical properties changes induced in nanocrystalline ZrC thin films by Ar ion irradiation', *J. Nucl. Mater.*, vol. 468, pp. 78–83, Jan. 2016, doi: 10.1016/j.jnucmat.2015.11.012.
[60] Y. Yang, W.-Y. Lo, C. Dickerson, and T. R. Allen, 'Stoichiometry effect on the irradiation response in the microstructure of zirconium carbides', *J. Nucl. Mater.*, vol. 454, no. 1, pp. 130–135, 2014, doi: https://doi.org/10.1016/j.jnucmat.2014.07.071.
[61] B. Wei, Y. Wang, H. Zhang, D. Wang, S. Peng, and Y. Zhou, 'Microstructure evolution of nonstoichiometric ZrC0.6 with ordered carbon vacancies under ion irradiation', *Mater. Lett.*, vol. 228, pp. 254–257, Oct. 2018, doi: 10.1016/j.matlet.2018.06.010.
[62] D. Craciun *et al.*, 'Structural and mechanical properties changes induced in nanocrystalline ZrC thin films by Ar ion irradiation', *J. Nucl. Mater.*, vol. 468, pp. 78–83, Jan. 2016, doi: 10.1016/j.jnucmat.2015.11.012.
[63] R. W. Harrison and W. E. Lee, 'Processing and properties of ZrC, ZrN and ZrCN ceramics: a review', *Adv. Appl. Ceram.*, vol. 115, no. 5, pp. 294–307, Jul. 2016, doi: 10.1179/1743676115Y.0000000061.
[64] C. Gasparrini *et al.*, 'On the stoichiometry of zirconium carbide', *Sci. Rep.*, vol. 10, no. 1, Art. no. 1, Apr. 2020, doi: 10.1038/s41598-020-63037-0.
[65] Y. Yang, C. A. Dickerson, H. Swoboda, B. Miller, and T. R. Allen, 'Microstructure and mechanical properties of proton irradiated zirconium carbide', *J. Nucl. Mater.*, vol. 378, no. 3, pp. 341–348, Sep. 2008, doi: 10.1016/j.jnucmat.2008.06.042.
[66] G. S. Was, 'Radiation Damage in Metals and Alloys', in *Materials Science and Technology*, R. W. Cahn, P. Haasen, and E. J. Kramer, Eds. Weinheim, Germany: Wiley-VCH Verlag GmbH & Co. KGaA, 2015, pp. 1–117. doi: 10.1002/9783527603978.mst0451.
[67] L. L. Snead, Y. Katoh, and S. Kondo, 'Effects of fast neutron irradiation on zirconium carbide', *J. Nucl. Mater.*, vol. 399, no. 2–3, pp. 200–207, 2010, doi: doi:10.1016/j.jnucmat.2010.01.020.
[68] H. Zhang *et al.*, 'Discovery of carbon-vacancy ordering in Nb_4AlC_{3-x} under the guidance of first-principles calculations', *Sci. Rep.*, vol. 5, p. 14192, Sep. 2015, doi: 10.1038/srep14192.
[69] D. J. Hughes and R. B. Schwartz, 'NEUTRON CROSS SECTIONS : Table of Thermal Neutron Cross Sections of the Isotopes'. OSTI, Jul. 01, 1958. [Online]. Available: https://link.springer.com/content/pdf/bbm%3A978-3-642-87614-1%2F1.pdf
[70] J. Wang, J. Wang, Y. Zhou, and C. Hu, 'Phase stability, electronic structure and mechanical properties of ternary-layered carbide Nb4AlC3: An ab initio study', *Acta Mater.*, vol. 56, no. 7, pp. 1511–1518, Apr. 2008, doi: 10.1016/j.actamat.2007.12.003.

[71] 'Non dispersive infrared (ND-IR) spectroscopy | HiQ'. http://hiq.linde-gas.com/en/analytical_methods/infrared_spectroscopy/non_dispersive_infrared.html (accessed Feb. 18, 2019).
[72] HORIBA SCIENTIFIC, 'EMIA: Pursuing high precision speed, and ease of use.' [Online]. Available: http://www.horiba.com/fileadmin/uploads/Scientific/Documents/Emission/EMIA_V2.pdf
[73] 'X-ray Powder Diffraction (XRD)', *Techniques*. http://serc.carleton.edu/research_education/geochemsheets/techniques/XRD.html (accessed Aug. 10, 2016).
[74] P. P. Ewald, 'Introduction to the dynamical theory of X-ray diffraction', *Acta Crystallogr. A*, vol. 25, no. 1, pp. 103–108, Jan. 1969, doi: 10.1107/S0567739469000155.
[75] R. O. Wayne, *Light and Video Microscopy*. Academic Press, 2013.
[76] '5. Scattering and diffraction', *Institute of Physical Chemistry 'Rocasolano'*. http://www.xtal.iqfr.csic.es/Cristalografia/parte_05-en.html
[77] 'Inorganic Crystal Structure Database (ICSD) | Physical Sciences Data science Service'. https://www.psds.ac.uk/icsd (accessed Aug. 19, 2020).
[78] M. Hellenbrandt, 'The Inorganic Crystal Structure Database (ICSD)—Present and Future', *Crystallogr. Rev.*, vol. 10, no. 1, pp. 17–22, Jan. 2004, doi: 10.1080/08893110410001664882.
[79] Bruker-axs, 'DIFFRACplusTOPAS, TOPAS 4.2 Technical Reference', Bruker AXS GmbH, Karlsruhe, Germany., Technical reference, Jan. 2009.
[80] 'Scanning Electron Microscopy (SEM)', *Techniques*. https://serc.carleton.edu/research_education/geochemsheets/techniques/SEM.html (accessed Feb. 19, 2019).
[81] 'scanning electron microscopy - an overview | ScienceDirect Topics'. https://www.sciencedirect.com/topics/engineering/scanning-electron-microscopy (accessed Feb. 19, 2019).
[82] 'Components in a SEM', *Nanoscience Instruments*. https://www.nanoscience.com/techniques/scanning-electron-microscopy/components/ (accessed Feb. 20, 2019).
[83] JEOL Ltd., 'Scanning Electron Microscope A To Z', p. 32.
[84] 'Inside a scanning electron microscope: the SEM electron column explained'. http://blog.phenom-world.com/scanning-electron-microscope-sem-electron-column (accessed Feb. 20, 2019).
[85] 'Electron-matter interactions | MyScope'. http://111.118.160.118/myscope/sem/background/concepts/interactions.php (accessed Feb. 20, 2019).
[86] D. K. Bowen and C. R. Hall, *Microscopy of Materials: Modern Imaging Methods Using Electron, X-ray and Ion Beams*. Macmillan International Higher Education, 1975.
[87] T. E. Everhart and R. F. M. Thornley, 'Wide-band detector for micro-microampere low-energy electron currents', *J. Sci. Instrum.*, vol. 37, no. 7, pp. 246–248, Jul. 1960, doi: 10.1088/0950-7671/37/7/307.

[88] 'SEM working principle: the detection of backscattered electrons'. http://blog.phenom-world.com/backscattered-electrons-sem (accessed Feb. 19, 2019).
[89] 'Different Types of SEM Imaging – BSE and Secondary Electron Imaging', *AZoM.com*, Aug. 04, 2017. https://www.azom.com/article.aspx?ArticleID=14309 (accessed Feb. 19, 2019).
[90] Bruker-axs, 'ESPRIT 2 Microanalysis Software', *Bruker.com*. https://www.bruker.com/products/x-ray-diffraction-and-elemental-analysis/eds-wds-ebsd-sem-micro-xrf-and-sem-micro-ct/esprit-2.html (accessed Oct. 04, 2020).
[91] E. Smith and G. Dent, *Modern Raman Spectroscopy: A Practical Approach*. 2005. doi: 10.1002/0470011831.ch5.
[92] J. Hodkiewicz and T. F. Scientific, 'Characterizing Carbon Materials with Raman Spectroscopy', *Applciation Notes Thermoscientific*, p. 5.
[93] D. B. Schuepfer *et al.*, 'Assessing the structural properties of graphitic and non-graphitic carbons by Raman spectroscopy', *Carbon*, vol. 161, pp. 359–372, May 2020, doi: 10.1016/j.carbon.2019.12.094.
[94] Wavemetrics, *Igor Pro from WaveMetrics | Igor Pro by WaveMetrics*. Wavemetrics. Accessed: Oct. 04, 2020. [Online]. Available: https://www.wavemetrics.com/
[95] *Origin Pro*. Origin Lab. Accessed: Oct. 04, 2020. [Online]. Available: https://www.originlab.com/index.aspx?go=Company&pid=1130
[96] 'NMR studies of electronic properties of solids - Scholarpedia'. http://www.scholarpedia.org/article/NMR_studies_of_electronic_properties_of_solids#Knight_shifts_in_Metals (accessed Aug. 17, 2016).
[97] 'Principles of NMR'. http://www.process-nmr.com/nmr1.htm (accessed Aug. 18, 2016).
[98] 'What is Dynamic Nuclear Polarization (DNP-NMR)? | Bridge12'. http://www.bridge12.com/learn/dynamic-nuclear-polarization-dnp-nmr (accessed Aug. 17, 2016).
[99] M. H. Levitt, *Spin Dynamics: Basics of Nuclear Magnetic Resonance*. Wiley, 2001.
[100] M. Rangus, 'NMR spectroscopy in solids: A comparison to NMR spectroscopy in liquids'. [Online]. Available: http://www-f9.ijs.si/~krizan/sola/sempod/0607/rangus-seminar.pdf
[101] K. J. D. MacKenzie and M. E. Smith, *Multinuclear Solid-State Nuclear Magnetic Resonance of Inorganic Materials*. Elsevier, 2002.
[102] 'Okayama University'. https://www.okayama-u.ac.jp/user/kouhou/ebulletin/research_highlights/vol24/highlights_003.html (accessed Aug. 06, 2020).
[103] M. J. Duer, *Introduction to Solid-State NMR Spectroscopy*. Wiley, 2005.
[104] E. L. Hahn, 'Spin Echoes', *Phys. Rev.*, vol. 80, no. 4, pp. 580–594, Nov. 1950, doi: 10.1103/PhysRev.80.580.
[105] 'National Institute of Advanced Industrial Science and Technology (AIST)'. http://sdbs.db.aist.go.jp/sdbs/cgi-bin/direct_frame_top.cgi (accessed Aug. 29, 2016).
[106] S. Hayashi and K. Hayamizu, 'Chemical Shift Standards in High-Resolution Solid-State NMR (1) 13C, 29Si, and 1H Nuclei', *Bull. Chem. Soc. Jpn.*, vol. 64, no. 2, pp. 685–687, 1991, doi: 10.1246/bcsj.64.685.

[107] 'The theory of the anomalous skin effect in metals', *Proc. R. Soc. Lond. Ser. Math. Phys. Sci.*, vol. 195, no. 1042, pp. 336–364, Dec. 1948, doi: 10.1098/rspa.1948.0123.
[108] R. P. Feynman, Leighton, and Sands, *The Feynman lectures on physics. Volume 2: Mainly electromagnetism and matter*, vol. Volume II. 1964. Accessed: Aug. 02, 2020. [Online]. Available: https://ui.adsabs.harvard.edu/abs/1964flp..book.....F/abstract
[109] E. K. Storms and P. Wagner, 'Thermal conductivity of sub-stoichiometric ZrC and NbC', *High Temp. Sci.*, vol. 5, no. 6, pp. 454–462, 1973.
[110] R. K. Dash, G. Yushin, and Y. Gogotsi, 'Synthesis, structure and porosity analysis of microporous and mesoporous carbon derived from zirconium carbide', *Microporous Mesoporous Mater.*, vol. 86, no. 1, pp. 50–57, Nov. 2005, doi: 10.1016/j.micromeso.2005.05.047.
[111] 'Raman spectroscopy of graphene and graphite: Disorder, electron–phonon coupling, doping and nonadiabatic effects', *Solid State Commun.*, vol. 143, no. 1–2, pp. 47–57, Jul. 2007, doi: 10.1016/j.ssc.2007.03.052.
[112] J.-X. Wang *et al.*, 'Synthesis of nanocrystallized zirconium carbide based on an aqueous solution-derived precursor', *RSC Adv.*, vol. 7, no. 37, pp. 22722–22727, 2017, doi: 10.1039/c7ra02586f.
[113] S.-K. Jerng, D. Seong Yu, J. Hong Lee, C. Kim, S. Yoon, and S.-H. Chun, 'Graphitic carbon growth on crystalline and amorphous oxide substrates using molecular beam epitaxy', *Nanoscale Res. Lett.*, vol. 6, p. 565, Oct. 2011, doi: 10.1186/1556-276X-6-565.
[114] J. Aihara, T. Yamabe, and H. Hosoya, 'Aromatic character of graphite and carbon nanotubes', *Synth. Met.*, vol. 64, no. 2–3, pp. 309–313, Jun. 1994, doi: 10.1016/0379-6779(94)90128-7.
[115] A. Dychalska, P. Popielarski, W. Franków, K. Fabisiak, K. Paprocki, and M. Szybowicz, 'Study of CVD diamond layers with amorphous carbon admixture by Raman scattering spectroscopy', *Mater. Sci.-Pol.*, vol. 33, no. 4, pp. 799–805, Dec. 2015, doi: 10.1515/msp-2015-0067.
[116] † Tamar Sternfeld *et al.*, 'Fullerene Anions of Different Sizes and Shapes: A 13C NMR and Density-Functional Study', May 16, 2003. https://pubs.acs.org/doi/10.1021/jo030106n (accessed Jun. 20, 2019).
[117] L. L. Snead, Y. Katoh, and S. Kondo, 'Effects of fast neutron irradiation on zirconium carbide', *J. Nucl. Mater.*, vol. 399, no. 2–3, pp. 200–207, Apr. 2010, doi: 10.1016/j.jnucmat.2010.01.020.
[118] M. S. Solum, A. F. Sarofim, R. J. Pugmire, T. H. Fletcher, and H. Zhang, '13C NMR Analysis of Soot Produced from Model Compounds and a Coal', *Energy Fuels*, vol. 15, no. 4, pp. 961–971, Jul. 2001, doi: 10.1021/ef0100294.
[119] Y. Nagano *et al.*, 'Air oxidation of carbon soot generated by laser ablation', *Carbon*, vol. 37, no. 10, pp. 1509–1515, 1999, doi: https://doi.org/10.1016/S0008-6223(99)00027-5.
[120] C. S. Yannoni, R. D. Johnson, G. Meijer, D. S. Bethune, and J. R. Salem, 'Carbon-13 NMR study of the C60 cluster in the solid state: molecular motion and carbon chemical shift anisotropy', *J. Phys. Chem.*, vol. 95, no. 1, pp. 9–10, Jan. 1991, doi: 10.1021/j100154a005.

[121] A. I. Gusev, 'Short-range Order and Local Displacements of the Atoms in Non-stoichiometric Compounds', *Russ. Chem. Rev.*, vol. 57, no. 10, pp. 913–928, Oct. 1988, doi: 10.1070/RC1988v057n10ABEH003401.

[122] A. I. Gusev, A. A. Rempel, and A. J. Magerl, *Disorder and Order in Strongly Nonstoichiometric Compounds: Transition Metal Carbides, Nitrides and Oxides*. Springer Science & Business Media, 2013.

[123] Y. Zhang, B. Liu, and J. Wang, 'Self-assembly of Carbon Vacancies in Sub-stoichiometric ZrC1−x', *Sci. Rep.*, vol. 5, p. 18098, Dec. 2015, doi: 10.1038/srep18098.

[124] E. K. Storms and J. Griffin, 'The vaporization behavior of the defect carbides. IV. The zirconium-carbon system', *High Temp. Sci.*, vol. 5, no. 4, pp. 291–310, 1973.

[125] Taylor and Storms, 'THERMAL TRANSPORT IN REFRACTORY CARBIDES', in *International Conference on TheProceedings of the Fourteenth International Conference on Thermal Conductivity*, Connecticut, Jun. 1975, pp. 161–173. doi: 10.1007/978-1-4899-3751-.

[126] C. Nachiappan, L. Rangaraj, C. Divakar, and V. Jayaram, 'Synthesis and Densification of Monolithic Zirconium Carbide by Reactive Hot Pressing', *J. Am. Ceram. Soc.*, vol. 93, no. 5, pp. 1341–1346, May 2010, doi: 10.1111/j.1551-2916.2010.03608.x.

[127] J. T. Norton and R. K. Lewis, 'Properties Of Non-Stoichiometric Metallic Carbides', Advanced Metals Research Corporation, Somerville, Nasa Report Naw-663, 1964. [Online]. Available: https://ntrs.nasa.gov/archive/nasa/casi.ntrs.nasa.gov/19650026243.pdf

[128] F. Almeida Costa Oliveira, B. Granier, J.-M. Badie, J. Cruz Fernandes, L. Guerra Rosa, and N. Shohoji, 'Synthesis of tungsten sub-carbide W2C from graphite/tungsten powder mixtures by eruptive heating in a solar furnace', *Int. J. Refract. Met. Hard Mater.*, vol. 25, no. 4, pp. 351–357, Jul. 2007, doi: 10.1016/j.ijrmhm.2006.10.002.

[129] Y. Zhou, T. W. Heitmann, W. G. Fahrenholtz, and G. E. Hilmas, 'Synthesis of ZrCx with controlled carbon stoichiometry by low temperature solid state reaction', *J. Eur. Ceram. Soc.*, vol. 39, no. 8, pp. 2594–2600, Jul. 2019, doi: 10.1016/j.jeurceramsoc.2019.03.004.

[130] 'Hall–Petch relation and boundary strengthening', *Scr. Mater.*, vol. 51, no. 8, pp. 801–806, Oct. 2004, doi: 10.1016/j.scriptamat.2004.06.002.

[131] S. H. Whang, 'Introduction', in *Nanostructured Metals and Alloys*, Elsevier, 2011, pp. xxi–xxxv. doi: 10.1016/B978-1-84569-670-2.50028-9.

[132] E. O. Hall, 'The Deformation and Ageing of Mild Steel: III Discussion of Results', *Proc. Phys. Soc. Sect. B*, vol. 64, no. 9, pp. 747–753, Sep. 1951, doi: 10.1088/0370-1301/64/9/303.

[133] C. Ang, T. Williams, A. Seeber, H. Wang, and Y.-B. Cheng, 'Synthesis and Evolution of Zirconium Carbide via Sol–Gel Route: Features of Nanoparticle Oxide–Carbon Reactions', *J. Am. Ceram. Soc.*, vol. 96, no. 4, pp. 1099–1106, 2013, doi: 10.1111/jace.12260.

[134] Z. Dong *et al.*, 'Synthesis and pyrolysis behavior of a soluble polymer precursor for ultra-fine zirconium carbide powders', *Ceram. Int.*, vol. 41, no. 6, pp. 7359–7365, 2015, doi: https://doi.org/10.1016/j.ceramint.2015.02.039.

[135] Puech *et al.*, 'Analyzing the Raman Spectra of Graphenic Carbon Materials from Kerogens to Nanotubes: What Type of Information Can Be Extracted from Defect Bands?', *C — J. Carbon Res.*, vol. 5, no. 4, p. 69, Nov. 2019, doi: 10.3390/c5040069.
[136] P. Mallet-Ladeira *et al.*, 'A Raman study to obtain crystallite size of carbon materials: A better alternative to the Tuinstra–Koenig law', *Carbon*, vol. 80, pp. 629–639, Dec. 2014, doi: 10.1016/j.carbon.2014.09.006.
[137] A. C. Ferrari and J. Robertson, 'Interpretation of Raman spectra of disordered and amorphous carbon', *Phys. Rev. B*, vol. 61, no. 20, pp. 14095–14107, May 2000, doi: 10.1103/PhysRevB.61.14095.
[138] I. Childres, L. Jauregui, W. Park, H. Caoa, and Y. P. Chena, 'Raman Spectroscopy of Graphene and Related Materials', *New Dev. Photon Mater. Res.*, pp. 403–418, Jan. 2013.
[139] F. Tuinstra and J. L. Koenig, 'Raman Spectrum of Graphite', *J. Chem. Phys.*, vol. 53, no. 3, pp. 1126–1130, Aug. 1970, doi: 10.1063/1.1674108.
[140] T. Allen, J. Busby, M. Meyer, and D. Petti, 'Materials challenges for nuclear systems', *Mater. Today*, vol. 13, no. 12, pp. 14–23, Dec. 2010, doi: 10.1016/S1369-7021(10)70220-0.
[141] S. J. Zinkle and J. T. Busby, 'Structural materials for fission & fusion energy', *Mater. Today*, vol. 12, no. 11, pp. 12–19, Nov. 2009, doi: 10.1016/S1369-7021(09)70294-9.
[142] W. L. Dunn and J. K. Shultis, *Exploring Monte Carlo Methods*. Elsevier, 2011.
[143] G. H. Kinchin and R. S. Pease, 'REVIEW ARTICLES: The Displacement of Atoms in Solids by Radiation', *Rep. Prog. Phys.*, vol. 18, pp. 1–51, Jan. 1955, doi: 10.1088/0034-4885/18/1/301.
[144] R. E. Stoller, M. B. Toloczko, G. S. Was, A. G. Certain, S. Dwaraknath, and F. A. Garner, 'On the use of SRIM for computing radiation damage exposure', *Nucl. Instrum. Methods Phys. Res. Sect. B Beam Interact. Mater. At.*, vol. 310, no. Supplement C, pp. 75–80, Sep. 2013, doi: 10.1016/j.nimb.2013.05.008.
[145] J. Gan, Y. Yang, C. Dickson, and T. Allen, 'Proton irradiation study of GFR candidate ceramics', *J. Nucl. Mater.*, vol. 389, no. 2, pp. 317–325, May 2009, doi: 10.1016/j.jnucmat.2009.02.021.
[146] T. Fischer, *Materials Science for Engineering Students*. Academic Press, 2009.
[147] P. Rudolph, *Handbook of Crystal Growth: Bulk Crystal Growth*. Elsevier, 2014.
[148] N. Eliaz, *Degradation of Implant Materials*. Springer Science & Business Media, 2012.
[149] T. A. Mellan, A. I. Duff, B. Grabowski, and M. W. Finnis, 'Fast anharmonic free energy method with an application to vacancies in ZrC', *Phys. Rev. B*, vol. 100, no. 2, p. 024303, Jul. 2019, doi: 10.1103/PhysRevB.100.024303.
[150] P. Barnier, C. Brodhag, and F. Thevenot, 'Hot-pressing kinetics of zirconium carbide', *J. Mater. Sci.*, vol. 21, no. 7, pp. 2547–2552, Jul. 1986, doi: 10.1007/BF01114305.
[151] S. K. Sarkar, A. D. Miller, and J. I. Mueller, 'Solubility of Oxygen in ZrC', *J. Am. Ceram. Soc.*, vol. 55, no. 12, pp. 628–630, Dec. 1972, doi: 10.1111/j.1151-2916.1972.tb13457.x.
[152] W. Hu *et al.*, 'Superstructural nanodomains of ordered carbon vacancies in nonstoichiometric ZrC0.61', *J. Mater. Res.*, vol. 27, no. 9, pp. 1230–1236, May 2012, doi: http://dx.doi.org/10.1557/jmr.2012.72.

[153] M. Gendre, A. Maître, and G. Trolliard, 'A study of the densification mechanisms during spark plasma sintering of zirconium (oxy-)carbide powders', *Acta Mater.*, vol. 58, no. 7, pp. 2598–2609, Apr. 2010, doi: 10.1016/j.actamat.2009.12.046.

[154] W. F. Cureton *et al.*, 'Effects of irradiation temperature on the response of CeO2, ThO2, and UO2 to highly ionizing radiation', *J. Nucl. Mater.*, vol. 525, pp. 83–91, Nov. 2019, doi: 10.1016/j.jnucmat.2019.07.029.

[155] *Handbook of Ceramics Grinding and Polishing*. Accessed: Jun. 05, 2020. [Online]. Available: https://books.google.com/books/about/Handbook_of_Ceramics_Grinding_and_Polish.html?id=E0R0AwAAQBAJ

[156] P. Borowicz, 'Depth-Sensitive Raman Investigation of Metal-Oxide-Semiconductor Structures: Absorption as a Tool for Variation of Exciting Light Penetration Depth', *J. Spectrosc.*, vol. 2016, pp. 1–14, 2016, doi: 10.1155/2016/1617063.

[157] P. Borowicz, M. Latek, W. Rzodkiewicz, A. Łaszcz, A. Czerwinski, and J. Ratajczak, 'Deep-ultraviolet Raman investigation of silicon oxide: thin film on silicon substrate versus bulk material', *Adv. Nat. Sci. Nanosci. Nanotechnol.*, vol. 3, no. 4, p. 045003, Sep. 2012, doi: 10.1088/2043-6262/4/045003.

[158] R. Silva and S. R. P. Silva, *Properties of Amorphous Carbon*. IET, 2003.

[159] C. Schorn, B. F. Taylor, and B. J. Taylor, *NMR-Spectroscopy: Data Acquisition*. John Wiley & Sons, 2004.

[160] G. W. Keilholtz and R. E. Moore, 'Fast neutron stability of refractory metal carbides at high temperatures', *Trans. Am. Nucl. Soc.*, vol. 12, no. 1, pp. 101–105, 1969.

[161] *The Chemistry of the Actinide and Transactinide Elements (Set Vol.1-6)*. Accessed: Jun. 16, 2020. [Online]. Available: https://books.google.com/books/about/The_Chemistry_of_the_Actinide_and_Transa.html?id=9vPuV3A0UGUC

[162] M. Szuta, 'UO2 GRAIN SUBDIVISION FOR VERY DEEP BURN-UP AND RELATIVELY LOW TEMPERATURE AND ITS IMPACT ON FISSION GAS RELEASE', Institute of Atomic Energy ANNUAL REPORT 2007 Nuclear Technology in Energy Generation, 2007. [Online]. Available: https://inis.iaea.org/collection/NCLCollectionStore/_Public/39/101/39101892.pdf

[163] J. Rest and G. L. Hofman, 'Dynamics of irradiation-induced grain subdivision and swelling in U3Si2 and UO2 fuels', *J. Nucl. Mater.*, vol. 210, no. 1–2, pp. 187–202, Jun. 1994, doi: 10.1016/0022-3115(94)90237-2.

[164] E. H. Martins Ferreira *et al.*, 'Evolution of the Raman spectra from single-, few-, and many-layer graphene with increasing disorder', *Phys. Rev. B*, vol. 82, no. 12, p. 125429, Sep. 2010, doi: 10.1103/PhysRevB.82.125429.

[165] M. A. Pimenta, G. Dresselhaus, M. S. Dresselhaus, L. G. Cançado, A. Jorio, and R. Saito, 'Studying disorder in graphite-based systems by Raman spectroscopy', *Phys Chem Chem Phys*, vol. 9, no. 11, pp. 1276–1290, 2007, doi: 10.1039/B613962K.

[166] M. M. Lucchese *et al.*, 'Quantifying ion-induced defects and Raman relaxation length in graphene', *Carbon*, vol. 48, no. 5, pp. 1592–1597, Apr. 2010, doi: 10.1016/j.carbon.2009.12.057.

[167] M. Szuta, 'Xenon concentration in sub-divided fuel for very high burn-up in terms of defect trap model', Institute of Atomic Energy, Otwock-Świerk, Poland. [Online]. Available: https://www.osti.gov/etdeweb/servlets/purl/20593498

[168] D. W. Lee and J. S. Haggerty, 'Plasticity and Creep in Single Crystals of Zirconium Carbide', *J. Am. Ceram. Soc.*, vol. 52, no. 12, pp. 641–647, Dec. 1969, doi: 10.1111/j.1151-2916.1969.tb16067.x.

[169] J. S. Moya, M. Diaz, J. F. Bartolomé, E. Roman, J. L. Sacedon, and J. Izquierdo, 'Zirconium oxide film formation on zircaloy by water corrosion', *Acta Mater.*, vol. 48, no. 18–19, pp. 4749–4754, Dec. 2000, doi: 10.1016/S1359-6454(00)00267-6.

[170] A. Bellucci, D. Gozzi, T. Kimura, T. Noda, and S. Otani, 'Zirconia growth on zirconium carbide single crystals by oxidation', *Surf. Coat. Technol.*, vol. 197, no. 2–3, pp. 294–302, Jul. 2005, doi: 10.1016/j.surfcoat.2004.05.035.

[171] G. Pezzotti and A. A. Porporati, 'Raman spectroscopic analysis of phase-transformation and stress patterns in zirconia hip joints', *J. Biomed. Opt.*, vol. 9, no. 2, p. 372, 2004, doi: 10.1117/1.1647547.

[172] F. Réjasse, O. Rapaud, G. Trolliard, O. Masson, and A. Maître, 'Experimental investigation and thermodynamic evaluation of the C–O–Zr ternary system', *RSC Adv.*, vol. 6, no. 102, pp. 100122–100135, 2016, doi: 10.1039/C6RA21967E.

[173] R. Yan, Y. Dong, Y. Zhou, X. Sun, and Z. Li, 'Investigation of oxidation behaviors of nuclear graphite being developed and IG-110 based on gas analysis', *J. Nucl. Sci. Technol.*, Sep. 2017, Accessed: May 20, 2020. [Online]. Available: https://www.tandfonline.com/doi/abs/10.1080/00223131.2017.1344579

[174] M. Vannerem, 'Chemistry Of Operating Civil Nuclear Reactors', Office for Nuclear Regulation, Nuclear Safety Technical Assessment Guide NS-TAST-GD-088 Revision 2. [Online]. Available: http://www.onr.org.uk/operational/tech_asst_guides/ns-tast-gd-088.pdf

[175] D. Rana, E. Z. Solvas, W. E. Lee, and I. Farnan, 'An investigation of the long-range and local structure of sub-stoichiometric zirconium carbide sintered at different temperatures.', *(Submitted)*.

[176] E. N. Hoffman, D. W. Vinson, R. L. Sindelar, D. J. Tallman, G. Kohse, and M. W. Barsoum, 'MAX phase carbides and nitrides: Properties for future nuclear power plant in-core applications and neutron transmutation analysis', *Nucl. Eng. Des.*, vol. 244, pp. 17–24, Mar. 2012, doi: 10.1016/j.nucengdes.2011.12.009.

[177] W. M. Kriven, J. Wang, Y. Zhou, D. Zhu, and G. Costa, *Developments in Strategic Ceramic Materials II: A Collection of Papers Presented at the 40th International Conference on Advanced Ceramics and Composites, January 24-29, 2016, Daytona Beach, Florida*. John Wiley & Sons, 2017.

[178] Y. Bai, X. He, R. Wang, and C. Zhu, 'An ab initio study on compressibility of Al-containing MAX-phase carbides', *J. Appl. Phys.*, vol. 114, no. 17, 2013, doi: 10.1063/1.4829282.

[179] K. Lambrinou1, T. Lapauw, B. Tunca, and J. Vleugels, 'MAX Phase Materials for Nuclear Applications', in *Developments in Strategic Ceramic Materials II*, W. M. Kriven, J. Wang, Y. Zhou, D. Zhu, and G. K. Costa, Eds. John Wiley & Sons, Inc., 2017, pp. 223–233. doi: 10.1002/9781119321811.ch21.

[180] M. Sokol, V. Natu, S. Kota, and M. W. Barsoum, 'On the Chemical Diversity of the MAX Phases', *Trends Chem.*, vol. 1, no. 2, pp. 210–223, 2019, doi: 10.1016/j.trechm.2019.02.016.

[181] U. Carvajal Nuñez *et al.*, 'Coupling XRD, EXAFS, and 13C NMR to Study the Effect of the Carbon Stoichiometry on the Local Structure of UC1±x', *Inorg. Chem.*, vol. 52, no. 19, pp. 11669–11676, Oct. 2013, doi: 10.1021/ic402144g.

[182] M. Cuppari and S. Santos, 'Physical Properties of the NbC Carbide', *Metals*, vol. 6, no. 10, p. 250, Oct. 2016, doi: 10.3390/met6100250.

[183] R. V. Sara, 'The System Zirconium—Carbon', *J. Am. Ceram. Soc.*, vol. 48, no. 5, pp. 243–247, May 1965, doi: 10.1111/j.1151-2916.1965.tb14729.x.